

AN ABSTRACT OF THE THESIS OF

Alexei Shatalov for the degree of Doctor of Philosophy in Physics presented on July 21, 2000.

Title: Radiation Effects in III-V Semiconductors and Heterojunction Bipolar Transistors.

Redacted for privacy

Abstract approved: —

Subramanian Sivaramakrishnan

The electron, gamma and neutron radiation degradation of III-V semiconductors and heterojunction bipolar transistors (HBTs) is investigated in this thesis. Particular attention is paid to *InP* and *InGaAs* materials and *InP/InGaAs* abrupt single HBTs (SHBTs). Complete process sequences for fabrication of *InP/InGaAs* HBTs are developed and subsequently employed to produce the devices, which are then electrically characterized and irradiated with the different types of radiation. A comprehensive analytical HBT model is developed and radiation damage calculations are performed to model the observed radiation-induced degradation of SHBTs.

The most pronounced radiation effects found in SHBTs include reduction of the common-emitter DC current gain, shift of the collector-emitter (CE) offset voltage and increase of the emitter, base and collector parasitic resistances. Quantitative analysis performed using the developed model demonstrates that increase of the neutral bulk and base-emitter (BE) space charge region (SCR) components of the base current are responsible for the observed current gain degradation. The rise of the neutral bulk recombination is attributed to decrease in a Shockley-Read-

Hall (SRH) carrier lifetime, while the SCR current increase is caused by rising SCR SRH recombination and activation of a tunneling-recombination mechanism. On the material level these effects are explained by displacement defects produced in a semiconductor by the incident radiation. The second primary change of the SHBT characteristics, CE offset voltage shift, is induced by degradation of the base-collector (BC) junction. The observed rise of the BC current is brought on by diffusion and recombination currents which increase as more defects are introduced in a semiconductor. Finally, the resistance degradation is attributed to deterioration of low-doped layers of a transistor, and to degradation of the device metal contacts.

©Copyright by Alexei Shatalov

July 21, 2000

All rights reserved

Radiation Effects in III-V Semiconductors and

Heterojunction Bipolar Transistors

by

Alexei Shatalov

A Thesis

submitted to

Oregon State University

in partial fulfillment of
the requirements for the
degree of

Doctor of Philosophy

Completed July 21, 2000
Commencement June 2001

Doctor of Philosophy thesis of Alexei Shatalov presented on July 21, 2000

APPROVED:

Redacted for privacy

Major Professor, representing Physics

Redacted for privacy


Chair of the Department of Physics

Redacted for privacy

Dean of the Graduate School

I understand that my thesis will become part of the permanent collection of Oregon State University libraries. My signature below authorizes release of my thesis to any reader upon request.

Redacted for privacy

 Alexei Shatalov, Author

ACKNOWLEDGMENT

I would like to thank my advisor, Dr. S. Subramanian, for his guidance, help and inspiration during different stages of my work. In particular, his encouragement and advice during my first few steps in this project were simply invaluable.

I am also indebted to my family and especially my parents, Alexander and Valentina Shatalov, for their love, support, and understanding throughout the years of my studies at OSU and the long and often painful process of the dissertation writing.

This work was supported in part by the Air Force Office of Scientific Research Grant # F49620-9610173.

TABLE OF CONTENTS

	<u>Page</u>
1 INTRODUCTION	1
2 RADIATION DAMAGE FUNDAMENTALS	6
2.1 Fundamental Quantities	6
2.2 Radiation Environments	9
2.3 Radiation-Induced Damage	10
2.3.1 Displacement Damage Effects and Non-Ionizing Energy Loss	10
2.3.2 Total Dose Effects	14
2.3.3 PKA Energy Partitioning, Lindhard's Theory	17
2.3.4 Single Event Effects	20
2.4 Radiation Effects in III-V Compound Semiconductors	22
2.5 Radiation Effects in Bipolar Transistors	25
3 RADIATION DAMAGE IN III-V MATERIALS	27
3.1 Electron Irradiation	28
3.1.1 Interaction of Electron Irradiation with Matter	28
3.1.1.1 Electron Collision Stopping	29
3.1.1.2 Radiative Stopping Power	32
3.1.1.3 CSDA Range and Ionizing Energy Deposition	34
3.1.1.4 Nuclear Stopping Power	37
3.1.1.5 Displacement Damage, NIEL Calculations	39
3.1.2 Beta Irradiation Source	43
3.1.3 Experimental Details	47
3.2 Neutron Irradiation	48
3.2.1 Interaction of Neutron Irradiation with Matter	48
3.2.1.1 Absorption (n, γ) reactions	49

TABLE OF CONTENTS (Continued)

	<u>Page</u>
3.2.1.2 Elastic Scattering	51
3.2.1.3 Discrete Inelastic Scattering	52
3.2.1.4 Continuous Inelastic Scattering (n,n') and (n,2n) Reactions	52
3.2.1.5 (n, particle) Reactions	53
3.2.2 Implementation and Results	54
3.2.3 Displacement Damage Function	55
3.2.4 Neutron Damage Equivalence and NIEL	59
3.2.5 Experimental Details	64
3.3 Gamma Irradiation	64
3.3.1 Gamma Interactions in Matter	65
3.3.1.1 Compton Effect	66
3.3.1.2 Photoelectric Effect	69
3.3.1.3 Spectrum Resulting from Electron Slowing Down	72
3.3.2 Co^{60} Gamma-Source	73
3.3.3 Displacement Damage	74
3.3.4 Absorbed Dose	75
3.3.5 Possible Limitations	78
3.4 Summary	80
4 HETEROJUNCTION BIPOLAR TRANSISTORS	82
4.1 HBT Basics	83
4.1.1 HBT Materials, Structures and Performance	83
4.1.2 Terminal Currents	87
4.1.3 Operation	89
4.2 Bipolar Transistor Electrical Characterization	91
4.3 Compact Models	93
4.3.1 Junction Currents	95
4.3.2 Parameter Extraction	100

TABLE OF CONTENTS (Continued)

	<u>Page</u>
4.3.3 Calculation of $I_C - V_{CE}$ Characteristics	105
4.4 Analytical Model.....	106
4.4.1 Emitter-Base Heterojunction Modeling	107
4.4.2 Carrier Transport in HBT	112
4.4.3 Base Recombination Currents	117
4.4.4 Tunnel-Assisted Trapping	129
4.4.5 High Level Injection Effects	133
4.5 Ebers-Moll and Gummel-Poon Models.....	135
4.5.1 Collector Current in Active Mode	140
4.5.2 Base Currents in Active Mode	141
4.5.3 Saturation Mode Analysis	142
4.6 HBT High Frequency Performance	145
4.7 Summary	151
5 HBT FABRICATION.....	153
5.1 SHBT Heterostructure Growth.....	153
5.2 Mask Set Design	155
5.2.1 DC HBT Unit Cells	157
5.2.2 RF HBT and RF Calibration Structures Unit Cells	159
5.2.3 Test Structures	161
5.2.4 Alignment Marks	163
5.2.5 DIE Layout. Mask Plates	163
5.3 Processing Steps	164
5.3.1 Cleaning	165
5.3.2 Photolithography	167
5.3.3 Wet Etches	168

TABLE OF CONTENTS (Continued)

	<u>Page</u>
5.3.4 Passivation Techniques	170
5.3.5 Reactive Ion Etching	172
5.3.6 Metallization	173
5.4 Process Flow	177
 6 IRRADIATION EFFECTS	 180
6.1 Beta Irradiation	181
6.1.1 Experimental Details	182
6.1.2 Experimental Results and Discussion	183
6.1.2.1 Analysis of BC Diode Saturation Current	191
6.1.2.2 Gummel Plots and Gain Degradation Mechanisms	192
6.1.2.3 Comparison with Unpassivated Devices	196
6.1.2.4 P/A Ratio Dependence of Gain Degradation	199
6.1.2.5 Degradation Variation	200
6.1.3 Conclusions	202
6.2 Neutron Irradiation	204
6.2.1 Experimental Details	205
6.2.2 Radiation-Induced Device Degradation	206
6.2.2.1 Gain Degradation Mechanisms	207
6.2.2.2 Gain Degradation Coefficient	227
6.2.2.3 Base Collector Diode Degradation	228
6.2.2.4 $V_{CE,off}$ shift	230
6.2.3 Conclusions	237
6.3 Gamma Irradiation	237
6.3.1 Experimental Details	238
6.3.2 Results and Discussion	239
6.3.3 Radiation-hard Metallization Schemes	244
6.3.4 Summary	249

TABLE OF CONTENTS (Continued)

	<u>Page</u>
6.4 Conclusions	250
7 CONCLUSIONS AND RECOMMENDATIONS FOR FUTURE WORK .	254
BIBLIOGRAPHY	263

LIST OF FIGURES

<u>Figure</u>	<u>Page</u>
1.1 Radiation-induced effects modeling tree.	4
2.1 Defect and subcluster formation as a function of initial PKA energy.	11
2.2 Electrical effects associated with defect energy levels introduced in semiconductor bandgap by irradiation.	13
2.3 Fraction of PKA energy available for dislodging atoms as a function of PKA energy.	20
2.4 Ionization channel induced by an incident heavy particle in MOS transistor. Examples of induced current transients flowing between terminals of MOS transistor.	21
3.1 Interactions of electrons with matter – mechanisms involved in energy transfer.	29
3.2 Electron collision mass stopping powers for electrons in <i>Si</i> , <i>InP</i> , <i>InGaAs</i> , <i>Au</i> and polyimide.	32
3.3 Radiative mass stopping powers for electrons in <i>Si</i> , <i>InP</i> , <i>InGaAs</i> , <i>Au</i> and polyimide.	34
3.4 CSDA ranges for electrons in <i>Si</i> , <i>InP</i> , <i>InGaAs</i> , <i>Au</i> and polyimide.	35
3.5 Total ionizing dose rate for electrons of energy 1 MeV in layer of silicon.	37
3.6 Calculated non-ionizing energy loss for electrons in <i>Si</i> , <i>GaAs</i> , <i>InGaAs</i> and <i>InP</i>	41
3.7 Schematic of β -source and sample positioning for irradiation.	44
3.8 Series of beta-emitting transitions taking place in the $^{90}\text{Sr}/^{90}\text{Y}$ beta source. The initial cooling down of ^{90}Y by gamma emission (half-life of 3.19 hours) is not shown.	45
3.9 Beta energy spectrum of $^{90}\text{Sr}/^{90}\text{Y}$ beta-source in secular equilibrium (dashed line) and the calculated slowed down spectrum (solid line).	46

LIST OF FIGURES (Continued)

<u>Figure</u>	<u>Page</u>
3.10 Cross sections for radiative capture and elastic, continuum inelastic and discrete inelastic scattering as function of incident neutron energy for <i>Si</i>	50
3.11 Calculated displacement kermas for indium, gallium and arsenic. . .	56
3.12 Calculated displacement kermas for <i>In</i> , <i>P</i> and <i>InP</i>	57
3.13 Calculated displacement kermas for <i>InGaAs</i>	58
3.14 Gallium arsenide damage function, F_D^{GaAs} , normalized by factor of 2.2, and displacement kerma, K_D^{GaAs} , and silicon displacement kerma function, K_D^{Si}	59
3.15 Neutron damage efficiency function for gallium arsenide.	60
3.16 Differential neutron energy spectrum at position of sample during neutron irradiation.	61
3.17 Cross sections for Compton and Rayleigh scattering, photoelectric and photonuclear effects and electron-positron pair production in electron and nuclear fields in <i>InP</i>	66
3.18 Single Compton scattering event.	67
3.19 Compton electron differential energy flux, i.e. Klein-Nishina energy differential cross section, and the slowed down energy spectrum calculated for <i>InGaAs</i>	68
3.20 Cross sections for Compton scattering and photoelectric effect for <i>InGaAs</i> , <i>GaAs</i> , <i>Si</i> , <i>Au</i> and polyimide.	70
3.21 Differential flux of slowed down Compton electrons for <i>InGaAs</i> , <i>InP</i> , <i>GaAs</i> , <i>Si</i> , <i>Au</i> and polyimide.	73
3.22 a) Typical plot of energy deposition in material; b) schematic illustration of dose enhancement effects at low photon energies.	79
3.23 Schematic illustration of dose enhancement effects at high photon energies.	81

LIST OF FIGURES (Continued)

<u>Figure</u>	<u>Page</u>
4.1 Energy band structure of (a) bipolar junction transistor and (b) heterojunction bipolar transistor biased in the active mode.	84
4.2 Energy band diagrams of (a) abrupt single HBT, (b) graded single HBT, (c) abrupt double HBT and (d) graded double HBT.	85
4.3 Currents within npn HBT.	88
4.4 Common-emitter current-voltage characteristics.	90
4.5 BE, BC, and CE voltages as a function of V_{CE} at $I_B = 60 \mu A$ in common-emitter configuration.	91
4.6 Measurement setup, consisting of a PC, SPA HP4145B and a microprobe station equipped with microscope, used for current-voltage characterization of devices.	92
4.7 Circuit configurations used for measurements of (a) common emitter $I - V$ characteristics ($I_C - V_{CE}$), (b) Gummel plots of base and collector currents, and (c) inverse Gummel plots of emitter and base currents.	93
4.8 Common-emitter current-voltage characteristics of device AN3m measured at different base currents (solid line), and characteristics calculated using Gummel-Poon model (dashed line).	94
4.9 Gummel plots of collector and base currents for device AN3m (solid lines), and calculated curves including leakage current (dashed lines).	95
4.10 Inverse Gummel plots of base and emitter currents for device AN3m (solid lines), and calculated curves (dashed lines).	96
4.11 Equivalent circuit of an npn-HBT including parasitic resistances of emitter, base and collector.	100
4.12 Forward Gummel plots of collector and base currents demonstrating parasitic effects of emitter, collector and base resistance.	102
4.13 Estimation of the emitter parasitic resistance from the slope of ΔV_{BE} vs I_E	104

LIST OF FIGURES (Continued)

<u>Figure</u>	<u>Page</u>
4.14 Energy band diagrams of n-type <i>InP</i> emitter and p-type <i>InGaAs</i> base layers (a) before and (b) after heterojunction formation.	107
4.15 Energy band diagram of forward-biased <i>InP/InGaAs</i> emitter-base heterojunction.	109
4.16 Field emission tunneling coefficient as a function of applied base-emitter voltage.	111
4.17 Energy band diagram of an SHBT biased in the active mode.	113
4.18 Calculated collector current density as a function of base emitter voltage.	118
4.19 Inverse current gain as a function of perimeter-to-area ratio for devices with different geometry.	120
4.20 Calculated collector current and neutral bulk and space charge base recombination currents.	123
4.21 Calculated SRH recombination rate, electron and hole concentrations as function of position in the base layer (midgap traps; BE bias is 0.8 V).	126
4.22 Recombination rate as a function of position and applied BE bias.	127
4.23 Base SCR recombination current as a function of BE applied voltage for different electron lifetimes at fixed hole lifetime.	128
4.24 Base SCR recombination current as a function of BE applied voltage for different hole lifetimes at fixed electron lifetime.	129
4.25 Base SCR recombination current as a function of BE applied voltage for different single level traps.	130
4.26 (a) Diagram illustrating multistep electron tunneling process in <i>Si</i> junction; (b), (c) and (d) three major current transport mechanisms involving tunneling of electron into trap states in <i>InP/InGaAs</i> heterojunctions.	132
4.27 Energy band diagram of an SHBT biased in the active mode operated in the quasi-saturation regime.	136

LIST OF FIGURES (Continued)

<u>Figure</u>	<u>Page</u>
4.28 BJT Ebers-Moll static model implemented in SPICE.	137
4.29 BJT Gummel-Poon static model implemented in SPICE.	139
4.30 Experimental and calculated forward Gummel plots for device BAxM3.	140
4.31 Experimental and calculated forward Gummel plots for device BAxM1.	143
4.32 Experimental and calculated $I_C - V_{CE}$ characteristics for five differ- ent devices at $I_B = 40 \mu A$	145
4.33 Two-port linear network representation of a transistor: (a) general case, (b) y-parameter model.	147
4.34 Hybrid-pi representation of a transistor.	148
4.35 Two-port S-parameter definition schematic.	149
5.1 Qualitative cross-section of $InP/InGaAs$ polyimide-passivated SHBT.	154
5.2 Layout of DC HBT showing different layers of the mask.	158
5.3 Mask layout of DC HBT unit cells.	160
5.4 Mask layout of RF HBT unit cell.	160
5.5 RF structures for calibration of RF vector network analyzer.	161
5.6 Mask layout of the unit cell with the test structures.	162
5.7 Alignment marks used in the mask layout.	164
5.8 Mask layout of the entire unit cell for HBT fabrication.	165
5.9 Level #1 of the mask (includes nine unit cells).	166
5.10 Two layers of mask layout for diode fabrication.	167
5.11 Plates 1 and 2 with the eight levels of mask layout.	167
5.12 Metal patterning by lift-off with chlorobenzene soak.	175

LIST OF FIGURES (Continued)

<u>Figure</u>	<u>Page</u>
5.13 Schematic of HBT cross section after the base mesa etch.	178
5.14 Schematic of HBT cross section after the isolation mesa etch.	178
5.15 Schematic of HBT cross section after the isolation mesa etch and deposition of the terminal contacts.	179
6.1 The common emitter $I - V$ ($I_C - V_{CE}$) characteristics of an <i>InP/InGaAs</i> SHBT at different base currents (I_B) prior to irra- diation. Emitter area of $750 \mu m^2$	184
6.2 The common emitter $I - V$ ($I_C - V_{CE}$) characteristics of the same device (as in Fig. 6.1) at different base currents (I_B) after electron irradiation.	185
6.3 The common emitter $I - V$ ($I_C - V_{CE}$) characteristics of the same device (as in Fig. 6.1) at base current of $50 \mu A$ for various interme- diate doses.	186
6.4 DC current gain as a function of electron fluence.	187
6.5 Gummel plots of I_C and I_B for various intermediate doses.	188
6.6 Collector current gain of DC current gain for different intermediate doses. The measurements are performed at $V_{CE} = 1.5$	189
6.7 Semilog plot of BC diode current-voltage characteristics for different intermediate doses.	190
6.8 BC diode generation-recombination saturation current as a function of electron fluence.	192
6.9 Energy of incident electrons, E , and TIDR for electrons as they pass through layers of SHBT.	197
6.10 BC diode generation-recombination saturation current as a function of electron fluence.	200
6.11 Initial DC gain distribution for entire device "population".	201
6.12 Distribution of radiation-induced changes in DC gain parameter for entire device "population" after the highest dose.	202

LIST OF FIGURES (Continued)

<u>Figure</u>	<u>Page</u>
6.13 Distribution of radiation-induced changes in $V_{CE,sat}$ for entire device “population” after the highest dose.	203
6.14 The common emitter $J_C - V_{CE}$ characteristics measured at base currents of 0, 10, 20, 30, 40, 50 and 60 μA before and after $2.0 \times 10^{14} \text{ n/cm}^2$ (1 MeV (InGaAs)) irradiation for device ID:BAxM. . . .	207
6.15 The common emitter $J_C - V_{CE}$ characteristics of the same device (as in Fig. 6.14) at base current of 40 μA for different intermediate doses.	208
6.16 DC current gain as a function of the collector current density for different intermediate doses.	210
6.17 Inverse DC current gain as a function of neutron fluence for $V_{BE} = 0.65 \text{ V}$ and $V_{BE} = 0.95 \text{ V}$	211
6.18 DC current gain degradation coefficient as a function of collector current.	212
6.19 Gummel plots of J_C and J_B for various intermediate doses.	213
6.20 Initial, β_0 , and final, β_f , DC current gains measured at constant $J_C = 250 \text{ A/cm}^2$ as a function of perimeter-to-area ratio for different devices.	215
6.21 Normalized DC current gain degradation as a function of perimeter-to-area ratio for different devices.	216
6.22 Measured (thick lines) and calculated (thin grey lines) current-voltage characteristics of large-area BE diodes for different intermediate doses.	220
6.23 Measured and calculated forward Gummel plots for unirradiated device BA1M0.	222
6.24 Measured (solid lines) and calculated (dashed lines) forward Gummel plots for devices irradiated to (a) 2.3×10^{13} and (b) $6.7 \times 10^{13} \text{ n/cm}^2$ (1 MeV (InGaAs)).	224

LIST OF FIGURES (Continued)

<u>Figure</u>	<u>Page</u>
6.25 Measured (solid lines) and calculated (dashed lines) forward Gummel plots for devices irradiated to (a) 2×10^{14} and (b) $6 \times 10^{14} \text{ n/cm}^2$ (1 MeV (InGaAs)).	226
6.26 Inverse Gummel plots of J_B and J_E for various intermediate doses. .	229
6.27 Experimental and calculated $I_C - V_{CE}$ characteristics for five different devices at $I_B = 40 \text{ } \mu\text{A}$	233
6.28 I_C ($I_{C,BE}$) from forward Gummel plots and I_B ($I_{C,BC}$) from inverse Gummel plots for various intermediate doses.	235
6.29 $V_{CE,off}$ extracted from $J_C - V_{CE}$ and Gummel plots as a function of neutron fluence.	236
6.30 The common emitter $I_C - V_{CE}$ characteristics at base current of $40 \text{ } \mu\text{A}$ for different intermediate doses (device ID:AN1Q).	240
6.31 Gummel plots of I_C and I_B for various intermediate doses (device ID:AN1Q).	241
6.32 Inverse Gummel plots of I_B and I_E for various intermediate doses (device ID:AN1Q).	242
6.33 DC current gain as a function of collector current for different intermediate doses (device ID:AN1Q).	243
6.34 The common emitter $I_C - V_{CE}$ characteristics at base current of $40 \text{ } \mu\text{A}$ for different intermediate doses (device ID:AN2Y).	244
6.35 DC current gain as a function of collector current for different intermediate doses (device ID:AN2Y).	245
6.36 Gummel plots of I_C and I_B for various intermediate doses (device ID:AN2Y).	246
6.37 Inverse Gummel plots of I_B and I_E for various intermediate doses (device ID:AN2Y).	247
6.38 Semilogarithmic plot of $I - V$ characteristics of BE diode for various intermediate doses (device ID:AN2Y).	248

LIST OF FIGURES (Continued)

<u>Figure</u>	<u>Page</u>
6.39 Semilogarithmic plot of $I - V$ characteristics of BC diode for various intermediate doses (device ID:AN2Y).	249
6.40 The common emitter $I_C - V_{CE}$ characteristics at base current of $40 \mu A$ for different intermediate doses (device ID:AN4O).	250
6.41 Gummel plots of I_C and I_B for various intermediate doses (device ID:AN4O).	251
6.42 Cumulative number of degraded HBT's as a function of total gamma dose.	252
7.1 Modeling tree used to explain/simulate HBT degradation effects induced by irradiation.	256

LIST OF TABLES

<u>Table</u>	<u>Page</u>
2.1 Displacement threshold energies for different semiconductor materials.	19
2.2 Trap energy and capturing cross section for H3, H4, H5, EA and EB traps in <i>InP</i>	24
3.1 Material parameters used for calculation of stopping powers for <i>Al</i> , <i>Si</i> , <i>P</i> , <i>Ga</i> , <i>As</i> , <i>In</i> , <i>Au</i> , <i>InGaAs</i> , <i>InP</i> and polyimide ($C_{22}N_2H_5(OH)_5$ composition is assumed for polyimide).	33
3.2 Electron-collision and radiative stopping powers, ionizing dose introduced by one electron and total ionizing dose rate of electron flux at incident electron energy of 1 <i>MeV</i> for <i>Si</i> , <i>Au</i> , <i>InGaAs</i> , <i>InP</i> and polyimide.	38
3.3 Displacement introduction rate, non-ionizing energy loss for 1 <i>MeV</i> electrons and number of displacements produced by flux of 1 <i>MeV</i> electrons that introduce 1 <i>rad</i> (<i>Si</i>) of ionizing dose.	43
3.4 Exposure durations used in the study and corresponding cumulative electron fluences, ionizing doses, displacement doses, and number of radiation-induced displacements calculated for the base region of an HBT.	47
3.5 Reactions used in calculations of displacement kerma for <i>Si</i> , <i>P</i> , <i>Ga</i> , <i>As</i> and <i>In</i> . Indices in (n, n'_i) row refer to discrete level reactions. . .	55
3.6 Damage functions (displacement kerma in case of <i>InGaAs</i> and <i>InP</i>) at 1 <i>MeV</i> , 1 <i>MeV</i> equivalent fluxes for epi-thermal and fast neutrons and total 1 <i>MeV</i> equivalent flux at RSR facility for <i>Si</i> , <i>GaAs</i> , <i>InGaAs</i> and <i>InP</i> . Equivalent flux values are for reactor operated at 100 <i>kW</i>	62
3.7 Damage function (displacement kerma in case of <i>InGaAs</i> and <i>InP</i>), neutron NIEL and displacement introduction rate at 1 <i>MeV</i> for <i>Si</i> , <i>GaAs</i> , <i>InGaAs</i> and <i>InP</i>	63
3.8 Exposure duration, corresponding total neutron fluence and 1 <i>MeV</i> equivalent fluences for <i>Si</i> , <i>InGaAs</i> and <i>InP</i> for neutron irradiation experiment.	64

LIST OF TABLES (Continued)

<u>Table</u>	<u>Page</u>
3.9 Cross sections for Compton scattering and photoelectric effect at $E_\gamma = 1.25 \text{ MeV}$, corresponding total primary Compton electron flux and total slowed down Compton electron flux produced by one incident gamma for <i>Si</i> , <i>Au</i> , <i>GaAs</i> , <i>InGaAs</i> , <i>InP</i> and polyimide. . .	71
3.10 Non-ionizing energy loss, displacement dose for 1.25 <i>MeV</i> photon, and equivalent 1 <i>MeV</i> electron fluence and number of displacements for 1 <i>Mrad(Si)</i> for <i>Si</i> , <i>GaAs</i> , <i>InGaAs</i> and <i>InP</i>	76
3.11 Results of dosimetry and damage production calculations for electron, gamma and neutron irradiation for <i>Si</i> , <i>GaAs</i> , <i>InGaAs</i> and <i>InP</i>	81
4.1 Extracted values of saturation currents and ideality factors for base and collector currents.	101
4.2 Heterostructure and bulk <i>InP</i> and <i>InGaAs</i> parameters used in calculations (at 300 <i>K</i> , low frequency).	117
4.3 Gummel-Poon model parameters used to simulate $V_{CE,off}$ shift observed in different devices.	146
5.1 MOCVD grown HBT heterostructure parameters (wafer I3420). . . .	155
5.2 Emitter perimeters, areas and perimeter-to-area ratios for the devices in DC HBT unit cells.	159
5.3 Emitter perimeters, areas and perimeter-to-area ratios for the RF and test HBTs.	161
5.4 Typical wet etch mixtures and etch times used to remove layers of HBT heterostructure (wafer I3420).	169
5.5 Typical PECVD process parameters used for deposition of silicon nitride, dioxide and oxynitride.	173
5.6 RIE process parameters used for etching of polyimide, cyclotene, silicon nitride and silicon dioxide.	174

LIST OF TABLES (Continued)

<u>Table</u>	<u>Page</u>
6.1 Base-collector ideality factor, n_{BC} , base-collector diode saturation current, I_{BC}^{sat} at $V_{BC} = 0.29 \text{ V}$ (determined by fitting the inverse Gummel plots).....	193
6.2 Saturation current and ideality factor for the collector current, and emitter series resistance extracted from forward Gummel plots of the collector current for different neutron fluences.	214
6.3 GP and analytical model parameters used to fit base current at different intermediate doses. (“t/n” – term neglected).....	218
6.4 Saturation current and ideality factor parameters used to fit current of large-area BE diodes in low bias regime at different intermediate doses.	221
6.5 Saturation currents and ideality factors determined from inverse Gummel plots of base current before and after neutron irradiation. .	231
6.6 Saturation currents of the diffusion and recombination J_{BC} components determined from inverse Gummel plots of base current after neutron irradiation.	232
6.7 Stability of gamma-irradiated various metal films deposited on different substrates.	253

RADIATION EFFECTS IN III-V SEMICONDUCTORS AND HETEROJUNCTION BIPOLAR TRANSISTORS

1. INTRODUCTION

Since the first discovery of radiation-induced failures¹ in electronic devices in 1954 [1], tremendous efforts have been put into research of the radiation degradation of semiconductors. Due to its commercial success silicon has received most of the attention, while gallium arsenide, indium phosphide and other III-V compound materials stayed in a background. Only in the late 1970s and early 1980s, major technological breakthroughs, mainly development of molecular beam epitaxy (MBE) and metal-organic chemical vapor deposition (MOCVD) made a wide variety of III-V semiconductors available to engineer high-performance devices. Superior electron transport properties and opportunity to control material bandgap during device fabrication are examples of many advantages of III-V compounds over conventional silicon. Since then a large number of *GaAs* and *InP* based technologies/devices have been developed and industrially implemented. Among them, one of the most important devices is the heterojunction bipolar transistor (HBT), which is similar to a bipolar junction transistor (BJT), but uses a wide

¹electronic failures during nuclear bomb tests

bandgap material for the emitter layer. Main applications of these devices are in high performance lightweight electronic communication systems used in military and commercial space satellites. The recent boost of wireless and other high-end communications continues to draw more and more attention to reliable long-term performance of these devices under irradiation. As a result, the radiation reliability of compound semiconductor heterostructure devices has received much attention in the recent years [2–7]. First experimental studies showed that III-V based HBTs show superior resistivity to electron, gamma and neutron radiations comparing to that of high-performance *Si* BJTs [8–10]. Theoretical work so far has been mostly focused on the bulk semiconductor damage, not touching the problem of degradation of the device as a whole. Furthermore, even when considering material damage, only popular *GaAs* and *InP* have been studied to some extent, leaving *InGaAs* territory virtually unexplored.

Still “immature”, HBTs lattice matched to *InP* substrates (based on *InP/InGaAs* and *InAlAs/InP* heterojunctions) are finding increased use in a number of high-speed analog, digital and mixed signal applications [11]. Attractive features of these devices include higher electron mobility in the *InGaAs* base layer, higher velocity overshoot in the collector, lower surface recombination velocity compared to the *AlGaAs/GaAs* HBTs and higher thermal conductivity of the *InP* substrates. In addition, the higher radiation tolerance of *InP* is an important consideration for radiation environment applications.

The primary purpose of this thesis is to experimentally study the radiation degradation of *InP/InGaAs* HBTs and to form a theoretical basis needed for evaluation/modeling of radiation-induced effects in these devices. Indisputably success of this work requires solid understanding of radiation degradation of semiconductor materials and details of HBT operation. Moreover, in order to model the radia-

tion effects quantitatively, comprehensive models for the both radiation damage and HBT operation are needed. To explain the steps involved in the process of analysis and modeling of the device radiation degradation, we consider the diagram shown in Fig. 1.1. First, experimentally observed individual changes in the device characteristics are categorized. These effects are then considered separately to identify changes in the material parameters which may be responsible for the detected damage. On this step device models have to be engaged to connect the two levels of the diagram. Depending on the situation device models of different complexity may be needed. Relatively simple compact empirical models are used to separate terminal currents of the device into individual components representing different current transport mechanisms. Also more advanced Ebers-Moll and Gummel-Poon models are employed for the same task. Additionally, they can be used to relate the device output characteristics with the parameters of the HBT structure. On the next level of the diagram an analytical HBT model is employed to establish a link between the parameters of the device and properties of the device layers. The analytical model should therefore account for all the important current components, for example, thermionic-field-emission current, SRH recombination currents in depletion and neutral base regions, recombination-tunneling currents, Auger and radiative recombination currents, and so on.

To summarize, we once again present a list of individual steps required to accomplish our goal:

1. Calculations of radiation induced damage in the layers of an HBT.
2. HBT models of different levels and complexity.
3. Experimental studies of radiation-induced degradation of HBTs.

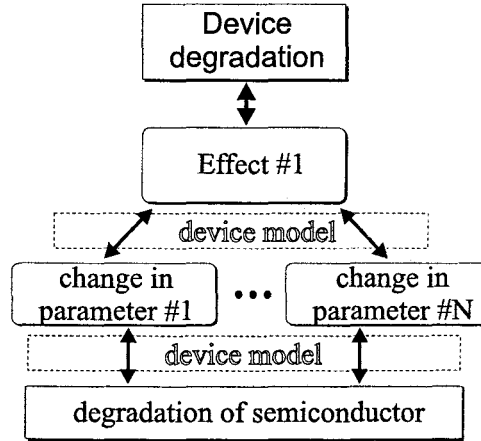


FIGURE 1.1. Radiation-induced effects modeling tree.

4. Detailed analysis of the observed degradation to identify and model changes in:

- (a) output characteristics of the device;
- (b) individual current components;
- (c) device layer parameters.

Having performed all of these steps the device response to any given radiation environment can be estimated.

The structure of this thesis (and its chapters) is built to accomplish the tasks set above. Chapter 2 introduces fundamental dosimetry and damage theory quantities and gives a brief overview of radiation effects observed in semiconductors and bipolar transistors. Chapter 3 presents the damage production calculations for beta, neutron (epi-thermal and fast neutrons) and gamma irradiation. Chapter 4 investigates the theory of HBT operation and concentrates on the development of a comprehensive device model. Chapter 5 covers techniques and processes em-

ployed in the fabrication of *InP/InGaAs* and *AlGaAs/GaAs* HBTs. Chapter 6 offers results and discussion of *InP/InGaAs* HBT electron, neutron and gamma irradiation experiments. Finally, Chapter 7 presents the conclusions of this work.

2. RADIATION DAMAGE FUNDAMENTALS

Energetic particles such as neutrons, protons, electrons, gammas, and ions present in the natural space and other radiation environments can create significant damage in semiconductor materials and devices by displacing atoms and generating charges as the particles traverse the material. Based on the nature of damage created by radiation effects they are usually divided into three primary groups (1) Displacement damage effects (DDE) result from the dislodgement of the atoms from their sites in a crystal lattice that affect the bulk properties of the materials mostly. (2) Total dose effects (TDE) are those which result from the charge and charge center generation by ionizing radiation. These effects are mainly responsible for degradation of devices sensitive to the surface condition (e.g. MOS technologies). (3) Finally, there are single event effects (SEE) resulting from the interactions with a single or a burst of high energy particles passing through the device. For example, an energetic heavy ion can produce displacement spikes and/or induce the so-called ionization channels up to a few microns in diameter. Produced charge can cause significant current and/or voltage transients which may change the state of a circuit or even result in a permanent damage.

The objective of this chapter is to define the fundamental quantities, introduce the physical mechanisms responsible for the radiation damage induced by electron, gamma and neutron irradiation, and present brief literature review on the radiation degradation of III-V compound semiconductors and bipolar devices.

2.1. Fundamental Quantities

Before continuing with the discussion of the radiation effects and the damage production theory it is necessary to introduce a few fundamental quantities.

Most of the definitions provided herein follow the recommendations of the International Committee on Radiation Units and Measurements (ICRU).

The particle fluence Ψ is the total number of all particles entering a sphere of unit cross-sectional area

$$\Psi = \frac{dN_{tot}}{da} \quad (2.1)$$

In terms of differential particle fluence, $\psi = d\Psi/dE$, the particle fluence may be written as

$$\Psi = \int_0^{\infty} \frac{d\psi(E)}{dE} dE \quad (2.2)$$

The total and differential particle fluxes are simply defined as $\Phi = d\Psi/dt$ and $\phi = d\psi/dt$, respectively.

The mean energy, E_D , deposited in the mass element dm by ionizing radiation is given by

$$E_D = \sum E_{in} - \sum E_{out} + \sum Q \quad (2.3)$$

where E_{in} is the energy of ionizing radiation entering dm , E_{out} is the energy leaving it, and $\sum Q$ is the total energy produced in dm . The quotient of the mean absorbed energy dE_D by dm is called **the absorbed dose**

$$D = \frac{dE_D}{dm} \quad (2.4)$$

and is measured in units of *gray* – 1 *gray* = 1 J/kg. It is more customary, however, to use units of *rad* – 1 *rad* = 10⁻² *gray*.

For indirectly ionizing radiation, e.g. neutrons, the kerma factor is used instead of the absorbed dose. The **kerma** K is defined as

$$K = \frac{dE_K}{dm} \quad (2.5)$$

where dE_K is the initial kinetic energy received by all the charged particles in a volume element of mass dm .

Attenuation is described as a reduction in the intensity of an incident beam as it traverses material. Denoting $d\phi/\phi$ as a fraction of particles that experience reactions, **cross section** σ can be defined as the reaction probability per incident particle divided by the number of targets per unit area:

$$\sigma = \frac{-d\phi/\phi}{n_v dx} \quad (2.6)$$

where n_v is the number of targets per unit volume and dx is thickness of the target material. **Attenuation coefficient** μ is defined as

$$\mu = n_v \sigma \quad (2.7)$$

Then the number of particles as a function of thickness can be written as

$$N(x) = N(0)e^{-\mu x} \quad (2.8)$$

For independent processes the attenuation coefficients (cross sections) can be added to obtain the total attenuation (cross section)

$$\mu = \sum_i \mu_i \quad (2.9)$$

The mass energy transfer coefficient μ_{tr}/ρ is defined as

$$\mu_{tr}/\rho = \frac{dE_{tr}/NE}{\rho dx} \quad (2.10)$$

where dE_{tr}/NE represents the fraction of the incident particle kinetic energy transferred to kinetic energy of liberated charged particles. **The mass energy absorption coefficient** μ_{en}/ρ

$$\mu_{en}/\rho = \frac{dE_{absorbed}/NE}{\rho dx} \quad (2.11)$$

serves as a measure of the energy absorbed in the layer dx . For compounds or mixtures of materials $(\mu/\rho)_{mix}$ is found as weighted sum of $(\mu/\rho)_i$ for all the constituents

$$(\mu/\rho)_{mix} = \sum_i w_i (\mu/\rho)_i \quad (2.12)$$

Finally, since needed for further calculations, recall that the number of atoms per unit volume can be calculated from

$$n_a = \frac{\rho}{A} N_A \quad (2.13)$$

where ρ and A are the density and atomic weight of the material, respectively, and N_A is Avogadro's number.

2.2. Radiation Environments

In our time semiconductor devices can be found in practically any piece of equipment, and are operated in a wide variety of conditions. While some applications offer clean mild environments, others may subject semiconductor systems to a lot of stress including radiation. Military and commercial space satellites are constantly exposed to natural radiation present in the natural space environment. High energy electrons (few MeV) and protons (few hundred MeV) trapped in the magnetic field of the Earth, cosmic rays (nuclei with energies up to few ZeV), solar particles and cascades of gammas and neutrons are the typical radiation hazards present in space [12]. Relative and absolute magnitude of the fluxes and energies of different particles typically vary as a function of altitude and position. But even at the lower end, in the orbits of the manned spacecraft missions, potentially dangerous radiation levels are detected [12, 13]. Other radiation environments include military applications where significant exposures to neutron and gamma radiation

are expected; semiconductor manufacturing (ions, betas and x-rays) and medicine (gammas, x-rays, betas and neutrons).

2.3. Radiation-Induced Damage

Having introduced the fundamental quantities we proceed with the more detailed discussion of the radiation damage effects. At this point we will not concern ourselves with the particular interaction mechanisms, which depend on the type of radiation and material; only the effects resulting from these interactions will be considered.

2.3.1. Displacement Damage Effects and Non-Ionizing Energy Loss

A high energy particle, e.g. neutron, traversing the material can displace atoms from their normal sites in the lattice. A struck and displaced atom, often called primary knock-on atom (PKA), propagates through the solid and, providing it has sufficient energy, can also dislodge other matrix atoms before coming to rest. Furthermore, in some cases the secondary knock-on atoms can obtain energy sufficient to displace more atoms, therefore forming the so-called collision subcascades. Three possible situations showing the single defects, cascades and subcascades formed by the PKAs of different energy are illustrated in Fig. 2.1. At low PKA energies, (few keV) pairs of interstitials and vacancies (Frenkel defects) are formed. In the intermediate range (typically few tens of keV) PKAs have enough energy to move through the solid and create a damage cascade-cluster. At the high energies PKAs make subcascades and cause most of the damage.

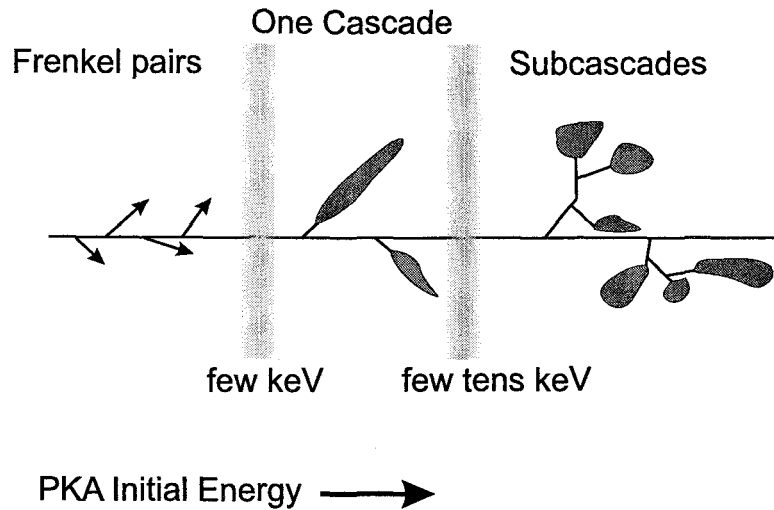


FIGURE 2.1. Defect and subcluster formation as a function of initial PKA energy.

Produced defects can be viewed as new energy levels introduced in the energy bandgap of the material. Depending on their energy position (see Fig. 2.2) the defect levels may act as [14]:

1. Generation centers. Associated with the mid-gap energy levels, these centers are responsible for generation of electron-hole pairs, whenever the local free carrier concentration is below its equilibrium value, for example, in junction space charge regions of the device. Increasing saturation current of the base-emitter and base-collector junctions of a transistor is one of the macroscopically observed effects of the increasing concentration of the generation centers.
2. Recombination centers. Recombination of electron-hole pairs can occur simply by capturing both positive and negative carriers at a defect center. Since the excess carrier lifetime is determined by the recombination processes, the

recombination centers can play very important role in the operation of a bipolar transistor.

3. Trapping centers can significantly reduce the effective carrier concentration by temporarily capturing majority or minority carriers, with their subsequent re-emission or recombination. As a result an increase in electrical resistance and decrease in carrier mobility can be observed.
4. Compensation centers, as shown in Fig. 2.2, can reduce the majority carrier concentration by acting as dopants which introduce carriers of the opposite sign. In general, there can be several competing n- and p-compensation centers.
5. Finally, tunneling centers are thought to assist in the tunneling of carriers through a heavily doped junction.

In addition to these effects, Frenkel defects produced very close to each other may form electrically active displacement clusters surrounded by a space charge region [15] which are capable of efficiently trapping the majority carriers.

To summarize, the minority carrier lifetime, effective doping and carrier mobility can be changed significantly through one or a combination of the radiation-induced effects. As a result, electrical properties of the semiconductor and therefore operation parameters of the semiconductor device, may also degrade.

Empirically, the radiation-induced degradation of any physical property is often described through the so-called degradation constant, K . For instance, the minority carrier lifetime, τ , as a function of incident fluence, Ψ , is given by

$$\boxed{1/\tau = 1/\tau_0 + K_\tau \Psi} \quad (2.14)$$

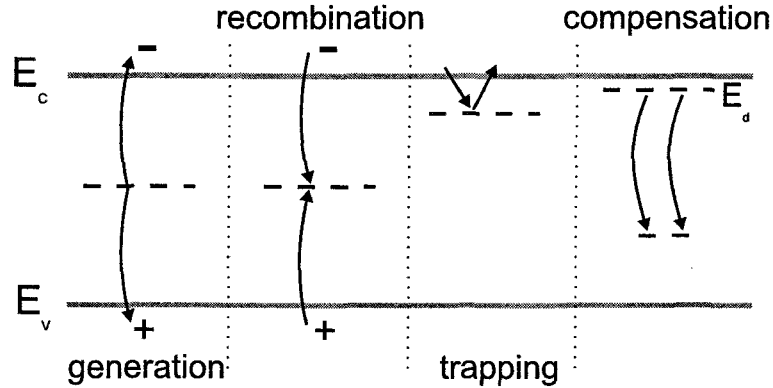


FIGURE 2.2. Electrical effects associated with defect energy levels introduced in semiconductor bandgap by irradiation.

Similar expressions are used to describe the degradation of the carrier concentration N and mobility μ with K_N and K_μ used in place of K_τ . This approach however does not provide any insight into the deterioration mechanisms and is not strictly valid for large fluences. The more physically-based calculations would require exhaustive transport simulations, relying on the knowledge of the inter-atomic potentials. Furthermore, a link between a complex structure of the defect clusters and induced changes in macroscopic properties of the material would have to be determined. Up to this day, despite significant effort put into understanding of the physical manifestations of the structure of the damage clusters there is no well-established theory explaining the experimentally observed degradation.

Summers *et al.* [16] have demonstrated that the semiconductor/device degradation due to the displacement damage can be correlated with the calculated non-ionizing energy deposited in the material. In a subsequent study [17] they showed that the results of analytical **Non-Ionizing Energy Loss** (NIEL) calculations agree very well with the Monte Carlo transport simulations. It was

also suggested that NIEL can be directly used to calculate the degradation of the bulk properties of materials. Due to its success the NIEL hypothesis is currently widely used in solar cell community for theoretical predictions of damage produced by different particles of different energies [17–22]. Though, fairly complicated, theoretical calculations of the displacement damage can be performed for various materials and different types of radiation. This, in turn, allows one to theoretically predict radiation-induced material and device degradation. The estimation of the equivalent doses for different types of irradiation experiments also becomes possible. For example, results of some experiment, where ^{60}Co γ -source was used, can be expressed in terms of irradiation doses resulting from equivalent fluence of 1 *MeV* electrons.

Even though effects of annealing, channeling and different cluster configuration are not included in the NIEL calculation, the theory produces amazingly accurate results when applied to silicon. However, in case of gallium arsenide slight deviations were noticed in the irradiation experiments with fast neutrons [23–26]. The observed discrepancies are attributed to variation in the defect production efficiency for damage clusters of different size. Due to the nature of the effects (see Chapter 3 for detailed discussion) they are also expected to be noticeable in other III-V materials which have low displacement thresholds. At the moment, however, no experimental results are available to verify this hypothesis.

2.3.2. Total Dose Effects

Ionizing radiation is radiation that has sufficient energy to create electron-hole pairs by breaking atomic bonds in the material. In the case of bulk semiconductors with no electric fields, the created charges can quickly recombine and

hence no permanent effects/damage may be observed. When an electric field is present, as in the case of junctions, the generated charges of opposite polarity get separated resulting in undesired or even fatal current or voltage transients. Apart from the possible damage by current/voltage transients there should be no significant permanent damage induced as the charge finally recombines in the bulk of semiconductor or at the device contacts.

The situation is somewhat different in the case of insulators. Most of the electrons produced, being very mobile, are swept out of the insulator, while only a small fraction may get trapped. The positively charged holes stay either trapped or slowly move by means of trap-hopping process [27]. In addition to that, interactions at the insulator/semiconductor interface can induce new levels in the energy bandgap resulting in formation of the interface traps. The net effect of these two degradation mechanisms is the change of the electric field in the semiconductor in the vicinity of the interface, which may lead to significant changes of device characteristics, through, for example, surface inversion.

Due to the tremendous success of MOS technology the total dose effects in SiO_2 were studied quite intensively for the last few decades. A relatively exhaustive overview and a large number of references on the subject can be found in Ref. [27, 28].

For a quantitative analysis, we need to introduce a few very important parameters. The stopping power of the medium, s , is defined as energy loss dT of an incident particle as it traverses material layer of thickness dx , i.e. $s = dT/dx$. Linear Energy Transfer (LET) is another term used to refer to this quantity. These quantities determine the density of electron-hole pairs produced by the ionizing radiation. The most commonly used units of LET are MeV/cm. Very often it is

more convenient to use mass stopping power, S , which is defined as

$$S = \frac{dT}{\rho dx} \quad (2.15)$$

where ρ is material density.

To be able to predict the effects of ionizing radiation one has to analyze the carrier generation-recombination process. The total number of electron-hole pairs generated in a material can be found by dividing the total absorbed ionizing energy by the average energy required to create an electron-hole pair. The latter, for instance, in silicon dioxide is about 17 ± 1 eV [27]. The net recombination of carriers depends strongly on the electric field in the insulator and the type of ionizing radiation used (see, for example Ref. [27]).

Finally, in most cases the ionizing radiation does not cause any permanent damage in semiconductors. Insulators, on the other hand, are very sensitive to this type of radiation, as they build up a significant amount of charge, which may result in the change of the threshold (flatband) voltage or shift of the semiconductor Fermi level at the semiconductor/insulator interface. Indeed the MOSFET technology, where the device performance strongly depends on the gate oxide condition and the threshold voltage is one of the critical device parameters, suffers from the ionizing radiation to much higher degree than bipolar transistors which use insulators only as passivation. Although bipolar transistors are much less vulnerable to ionizing damage the shift of the semiconductor Fermi level at the junction boundaries due to charge trapped in the passivation layer may result in some parasitic leakage currents, degrading performance of the devices.

2.3.3. PKA Energy Partitioning. Lindhard's Theory

As the incident particle traverses a solid, it interacts with material atoms and loses its kinetic energy to atomic electrons and/or atoms. The probability of these processes is determined by corresponding reaction cross sections and can be estimated. The situation, however, is much more complicated as one has to account for all the created secondary particles (electrons and atoms), which in some cases are responsible for most of the introduced damage. In contrast to the secondary electrons, which, as a rule, do not have enough energy to cause further ionization or atomic displacements, PKAs can sometime induce whole collision cascades and subcascades, resulting in considerable ionizing and displacement damage. Furthermore, in cases with “nonionizing” radiation, for example, neutrons, practically all of the damage is created by PKAs and their secondaries.

Lindhard *et al.* [29] were the first to develop a successful analytical theory addressing the problem of the division of the PKA dissipated energy between electrons and recoiling atoms – corresponding to ionizing and displacement damage effects, respectively. They formulated integral equations describing the process of PKA slowing down in an arbitrary medium. Knowing the details of PKA's interaction with electrons of the media and interatomic potentials these equations can be solved numerically. In obtaining an analytical solution one needs to make a few approximations, namely:

- Atomic binding energy (typically few eV) is neglected on the scale of PKA kinetic energy (usually keV range)
- Secondary electrons do not produce recoil atoms

- Nuclear and electronic collisions are considered separate and independent of each other
- Energy lost to electrons is small compared to the PKA's energy
- Energy transferred to a recoil is small compared to the PKA's energy

Most of these approximations are fairly safe and hold very well if the particle energy is not too low.

The solution of the Lindhard's integral equation provides us with an expression for the dimensionless kinetic energy, $L(\epsilon)$, transferred to the atoms by a PKA of initial dimensionless energy ϵ . $L(\epsilon)$ is also called Lindhard partition function and is usually written in the form [30]

$$L(\epsilon) = \frac{\epsilon}{1 + k_L g(\epsilon)} \quad (2.16)$$

$$g_L(\epsilon) = \epsilon + 0.40244\epsilon^{3/4} + 3.4008\epsilon^{1/6} \quad (2.17)$$

$$k_L = \frac{0.0793 Z_R^{2/3} Z_L^{1/2} (A_R + A_L)^{3/2}}{\left(Z_R^{2/3} + Z_L^{2/3} \right)^{3/4} A_R^{3/2} A_L^{1/2}}$$

$$\epsilon = \frac{\lambda_0 A_L T}{27.2 Z_R Z_L \left(Z_R^{2/3} + Z_L^{2/3} \right)^{1/2} (A_R + A_L)}$$

where T is the kinetic energy of the PKA and A_R , Z_R , A_L and Z_L are the atomic mass and number for the lattice and recoil atoms respectively. Clearly, $L(\epsilon)/\epsilon$ gives the fraction of PKA energy available for dislodging atoms. An example of the normalized $L(\epsilon)/\epsilon$ for bulk gallium is shown in Fig. 2.3.

One of the quantities of our interest is the number of atoms displaced in a collision cascade. There are several different approaches (see for example [31–33]) to the problem of calculating the number of the displacements, ranging from simple Kinchin-Pease analytical equations to very computer-time-consuming molecular dynamics simulations. Norgett *et al.* [33] proposed relatively successful model

based on the modified Kinchin-Pease formula and the Lindhard's energy partition theory. According to them the number of displacements produced by one PKA is

$$\nu(T) = \frac{\kappa L(\epsilon)}{\epsilon} \frac{T}{2E_d} \quad (2.18)$$

where $\kappa = 0.8$ is the displacement efficiency and E_d is displacement threshold energy for a given atom in the material. There is some uncertainty in the values of E_d , as different theoretical and experimental methods give different estimates. Sometimes E_d is even used as an empirical parameter to fit the theory to the measured results. The displacement energy values listed in Table 2.1 [19] are the ones most commonly used by the radiation-hardness community and therefore will be used in this work.

Atom	Material	E_d (eV)
<i>Si</i>	<i>Si</i>	21
<i>Ga</i>	<i>GaAs</i>	10
<i>As</i>	<i>GaAs</i>	10
<i>In</i>	<i>InP</i>	6.7
<i>P</i>	<i>InP</i>	8.7

TABLE 2.1. Displacement threshold energies for different semiconductor materials.

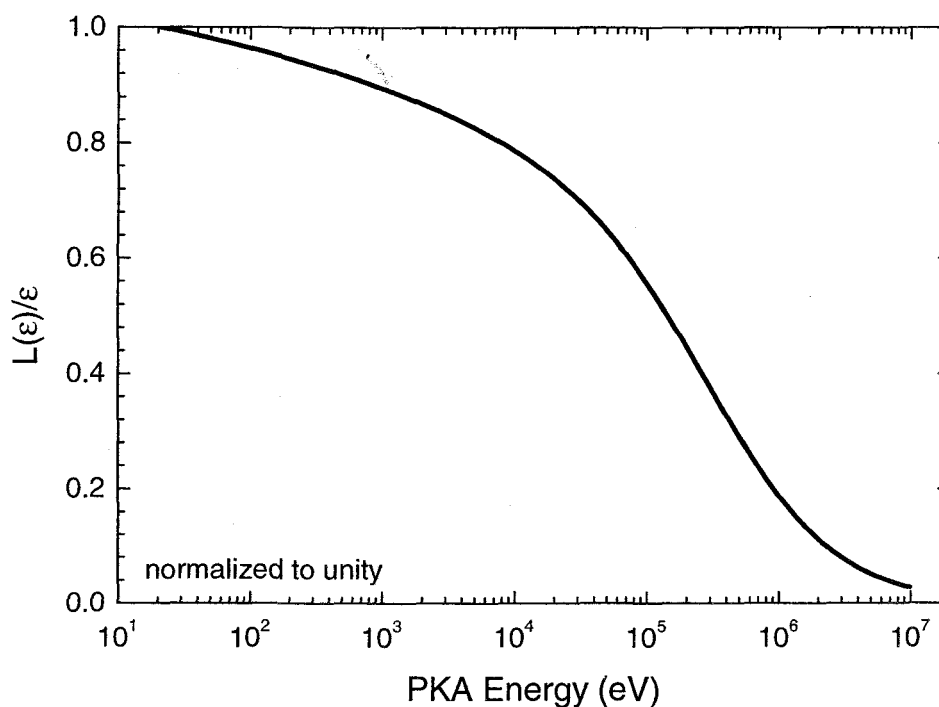


FIGURE 2.3. Fraction of PKA energy available for dislodging atoms as a function of PKA energy.

2.3.4. Single Event Effects

As already explained, the single event effects are due to creation of high density defect and/or charge tracks by incident energetic particles. Consider, for example, a heavy ion incident on the gate of an MOS transistor (see Fig. 2.4). As the ion passes through the gate, gate oxide and finally the semiconductor substrate it produces a wide ionization track along its way. Under some bias conditions, as the generated charge is collected, the ionization track may serve as a path for a flow of current between, e.g. gate and drain, source and drain, drain and substrate, gate and substrate, etc. These current transients may cause the so-called “soft” or even “hard” errors in the circuit. An example of the soft error is a change of the state

of an SRAM memory cell. Although, they cause malfunctioning of the circuit, the soft errors are usually not associated with permanent damage. In contrast, the hard errors, caused by higher currents, represent the permanent failures of the device/circuit. By far the most “famous” errors are the gate rupture, burnout and latchup.

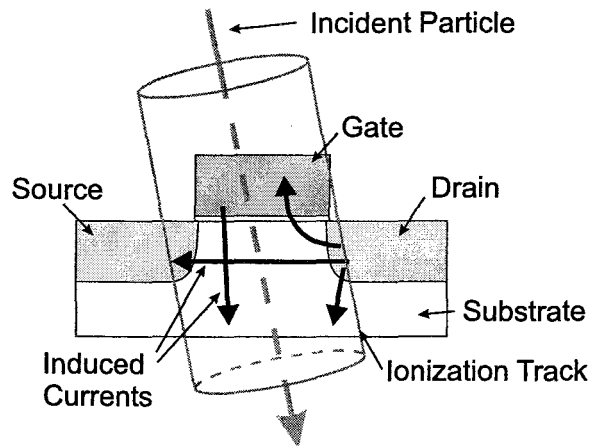


FIGURE 2.4. Ionization channel induced by an incident heavy particle in MOS transistor. Examples of induced current transients flowing between terminals of MOS transistor.

Estimation of the circuit response to SEE is extremely difficult task, since the outcome depends strongly on the position and direction of the particle track. Furthermore, the induced current and voltage transients, and extent of the produced damage depend on the biasing conditions of the device penetrated by the track. To characterize the device vulnerability the so-called upset cross sections and device LET thresholds are used – the more sensitive devices tend to have the larger cross sections and lower LET thresholds. More detailed information on this subject can be found in Ref. [34]. ✓

Currently SEE are one of the major concerns in the development of the radiation-hard devices and circuits. To improve radiation tolerance, systems are designed with built-in capabilities for self recovery from the soft errors (through, for example, redundancy), additionally, individual device structures are optimized to reduce cross sections for the both, soft and hard, SEE. In the future, as device critical dimensions continue to shrink the susceptibility of devices to SEE is expected to increase further forcing researchers to put even more effort into development of the SEE-resistant devices/circuits.

2.4. Radiation Effects in III-V Compound Semiconductors

Radiation effects in silicon and gallium arsenide have been studied extensively owing to a large number of commercial applications based on these materials [16–21, 35]. Indium phosphide has also received some attention due to its wide use in solar cells [17, 22]. With the exception of only a few reports [36–39] the degradation of *InGaAs* is not well characterized.

As already discussed the degradation coefficients can be expressed in terms of NIEL. Large number of the experiments demonstrates simply a linear correlation

$$\boxed{K \propto NIEL} \quad (2.19)$$

for *Si*, *GaAs* and *InP*, both n- and p-type, irradiated with protons (see, for example, Ref. [17]). In case of electron irradiation, however, the p-doped materials exhibit the quadratic correlation [21, 19]

$$K \propto NIEL^2 \quad (2.20)$$

while for n-type materials K still correlates linearly with $NIEL$. Finally, for the irradiation with heavy ions the linear relation between K and $NIEL$ has been observed [19].

For $InGaAs$, currently, there is no sufficient data available to draw any conclusions regarding the link between the damage degradation and $NIEL$. However, it is most likely that the $K - NIEL$ relationship is going to be analogous to the correlations observed in the other studied semiconductors.

Positioning of the defect levels in the bandgap of semiconductor determines their influence on the electrical properties of the material. Hence, the energy spectrum of the created defects has to be known in order to estimate the degradation effects. Deep Level Transient Spectroscopy (DLTS) is undoubtedly one of the most popular experimental techniques used to estimate the concentration, capturing cross sections, and energy levels of traps.

In InP , electron- and gamma-induced defects have been studied very extensively (see, e.g., [40–43]). Strictly speaking, the process of formation, and configuration of the defect states depend on the origin, i.e. growth method, and doping of the material. However, in most cases three major hole (H3, H4 and H5) and two electron (EA and EB) traps are observed after irradiation. Walters *et al.* [44] have also detected H5 and EA defects in their proton irradiation experiments. Table 2.2 lists the trap energy and capturing cross section for the observed traps (after [41]). The introduction rates reported by different authors vary drastically, but in general, for irradiation with 1 MeV electrons fall into $10^{-3} - 10^{-4} \text{ cm}^{-1}$ range. For the ^{60}Co gamma irradiation Koyama *et al.* [42] reported the introduction rate of 0.05 cm^{-1} for the EB trap.

In $InGaAs$ two levels, E1(0.1 eV) and E2(0.29 eV), can be detected after irradiation with 1 MeV electrons [36]. E2 with the introduction rate of 0.07 cm^{-1}

Trap	Energy (eV)	$\sigma (\times 10^{-15} \text{ cm}^2)$
H3	0.30	0.65
H4	0.34	0.50
H5	0.54	7.7
EA	0.22	4.4
EB	0.76	1400

TABLE 2.2. Trap energy and capturing cross section for H3, H4, H5, EA and EB traps in *InP*.

was shown to be effective generation-recombination center. In fast neutron irradiation experiments Ohyama *et al.* [38] detected 0.58, 0.37 and 0.45 eV electron traps and 0.25 eV hole traps induced in the material.

In summary, having detailed information about the trap levels can be very useful when trying to quantify generation and recombination processes in the semiconductor/device, for example, in calculation of a leakage current of a reverse-biased junction. At the same time, knowledge of the correlation between the degradation coefficient K and NIEL can be used to predict the material/device response to any radiation environment simply by using results of, for example, a 1 MeV electron irradiation experiment.

2.5. Radiation Effects in Bipolar Transistors

A detailed discussion of the transistor degradation mechanisms is postponed till the later chapters, where the physics of device operation is introduced and the analytical device theory is presented. At this point we restrict ourselves to simply listing the possible macroscopic effects which may be responsible for the transistor deterioration:

1. surface recombination and/or leakage currents
2. recombination/generation currents of space charge regions
3. neutral bulk recombination currents
4. diffusion currents

The surface-related currents are typically caused by the total dose effects while the rest are induced by the displacement damage. Depending on the device structure, materials and the fabrication procedure the relative contribution of the different components may vary considerably. Most often, however, the bulk mechanisms dominate the degradation. In that case the dc current gain β of a transistor is reduced simply as a result of reduction of the minority carrier lifetime. This allows us to express β using an expression similar to Eq. 2.14, i.e.,

$$\boxed{1/\beta = 1/\beta_0 + K_\beta \Psi} \quad (2.21)$$

This equation, first suggested by Messenger and Spratt [45] has been widely used by the radiation testing community.

Summers et al. [16] have studied the correlation between the gain degradation coefficient and NIEL for silicon BJTs. They showed that the damage factor

is linearly proportional to NIEL for irradiations with protons, deuterons, alpha-particles and neutrons. They also demonstrated that independently of the collector current the gain degradation coefficient K_β scales linearly with NIEL over the entire energy range.

3. RADIATION DAMAGE IN III-V MATERIALS

Radiation degradation of semiconductor devices is caused by deterioration of individual semiconductor layers from which the device is built. Total dose and displacement effects introduced in Chapter 2 may induce some changes in the layer parameters, hence modifying behavior of the device as a whole. For this reason, when studying radiation degradation of semiconductor devices, it is vitally important to know and be able to predict the response of materials to different radiation environments.

This chapter is to address the issue of radiation effects observed in individual layers of HBTs. Results of damage production calculations performed in this chapter, when combined with a device analytical model, can be used to estimate device response to any given radiation (consisting of beta, gamma and neutron fluxes).

The first three sections of the chapter are concerned with radiation effects of electron, neutron and gamma radiation, respectively. In each section, the methods for evaluating absorbed dose, displacement damage and number of defects are presented. Also, some attention is paid to dosimetry and energy spectra of the sources used in our irradiation experiments. At the end of each section the results of the dosimetry and damage production calculations are presented in the form useful for the analysis of the device degradation performed later in Chapter 6. The chapter is concluded with a brief comparison and discussion of the results for the different types of radiation.

3.1. Electron Irradiation

In this section the theory of electron irradiation effects in semiconductor materials is presented. Particular attention is paid to degradation of *InP* and *InGaAs* compounds. First, the interactions of electron irradiation with matter are introduced and the methods for calculation of the stopping powers, ranges and absorbed doses are described. Then production of atomic displacements is considered, and non-ionizing energy loss and displacement doses are calculated. Finally, as it is necessary for the calculations and analysis of experimental results, an energy spectrum of $^{90}\text{Sr}/^{90}\text{Y}$ beta-source and related dosimetry issues are discussed.

3.1.1. Interaction of Electron Irradiation with Matter

Energetic electrons passing through a solid interact with atoms and electrons of the medium leading to a wide variety of physical processes. Possible energy transfer mechanisms, that may be responsible for electron slowing down, are shown in Fig. 3.1. At relatively high energies, on the order of few hundred *MeV* and higher, electrons are slowed down by emitting Cherenkov and bremsstrahlung radiation, and through nuclear reactions. At lower energies, however, the interaction cross sections for these reactions drop significantly and the so-called electronic and nuclear slowing down become most dominant. Bremsstrahlung radiation plays some role at very low energies, typically few hundred *eV* and lower. As we are interested in the low energy range ($\leq 1.5 \text{ MeV}$) only the last three mechanisms will be considered in some detail.

It is then customary to separate the total stopping power into three components, corresponding to electron collision, nuclear collision, and radiative stopping,

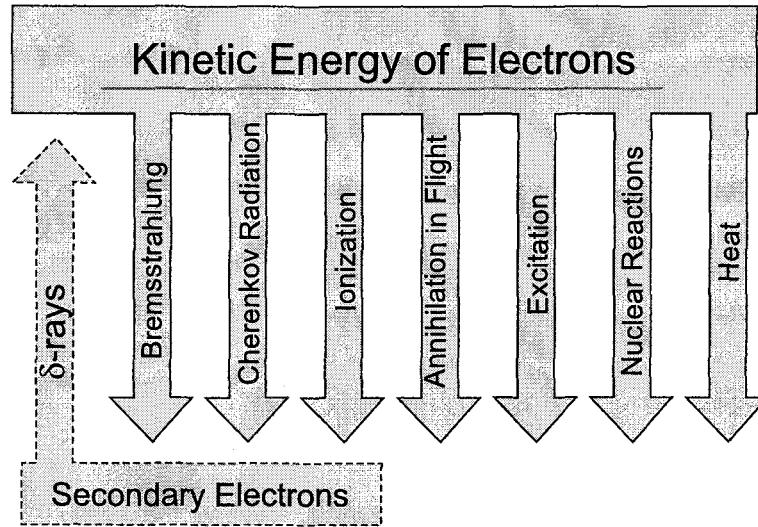


FIGURE 3.1. Interactions of electrons with matter -- mechanisms involved in energy transfer.

S_{ce} , S_{cn} and S_r , respectively:

$$S = S_{ce} + S_{cn} + S_r \quad (3.1)$$

In the subsequent sections these individual stopping mechanisms will be considered in detail in order to calculate the damage effects induced by beta-irradiation.

3.1.1.1. Electron Collision Stopping

Inelastic Coulomb collisions with bound atomic electrons is the most effective slowing down mechanism for incident beta-rays in the low energy range (few MeV). Providing the incident beta-rays have sufficient kinetic energy they may cause excitation and ionization of atoms in a solid, therefore producing electron-

hole pairs. The mass collision stopping power can be written as [46]

$$S_{ce} = n_a \rho Z \int_0^{E_{max}} E \frac{d\sigma}{dE} dE \quad (3.2)$$

where n_a is the atomic density measured in *atoms/cm³*, Z is the atomic number, E_{max} is the largest possible energy transfer, and $d\sigma/dE$ is the differential cross section for the transfer of energy E from the incident beta to an atomic electron. For mixtures of elements the effective atomic number, Z_{eff} is used in place of Z :

$$Z_{eff} = \frac{\sum f_i Z_i^2}{\sum f_i Z_i} \quad (3.3)$$

where f_i is the weight fraction of i^{th} element having atomic number Z_i .

The original theory for calculating Eq. 3.2 was developed by Bethe and Bloch [47] and is based on the classical approach and does not take into account quantum mechanical aspects of the problem. Further developed Moller's approach [48] includes relativistic, spin and exchange effects and is the one most commonly used nowadays. According to Moller the mass stopping power can be expressed in the following form:

$$S_{ce} = k(Z) \frac{(T + m_0 c^2)^2}{T(T + 2m_0 c^2)} \left[\ln \left\{ \frac{2(T + 2m_0 c^2)}{m_0 c^2 (I/m_0 c^2)^2} \right\} + F(T) - \delta - \lambda \right] \quad (3.4)$$

where

$$k(Z) = \frac{2\pi N_A Z r_0^2}{A \beta^2}, \quad (3.5)$$

$$F(T) = 1 - \frac{(T + m_0 c^2)^2}{T(T + 2m_0 c^2)} + 2 \ln \left\{ \frac{T}{2(m_0 c^2)} \right\} - \frac{T^2/8 + m_0 c^2 (2T + m_0 c^2) \ln 2}{T(T + 2m_0 c^2)}, \quad (3.6)$$

$$\lambda = \frac{2\pi N_a r_0^2}{A}. \quad (3.7)$$

where T and $m_0 c^2 = 0.511 \text{ MeV}$ are the kinetic and rest energy of an electron, respectively, and $r_0 = e^2/4\pi\epsilon_0 m_0 c^2$ is the classical electron radius. The first term

in the square brackets of Eq. 3.4 represents the so-called "soft" collision stopping power, representing the case when the incident beta passes an atom at a large distance, $F(T)$ accounts for knock-on collisions, δ is the correction term accounting for the polarization of the medium by the incident electron and, finally, λ is the so-called shell correction, which accounts for the fact that, at low energies for light elements and at all energies for heavy elements, the probability of collision with the inner shell electrons is negligible. I is the mean excitation potential of the struck atoms, or in case of material mixture – compound's mean excitation potential. It is typically extracted from the experimentally measured proton and alpha particle stopping powers and ranges [49]. Theoretically calculated density correction parameter δ [50] and the shell correction λ are tabulated for numerous elements and compounds, see e.g. Estar database [51].

In case of thin objects secondary electrons produced in collisions of the incident beta-particles with atomic electrons may have enough kinetic energy to leave the sample volume and deposit their energy outside of the object. The method of calculating the absorbed dose should then be adjusted and one must use the restricted mass stopping power instead of the total mass stopping power. In this case cutoff energy is introduced as limiting electron kinetic energy needed for electron in order to escape the volume of the sample. Although restricted mass stopping power $(S_{ce})_{\Delta}$ is usually somewhat smaller than the total mass stopping power, to keep the analysis reasonably simple we will to use S_{ce} only.

Calculated electron mass collision stopping powers for electrons in *Si*, *InP*, *InGaAs*, *Au* and polyimide are shown in Fig. 3.2. Material parameters used for the calculations are listed in Table 3.1

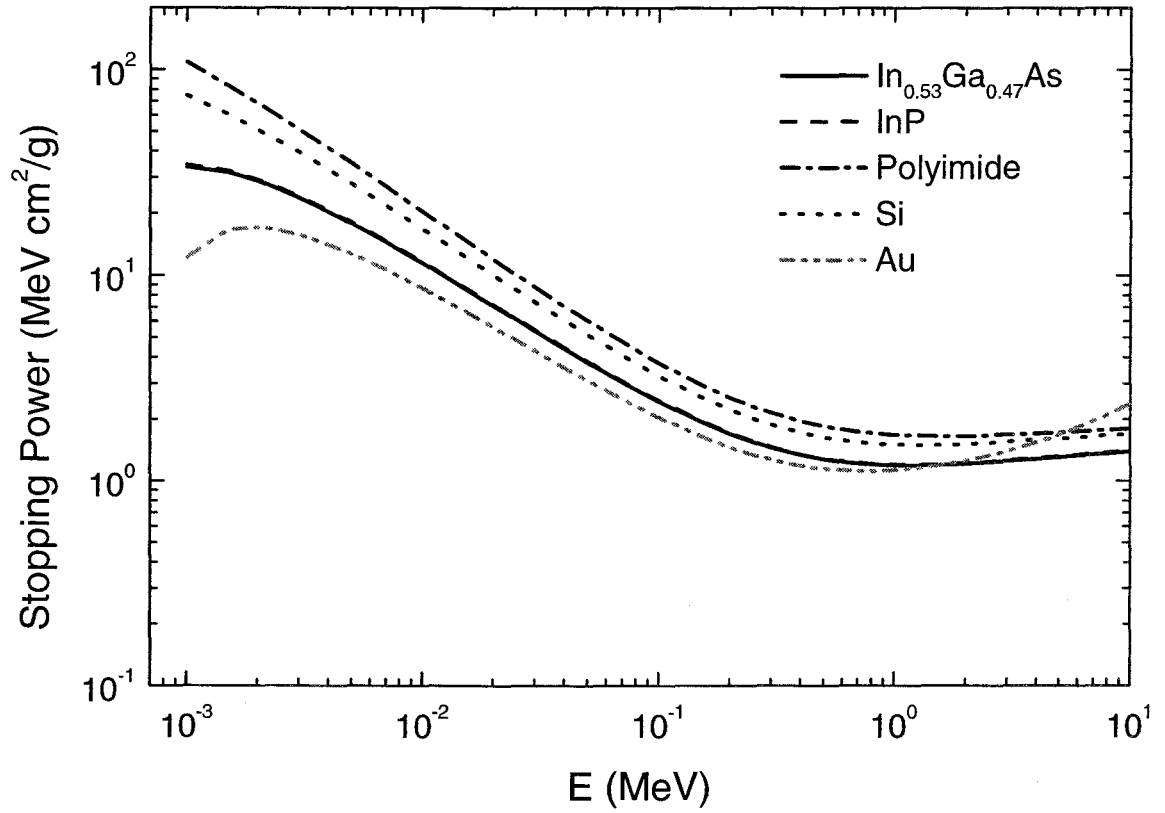


FIGURE 3.2. Electron collision mass stopping powers for electrons in *Si*, *InP*, *InGaAs*, *Au* and polyimide.

3.1.1.2. Radiative Stopping Power

At low energies, on the order of few tens eV, incident electrons can not participate in inelastic scattering on atomic electrons, as their energy is not sufficient to excite/ionize atoms of the medium. In this case the bremsstrahlung emission, also called radiative stopping, becomes dominant slowing-down mechanism. The radiative stopping power calculated from electromagnetic and relativistic theory is

Material	Z	A	ρ (g/cm^3)	n_a (cm^{-3})	I (eV)
<i>Al</i>	13	26.98	2.69	6.00×10^{22}	166
<i>Si</i>	14	28.09	2.32	4.97×10^{22}	173
<i>P</i>	15	30.97	2.20	4.28×10^{22}	173
<i>Ga</i>	31	69.72	5.90	5.08×10^{22}	334
<i>As</i>	33	74.95	5.73	4.60×10^{22}	347
<i>GaAs</i>	32	72.33	5.32	4.84×10^{22}	385
<i>In</i>	49	114.8	7.30	3.83×10^{22}	488
<i>Au</i>	79	197.0	19.32	5.90×10^{22}	790
<i>In_{0.53}Ga_{0.47}As</i>	—	84.28	5.48	3.91×10^{22}	439
<i>InP</i>	—	72.88	4.81	3.97×10^{22}	432
polyimide	—	—	1.45		80

TABLE 3.1. Material parameters used for calculation of stopping powers for *Al*, *Si*, *P*, *Ga*, *As*, *In*, *Au*, *InGaAs*, *InP* and polyimide ($C_{22}N_2H_5(OH)_5$ composition is assumed for polyimide).

given by [52]

$$S_r = \frac{n_a T Z(Z+1)e^4}{137 \rho m_0^2 c^4} \left[4 \ln \left\{ \frac{2T}{m_0 c^2} \right\} - \frac{4}{3} \right] \quad (3.8)$$

where c is the speed of light. Calculated radiative mass stopping powers for electrons in *Si*, *InP*, *InGaAs*, *Au* and polyimide are shown in Fig. 3.3. Below 10 MeV, the radiative stopping powers are considerably less than the electron collision stopping powers and can be safely neglected, except, of course, very low energy end, where the collision stopping powers drop to zero. At energies above

10 MeV the bremsstrahlung emission becomes one of the dominant mechanisms for the beta energy loss.

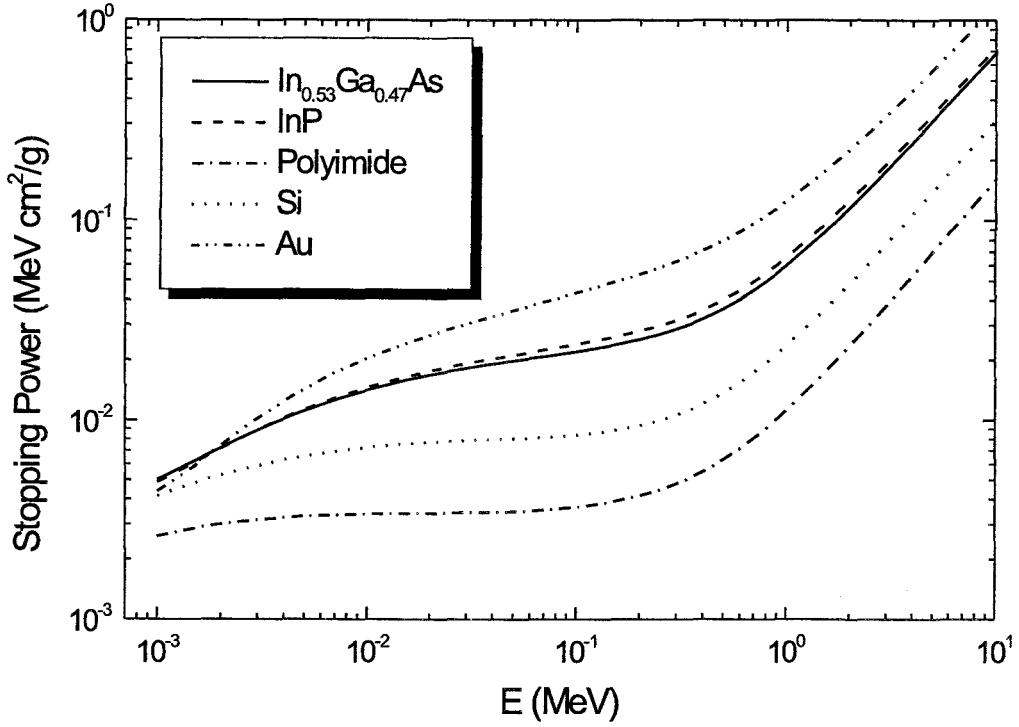


FIGURE 3.3. Radiative mass stopping powers for electrons in *Si*, *InP*, *InGaAs*, *Au* and polyimide.

3.1.1.3. CSDA Range and Ionizing Energy Deposition

As electron traverses material it continuously interacts with atomic electrons, nuclei and atoms as a whole. As a result of these inelastic and elastic scattering events the incident beta slows down by losing its energy to electrons and nuclei. This process is a statistical process and there is a distribution of possi-

ble energy losses for each collision. It is, however, a relatively good approximation to neglect the energy loss fluctuations and assume that the electron loses its energy according to the mean energy loss per unit pathlength given by the stopping power. In this so-called Continuous Slowing Down Approximation (CSDA) the average path length traveled by a beta of initial energy T_0 before it comes down to rest is given by

$$R_{CSDA} = \int_0^{T_0} \left(\frac{dT}{\rho dx} \right)^{-1} dT \quad (3.9)$$

Calculated CSDA ranges for electrons in *Si*, *InP*, *InGaAs*, *Au* and polyimide are shown in Fig. 3.4.

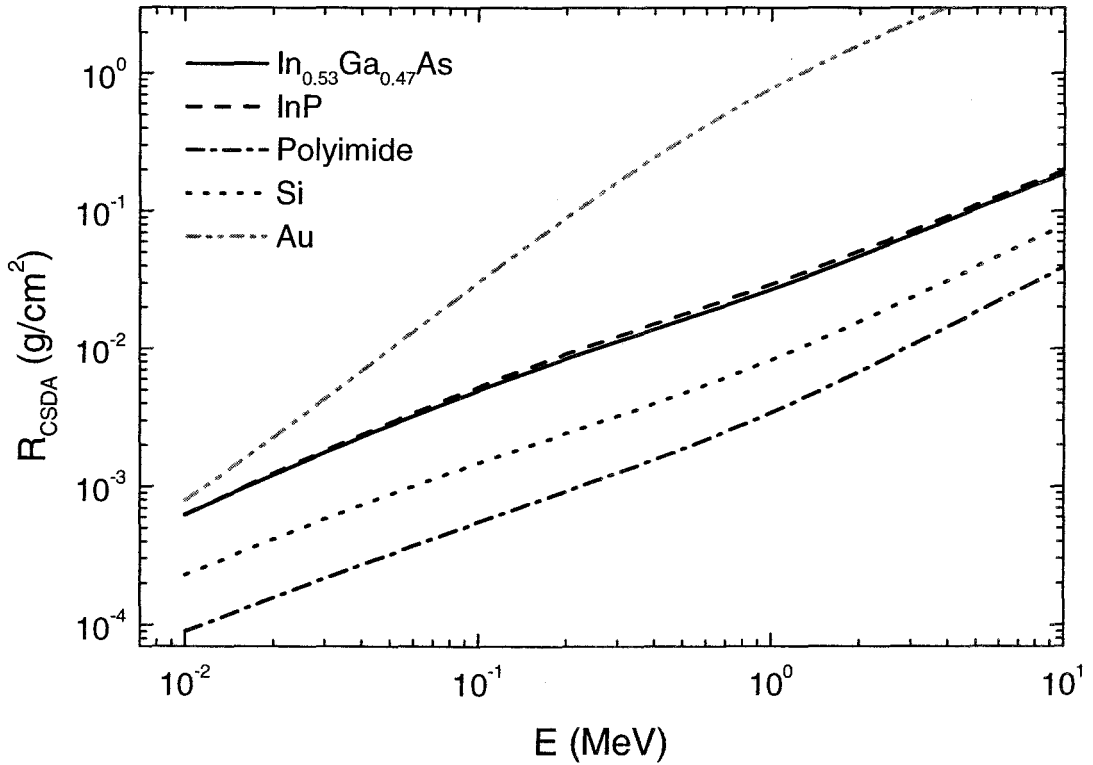


FIGURE 3.4. CSDA ranges for electrons in *Si*, *InP*, *InGaAs*, *Au* and polyimide.

Using the CSDA ranges, mass stopping powers and the thickness of the active layers of the device given in Table 5.1, the slowing down of electrons in the active volume of the device is found to be very small. Hence, the total dose deposited in the device volume by a monoenergetic beam of characteristic energy E and fluence $\Psi(E)$ is easily calculated from the electron-collision mass stopping power $S_{ce}(E)$ shown in Fig. 3.2 by using the relation

$$D(E) = \Psi(E) S_{ce}(E) \text{ MeV/g} \quad (3.10)$$

Note that the radiative and nuclear collision stopping powers are neglected and only electron collision stopping power is used. This approximation does not introduce any significant error for the energy range of the interest (about 1 MeV). Converting units to conventional *rads* one obtains

$$D(E) = 1.6 \times 10^{-8} \Psi(E) \cdot S_{ce}(E) \text{ rad} \quad (3.11)$$

In case of a continuous electron energy distribution the energy spectrum of the electrons should be combined with the energy dependence of the stopping power

$$D = 1.6 \times 10^{-8} \int_0^{E_{max}} \frac{d\Psi(E)}{dE} S_{ce}(E) dE \text{ rad} \quad (3.12)$$

It is clear, of course, that this equation is the exact expression for the Total Ionizing Dose (TID), which is very close to the total absorbed dose for the beta radiation of the given energy range. Fig 3.5 shows depth profile of TID rate for electrons of initial energy 1 MeV (mean energy of β -rays emitted by $^{90}\text{Sr}/^{90}\text{Y}$ source) in a thick layer of silicon. Keeping in mind that the typical total thickness of the studied devices is about 1 – 2 μm it must be concluded that the absorbed energy is almost the same in all regions of the device. Therefore all subsequent calculations will be performed for monoenergetic electrons of 1 MeV.

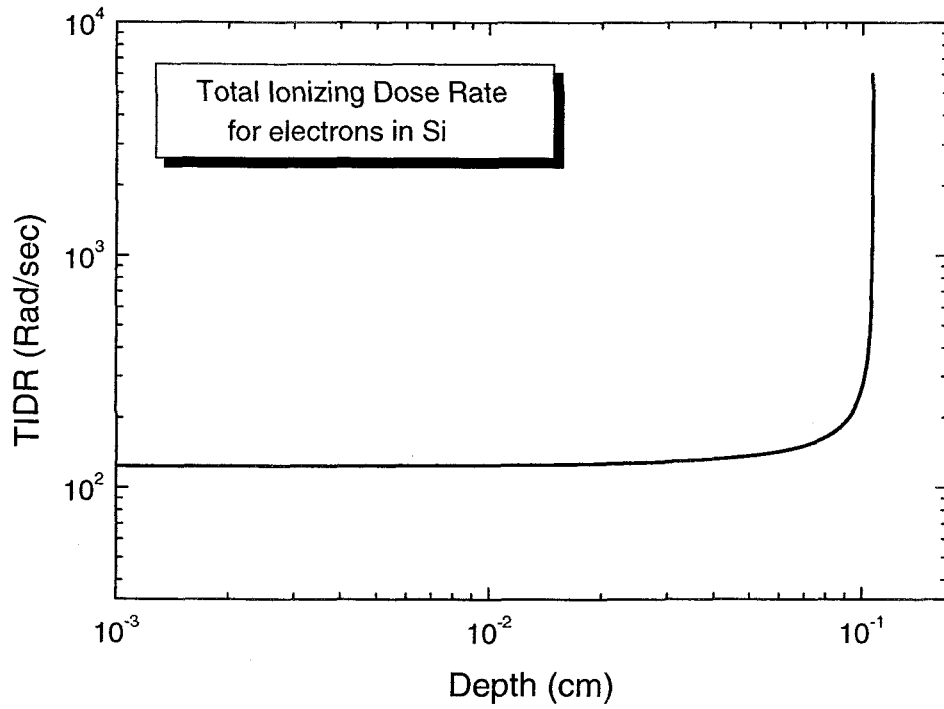


FIGURE 3.5. Total ionizing dose rate for electrons of energy 1 MeV in layer of silicon.

3.1.1.4. Nuclear Stopping Power

Elastic scattering of an electron by a nucleus can result in transfer of significant amount of energy from highly energetic electron to initially "resting" atom. Kinetic energy of recoiling primary knock-on atom (PKA), T_a , is calculated from momentum and energy conservation

$$T_a = \frac{2T_e(T_e + 2m_0c^2)}{M_0c^2} \sin^2 \frac{\theta}{2} \quad (3.13)$$

or

$$T_a = T_m \sin^2 \frac{\theta}{2} \quad (3.14)$$

$$T_m = \frac{2T_e(T_e + 2m_0c^2)}{M_0c^2} \quad (3.15)$$

Material	S_{ce}	S_r	D	dD/dt
	($MeVcm^2/g$)	($MeVcm^2/g$)	(Rad/e^-)	(Rad/s)
<i>Si</i>	1.51	0.024	2.4×10^{-8}	226
<i>Au</i>	1.13	0.125	1.8×10^{-8}	170
<i>InGaAs</i>	1.20	0.059	1.9×10^{-8}	179
<i>InP</i>	1.20	0.065	1.9×10^{-8}	179
<i>Polyimide</i>	1.68	0.011	2.7×10^{-8}	254

TABLE 3.2. Electron-collision and radiative stopping powers, ionizing dose introduced by one electron and total ionizing dose rate of electron flux at incident electron energy of 1 *MeV* for *Si*, *Au*, *InGaAs*, *InP* and polyimide.

where T_m is the maximum possible energy transferred to the nucleus by an electron of energy T_e scattered at angle θ , M_0c^2 is nucleus rest mass. For high energy electrons Darwin-Rutherford formula can not be applied and relativistic Coulomb scattering cross sections presented by Mott [53] in the form of a conditionally convergent infinite series must be used instead:

$$\frac{d\sigma_M(T_e, \theta)}{d\Omega} = \frac{\hbar^2(1 - \beta^2)}{m_0^2v^2} \left[q^2(1 - \beta^2) |F|^2 \csc^2 \frac{\theta}{2} + |G|^2 \sec^2 \frac{\theta}{2} \right] \quad (3.16)$$

where

$$F = F_0 + F_1 \quad (3.17)$$

$$F_0 = \frac{i}{2} \frac{\Gamma(1 - iq)}{\Gamma(1 + iq)} e^{iq \ln[\sin^2 \frac{\theta}{2}]} \quad (3.18)$$

$$F_1 = \frac{i}{2} \sum_{k=0}^{\infty} [kD_k + (k+1)D_{k+1}] (-1)^k P_k(\cos \theta) \quad (3.19)$$

$$G = G_0 + G_1 \quad (3.20)$$

$$G_0 = -iqF_0 \cot^2 \frac{\theta}{2} \quad (3.21)$$

$$G_1 = \frac{i}{2} \sum_{k=0}^{\infty} [k^2 D_k - (k+1)^2 D_{k+1}] (-1)^k P_k(\cos \theta) \quad (3.22)$$

$$D_k = \frac{\Gamma(k - iq)}{\Gamma(k + 1 + iq)} e^{i\pi k} - \frac{\Gamma(\sqrt{k^2 - \alpha^2} - iq)}{\Gamma(\sqrt{k^2 - \alpha^2} + 1 + iq)} e^{i\pi \sqrt{k^2 - \alpha^2}} \quad (3.23)$$

where $\alpha = Z/137$, $q = \alpha/\beta$, $\beta = v/c$, v is the electron velocity and Γ is the complex gamma function.

3.1.1.5. Displacement Damage. NIEL Calculations

The total average number of atoms displaced by an incident electron with kinetic energy T_e as it traverses a layer of thickness w is found from

$$\overline{N}_d(T_e) = n_a \int_0^w dx \int_0^\pi \nu[T_a(T_e, \theta)] \frac{d\sigma_M(T_e, \theta)}{d\Omega} d\Omega \quad (3.24)$$

where the total number of displacements per PKA, $\nu[T_a(T_e, \theta)]$, is given by the modified Kinchin-Pease equation (see Eq. 2.18 and Section 2.3.3), $T_a(T_e, \theta)$ is the PKA initial kinetic energy, θ is the scattered electron angle and $d\sigma_M(\theta)/d\Omega$ is Mott differential cross section for the elastic Coulomb scattering of electrons. Assuming that w is so small that the incident electron kinetic energy does not change significantly (this is the case for all our device structures) then all functions inside the second integral can be thought of as independent of x and the expression can be

rewritten as

$$\bar{N}_d(T_e) = n_a w \int_0^\pi \frac{L[T_a(T_e, \theta)]}{\epsilon} \frac{\kappa T_a(T_e, \theta)}{2E_d} \frac{d\sigma_M(T_e, \theta)}{d\Omega} d\Omega \quad (3.25)$$

where $L[T_a(T_e, \theta)]$ is the Lindhard's partition function, that is the part of primary knock-on atom energy available to cause atomic displacements. Relatively accurate theoretical approximations for the Lindhard partition function (see Section 2.3.3) as well as Mott differential cross sections (see Section 3.1.1.4) allow numerical evaluation of these expressions for different materials and types of radiation.

Then the density of displacements introduced by a fluence of electrons is given by

$$N_d = n_a \int_0^{T_e^{max}} dT_e \int_0^\pi \frac{L[T_a(T_e, \theta)]}{\epsilon} \frac{\kappa T_a(T_e, \theta)}{2E_d} \frac{d\Psi(T_e)}{dT_e} \frac{d\sigma_M(T_e, \theta)}{d\Omega} d\Omega \quad (3.26)$$

Another useful quantity is the damage production rate a_T relating the number of displacements N_d to the electron fluence Ψ_e through the relation

$$N_d = a_T \Psi_e \quad (3.27)$$

Calculated values of a_T introduced by 1 MeV electrons in different materials (*Si*, *GaAs*, *InGaAs* and *InP*) are listed in Table. 3.3.

It is very useful to introduce a new quantity – defect introduction rate per unit ionizing dose deposited in the material. This introduction rate denoted as A_T has units of $rad^{-1}(Si) \cdot cm^{-3}$ and can be used to calculate defect concentration through simple multiplication by absorbed dose D measured by a dosimeter. Calculated values of A_T for *Si*, *GaAs*, *InGaAs* and *InP* are listed in Table. 3.3.

Calculation of NIEL, S_d , for electrons consists of evaluation of the following integral [17]

$$S_d = \frac{N_A}{A} \int_0^{180^\circ} L[T(\Theta)]T(\Theta) \frac{d\sigma(\Theta)}{d\Omega} d\Omega \quad (3.28)$$

Fig. 3.6 shows calculated NIEL for electrons in *Si*, *GaAs*, *InGaAs* and *InP* with the threshold displacement energies of $E_{th}(Si) = 21 \text{ eV}$ (12.9 eV), $E_{th}(Ga) = 10 \text{ eV}$, $E_{th}(As) = 10 \text{ eV}$, $E_{th}(In) = 6.7 \text{ eV}$ and $E_{th}(P) = 8.7 \text{ eV}$ (*Si*, *GaAs* and *InP* after [17]).

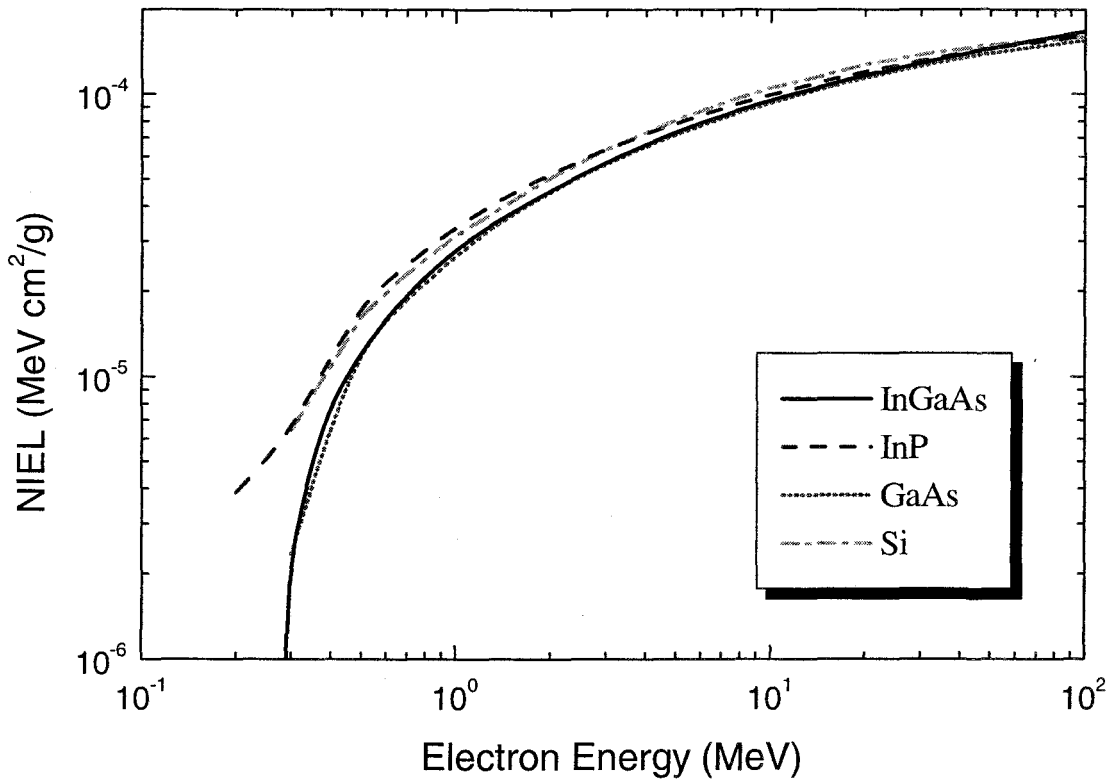


FIGURE 3.6. Calculated non-ionizing energy loss for electrons in *Si*, *GaAs*, *InGaAs* and *InP*.

The displacement damage dose D_d for electrons of energy E in n-type materials can be calculated as

$$D_d = 1.6 \times 10^{-8} \int_0^{E_{max}} S_d(E) \frac{d\Psi(E)}{dE} dE \quad (3.29)$$

In the simplest case when the electron fluence, $\Psi(E)$, consists of monoenergetic electrons this equation reduces to

$$D_d = 1.6 \times 10^{-8} S_d(E) \Psi(E) \text{ rad} \quad (3.30)$$

For p-type materials this expression needs to be modified slightly to include the so-called quality factor $Q(E) = S_d(E)/S_d(E_{ref})$ defined with respect to some reference energy E_{ref} typically 1 MeV [19]. The equivalent displacement dose is then given by

$$D_d^{eq}(1 \text{ MeV}) = 1.6 \times 10^{-8} \int_0^{E_{max}} Q(E) S_d(E) \frac{d\Psi(E)}{dE} dE \quad (3.31)$$

Again in the case of monoenergetic electron fluence this simplifies to

$$D_d^{eq}(1 \text{ MeV}) = 1.6 \times 10^{-8} Q(E) S_d(E) \Psi(E) \quad (3.32)$$

In the case of compounds, special care should be taken while calculating the displacement damage. Denote electron scattering cross section for a matrix atom of element "i" as σ^i . i^{th} PKA produced by an elastic scattering event can induce damage cascades as it slows down through the solid. In the first approximation we calculate corrected Lindhard's partition function, $\mathcal{L}^i[T_a^i(T_e, \theta)]$ as a weighted sum of the partition functions for all possible combinations of materials of lattice and recoils, i.e.

$$\mathcal{L}^i[T_a^i(T_e, \theta)] = \sum_j w_j L^{ij}[T_a^i(T_e, \theta), A_R^i, A_L^j, Z_R^i, Z_L^j, E_d^i] \quad (3.33)$$

NIEL is simply calculated from

$$S_d = 2\pi N_A \sum_i \frac{w_i}{A_i} \int_{\theta_{\min}(T_e)}^{\pi} \sum_j w_j L^{ij} [T_a^i(T_e, \theta)] T_a^i(T_e, \theta) \frac{d\sigma^i(T_e)}{d\Omega} \sin \theta d\theta \quad (3.34)$$

Material	a_T (cm^{-1})	S_d ($eV \frac{cm^2}{g}$)	A_T^β ($Rad^{-1}(Si) \cdot cm^{-3}$)
<i>Si</i>	1.4	31.4	0.6×10^8
<i>GaAs</i>	5.6	26.5	2.3×10^8
<i>In_{0.53}Ga_{0.47}As</i>	6.2	28.5	2.6×10^8
<i>InP</i>	7.4	33.5	3.1×10^8

TABLE 3.3. Displacement introduction rate, non-ionizing energy loss for 1 *MeV* electrons and number of displacements produced by flux of 1 *MeV* electrons that introduce 1 *rad(Si)* of ionizing dose.

3.1.2. Beta Irradiation Source

100 *mCi* active ^{90}Sr SIF.1177 beta source (supplied by Amersham Corp., currently AEA Technologies) was used in all beta irradiation experiments. The schematic diagram of the source cross section is shown in Fig. 3.7. A thin radioactive layer of $^{90}_{38}Sr$ -containing compound is deposited on a ceramic substrate encapsulated in a stainless steel capsule (X.117) efficiently absorbing emitted betas. The radiation escapes only in one direction (straight down on the diagram)

through a thin $50\ \mu\text{m}$ silver window physically protecting the active layer of the source.

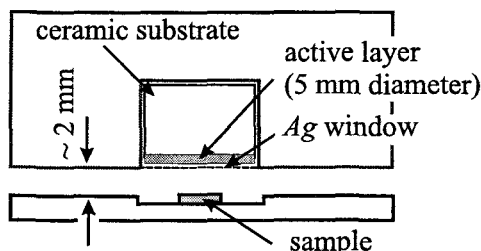


FIGURE 3.7. Schematic of β -source and sample positioning for irradiation.

$^{90}_{38}\text{Sr}$ is a radioactive element with a halflife of 29.12 years [54]. It decays to $^{90}_{39}\text{Y}$ by emitting β^- with the cutoff energy of $0.546\ \text{MeV}$. $^{90}_{39}\text{Y}$ is also highly unstable with halflife of 3.19 hours and first cools down by emitting one or two relatively low energy gammas. The cooled less active $^{90}_{39}\text{Y}$ with the lifetime of 64.0 hours decays to stable $^{90}_{40}\text{Zr}$ by emitting a beta spectrum with a maximum energy of $2.25\ \text{MeV}$. Due to the short 64 hour halflife of the daughter nuclide $^{90}_{39}\text{Y}$ secular equilibrium of the source is reached quickly and hence the combined spectrum of strontium and yttrium has to be used in the analysis. The combined spectrum of the $\text{Sr} - \text{Y}$ source in secular equilibrium is shown in Fig. 3.9.

Unfortunately the protective silver window in the source adds more complexity as one has to account for possible electron slowing down on its way from the source to a target. Among a number of different techniques electron transport simulations can be used to calculate the slowed down spectrum [55]. Solid line in Fig. 3.9 shows the calculated spectrum of electrons after passing through the

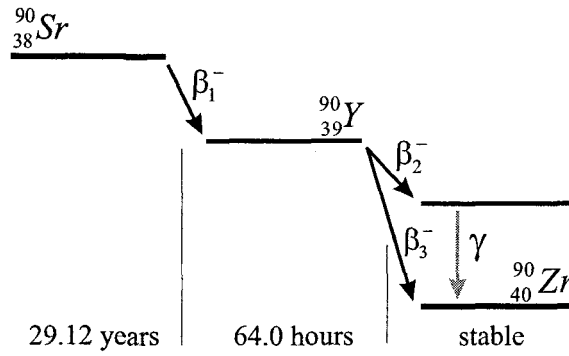


FIGURE 3.8. Series of beta-emitting transitions taking place in the $^{90}\text{Sr}/^{90}\text{Y}$ beta source. The initial cooling down of ^{90}Y by gamma emission (half-life of 3.19 hours) is not shown.

source silver protective window [55]. The slowed-down spectrum closely resembles ^{90}Y emission spectrum as most of ^{90}Sr electrons are absorbed by the protection layer. The average beta energy of the slowed down spectrum is just below 0.9 MeV. Having neglected slowing down in 2 mm of air, this spectrum is assumed for the flux of betas incident on the surface of the sample.

To proceed with the calculation of the electron flux we assume that due to the isotropic nature of the emitted radiation only one half of the produced betas leave the source in the direction of the sample. Then the flux of electrons incident on the center part of a sample for the experimental configuration shown in Fig. 3.7 is simply

$$F \approx \frac{dN}{2dA}$$

where dN is the total number of electrons produced by the source, dA is area of the thin ^{90}Sr source and factor of 2 accounts for the fact that the sample “covers” solid angle of $2\pi = 4\pi/2$ only. Recall that unit of radioactivity *Curie* is defined as 3.7×10^{10} disintegrations per second, then total fluence of electrons reaching the

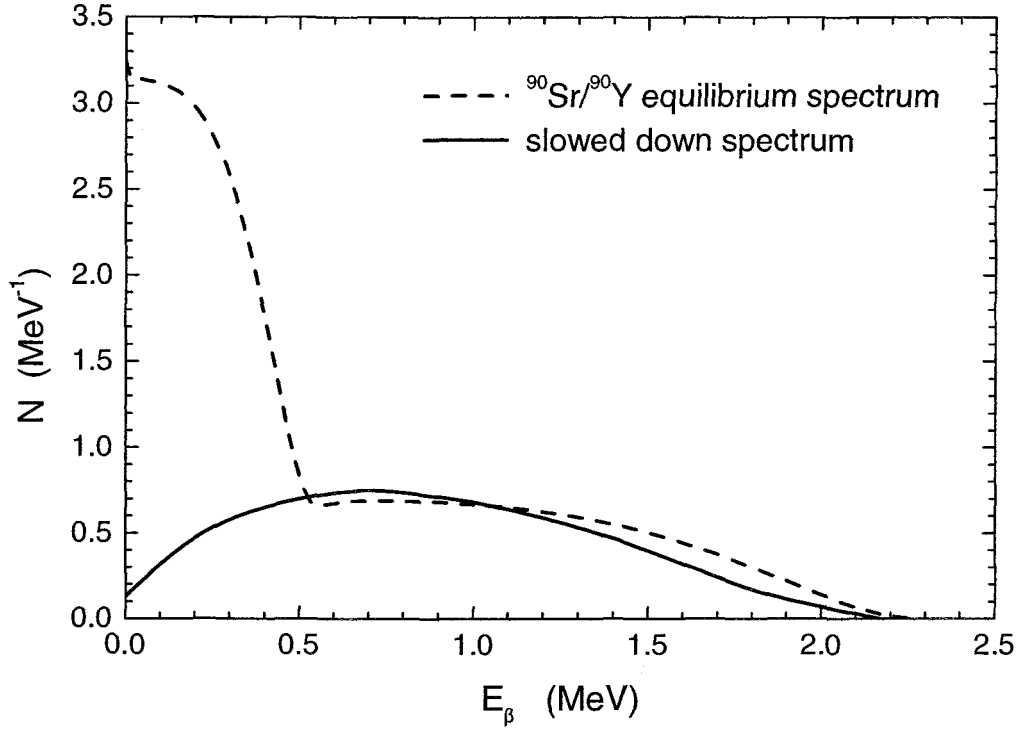


FIGURE 3.9. Beta energy spectrum of $^{90}\text{Sr}/^{90}\text{Y}$ beta-source in secular equilibrium (dashed line) and the calculated slowed down spectrum (solid line).

surface of the sample is readily obtained as

$$\Phi = \int_0^{t_\beta} F(t) dt = F \cdot t_\beta \approx \frac{3.7 \times 10^9 \text{ s}^{-1}}{2\pi d^2/4} t_\beta \approx 9.42 \times 10^9 \cdot t_\beta \text{ s}^{-1} \text{ cm}^{-2} \quad (3.35)$$

where t_β is the irradiation time and d is the diameter of the source.

It should be noted that in further calculations, based on the geometry of the experimental setup, very few electrons are expected to enter the sample at low angles. Hence all the electrons are assumed to be impinging perpendicular to the sample surface. As a result, electrons traveling through the very thin device structure do not lose enough energy to cause a significant change in the stopping powers. This assumption may lead to some inaccuracy in case of low energy

electrons only. Dose calculations are performed by integrating the monoenergetic expression over the entire electron energy spectrum.

3.1.3. Experimental Details

All of our electron irradiation experiments were performed at the OSU Radiation Center using already described $^{90}\text{Sr}/^{90}\text{Y}$ 100 *mCi* beta-radiation source. The wafer was placed directly under the source in close proximity of about 2 mm (see Fig. 3.7).

Exposure durations used in the studies and the corresponding calculated cumulative electron fluences, ionizing doses, displacement doses, and number of radiation-induced displacements are listed in Table 3.4.

Days	Ψ (e^-/cm^2)	Ψ_{tot} (e^-/cm^2)	D^{InGaAs} (<i>MRad</i>)	D^{Si} (<i>MRad</i>)	D_d^{InGaAs} (<i>kRad</i>)	N_d (cm^{-3})
1	8.14×10^{14}	8.14×10^{14}	19	24	0.3	6×10^{15}
2	1.63×10^{15}	2.44×10^{15}	57	72	0.8	1.8×10^{16}
4	3.26×10^{15}	5.70×10^{15}	132	166	2.0	4.2×10^{16}
4	3.26×10^{15}	8.96×10^{15}	208	262	3.1	6.6×10^{16}
8	6.51×10^{15}	1.55×10^{16}	360	454	5.4	1.1×10^{17}
14	1.14×10^{16}	2.68×10^{16}	622	784	9.4	2.0×10^{17}

TABLE 3.4. Exposure durations used in the study and corresponding cumulative electron fluences, ionizing doses, displacement doses, and number of radiation-induced displacements calculated for the base region of an HBT.

3.2. Neutron Irradiation

The purpose of this section is to present and quantify the physical mechanisms responsible for the semiconductor degradation due to bombardment by epi-thermal and fast neutrons. First, the theory for the individual neutron reactions is presented and the displacement cross sections (kerma factors) are evaluated for $10^{-11} - 10$ MeV neutron energy range. Then the concept of the displacement damage function is introduced and its correlation with kerma damage factor is discussed. Finally, the results of calculations for equivalent fluxes, NIEL, displacement doses and defect concentrations are presented.

3.2.1. Interaction of Neutron Irradiation with Matter

The production of atomic displacements by neutron irradiation occurs mainly through two different mechanisms – (1) nuclear reactions, the products of which can cause atomic displacements, or (2) by direct energy transfer through elastic or inelastic scattering. In both cases, the displacement is produced if the recoiling nucleus has an energy in excess of the displacement threshold, E_d . The recoil can have enough energy to produce further displacements before coming to rest in the lattice. The PKA energy deposition is described by the Lindhard's partition theory.

The purpose of this section is to calculate the partial displacement kerma (also called damage energy production cross section) for all the important nuclear reactions and the scattering mechanisms for *In*, *P*, *Ga*, *Si* and *As*. Finally, using the results of the calculations for the separate elements, the total displacement kerma for *InP* and *InGaAs* compounds can be evaluated. For *In*, *P*, *Ga* and *Si* the ENDF/B-VI library available from T-2 Nuclear Information Service of

Los Alamos National Laboratories was used [56]. Unfortunately the ENDF/B-VI library data does not provide adequate data for *As*, in which case the ENDL82 library available from the Radiation Safety Information Computational Center was employed.

3.2.1.1. Absorption (n, γ) reactions

For thermal neutrons, i.e. neutrons with energy less than 0.5 eV, the radiative capture is the dominating mechanism for the displacement damage production. In this reaction an incident neutron is absorbed by a nucleus, which then cools down to its ground state by emitting an energetic photon or a whole photon cascade. The kinetic energy of the recoil is estimated from the incident neutron "kick" and all the photons "kicks"

$$T(E_n, E_\gamma) = \frac{E_n}{A_R + 1} + \frac{\overline{E_\gamma^2}}{2(A_R + 1)mc^2} \quad (3.36)$$

where E_n is the neutron kinetic energy, A_R is the atomic number of the recoil, E_γ is the emitted photon energy and $\overline{E_\gamma^2}$ is the average photon energy calculated from the photon yield, $Y(E_n, E_\gamma)$, and energy distributions, $p(E_n, E_\gamma)$, given in files MF=12,13 of the corresponding databases

$$\overline{E_\gamma^2}(E_n) = \frac{\int_0^{E_\gamma^{max}} Y(E_n, E_\gamma) \cdot E_\gamma^2 \cdot p(E_n, E_\gamma) dE_\gamma}{\int_0^{E_\gamma^{max}} p(E_n, E_\gamma) dE_\gamma} \quad (3.37)$$

The calculated values are 8.5, 6.2, 17.2, 12.6 and 10.2 MeV² for *Si*, *In*, *Ga*, *P* and *As*, respectively.

The damage energy production cross section is obtained from

$$\sigma_d^{n,\gamma}(E_n) = \sigma^{n,\gamma}(E_n) \sum_\gamma \int_{-1}^1 d\mu f(E_n, \mu) L(T[E_n, E_\gamma, \mu]) \quad (3.38)$$

where $\sigma^{n,\gamma}$ is the cross section for the radiative capture reaction (file MF=3) (see for example Fig. 3.10 for *Si*), μ is the laboratory cosine, $f(E_n, \mu)$ is angular distribution function – assumed isotropic, i.e. $f(E_n, \mu) = 1/2$, for all the materials (file MF=4).

Purely for illustrative purposes the cross sections for some of the reactions used in the calculations for *Si* are shown in Fig. 3.10.

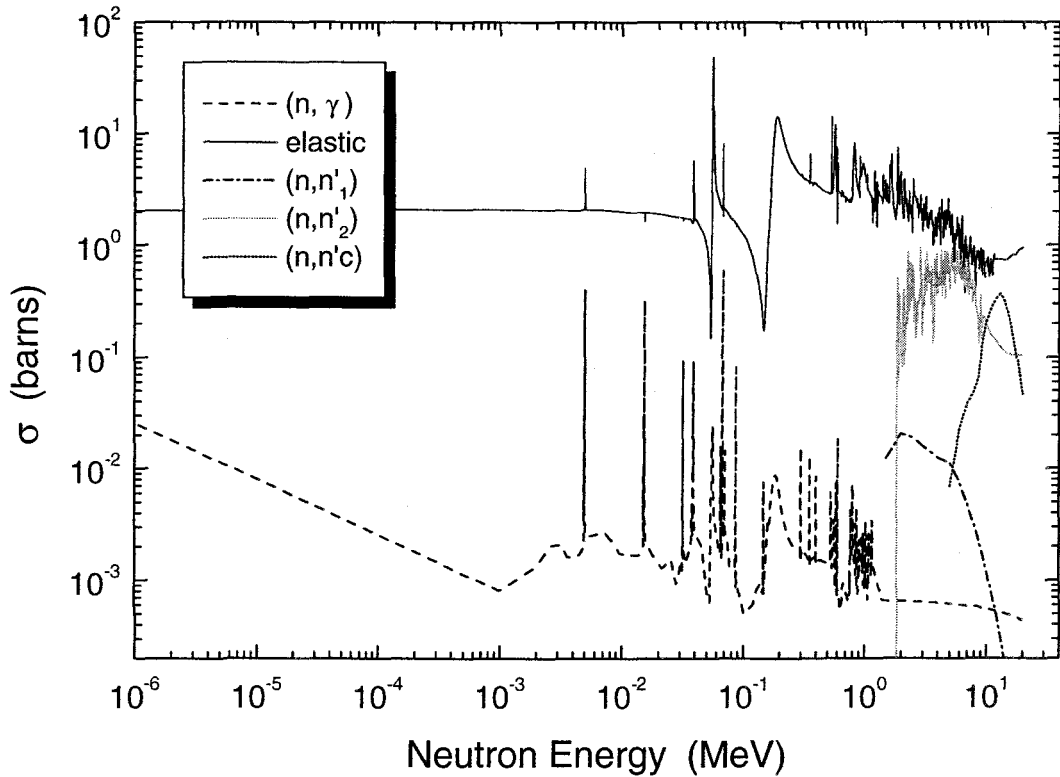


FIGURE 3.10. Cross sections for radiative capture and elastic, continuum inelastic and discrete inelastic scattering as function of incident neutron energy for *Si*.

3.2.1.2. Elastic Scattering

In the case of elastic scattering reaction the kinetic energy of a recoil, T_{el} , is calculated from the simple binary elastic-collision dynamics, which yields

$$T_{el}[E_n, \mu] = \frac{2A_R E_n}{(A_R + 1)^2} [1 - \mu] \quad (3.39)$$

The damage energy production cross section is obtained from

$$\sigma_d^{el}(E_n) = \sigma^{el}(E_n) \int_{-1}^1 d\mu f(E_n, \mu) L(T_{el}[E_n, \mu]) \quad (3.40)$$

where σ^{el} is the elastic scattering cross section given in file MF=3 (see for example Fig. 3.10 for Si), and the angular distribution $f(E_n, \mu)$ is either tabulated directly or is presented in the following form

$$f(\mu, E_n) = \sum_{l=0}^{N_l} \frac{2l+1}{2} a_l(E_n) P_l(\mu) \quad (3.41)$$

In this sum, $P_l(\mu)$ are the Legendre polynomials, a_l the l^{th} Legendre polynomial coefficients (file MF=4) and N_l is the polynomial order at which the sum can be truncated (file MF=4). Recurrent formula for the calculations of $P_l(\mu)$ and the first few polynomials are listed below:

$$P_{l+1}(\mu) = \frac{(2l+1)\mu P_l(\mu) - (l+1)P_{l-1}(\mu)}{l} \quad (3.42)$$

$$P_0(\mu) = 1, \quad P_1(\mu) = \mu \quad (3.43)$$

$$P_2(\mu) = \frac{1}{2}(3\mu^2 - 1)$$

The angular integration is performed using the Gauss-Legendre quadrature method (see for example Ref [57]).

3.2.1.3. Discrete Inelastic Scattering

For discrete inelastic scattering, when the nucleus can be excited to one of the resolved nuclear energy levels, the analysis should be based on conservation of the total energy of the system. Assuming that struck nucleus is excited into the i^{th} state with energy Q_i (file MF=3), kinetic energy of the recoil is given by

$$T_{n,n_i}(E_n, Q_i, \mu) = \frac{A_R E_n}{(A_R + 1)^2} \left[2 - 2\sqrt{1 + \frac{Q_i(A_R + 1)}{A_R E_n}} \mu + \frac{Q_i(A_R + 1)}{A_R E_n} \right] \quad (3.44)$$

Then the displacement kerma is given by

$$\sigma_d^{n,n_i}(E_n) = \sigma^{n,n_i}(E_n) \sum_i \int_{-1}^1 d\mu f(E_n, \mu) L(T_{n,n_i}[E_n, Q_i, \mu]) \quad (3.45)$$

where σ^{n,n_i} is the cross section for the i^{th} reaction given in file MF=3 (see for example Fig. 3.10 for Si), and the angular distribution is the same as for the elastic scattering mechanism.

3.2.1.4. Continuous Inelastic Scattering (n, n') and ($n, 2n$) Reactions

In the case of continuum (n, n') reaction the displacement kerma is obtained from

$$\sigma_d^{n,n'}(E_n) = \sigma^{n,n'}(E_n) \int_0^\infty dE'_n \int_{-1}^1 d\mu f(E_n, \mu) g(E_n, E'_n) L(T_{n,n'}[E_n, E'_n, \mu]) \quad (3.46)$$

where $\sigma^{n,n'}$ is the reaction cross section (file MF=3), and the recoil spectrum is given by

$$T_{n,n'}(E_n, E'_n, \mu) = \frac{1}{A_R} \left[E_n - 2\sqrt{E_n E'_n} \mu + E'_n \right] \quad (3.47)$$

The secondary neutron energy distribution, $g(E, E')$, is either directly tabulated in file MF=15 or calculated from the evaporation model [56, 30]

$$g(E, E') = \frac{E'}{I(E)} \exp - \frac{E'}{\Theta(E)} \quad (3.48)$$

$$I(E) = \Theta^2(E) [1 - e^{-x}(1 - x)] \quad (3.49)$$

$$x = \frac{E - U}{\Theta}$$

with $\Theta(E)$ tabulated in file MF=15. The angular distribution is assumed to be isotropic (file MF=4).

Similar procedure is used for (n,2n) reactions with the corresponding reaction cross sections $\sigma^{n,2n}$ from file MF=3 and secondary energy distributions $g(E_n, E'_{2n})$ from file MF=4.

$\sigma^{n,n'}$ and $\sigma^{n,2n}$ for *Si* are shown in Fig. 3.10.

3.2.1.5. (n, particle) Reactions

In the case of the (n, particle) reactions the recoil energy spectrum is given by

$$T = \frac{1}{A_R + 1} \left[E^* - 2\sqrt{aE^*E_a}\mu + aE_a \right] \quad (3.50)$$

$$E^* = \frac{A_R + 1 - a}{A_R + 1} E_n$$

where a is the mass ratio of the emitted particle to the neutron and the particle energy E_a is equal to the smaller of the available energy

$$Q + \frac{A_R E_n}{A_R + 1}$$

or the Coulomb barrier energy

$$\frac{1.029 \times 10^6 z Z}{A_R^{1/3} + a^{1/3}}$$

where z and Z are the charges of the emitted particle and the target atom, respectively. The displacement cross section is found from the expression similar to Eq. 3.40. The angular distribution is defaulted to isotropic (file MF=4).

3.2.2. Implementation and Results

Having calculated the displacement kerma for all the reactions the total damage energy production cross section is simply found as a sum of the cross sections for the individual processes:

$$\sigma_d = \sigma_d^{n,\gamma} + \sigma_d^{el} + \sum_i \sigma_d^{n,n_i} + \sigma_d^{n,n'} + \sigma_d^{n,2n} + \sum_X \sigma_d^{n,X} \quad (3.51)$$

A set of programs was written to implement the outlined calculations for the materials of the interest. Very briefly, the calculation of damage energy production cross section proceeds in the following manner. In the first step all the reaction cross sections, angular distribution data, secondary particle distributions, and photon yields are loaded into memory. Then the weights and abscissas for the Gauss-Legendre integration routine are initialized and energy distributions of the average photon energies and other secondary particles are calculated. Finally, looping through all the possible reactions the total kerma displacement is calculated as a function of energy in the range of $10^{-11} - 10 \text{ MeV}$. The scattering mechanisms and nuclear reactions included in the displacement kerma evaluation are listed in Table 3.5. Fig. 3.11 shows calculated the energy production cross sections for gallium, arsenic and indium, and Fig. 3.12 shows the cross section for phosphorus.

In case of *InGaAs* and *InP* compounds, the displacement kermas were evaluated for each of the elements separately. To account for the fact that in a compound material a recoiling atom can collide with atoms of different elements, the corrected Lindhard's partition function, \mathcal{L} (see Eq. 3.33), is used instead of the standard Lindhard partition function (Eq. 2.16). Then the displacement kerma for the compounds are calculated as a sum of the kermas for each element using

Reaction	<i>Si</i>	<i>P</i>	<i>Ga</i>	<i>As</i>	<i>In</i>
elastic scattering	✓	✓	✓	✓	✓
$(n, n'c)$	✓	✓	✓	✓	✓
(n, n'_i)	✓ ₁₋₂₁	—	—	✓ ₁₋₁₃	✓ ₁₋₂₈
$(n, 2n)$	✓	✓	✓	—	✓
(n, γ)	✓	✓	✓	✓	✓
(n, p)	✓	✓	—	—	✓

TABLE 3.5. Reactions used in calculations of displacement kerma for *Si*, *P*, *Ga*, *As* and *In*. Indices in (n, n'_i) row refer to discrete level reactions.

fraction weights, x_i , i.e.

$$K_{D,InGaAs} = \sum_{i=In,Ga,As} x_i K_{D,i} = \frac{1}{2} [0.53K_{D,In} + 0.475K_{D,Ga} + K_{D,As}] \quad (3.52)$$

The results for *InGaAs* and *InP* are shown in Figs. 3.13 and 3.12 respectively.

3.2.3. Displacement Damage Function

In cases when the bulk degradation effects present the dominant radiation damage mechanism (which is the case for bipolar transistors) K_D is considered to be an excellent measure of device performance degradation. For *GaAs* it has been reported, however, that experimentally observed bulk damage is not always linearly proportional to the displacement kerma [23, 26] – there is a considerable decrease in the damage production efficiency at the high neutron energies. Fig. 3.14 shows the theoretically calculated displacement kerma (K_D) and experimentally observed

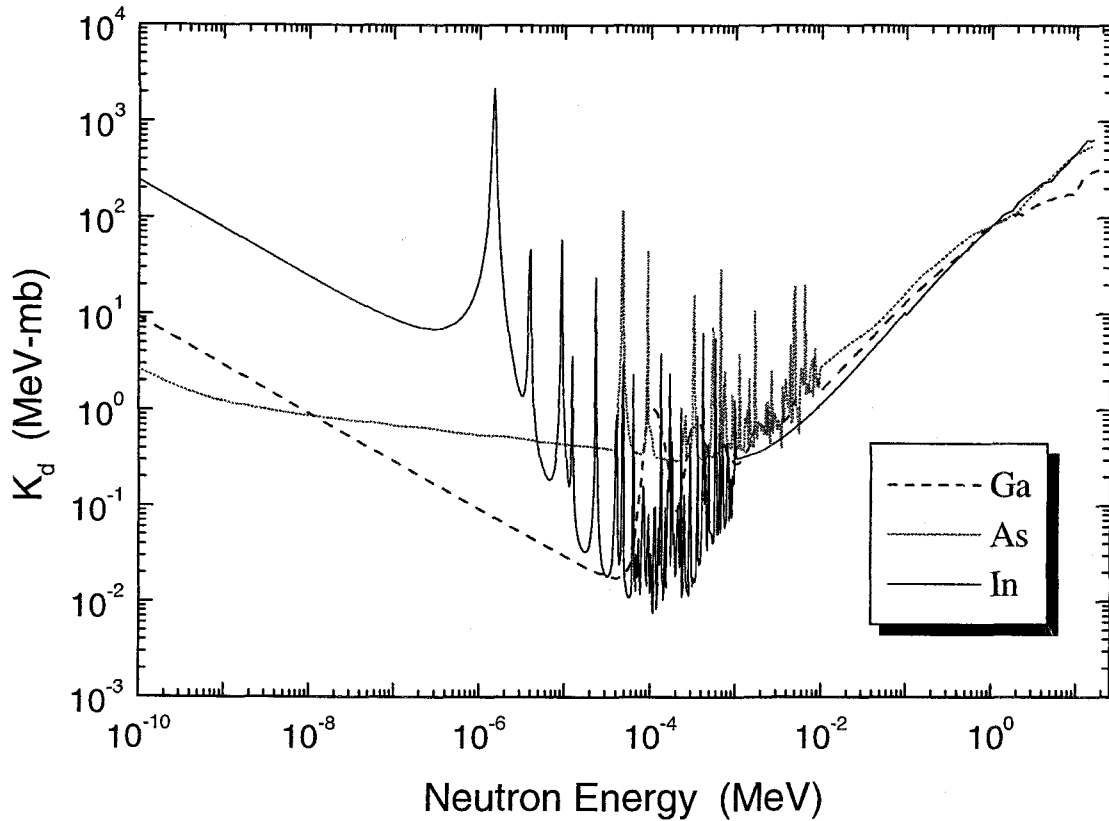


FIGURE 3.11. Calculated displacement kermas for indium, gallium and arsenic.

damage (F_D) – the so-called displacement damage function or simply damage function, defined as an energy dependent parameter proportional to the quotient of the observable displacement damage per target atom per neutron fluence. To compensate for the difference between K_D and F_D the PKA-dependent empirical model was proposed by Griffin *et al.* [23]. The observed effect is attributed to the so-called thermal spike effect resulting from the saturation in the size (not number!) of the produced clusters. Thermal spikes, first observed in some metals, occur if the local energy density – energy of the defect clusters – is high enough to cause local melting followed by recrystallization of the material. The effect is

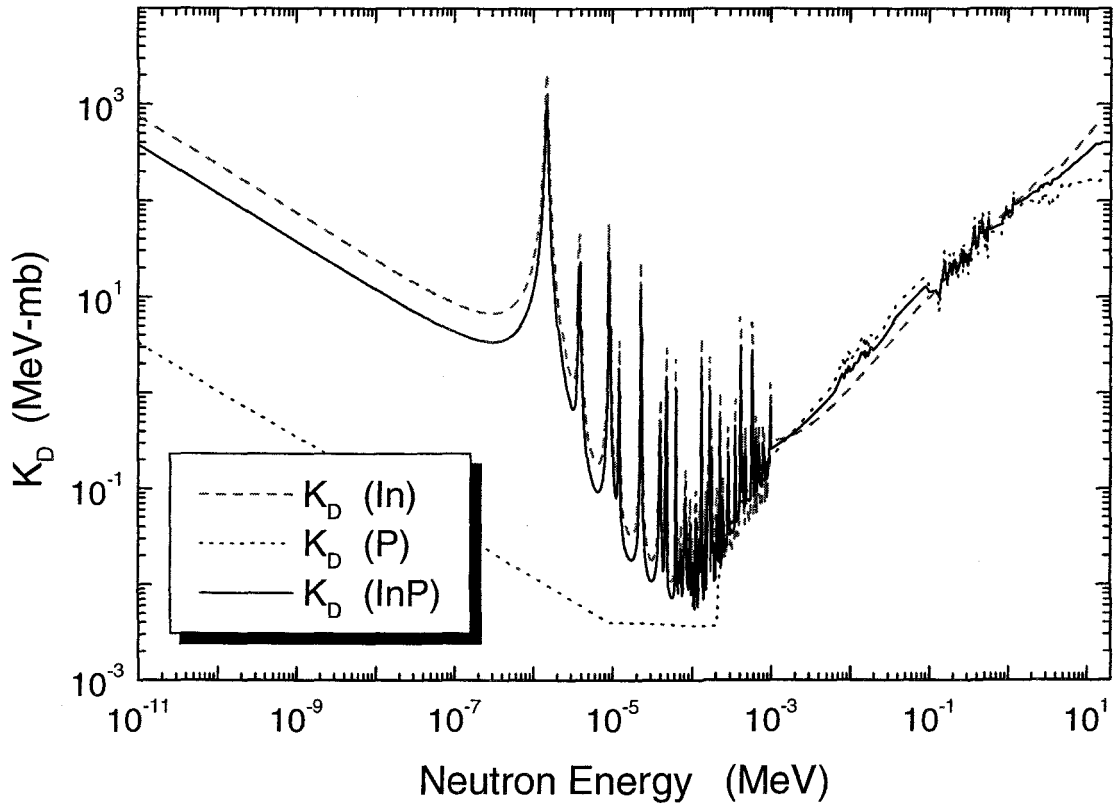


FIGURE 3.12. Calculated displacement kermas for *In*, *P* and *InP*.

not observed for silicon, for which the threshold displacement energy is somewhat higher (see Table 2.1), but can be expected to be very important for *InGaAs* and *InP*, where E_d 's are low as in the case of *GaAs*. Unfortunately there is no well developed theory to account for the possible annealing/recrystallization effects, therefore the only viable approach is to extract empirical efficiency factor from the extensive experimental studies using different neutron sources. For *GaAs* Griffin *et al.* suggested the following functional dependence for the damage efficiency, $\zeta(T)$,

$$\zeta(T) = a_0 + a_1 \log T + a_2 T^2 \log T + a_3 [\log T]^2 \quad (3.53)$$

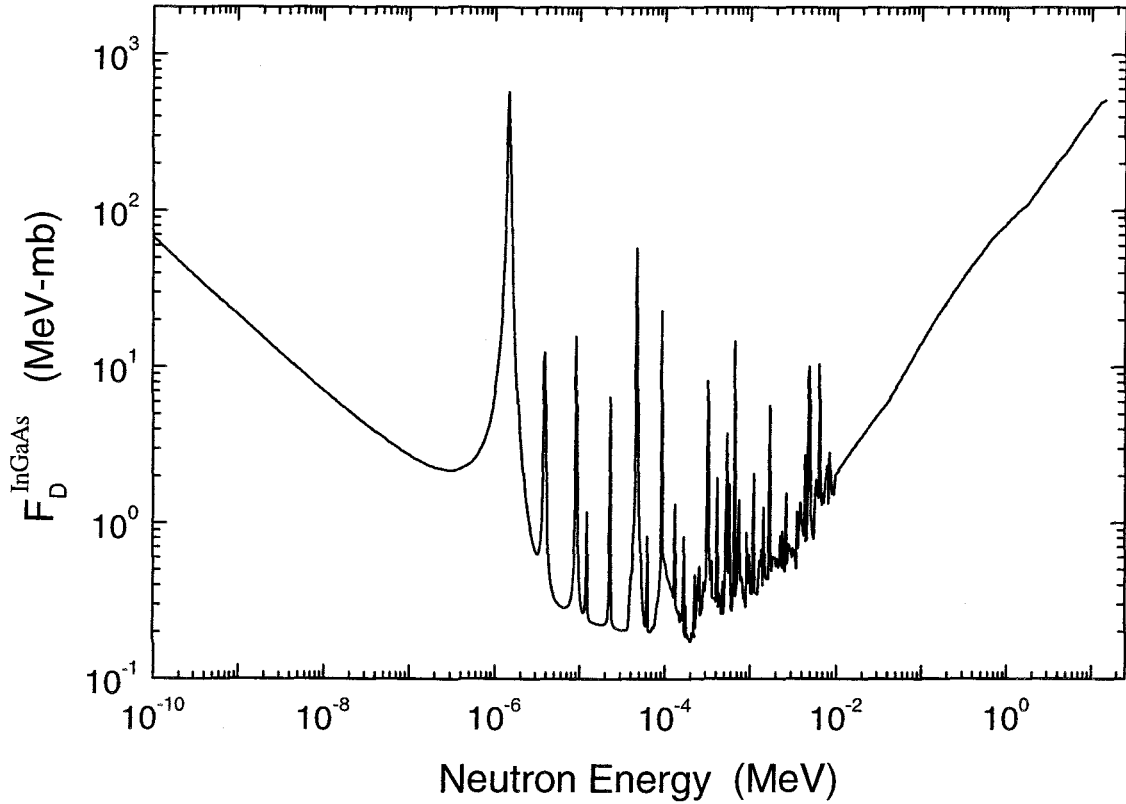


FIGURE 3.13. Calculated displacement kermas for *InGaAs*.

where T is the PKA recoil energy measured in keV , and a_i are the numerical coefficients determined by fitting the experimental data. The damage efficiency function and the corresponding values of a_i 's are shown in Fig. 3.15. As a result, when $\zeta(T)$ is used in the theoretical displacement kerma evaluation, calculated K_D matches the damage function.

Despite the obvious deficiencies the displacement kerma is still very useful as a measure of exposure to the damaging radiation. Moreover, unless used for comparison of the results for very high energy neutron sources, e.g. accelerators, the displacement kerma still gives very reasonably good estimate (within 10%) for

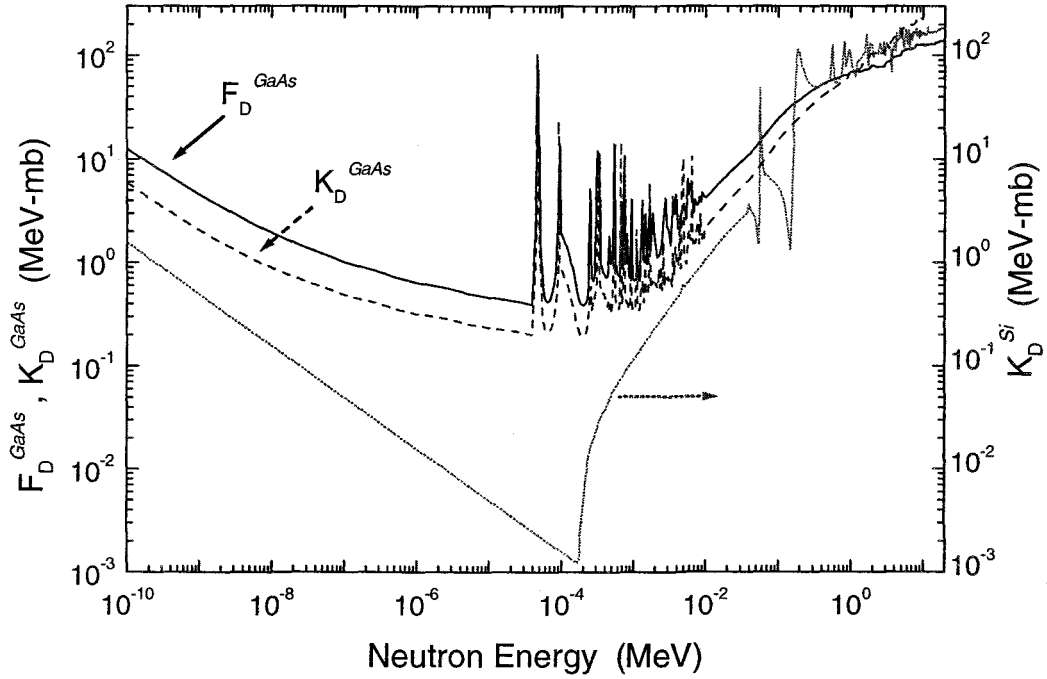


FIGURE 3.14. Gallium arsenide damage function, F_D^{GaAs} , normalized by factor of 2.2, and displacement kerma, K_D^{GaAs} , and silicon displacement kerma function, K_D^{Si} .

the introduced damage. Thus, as there are no results available for the damage efficiency functions for *InP* and *InGaAs*, the displacement kermas will be used in all further calculations for these materials.

3.2.4. Neutron Damage Equivalence and NIEL

All neutron irradiation experiments were conducted at OSU TRIGA “Marc II” 1 MW reactor operated at 100 kW. The samples were enclosed in cadmium boxes to block the thermal neutrons ($E_{th} < 0.5$ eV) and reduce ionization damage. For the irradiation the samples were positioned in the Rotating Specimen Rack

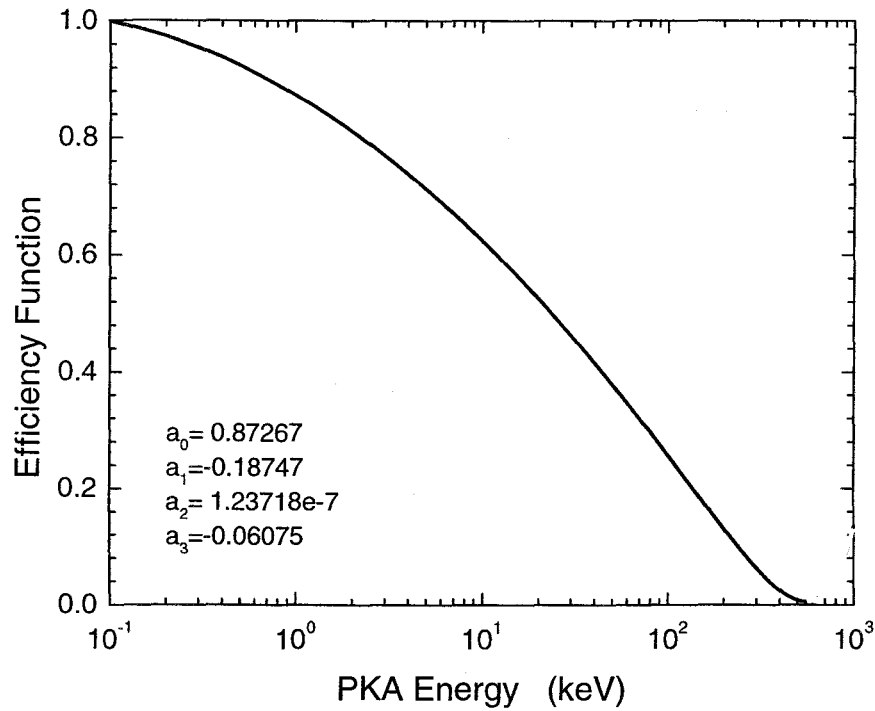


FIGURE 3.15. Neutron damage efficiency function for gallium arsenide.

(RSR), also called "Lazy Suzan". Differential neutron energy spectrum at the RSR – result of the Monte Carlo Neutron Photon (MCNP) transport simulation – is shown in Fig. 3.16 [58]. Furthermore, the total epi-thermal and fast neutron fluxes were measured using foil activation dosimetry technique, with results of 10^{10} cm^{-2} and $5 \times 10^{10} \text{ cm}^{-2}$ for epi-thermal ($0.5 \text{ eV} < E < 10 \text{ keV}$) and fast neutron ($E > 10 \text{ keV}$) fluxes, respectively, for the reactor operated at 100 kW. The integrated flux for the fast neutron part of the MCNP calculated spectrum was normalized to one and then multiplied by the fast neutron flux value obtained from the direct measurement. In other words, the MCNP results were used only to obtain the shape of the spectrum, while the absolute values of the flux were

determined from the dosimetry measurements. Similar procedure was used for the analysis of the epi-thermal neutron flux.

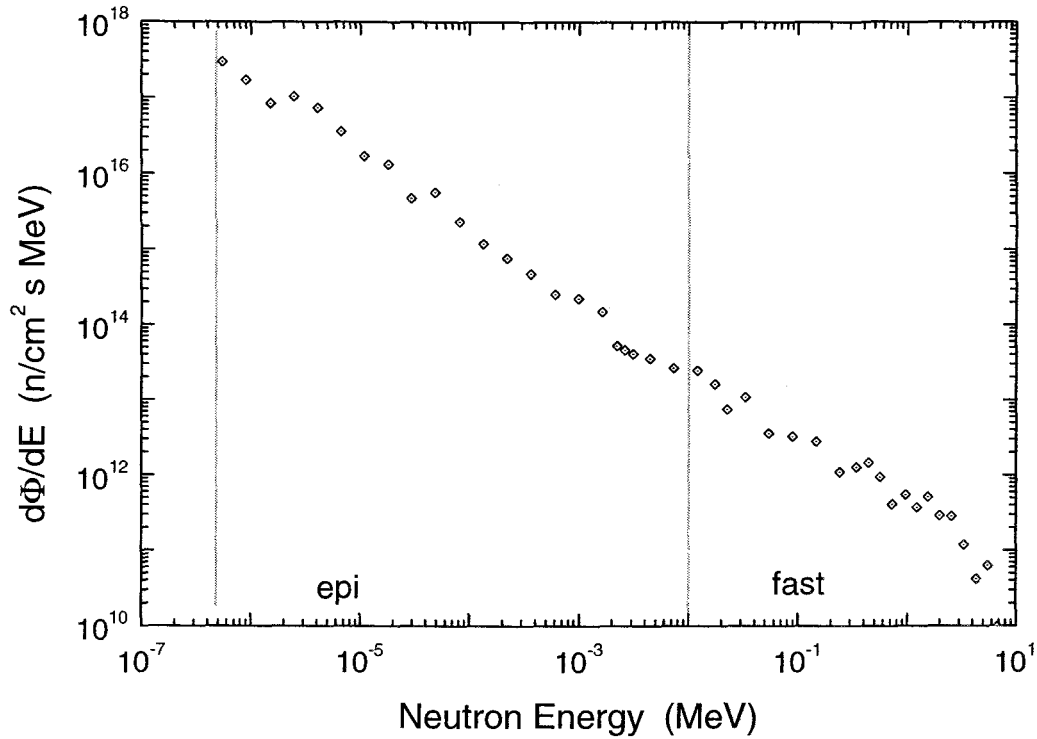


FIGURE 3.16. Differential neutron energy spectrum at position of sample during neutron irradiation.

Energy spectra of a neutron flux produced by an accelerator or nuclear reactor may vary drastically from one facility to another. To be able to interpret and compare the results of irradiations by sources of different energy spectra the so-called *equivalent monoenergetic neutron fluence* is often used. The method relies on the knowledge of the energy spectrum of the neutron source and the degradation effects as a function of energy. Using 1 MeV as a reference energy – standard value used by the radiation-hardness community – the equivalent monoenergetic neutron

flux can be calculated as

$$\Phi_{eq,1 \text{ MeV}} = \int_0^{\infty} \frac{d\Phi(E)}{dE} \frac{F_D(E)}{F_D(1 \text{ MeV})} dE \quad (3.54)$$

It should be noted that the damage function is different for different semiconductors and therefore $\Phi_{eq,1 \text{ MeV}}$ should be calculated separately for each material of the interest. Using the calculated displacement kerma for *InP* and *InGaAs* (see Figs. 3.12 and 3.13) and Lazy Suzan energy spectrum the integral is evaluated in the range of $0.5 \text{ eV} - 10 \text{ MeV}$ with the results listed in Table 3.6.

Material	$K_D(1 \text{ MeV})$ ($\text{MeV} \cdot \text{mb}$)	$\Phi_{eq,1 \text{ MeV}}^{epi}$ ($\text{cm}^{-2} \text{s}^{-1}$)	$\Phi_{eq,1 \text{ MeV}}^{fast}$ ($\text{cm}^{-2} \text{s}^{-1}$)	$\Phi_{eq,1 \text{ MeV}}^{total}$ ($\text{cm}^{-2} \text{s}^{-1}$)
<i>Si</i>	95	1.0×10^8	4.3×10^{10}	4.3×10^{10}
<i>GaAs</i>	70	5.3×10^8	4.5×10^{10}	4.5×10^{10}
<i>InGaAs</i>	82	1.4×10^9	5.4×10^{10}	5.6×10^{10}
<i>InP</i>	78	4.8×10^9	7.6×10^{10}	8.1×10^{10}

TABLE 3.6. Damage functions (displacement kerma in case of *InGaAs* and *InP*) at 1 MeV , 1 MeV equivalent fluxes for epi-thermal and fast neutrons and total 1 MeV equivalent flux at RSR facility for *Si*, *GaAs*, *InGaAs* and *InP*. Equivalent flux values are for reactor operated at 100 kW .

Although the damage function (or displacement kerma) can be used as a direct measure of the damage energy deposited in the material, it is more convenient to perform some unit conversion and present the results in terms of the non-

ionizing energy loss. Recalling that conventional units for NIEL are $\text{MeV} \cdot \text{cm}^2/\text{g}$ or $\text{rad} \cdot \text{cm}^2$ the conversion equation can be written as

$$\begin{aligned} S_d &= 10^{-27} \frac{K_D \times n_a}{\rho} [\text{MeV} \cdot \text{cm}^2/\text{g}] \\ &= 1.602 \times 10^{-35} \frac{K_D \times n_a}{\rho} [\text{rad} \cdot \text{cm}^2] \end{aligned} \quad (3.55)$$

The calculated values of NIEL at 1 MeV neutron energy for *Si*, *GaAs*, *InGaAs* and *InP* are listed in Table 3.7.

Displacement introduction rate can be simply calculated from the NIEL results using the modified Kinchin-Pease model (see Section 2.3.3)

$$a_T = \kappa \frac{S_d}{2E_d} \rho \quad (3.56)$$

Results for the 1 MeV neutrons are listed in Table 3.7.

Material	$K_D(1 \text{ MeV})$ ($\text{MeV} \cdot \text{mb}$)	$S_d(1 \text{ MeV})$ ($\text{MeV} \cdot \text{cm}^2/\text{g}$)	$a_T(1 \text{ MeV})$ (cm^{-1})
<i>Si</i>	95	2.04×10^{-3}	90
<i>GaAs</i>	70	0.64×10^{-3}	136
<i>InGaAs</i>	82	0.58×10^{-3}	127
<i>InP</i>	78	0.64×10^{-3}	141

TABLE 3.7. Damage function (displacement kerma in case of *InGaAs* and *InP*), neutron NIEL and displacement introduction rate at 1 MeV for *Si*, *GaAs*, *InGaAs* and *InP*.

3.2.5. Experimental Details

All the neutron irradiation experiments were carried out using the Rotating Specimen Rack facility of the OSU TRIGA "Marc II" 1 MW reactor operated at 100 kW. The samples were irradiated separately for radiation exposure time of 7, 20, 60 and 180 minutes. The calculated total neutron fluence (excluding thermal neutrons) and corresponding 1 MeV equivalent fluence for all individual irradiation times are listed in Table 3.8.

Sample #	t (min)	Ψ^{total} (n/cm^2)	$\Psi_{eq,Si}^{total}$ (n/cm^2)	$\Psi_{eq,InGaAs}^{total}$ (n/cm^2)	$\Psi_{eq,InP}^{total}$ (n/cm^2)
1	7.0	2.5×10^{13}	1.8×10^{13}	2.3×10^{13}	3.4×10^{13}
2	20.0	7.2×10^{13}	5.2×10^{13}	6.7×10^{13}	9.7×10^{13}
3	60.0	2.2×10^{14}	1.6×10^{14}	2.0×10^{14}	2.9×10^{14}
4	180.0	6.5×10^{14}	4.7×10^{14}	6.0×10^{14}	8.7×10^{14}

TABLE 3.8. Exposure duration, corresponding total neutron fluence and 1 MeV equivalent fluences for *Si*, *InGaAs* and *InP* for neutron irradiation experiment.

3.3. Gamma Irradiation

Unlike electrons, that are able to introduce displacements directly, gamma-rays may produce damage only through generating secondary betas, which then

may cause some atomic dislodgement. As a result both ionizing and non-ionizing energy can be deposited in the material. The purpose of this section is to introduce physical mechanisms responsible for the damage produced by the gamma radiation. The theoretical basis for calculations of displacement damage is developed, the most vital interactions are described and corresponding cross sections for delta-ray production are evaluated. Estimated slowed down electron spectra are applied to calculate some of the fundamental quantities, including NIEL and radiation-induced defect density.

3.3.1. Gamma Interactions in Matter

There are several types of physical interactions that can lead to production of secondary electrons, namely Compton (or incoherent) scattering, Rayleigh (or coherent) scattering, photoelectric and photonuclear effects and, finally, electron-positron pair production in electron and nuclear fields. To illustrate relative importance of the reactions the corresponding cross sections for *InP* for the energy range of $10^{-3} - 10^4$ MeV are shown in Fig. 3.17 [59]. Since most of the radiation testing work is done using gamma-rays with energies of only few MeV or lower, the pair production and photonuclear effects can be safely ignored. Furthermore, the coherent scattering does not result in virtually any energy deposition and therefore one is left to account for Compton and photoelectric reactions only.

In this section the basics of the Compton scattering and photoelectric effect are described and the physics necessary to evaluate the contribution of the reactions to the damage production is presented.

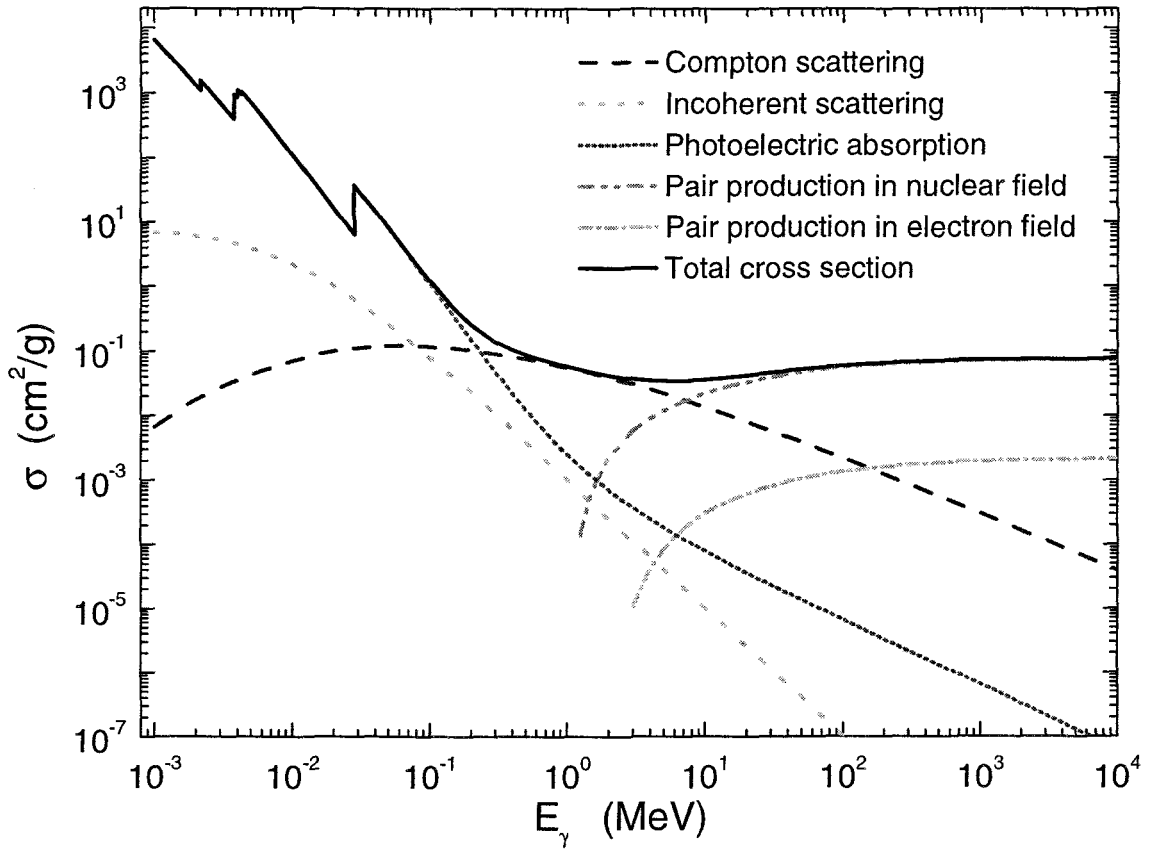


FIGURE 3.17. Cross sections for Compton and Rayleigh scattering, photoelectric and photonuclear effects and electron-positron pair production in electron and nuclear fields in *InP*.

3.3.1.1. Compton Effect

The simple diagram illustrating a single Compton scattering event is shown in Fig. 3.18. In this process the incident γ -photon of energy $E_\gamma = h\nu$ loses part of its energy T_e to the electron which departs at an angle θ . The photon is scattered at an angle ϕ and now possesses the energy of $h\nu' = h\nu - T_e$. It should be noted that depending on θ the energy of the kicked electron can have any value between

zero and T_e^{max} found from the momentum and energy conservation

$$T_e^{max} = \frac{2h\nu\alpha}{1 + 2\alpha} \quad (3.57)$$

where $\alpha = h\nu/m_e c^2$, and the electron is assumed to have zero binding and zero initial kinetic energy.

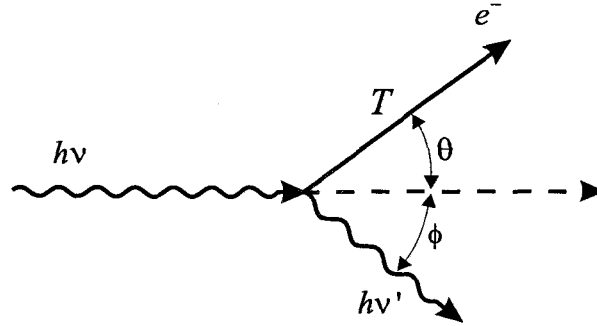


FIGURE 3.18. Single Compton scattering event.

For further analysis the differential cross section for the photon scattering needs to be evaluated. Simple kinematic approach as well as pure wave theory, however, do not produce appropriate predictions [47, 48]. Applying Dirac's relativistic theory Klein and Nishina removed the gap between the two theories and were able to accurately describe the scattering process. According to them the differential cross section for production of an electron with an energy T_e (or T'_e in $m_0 c^2$ units) is

$$\begin{aligned} \frac{d\sigma^C(E_\gamma, T_e)}{dT_e} &= \frac{\pi e^4}{m_0^2 c^4 E'_\gamma (E'_\gamma - T'_e)} \times \\ &\times \left[1 + \left(\frac{E'_\gamma - T'_e}{E'_\gamma} \right)^2 - 2 \frac{E'_\gamma + 1}{E'_\gamma} + \frac{(1 + 2E'_\gamma)(E'_\gamma - T'_e)}{E'^3_\gamma} + \frac{1}{E'_\gamma (E'_\gamma - T'_e)} \right] \end{aligned} \quad (3.58)$$

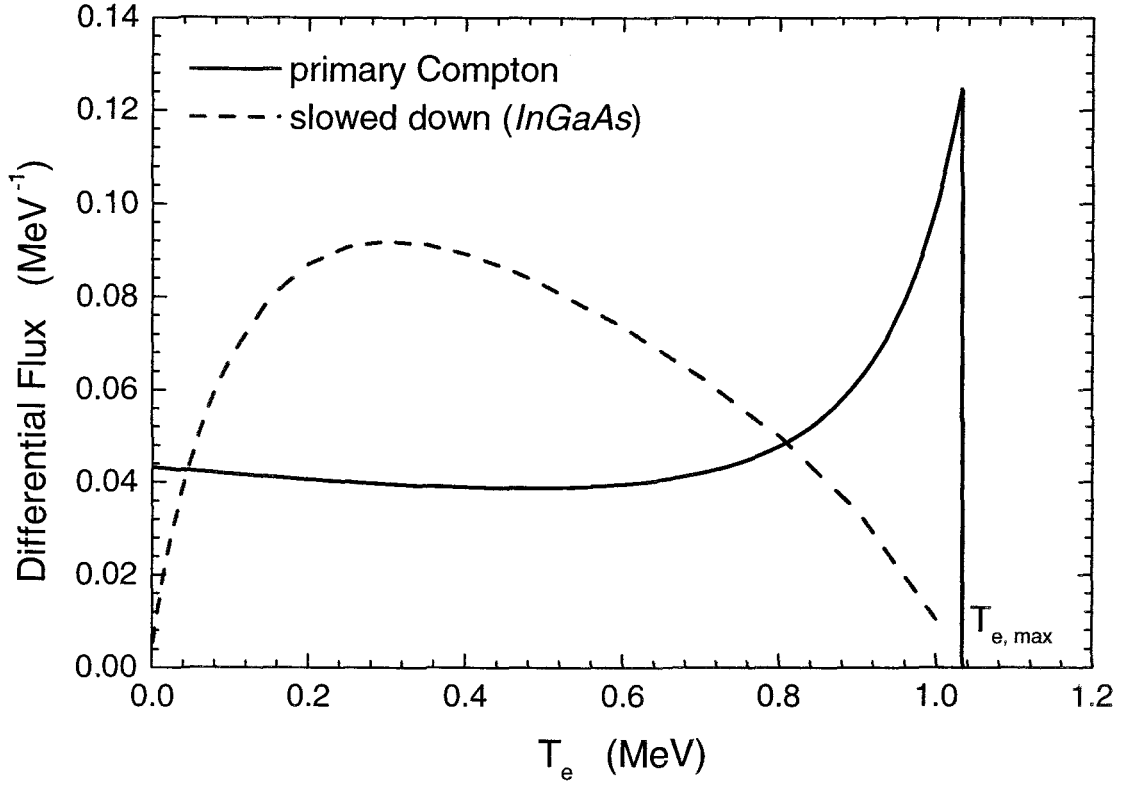


FIGURE 3.19. Compton electron differential energy flux, i.e. Klein-Nishina energy differential cross section, and the slowed down energy spectrum calculated for *InGaAs*.

where E'_γ is the incident gamma energy expressed in m_0c^2 units. The differential cross section simply presents the energy spectrum of the emitted Compton electrons. Calculated cross section for a 1.25 MeV photon is shown in Fig. 3.19. Integrating Eq. 3.58 from 0 to T_e^{max} one can evaluate the total Klein-Nishina cross section

$$\sigma_{KN}(E_\gamma) = \pi r_0^2 \left[\frac{2(1+\alpha)}{\alpha} \left(\frac{2(1+\alpha)}{1+2\alpha} - \frac{\ln(1+2\alpha)}{\alpha} \right) + \frac{\ln(1+2\alpha)}{\alpha} - \frac{2(1+3\alpha)}{(1+2\alpha)^2} \right] \quad (3.59)$$

The total KN cross section presents the attenuating properties of the material due to Compton scattering and provides the information necessary to estimate the produced Compton electron flux. As already mentioned the KN theory was derived for free electrons, in the low photon energy range, however, the correction has to be made to account for the interactions with strongly bound inner shell electrons. Sufficiently good results are achieved simply by multiplying the KN cross section by the so-called incoherent scattering function, which is defined as the probability that the atom will be excited or ionized after a Compton scattering event. The Hartree-Fock incoherent scattering functions have been calculated [60] for a wide variety of materials and are employed in XCOM database available through the NIST [59]. Calculated cross sections for Compton scattering including the correction for electron binding are shown in Fig. 3.20 for *InGaAs*, *GaAs*, *Si*, *Au* and polyimide [59]. The values of cross sections extracted at $E_\gamma = 1.25 \text{ MeV}$ are listed in the Table 3.9 and show virtually no dependence on the atomic number of the material. Corresponding differential and total fluxes of Compton electrons (per unit thickness) are calculated as

$$\phi_C(T_e) = n_a \frac{d\sigma_C(E_\gamma, T_e)}{dT_e} \Phi_\gamma \quad (3.60)$$

$$\Phi_C = n_a \sigma_C(E_\gamma) \Phi_\gamma \quad (3.61)$$

where σ_C is expressed in cm^2/g , and Φ_γ is the flux of the incident monoenergetic gamma rays. Calculated Φ_C are listed in the table below.

3.3.1.2. Photoelectric Effect

In addition to Compton scattering, gamma-electron collision may also result in the ejection of a bound electron from an atomic shell as a consequence of the

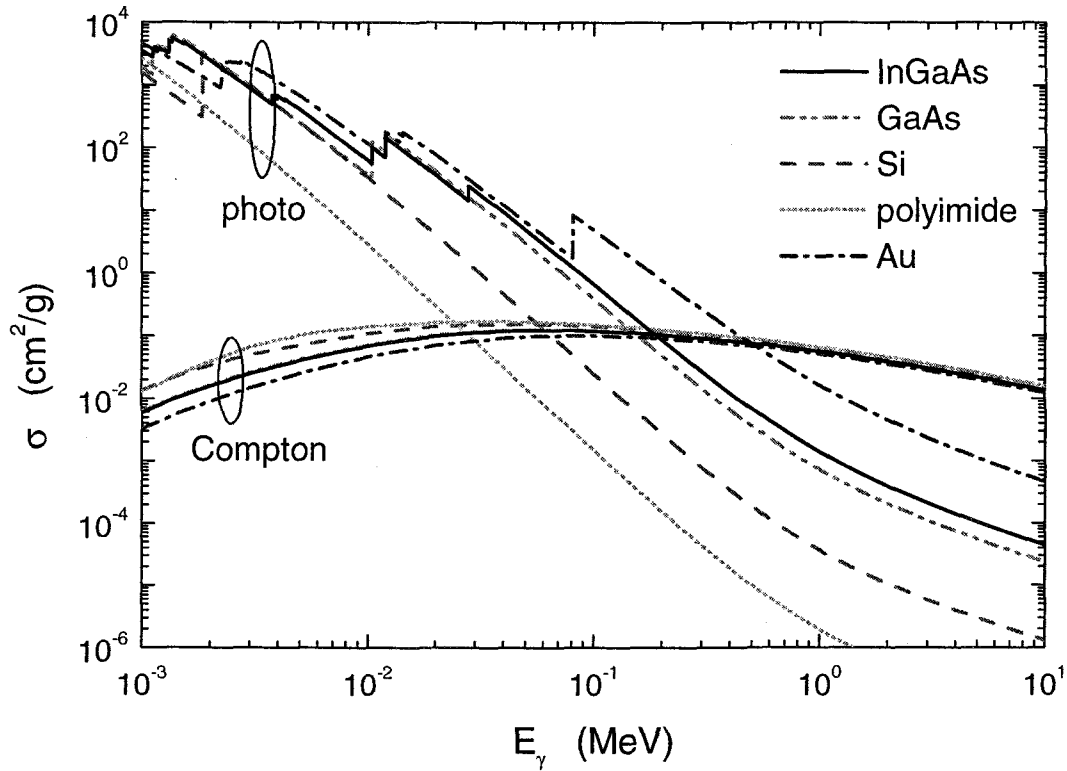


FIGURE 3.20. Cross sections for Compton scattering and photoelectric effect for *InGaAs*, *GaAs*, *Si*, *Au* and polyimide.

absorption of the incident photon. The kinetic energy of the liberated electron is given by

$$T_e = h\nu - E_b - T_{atom}$$

where E_b is the binding energy of the electron in the atom (typically few *keV*) and T_{atom} is the kinetic energy of the recoiling atom. If the gamma energy is on the order of *MeV*, T_{atom} and E_b can be safely neglected producing

$$T_e = h\nu \quad (3.62)$$

The photoelectric effect depends very strongly on the atomic shell structure and thus varies widely from element to element. Additionally, due to the threshold

Material	$\sigma_C(1.25 \text{ MeV})$	$\sigma_{pe}(1.25 \text{ MeV})$	Φ_C	Φ_{slowed}
	(cm^2/g)	(cm^2/g)	(cm^{-2})	(cm^{-2})
<i>Si</i>	0.058	2.33×10^{-5}	0.119	0.016
<i>Au</i>	0.056	1.04×10^{-2}	0.021	0.023
<i>GaAs</i>	0.051	4.63×10^{-4}	0.064	0.017
<i>InP</i>	0.052	1.62×10^{-3}	0.072	0.018
<i>InGaAs</i>	0.051	8.94×10^{-4}	0.064	0.018
polyimide	0.058	1.24×10^{-6}	0.168	0.014

TABLE 3.9. Cross sections for Compton scattering and photoelectric effect at $E_\gamma = 1.25 \text{ MeV}$, corresponding total primary Compton electron flux and total slowed down Compton electron flux produced by one incident gamma for *Si*, *Au*, *GaAs*, *InGaAs*, *InP* and polyimide.

nature of the absorption process some discontinuities corresponding to the shell absorption edges are introduced. As a result there is no simple universal expression for the cross sections. Using quantum mechanical approach some satisfactory approximations have been made for different photon energy ranges. Berger *et al.* have combined low energy Scofield's phase-shift calculations with asymptotic calculations of Pratt for high energy gammas [59]. The calculated cross sections for *InGaAs*, *GaAs*, *Si*, *Au* and polyimide are shown in Fig. 3.20 with $\sigma_{pe}(1.25 \text{ MeV})$ listed in Table 3.9 [59]. In contrast to Compton scattering the photoelectric effect demonstrates very strong dependence on the atomic number having much larger cross sections for higher-Z atoms – compare, for instance, the results for polyimide and *Au*. It should be noted that with the exception of gold the relative magnitude

of the electron production due to the photoelectric effect is negligible when comparing to the Compton scattered electrons. Therefore, if the material surrounding the device contains no or little high Z elements it is sufficient to perform the analysis using the Compton electrons only.

3.3.1.3. Spectrum Resulting from Electron Slowing Down

The electron spectrum incident on some layer in the device may not necessarily coincide with the initial photon-generated spectrum since electrons get slowed down along their path to the region of interest. As discussed in Chapter 3, high energy electrons dissipate their energy through a series of collisions. In the vast majority of collisions an electron loses only a very small fraction of its energy, and the probability of the large energy losses due to radiative or knock-on events is usually low. Under these conditions the spectrum resulting from the slowing down process is simply inversely proportional to the total electron stopping power in the media (see for example [19, 61]). Applying this rule to the Compton electrons introduced by the gamma radiation, the energy spectrum of the slowed down electrons can be evaluated as

$$\phi(T_e) = \left[\frac{dT_e}{dx}(T_e) \right]^{-1} \int_{T_e}^{T_e^{max}} N(T'_e) dT'_e \quad (3.63)$$

where $N(T'_e)$ gives the number of electrons generated by one photon in a unit volume per unit time. Calculated slowed down spectra for *Si*, *GaAs*, *InGaAs* and *InP* are shown in Fig. 3.21.

Finally, the total electron flux is calculated by integrating the slowed differential electron flux and results are listed in Table 3.9. It is very important to note that with the only exception of high Z *Au* the rest of the materials have almost

identical values of the electron flux, thus *the final, i.e. slowed, electron spectrum* incident on a region of interest is *the same* throughout the device, assuming, of course, that there is no high Z materials present in the neighborhood.

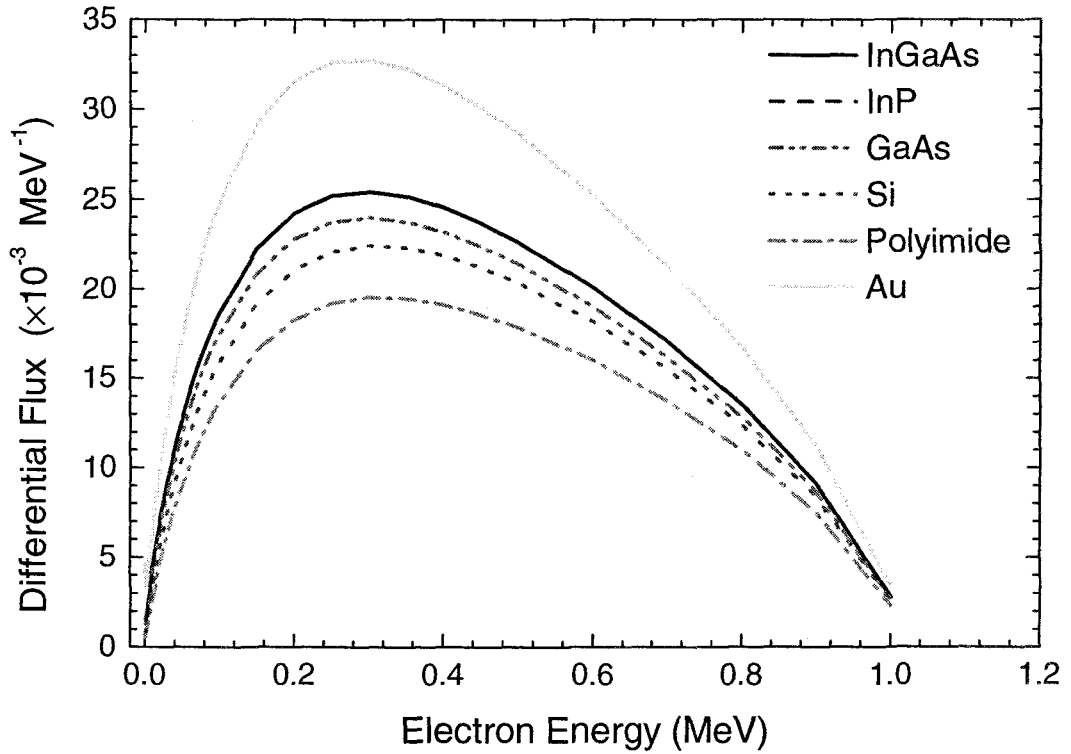


FIGURE 3.21. Differential flux of slowed down Compton electrons for *InGaAs*, *InP*, *GaAs*, *Si*, *Au* and polyimide.

3.3.2. Co^{60} Gamma-Source

Gammacell 200 Co^{60} gamma irradiator (Radiation Center, Oregon State University) was used in all gamma-irradiation experiments. The detailed infor-

mation on the source geometry and calculation of the current dose rates can be found in Ref. [62]. The so-called shielded-cavity configuration of the source results in a relatively hard gamma spectrum with small fraction of low energy Compton-scattered photons [63]. Only the source self-absorption and scattering distort the primary Co^{60} spectrum.

Unstable Co^{60} β -decays to Ni and then excited Ni cools down by the emission of two photons one at $E_{\gamma 1} \approx 1.173 \text{ MeV}$ (100% intensity) and the other at $E_{\gamma 2} \approx 1.332 \text{ MeV}$ (100% intensity). In the absence of strong nonlinearities in all the cross sections in this energy range, it is customary to simply use the average energy of $\bar{E}_{\gamma} \approx 1.25 \text{ MeV}$ for all the calculations. To finalize, the shielded-cavity Co^{60} -source is typically assumed to produce monoenergetic gamma flux at 1.25 MeV .

3.3.3. Displacement Damage

As already discussed photons produce displacement damage through the secondary electrons only. Thus, the cross section for atomic displacement by a photon can be written as a sum of the cross sections representing the contributions of the different gamma-to-electron energy-transfer processes, i.e.

$$\sigma_d(E_{\gamma}) = \sum_i \sigma_d^i(E_{\gamma}) \quad (3.64)$$

where i refers to Compton scattering, atomic photoelectric effect, pair production (when needed), etc. Each $\sigma_d^i(E_{\gamma})$ can be evaluated as (see Section 3.1)

$$\sigma_d^i(E_{\gamma}) = \int_{T_e^{min}}^{T_e^{max}} dT_e \frac{dN_e^i(T_e)}{dT_e} \int_0^{\pi} L[T(\Theta, T_e)] \frac{d\sigma_M(\Theta, T_e)}{d\Omega} d\Omega \quad (3.65)$$

where $N_e^i(T_e)$ is the slowed down “flux” of the secondary electrons produced through the i^{th} mechanism. The total electron flux is simply given by

$$\frac{dN_e(T_e)}{dT_e} = \left[\frac{dT_e}{dx}(T_e) \right]^{-1} N_a \Phi_\gamma \int_{T_e}^{T_e^{max'}} dT'_e \left[\underbrace{\frac{d\sigma_{PE}(E_\gamma, T'_e)}{dT'_e}}_{photoelectric} + \underbrace{\frac{d\sigma_C(E_\gamma, T'_e)}{dT'_e}}_{Compton} \right] \quad (3.66)$$

Then the total displacement cross section can be written as

$$\sigma_d(E_\gamma) = \int_{T_e^{min}}^{T_e^{max}} \frac{dN_e(T_e)}{dT_e} dT_e \int_0^\pi L[T(\Theta, T_e)] \frac{d\sigma_M(\Theta, T_e)}{d\Omega} d\Omega \quad (3.67)$$

Analogously, the non-ionizing energy loss is calculated as

$$S_d^\gamma(E_\gamma) = \frac{N_A}{A} \int_{T_e^{min}}^{T_e^{max}} \frac{dN_e(T_e)}{dT_e} dT_e \int_0^\pi T(\Theta, T_e) L[T(\Theta, T_e)] \frac{d\sigma_M(\Theta, T_e)}{d\Omega} d\Omega \quad (3.68)$$

Using Eq. 3.28 the final expression for the displacement dose can be written in the following form

$$D_d^\gamma = 1.6 \times 10^{-8} \int_{T_e^{min}}^{T_e^{max}} \frac{dN_e(T_e)}{dT_e} S_d^e(T_e) \Psi_\gamma(E_\gamma) dT_e \quad (3.69)$$

Calculated non-ionizing energy loss and displacement dose deposited by one 1.25 MeV photon in *Si*, *GaAs*, *InGaAs* and *InP* are listed in Table 3.10.

3.3.4. Absorbed Dose

The absorbed dose, D^γ , is generally defined as follows

$$D^\gamma = \int E \frac{\Psi(E)}{dE} \frac{\mu_{en}(E)}{\rho} dE \quad (3.70)$$

where $\mu_{en}(E)/\rho$ is the mass energy absorption coefficient. $\mu_{en}(E)/\rho$ is often calculated through similar quantity – the mass energy transfer coefficient, $\mu_{tr}(E)/\rho$.

Material	S_d^γ ($MeV \cdot cm^2/g$)	D_d^γ (rad)	$\Psi_{Si,equiv}, \times 10^{13}$ (cm^{-2})	$A_T, \times 10^7$ ($rad^{-1}(Si) \cdot cm^{-3}$)
<i>Si</i>	1.83×10^{-7}	2.93×10^{-15}	1.1	1.5
<i>GaAs</i>	1.42×10^{-7}	2.27×10^{-15}	1.0	5.6
<i>InP</i>	2.28×10^{-7}	3.65×10^{-15}	1.2	9.7
<i>InGaAs</i>	1.50×10^{-7}	2.40×10^{-15}	1.0	5.8

TABLE 3.10. Non-ionizing energy loss, displacement dose for 1.25 *MeV* photon, and equivalent 1 *MeV* electron fluence and number of displacements for 1 *Mrad(Si)* for *Si*, *GaAs*, *InGaAs* and *InP*.

The mass energy transfer coefficient, when multiplied by the photon energy fluence, gives kerma – the sum of the kinetic energies of all the primary particles released by photons per unit mass. In the energy range of our interest only Compton and photoelectric effects are responsible for the liberation of secondary electrons:

$$\mu_{tr}(E)/\rho = \frac{f_C \sigma_C + f_{pe} \sigma_{pe}}{1.66 \times 10^{-24} A} \quad (3.71)$$

where f_C and f_{pe} are the average fractions of the photon energy imparted to an electron in Compton scattering and photoelectric absorption events (see Sections 3.3.1.1 and 3.3.1.2) and $1.66 \times 10^{-24} g$ represents the atomic mass unit. Neglecting the energy loss due to the emission of the characteristic x-rays, f_{pe} becomes unity and $f_C = 1 - \overline{T}_e/E_\gamma$, where \overline{T}_e is the average energy of the Compton-scattered photon, calculated using the differential Klein-Nishina cross section. Subtracting the contribution of the further emission of radiation by the charged particles as

they travel through the medium we obtain the mass energy absorption coefficient:

$$\mu_{en}/\rho = [1 - g(E)] \mu_{tr}/\rho \quad (3.72)$$

where $g(E)$ is the energy dependent factor representing the average fraction of the secondary electron energy lost in photon-emitting processes. $g(E)$ can be evaluated through the integration of the radiative cross section along the track of a slowing down electron. For low photon energies (less than few MeV) in low Z materials g approaches zero and can be safely neglected [47, 48]. For example, at $E_\gamma = 1 MeV$, g is 0, 0.011 and 0.048 for carbon ($Z=6$), copper ($z=29$) and lead ($z=82$), respectively [47]. Therefore,

$$\mu_{en}/\rho \approx \mu_{tr}/\rho \Rightarrow D^\gamma = \int E \frac{\Psi(E)}{dE} \frac{\mu_{tr}(E)}{\rho} dE \quad (3.73)$$

Most commonly, Si -based dosimeters are used for calibration of gamma-sources; as a result the doses are usually given in $Mrad(Si)$. $Mrad(Si)$ can be converted into $Mrad(mat)$ (equilibrium absorbed dose in the device material) using the absorption coefficients for Si and material of interest

$$D_{mat} = D_{Si} \frac{(\mu_{en}/\rho)_{Si}}{(\mu_{en}/\rho)_{mat}} \quad (3.74)$$

or see, for example, Ref. [63] for more accurate approach. Then all the radiation damage quantities can be expressed in terms of the dose in this material or photon flux. It is most convenient, however, to relate all the damage parameters to $Mrad(Si)$, in which case the number of displacements and the total displacement energy can be calculated directly from the results of the dosimetry measurements. For this purpose, the equivalent 1 MeV electron fluence – fluence that produces the same damage effect as the actual photon fluence – is calculated.

$$\Psi_{equiv,Si} = \int Q(T_e) \frac{S_{niel}(T_e)}{S_{niel}(1 MeV)} \frac{d\Psi(T_e)}{dT_e} dT_e \quad (3.75)$$

The calculated equivalent 1 MeV electron fluences for 1 Mrad(Si) for Si, GaAs, InGaAs and InP are listed in Table 3.10. The number of displacements for 1 Mrad(Si) is calculated from

$$N = \kappa \frac{S_{niel}(1 \text{ MeV})}{2E_d} \rho \Psi_{equiv,Si} \quad (3.76)$$

with the results also listed in the table.

3.3.5. Possible Limitations

The principal errors in the dosimetry and damage production calculations are caused by the failure of charged particle equilibrium condition and the dose enhancement effects resulting from non-equilibrium electron transport in the proximity of material interfaces. Furthermore, in all the calculations above it was assumed that the secondary electron flux is produced in the studied material. This is not necessarily the case for the devices with very thin active layers. For example, shower of electrons created in the passivating dielectric or, say, packaging material is incident on the top-most emitter cap layer. Practically in every single layer of the device the net electron flux has components emerging from the other layers, or even surrounding material. To obtain an exact numerical solution, tedious transport simulation including the geometry effects has to be performed. At a closer look, however, one may notice that the shape and magnitude of the flux of secondary electrons liberated and subsequently slowed down in low Z materials do not change significantly between the lightest *polyimide* and the heaviest *InGaAs* (0.014 and 0.018, respectively). Therefore, in the absence of large amounts of high Z materials in the device surrounding or in the device itself, the secondary electron flux can be assumed to be that of, for example, *InGaAs*.

As the radiation penetrates the material the energy absorption changes with the depth as shown in Fig. 3.22a. Initially, there is some increase in the absorbed dose due to the build up of the flux of the secondary electrons, however, after some finite thickness, the dose reaches the maximum and starts decreasing as a result of gamma-ray attenuation. Therefore in the layers of the device close to the air-device interface the calculations may slightly overestimate the actual dose and/or damage. Again, to obtain an accurate solution the transport simulations need to be performed.

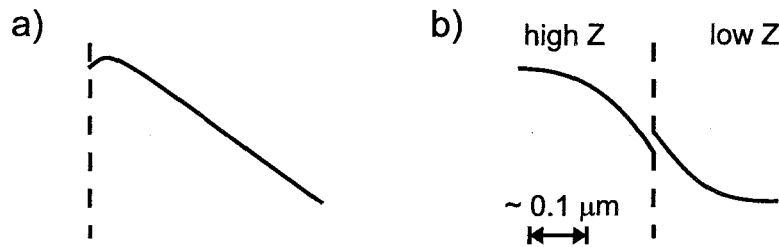


FIGURE 3.22. a) Typical plot of energy deposition in material; b) schematic illustration of dose enhancement effects at low photon energies.

Another factor adding more complexity to the problem is the particle transport through material heterointerfaces, for example metal-semiconductor. The energy deposited by secondary electrons near the interface may depend on the photon energy and direction, the atomic number of the layers and their thickness. An illustrative diagram showing the relative absorbed dose for the low ($\approx 0.1 \text{ MeV}$) and high ($\approx 1 \text{ MeV}$) energy photons is shown in Figs. 3.22b and 3.23, respectively [64]. At the low energies the dose enhancement effects do not show any significant correlation with the photon direction, however, depend strongly on the photon

energy and atomic number of materials. At the higher energies, when photons approach from the low Z side, the dose enhancement is observed on that side since a considerable fraction of the secondary electrons is backscattered from the high Z material interface. If the photon direction is reversed the absorbed doses in the materials near the interface are usually lower than the bulk doses. The situation can be slightly altered if a large number of highly energetic photoelectrons emerges from the high Z side. This component of the secondary electron flux may actually lead to some dose enhancement in the low Z material. Garth *et al.* [65] have performed extensive photon/electron transport simulations to estimate the displacement damage and dose enhancement effects at the $Au/GaAs$ interfaces. For gammas incident from the semiconductor side the dose enhancement in $GaAs$ next to Au was found to be about 1.35. The dose enhancement was shown to decrease rapidly as we move away from the interface. In case of the photon flux incident from the Au the dose enhancement, rising from the hard photoelectron component, was estimated to be 1.15. For InP and $InGaAs$, which have density and effective atomic mass similar to those of $GaAs$, the dose enhancement effects are expected to be on the same order of magnitude.

3.4. Summary

To conclude this chapter we summarize some of the calculation results in Table 3.11. In particular, to facilitate the displacement damage analysis the defect introduction rates are specified per unit of absorbed ionizing dose in silicon, $rad(Si)$, and per unit of incident particle flux, cm^{-1} . These calculated results are intensively used in the device analysis to identify and model the radiation effects responsible for the observed device degradation (see Chapter 6).

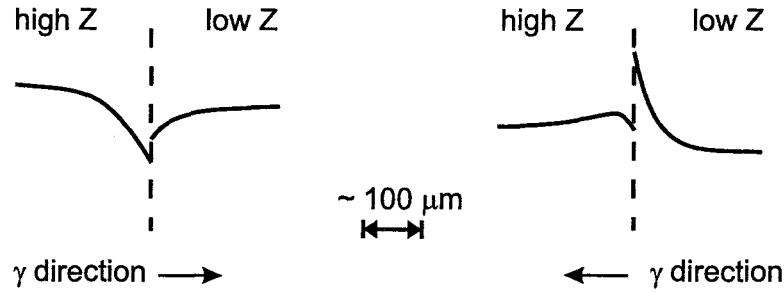


FIGURE 3.23. Schematic illustration of dose enhancement effects at high photon energies.

Quantity	<i>Si</i>	<i>GaAs</i>	<i>InGaAs</i>	<i>InP</i>
S ($\text{MeV} \cdot \text{cm}^2/\text{g}$)	1.51	1.52	1.25	1.26
S_d^β ($\text{eV} \cdot \text{cm}^2/\text{g}$)	31.4	26.5	28.5	33.5
$\Phi^{max,\beta}$ ($\text{cm}^{-2} \cdot \text{s}^{-1}$)	9.4×10^9	9.4×10^9	9.4×10^9	9.4×10^9
$D^{max,\beta}$ (Mrad)	784	—	622	627
a_T^β (cm^{-1})	1.4	5.6	6.2	7.4
A_T^β ($\text{rad}^{-1}(\text{Si}) \cdot \text{cm}^{-3}$)	0.6×10^8	2.3×10^8	2.6×10^8	3.1×10^8
S_d^γ ($\text{MeV} \cdot \text{cm}^2/\text{g}$)	1.8	1.4	1.5	2.3
$D^{max,\gamma}$ (Mrad)	44.3	—	—	—
A_T^γ ($\text{rad}^{-1}(\text{Si}) \cdot \text{cm}^{-3}$)	1.5×10^7	5.6×10^7	5.8×10^7	9.7×10^7
S_d^n ($\text{keV} \cdot \text{cm}^2/\text{g}$)	2.04	0.64	0.58	0.64
Φ_{equiv}^n ($\text{cm}^{-2} \cdot \text{s}^{-1}$)	4.3×10^{10}	—	5.5×10^{10}	8.0×10^{10}
a_T^n (cm^{-1})	90	136	127	141

TABLE 3.11. Results of dosimetry and damage production calculations for electron, gamma and neutron irradiation for *Si*, *GaAs*, *InGaAs* and *InP*.

4. HETEROJUNCTION BIPOLAR TRANSISTORS

The idea of a bipolar transistor with a wide-gap emitter was originally proposed by Shockley long ago, in 1948, but only technological advances of last few decades made fabrication of such devices possible. Developed in the late 70's molecular beam epitaxy (MBE) and metal-organic chemical vapor deposition (MOCVD) were the first techniques successful in the fabrication of high quality heterostructures. Due to a number of potential advantages a lot of effort was put into research and development of material systems, growth methods and structure optimization of HBTs. The field is still experiencing tremendous growth as HBTs continue to find more and more use in commercial applications. In this chapter a general introduction to HBT structures, operation and modeling is given. The main effort, however, is put into development of an analytical model for an abrupt Single-Heterojunction Bipolar Transistor (SHBT).

The chapter begins with a brief review of HBT device structures and electrical properties. Then the compact model approach is taken to describe the device operation. Simple procedures for extracting some of the HBT parameters are presented. Then a comprehensive analytical model is developed to simulate the terminal current-voltage characteristics of the device. Particular attention is paid to issues of thermionic-field-emission transport of carriers through the BE heterojunction. Shockley-Read-Hall (SRH) recombination in the junction Space-Charge-Region (SCR) and tunneling mechanisms of the base current are also incorporated in the model. Possible effects of high level injection on HBT performance are evaluated. Then the applicability of commercially available BJT SPICE models for the simulation of HBTs is explored. Finally, a short overview of HBT RF characterization techniques is presented.

4.1. HBT Basics

Assuming that the reader is familiar with a BJT device, we immediately proceed with an introduction of structure and operation of a typical HBT. Schematic energy band diagrams of an n-p-n BJT and HBT are shown in Figs. 4.1a and 4.1b, respectively. Use of a wide-gap material for the emitter in the HBT creates an additional potential barrier for the holes being injected from the base. This in turn assures very high emitter injection efficiency (practically unity), impossible to achieve in a BJT. Under these conditions the emitter doping concentration can be reduced and the base doping can be significantly increased resulting in lower base resistance, smaller base-emitter junction capacitance and shorter emitter charge storage time. Additionally, much higher Early voltages can be obtained and some of the high level injection effects can be minimized if not eliminated entirely. Another great consequence of having a heavily doped base is a considerable reduction of the critical base punch-through thickness. Hence the base can be made much thinner to decrease the base transit time.

In the next few sections we give an overview of the possible HBT structure configurations, their advantages and disadvantages, as well as the summary of the physical models describing their operation.

4.1.1. HBT Materials, Structures and Performance

Original idea of using a wide bandgap material for the emitter layer in a bipolar transistor can be further extended to improve the device performance. As shown in Fig. 4.2a difference in bandgaps between emitter and base (ΔE_g) introduces a notch in the conduction band and a step in the valence band at the heterojunction. In a better designed device, the conduction band spike would be

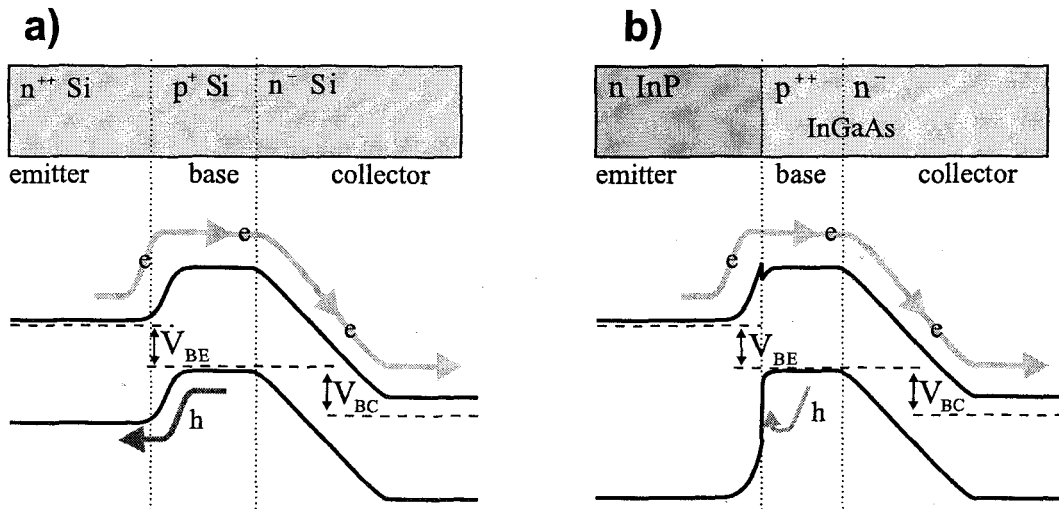


FIGURE 4.1. Energy band structure of (a) bipolar junction transistor and (b) heterojunction bipolar transistor biased in the active mode.

removed entirely to improve electron injection, and all of ΔE_g would be accommodated in the valence band to suppress hole injection. This can be achieved by compositionally grading a thin layer of material on the emitter side. The resulting energy band diagram for the graded HBT is shown in Fig. 4.2b. These heterostructures usually show better performance than abrupt HBTs, but are somewhat more difficult to grow.

So far only HBTs with a wide bandgap emitter were discussed. In these so-called single¹ heterojunction devices (SHBTs) base and collector are composed of the same narrow bandgap material. As a result the collector breakdown voltages can be unacceptably low, e.g. down to few volts. Additionally, due to the asymmetry of the base-emitter and base-collector junctions SHBTs exhibit non-

¹base-emitter is a heterojunction, base-collector - homojunction

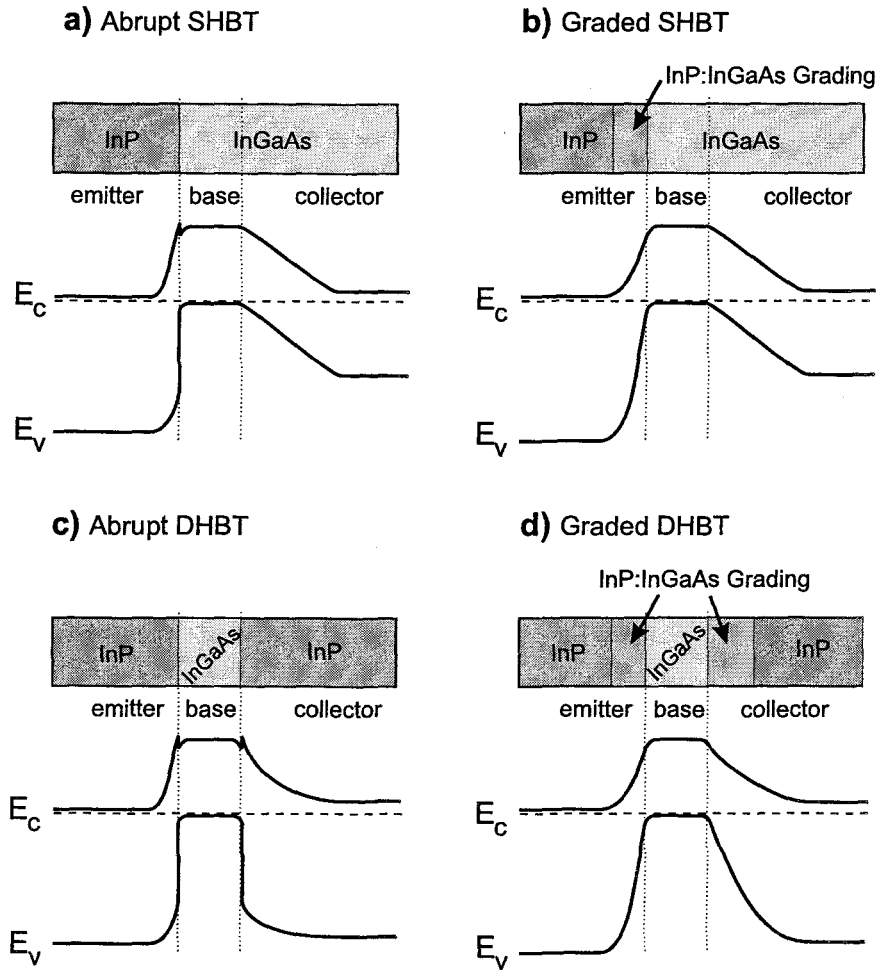


FIGURE 4.2. Energy band diagrams of (a) abrupt single HBT, (b) graded single HBT, (c) abrupt double HBT and (d) graded double HBT.

zero turn on voltages leading to a higher power consumption. In an attempt to remove or at least minimize these effects a wide bandgap material can be used for the collector layer also. A schematic energy band diagram of the so-called Double HBT (DHBT) is shown in Fig. 4.2c. Due to the fact that both heterojunctions are abrupt, there are conduction band spikes present at the heterointerfaces. The notch at the base-collector junction, being a potential barrier in the way of electrons diffusing through the base into the collector, can dramatically reduce the collector

current and therefore gain of the device. The abrupt DHBT structure can be optimized by grading both base-emitter and base-collector heterojunction as shown in Fig. 4.2d. Theoretically, graded DHBTs should offer near-ideal current-voltage output characteristics and a superior performance. In practice, however, technical difficulties associated with the growth of high quality graded heterostructures often do not allow fabrication of reliable high-performance devices.

Since early 1980's most of the research efforts were focused on *AlGaAs/GaAs* material systems while a few other systems, for example, *InP/InGaAs*, *AlGaAs/InGaAs* and *Si/SiGe* stayed in the background and became "popular" only relatively recently. Intensive studies in *AlGaAs/GaAs* HBT technology made this material system a standard III-V structure used in high performance industrial applications. *AlGaAs/GaAs* HBTs with cutoff frequencies f_T and maximum frequencies of oscillation f_{max} of 100 – 200 GHz have been reported [66].

InP/InGaAs HBTs fabricated by gas source MBE or MOCVD offer a higher electron mobility, lower surface recombination and higher drift velocity at high fields; and can perform at higher frequencies, e.g., $f_T = 200$ GHz and $f_{max} = 236$ GHz [67]. Additionally, narrow 0.75 eV bandgap of *InGaAs* is compatible with low dispersion/loss fiber optics, which makes *InGaAs*-based HBTs very attractive for high speed applications in optical communications.

For high power applications wide bandgap *GaN*-based *AlGaN/GaN* HBTs are studied intensively. Devices with collector breakdown voltages of up to 100 V and with $f_{max} = 6$ GHz have been reported [68]. As *GaN* is used for fabrication of blue lasers, possible applications of *AlGaN/GaN* material system in optical communications are also under serious studies.

Tremendous successes of the silicon technology stimulated the development of *Si/SiGe* HBTs possessing high speed capability, low surface recombination and $1/f$ noise. But by far the greatest advantage is an opportunity to incorporate *SiGe* HBTs in the standard well-developed silicon BiCMOS technology hence dramatically reducing the cost and complexity of processing. IBM researchers reported the devices with f_T 's up to 120 GHz [69].

In continuous search for a better device, a large number of material/structure variations has been explored. For example, $f_T = 156$ GHz and $f_{max} = 255$ GHz have been reported for *InGaP/GaAs* SHBTs [70]; *AlInAs/InGaAs* SHBTs have been demonstrated to reach $f_T = 127$ GHz and $f_{max} = 277$ GHz [71]; *InP/GaAsSb/InP* DHBTs with near-ideal characteristics operating at frequencies up to $f_T = 75$ GHz have also been reported [72].

4.1.2. Terminal Currents

A two-dimensional representation of an *npn* HBT structure is shown in Fig. 4.3a. There are four different ways of biasing base-emitter (BE) and base-collector (BC) junctions leading to four modes of operation: saturation ($V_{BE} > 0$, $V_{BC} > 0$), active ($V_{BE} > 0$, $V_{BC} < 0$), inverse active ($V_{BE} < 0$, $V_{BC} > 0$) and cutoff ($V_{BE} < 0$, $V_{BC} < 0$).

Most commonly HBTs are operated in the active mode, which is also sometimes called normal mode of operation. Figs. 4.3b and 4.3c show electron and hole currents within the HBT in the active mode. A flux of electrons (I_{nE}) is injected from the emitter into the base through the forward-biased base-emitter junction. While a small fraction of it recombines in the BE SCR and base, the rest diffuses through the thin base layer and then gets accelerated into the collector region by

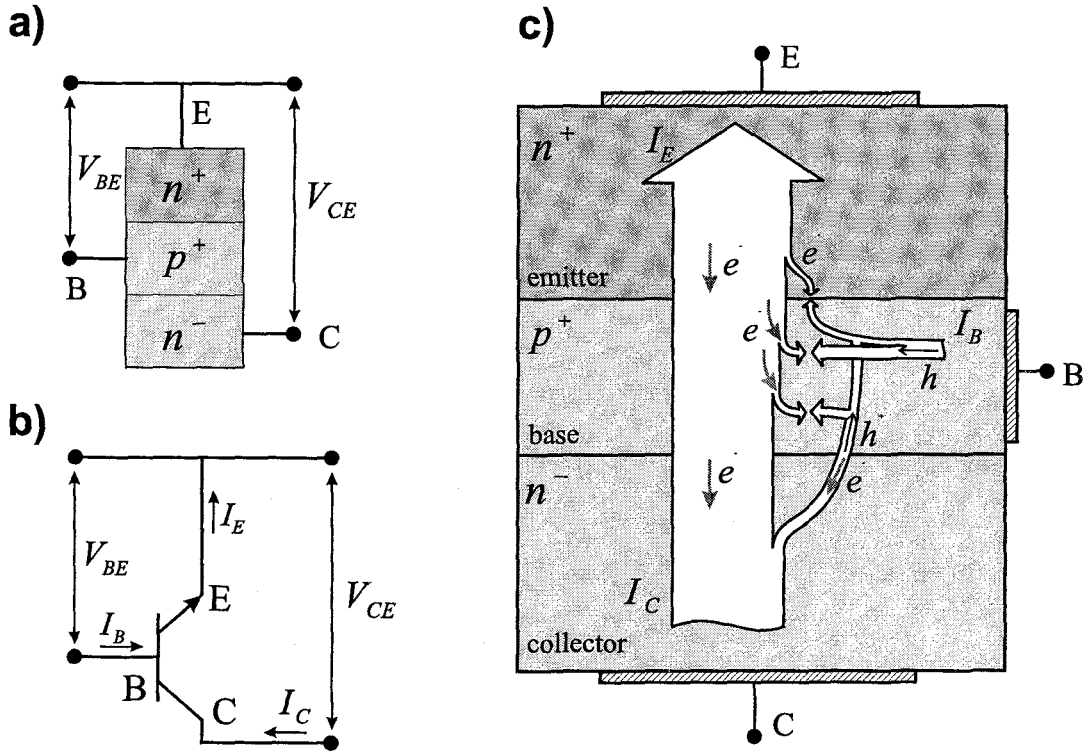


FIGURE 4.3. Currents within npn HBT.

the strong electric field of the reverse-biased BC junction. Base terminal current, I_B , consists of holes and can be divided into four main components, namely, I_{rec} – holes that recombine with electrons diffusing from the emitter to the collector region (I_{rec} accounts for recombination in the base neutral region only), I_{pB} – holes injected into the emitter, I_{scr} – holes recombining in the base-emitter depletion region and, finally, I_g – generation current of the reverse-biased base-collector junction. At last, the collector terminal current, I_C , is simply a sum of the emitter electron current diffused through the base, $I_{nE} - I_{rec}$, and the generation current I_g . Putting everything together we obtain equations for currents for all terminals of the transistor:

$$I_E = I_{nE} + I_{pB} + I_{scr} \quad (4.1)$$

$$I_B = I_{pB} + I_{rec} + I_{scr} - I_g \quad (4.2)$$

$$I_C = I_{nE} - I_{rec} + I_g \quad (4.3)$$

Neutral base recombination current can be further divided into the recombination currents of base bulk, I_{br} , and base periphery, I_{sr} .

4.1.3. Operation

In most practical applications HBTs are used as current amplifiers in the so-called common-emitter configuration (see Fig. 4.3b). In this case injected base current is a current to be amplified, and the output parameter is the collector terminal current. Typical $I_C - V_{CE}$ curves measured at base currents of 0 μA and 40 μA are shown in Fig. 4.4 for an abrupt SHBT. Consider $I_B = 40 \mu A$ curve. During V_{CE} sweep the BE and BC junction biases are adjusted in order to match the constant base current injected at the base terminal. At low V_{CE} the forward-biased BE heterojunction can not provide sufficient electron current necessary for the I_{rec} and I_{scr} components of the base current; the BC junction becomes forward-biased and the base hole current flows into the collector. As a result at low V_{CE} the collector current is negative and equal to the injected base current. This represents the reverse active mode of operation and, indeed, can be readily observed in the graph. The corresponding calculated BE and BC junction biases are shown in Fig. 4.5 as functions of collector-emitter applied bias for the base current of 60 μA .

As V_{CE} is increased the BE junction bias goes up and emitter injects more and more electrons into the base region giving rise to the base recombination currents. Consequently, since the hole injection into the collector has to be re-

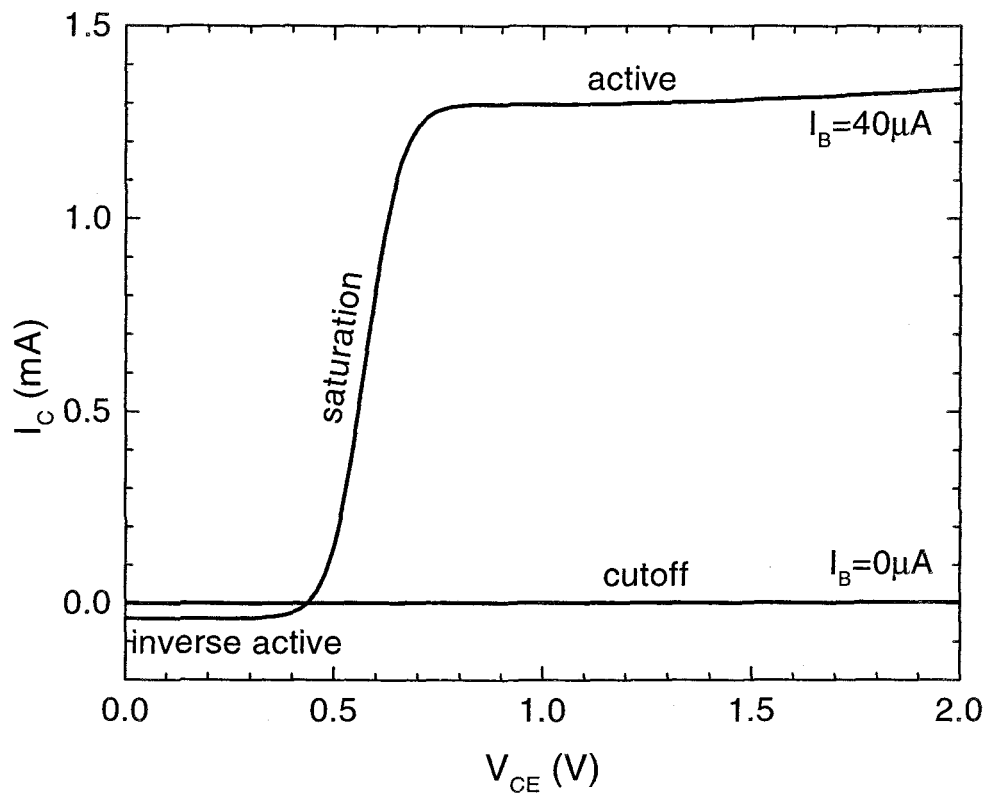


FIGURE 4.4. Common-emitter current-voltage characteristics.

duced, V_{BC} decreases. In this regime, often called saturation, the collector current increases rapidly and then starts to saturate. V_{CE} voltage where the collector current starts rising from zero is often called offset or turn-on voltage ($V_{CE,off}$) and is a very important parameter of the device.

As V_{CE} is increased further, at some value of V_{CE} , when the injected emitter current provides enough electrons for recombination with holes in the base layer, base-collector junction becomes reverse-biased and I_C stays constant for higher values of V_{CE} . This situation corresponds to the active mode of operation.

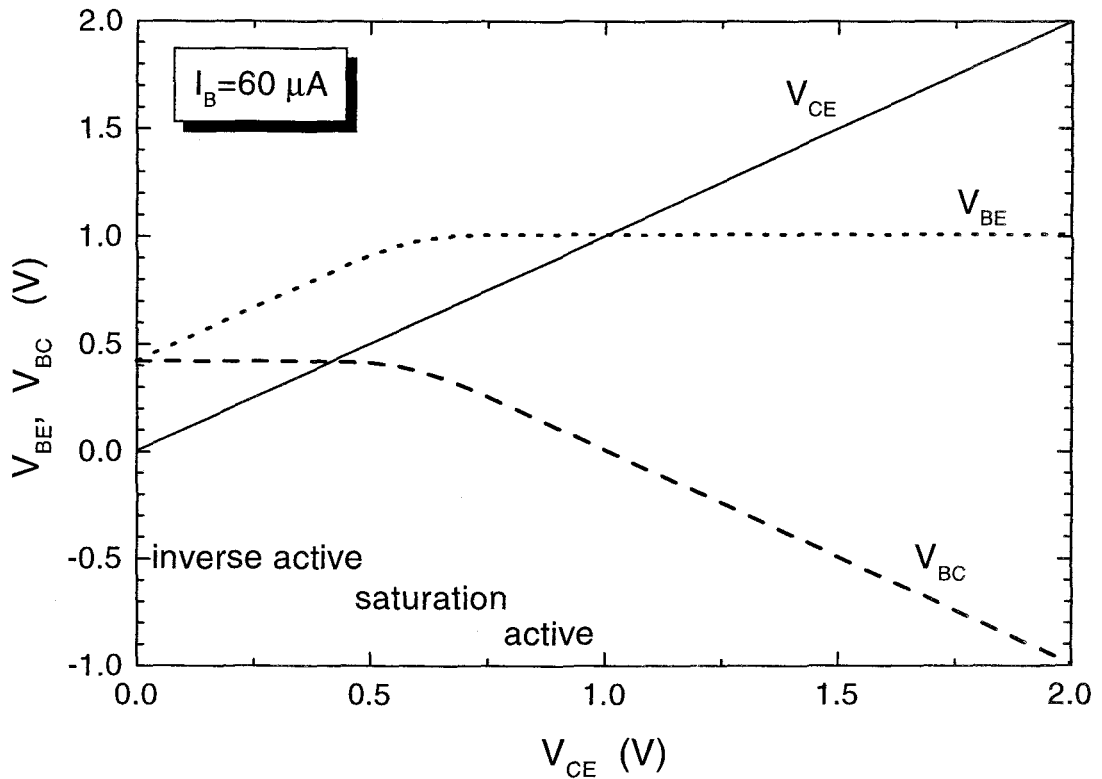


FIGURE 4.5. BE, BC, and CE voltages as a function of V_{CE} at $I_B = 60 \mu A$ in common-emitter configuration.

4.2. Bipolar Transistor Electrical Characterization

Current-voltage, $I - V$, characteristics of devices are measured using the measurement setup depicted schematically in Fig. 4.6. Probing pads of a tested device are contacted using gold-plated microprobes under a microscope. Measurements are performed using Hewlett-Packard HP4145B semiconductor parameter analyzer, which has high precision voltage and current sources as well as voltage and current meters built-in. The HP4145B connected to a PC is controlled via GPIB interface, which is also used to retrieve data to the computer. Special soft-

ware was written to automate the entire measurement and data storage process.

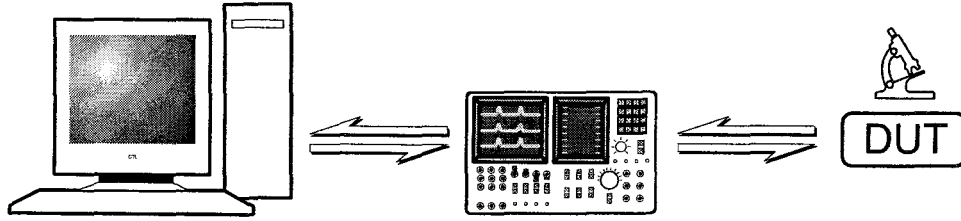


FIGURE 4.6. Measurement setup, consisting of a PC, SPA HP4145B and a micro-probe station equipped with microscope, used for current-voltage characterization of devices.

Figs. 4.7a-c show some of the measurement configurations used for HBT characterization. First, to obtain the common-emitter $I - V$ characteristics, the collector current is measured at different base currents (e.g. 0, 10, 20, 30, 40, 50 and 60 μA) by sweeping the collector-emitter voltage, V_{CE} , in the range of 0 – 2 V. A set of $I_C - V_{CE}$ curves obtained using this measurement is shown in Fig. 4.8 in solid lines. To gain a better understanding of the device operation and to facilitate extraction of the device parameters for modeling, the so-called Gummel plots of the collector and base currents are often used. The measurement is performed by sweeping the base-emitter bias, typically in the range of 0 – 1.3 V (forward bias), while having base and collector terminals shorted (see Fig. 4.7b). It should be noted that having the two external terminals shorted does not necessarily imply zero bias at the internal collector-base junction. As it will be shown later, the collector resistance may lead to forward biasing of the BC junction at high collector currents. Typical Gummel plots obtained from the same device are shown in Fig. 4.9 by solid lines. At last, similar to Gummel plots, the inverse Gummel

plots of the base and emitter currents are measured. In this case the base-collector bias is swept in the forward direction, while measuring currents flowing through the base and emitter shorted terminals (see Fig. 4.7b). Measured inverse Gummel plots are shown in Fig. 4.10 by solid lines.

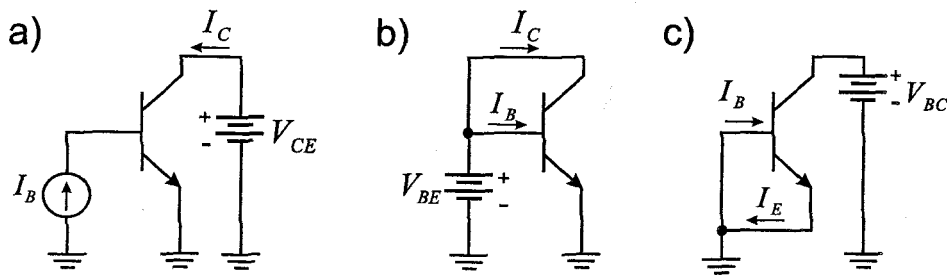


FIGURE 4.7. Circuit configurations used for measurements of (a) common emitter $I - V$ characteristics ($I_C - V_{CE}$), (b) Gummel plots of base and collector currents, and (c) inverse Gummel plots of emitter and base currents.

Additionally, current-voltage characteristics of the BE and BC diodes, and DC common emitter current gain are measured.

4.3. Compact Models

Though, in general, physical picture of HBT operation appears to be quite simple, the detailed quantitative analysis is complicated and often not very accurate. One of the simplest approaches to the HBT modeling is to use the so-called compact models. For example, in the case of well known Ebers-Moll model [73] the bipolar transistor is viewed as a pair of interacting diodes. Furthermore, the base-emitter and base-collector junctions are assumed to obey the ideal-diode laws

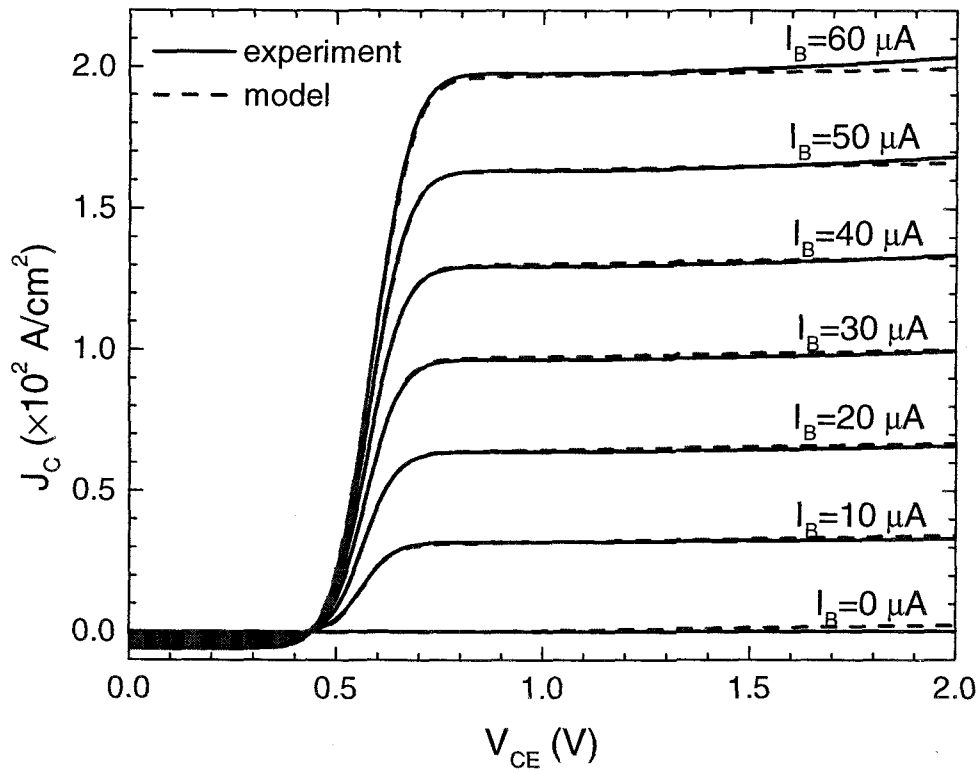


FIGURE 4.8. Common-emitter current-voltage characteristics of device AN3m measured at different base currents (solid line), and characteristics calculated using Gummel-Poon model (dashed line).

and then some ideality factors are “artificially” introduced to account for possible deviations from the ideal diode theory.

In this section the basics of HBT modeling are introduced. This includes some brief discussion of the transistor junction currents and possible resistance parasitic effects. An outline of some techniques used for the extraction of the model parameters is also presented.

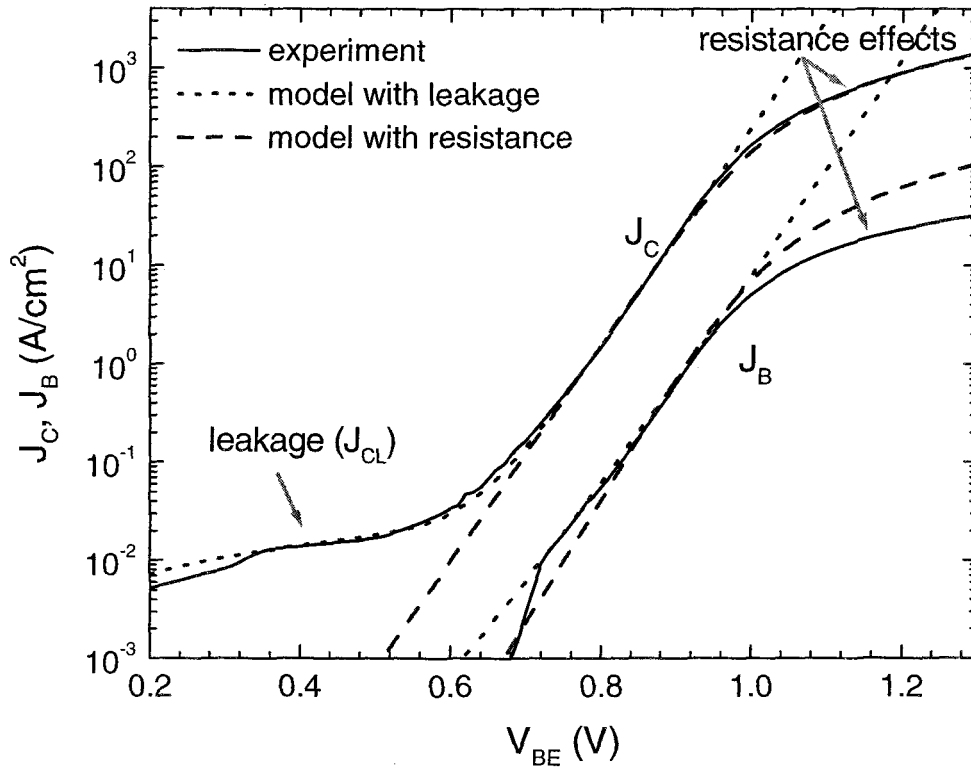


FIGURE 4.9. Gummel plots of collector and base currents for device AN3m (solid lines), and calculated curves including leakage current (dashed lines).

4.3.1. Junction Currents

First, consider the base-emitter junction (forward Gummel plots). The presence of the relatively large valence band discontinuity at the heterointerface leads to an effective suppression of the hole injection current from the base region into the emitter. Thus, the base current is mostly determined by the recombination of holes (majority carriers in the base) with electrons injected from the emitter and diffusing towards collector. As the base thickness is usually very small (less than 1000 \AA) majority of the electrons successfully reach the collector region, giving rise to the collector current. Due to the fact that emitter and base regions of HBT

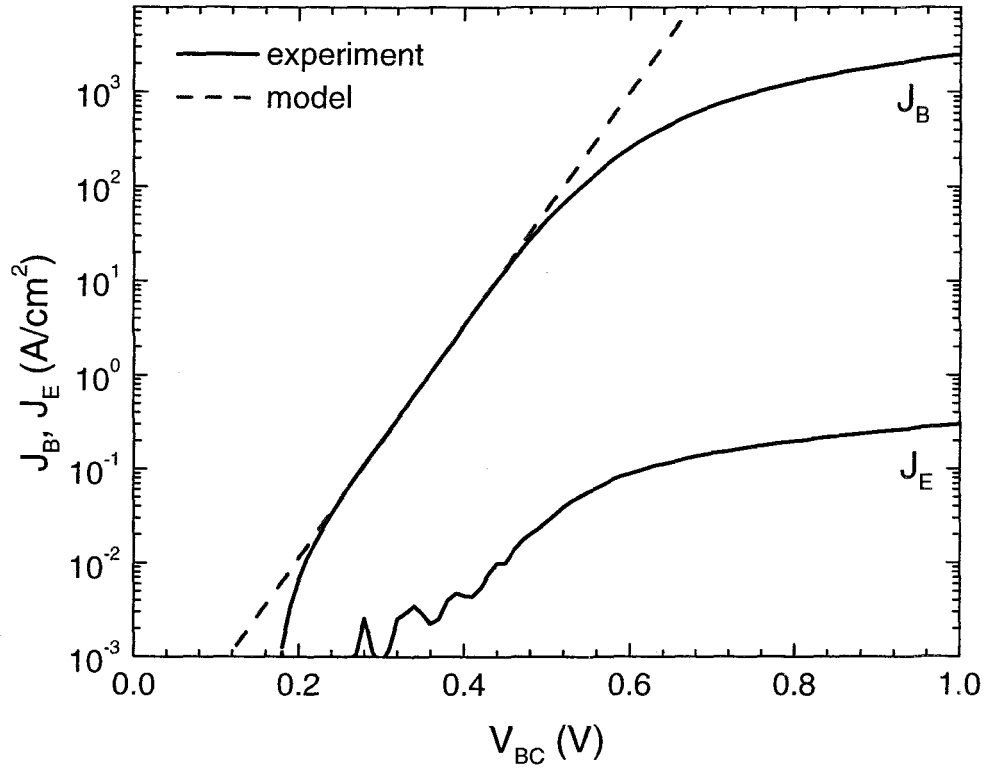


FIGURE 4.10. Inverse Gummel plots of base and emitter currents for device AN3m (solid lines), and calculated curves (dashed lines).

are heavily doped high level injection does not occur at normal operating voltages, allowing one to model the current-voltage characteristics using only one ideality factor for the whole region of operation (moderate to high biases). Thus, the base and collector currents can be written as

$$I_{B,BE} = I_{B,BE}^{sat} e^{qV_{BE}/n_{BE}kT} \quad (4.4)$$

$$I_{C,BE} = I_{C,BE}^{sat} e^{qV_{BE}/m_{BE}kT} \quad (4.5)$$

where $I_{B,BE}^{sat}$, $I_{C,BE}^{sat}$ and n_{BE} , m_{BE} are saturation currents and ideality factors for the base and collector currents, respectively.

In the presence of leakage currents or several recombination mechanisms one may have to modify these equations and add in expressions for the leakage currents and further divide the base current into components describing various recombination mechanisms. For example, in the case of the base current determined by two different recombination processes with ideality factors of n_{BE1} and n_{BE2} (see Section 4.4.3 for detailed discussion) one could write

$$I_{B,BE} = I_{B,BE1}^{sat} e^{qV_{BE}/n_{BE1}kT} + I_{B,BE2}^{sat} e^{qV_{BE}/n_{BE2}kT} \quad (4.6)$$

$$I_{C,BE} = I_{CL} + I_{C,BE}^{sat} e^{qV_{BE}/m_{BE}kT} \quad (4.7)$$

In general, the collector current ideality factor, mostly determined by the base-emitter heterojunction properties, can also have a noticeable voltage dependence as discussed in Section 4.4.2.

Collector leakage current commonly observed in HBTs [74, 75, 6] may be the dominant component of the collector current at low biases. Originating at the emitter-base, base-collector or collector-subcollector perimeters it is usually attributed to formation of conducting channels along the semiconductor surface. Liou *et al.* [74] on example of *AlGaAs/GaAs* HBTs showed that leakage currents depend strongly on the processing procedure, but are relatively independent of the type of the passivation dielectric used. According to their semi-empirical model the voltage dependence of the current exhibits a "soft" saturation of the following form

$$I_{CL} = I_{CL0} [1 - \exp \{-qV_{BE}/FkT\}] \quad (4.8)$$

with I_{CL0} being a leakage saturation current and F – process-dependent parameter, both to be extracted from the experimental data. The base and collector currents calculated using Eq. 4.4 and Eq. 4.7, respectively, are shown in Fig. 4.9 by dotted lines. The values of the model parameters used are listed in Table 4.1.

Similar analysis can be performed for the base-collector junction (inverse Gummel plots). Hole current injected from the heavily doped base into the collector is the dominant component of the current crossing the junction. The relatively low electron current injected from the collector region gets collected by the base contacts with only a small fraction escaping into the emitter. Thus, to a high degree of accuracy one can assume that the collector current equals the base current and emitter current is few orders of magnitude less, unless some mechanisms for emitter leakage currents were introduced during the device fabrication

$$I_{B,BC} = I_{C,BC} = I_{B,BC}^{sat} e^{qV_{BC}/n_{BC}kT} \quad (4.9)$$

Due to extremely low doping concentration in the collector region the high level injection leads to smaller currents than those predicted by Eq. 4.9 at large forward biases.

As one may notice I_C and I_B in Figs. 4.9 and 4.10 show some strong non-linear behaviour at the biases above 0.9 V and 0.5 V, respectively. This can be readily explained by introducing resistances for the three regions of HBT. Denote R_E , R_B and R_C as parasitic resistances of the emitter, base and collector regions, respectively. These resistances arise from having finite contact resistances, semiconductor bulk resistance, and wire and probe resistances. Contact resistance is often process-dependent and varies from sample to sample. It can be, and should be, minimized to some extent by choosing appropriate material system for the contacts. Semiconductor bulk resistance is determined by the materials and the doping concentrations in the different layers of the device and by the processing steps involved in the device fabrication. Finally, the wire and probe resistances are external to the device and can be easily accounted for by a simple calibration. Schematic of equivalent circuit for an HBT with R_E , R_B and R_C is shown

in Fig. 4.11. As some of the applied bias gets dropped across the resistances associated with different regions, the internal junction voltages (V'_{BE} or V'_{BC}) become less than the applied terminal voltages recorded/measured externally (V_{BE} or V_{BC} , respectively). The junction voltages can be written as

$$V'_{BE} = V_{BE} - I_E R_E - I_B R_B \quad (4.10)$$

$$V'_{BC} = V_{BC} + I_C R_C - I_B R_B \quad (4.11)$$

According to these equations, at low biases, when the current levels are low, parasitics have no effect. But as the current values increase, the voltage drops across the resistors become comparable to the applied biases leading to nonlinear behavior of $\log I$ vs V curves. Therefore, for the accurate quantitative modeling it is necessary to replace the applied biases by the corresponding internal junction voltages in equations for the base and collector currents introduced above

$$I_{B,BE} = I_{B,BE}^{sat} e^{q(V_{BE} - I_E R_E - I_B R_B)/n_{BE} kT} \quad (4.12)$$

$$I_{C,BE} = I_{C,BE}^{sat} e^{q(V_{BE} - I_E R_E - I_B R_B)/m_{BE} kT} + I_{CL} \quad (4.13)$$

$$I_{B,BC} = I_{C,BC} = I_{B,BC}^{sat} e^{q(V_{BC} + I_C R_C - I_B R_B)/n_{BC} kT} \quad (4.14)$$

The base and collector currents from the forward Gummel plots calculated using Eq. 4.12 and Eq. 4.13, respectively, are shown in Fig. 4.9 by dashed lines. The base current from the inverse Gummel plot modeled by Eq. 4.14 is plotted in Fig. 4.10 by a dashed line. The values of the parameters used in the calculations are listed in Table 4.1. The parasitic resistances were assumed to be $R_E = 15 \Omega$, $R_B = 10 \Omega$ and $R_C = 11 \Omega$

Finally, the total base and collector currents in the common-emitter configuration can be written as

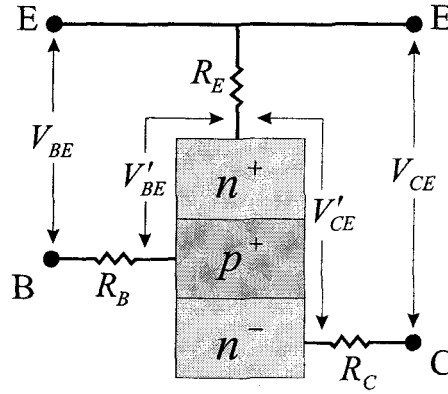


FIGURE 4.11. Equivalent circuit of an npn-HBT including parasitic resistances of emitter, base and collector.

$$I_B(V_{BE}, V_{BC}) = I_{B,BE}(V_{BE}) + I_{B,BC}(V_{BC}) \quad (4.15)$$

$$I_C(V_{BE}, V_{BC}) = I_{C,BE}(V_{BE}) - I_{C,BC}(V_{BC}) \quad (4.16)$$

4.3.2. Parameter Extraction

Our next task consists of extraction of the empirical parameters introduced in the current equations.

The saturation currents and ideality factors can be extracted from the forward and inverse Gummel plots by fitting linear part of $\log I$ vs V curves in the moderate bias range. In this region the effects of parasitic resistances are still insignificant and do not affect the results. Table 4.1 lists the extracted values of the parameters. Parasitic resistances can be estimated from the BE and BC current-voltage characteristics and the forward and inverse Gummel plots. Under a large forward bias the current of the BE diode with open BC junction is limited by the series resistance effects. Therefore, the slope of the $I - V$ curve can be used

to calculate $R_{BE} = R_E + R_B$. Similarly, from the BC diode $I - V$ characteristic $R_{BC} = R_C + R_B$ is estimated.

Current	I^{sat} (A)	Ideality factor
$I_{B,BE}$	7.2×10^{-15}	1.74
$I_{C,BE}$	4.1×10^{-14}	1.56
I_{CL}	1.9×10^{-6}	200
$I_{B,BC}$	1.6×10^{-10}	1.27

TABLE 4.1. Extracted values of saturation currents and ideality factors for base and collector currents.

In the most general case the forward Gummel plots may exhibit very pronounced effects of all the parasitic resistances. This is illustrated in Fig. 4.12, where the measured forward Gummel plots for HBT ID:AE4K are shown. For analysis of the plots we divide base current curve into the four regions corresponding to different current limiting mechanisms. In the region I, where $V_{BE} < 0.95$ V, the base current is determined by carrier recombination entirely. In the second region, 0.95 V $< V_{BE} < 1.15$ V, emitter current becomes large enough, so that $I_E R_E$ term in Eq. 4.12 becomes comparable to the applied bias, V_{BE} . Slopes of both current curves (I_B and I_C) therefore start to decrease rather rapidly, causing current "saturation". In the region III, 1.15 V $< V_{BE} < 1.3$ V, as the collector current increases further, the base-collector junction becomes forward-biased ($V'_{BC} = I_C R_C$) and a large flux of holes is injected from the base into the collector. This hole current,

given by Eq. 4.14, opposes the electron current flowing into the emitter. Thus, the total collector current decreases while the base current increases, i.e.

$$I_C = I_{C,BE} - I_{B,BC} \quad (4.17)$$

$$I_B = I_{B,BE} + I_{B,BC} \quad (4.18)$$

At biases above 1.3 V, region IV, base current reaches values at which $I_B R_B$ term becomes comparable to the applied biases and therefore leads to a slower rise of the both currents.

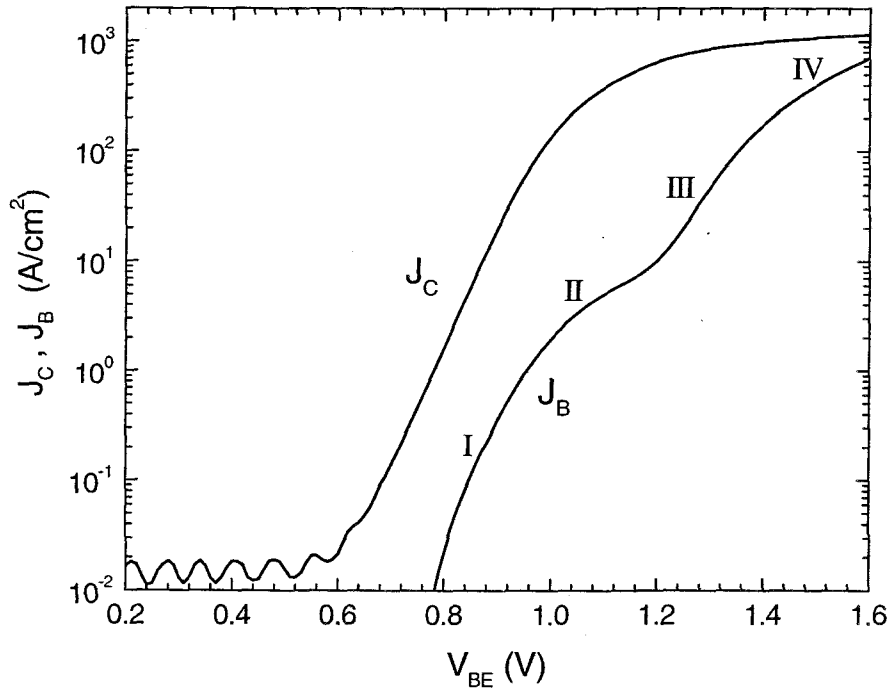


FIGURE 4.12. Forward Gummel plots of collector and base currents demonstrating parasitic effects of emitter, collector and base resistance.

Having identified the four regions we can now proceed with the extraction of the parasitic resistances. In the region II for any given value of base current the

internal junction voltage is estimated using

$$V'_{BE}(I_B) = \frac{n_{BE}kT}{q} \ln \left[\frac{I_B}{I_{B,BE}^{sat}} \right] \quad (4.19)$$

Using Eq. 4.10 we arrive at

$$\Delta V_{BE} = V_{BE} - V'_{BE} = I_E R_E + I_B R_B \approx I_E R_E = (I_C + I_B) R_E \approx I_C R_E \quad (4.20)$$

where $I_B R_B$ and $I_B R_E$ terms have been neglected. Also for the further analysis for high gain device it is safe to assume that I_E is approximately equal to measured I_C . Plot of ΔV_{BE} vs I_E should therefore be a straight line as shown in Fig. 4.13. At higher emitter currents, the collector parasitic resistance can lead to significant deviations from linearity. A similar procedure can be used to estimate R_E from $I_C - V_{BE}$. It should be noted that this technique can not be applied to the analysis of the base (collector) current on the inverse Gummel plots since the low doping of the collector region may give rise to significant high level injection effects.

Having extracted the emitter resistance, we can now estimate R_B and R_C from the measurements performed on the base-emitter and base-collector diodes

$$R_B = R_{BE} - R_E \quad (4.21)$$

$$R_C = R_{BC} - R_{BE} + R_E \quad (4.22)$$

In an alternative approach R_C and R_B can be estimated from the forward Gummel plot of the base current. In the region III the current of the forward-biased base-collector diode, $I_{B,BC}$, can be obtained by subtracting the base recombination current, $I_{B,BE}$, from the experimentally measured total base current I_B . Then

$$\Delta I_B = I_B - I_{B,BE} = I_{B,BC} = I_{B,BC}^{sat} e^{q(V_{BC} + I_C R_C - I_B R_B)/n_{BC}kT} \quad (4.23)$$

At relatively low values of I_B , plot of $\ln \Delta I_B$ vs I_C is a straight line. Rearranging this equation we obtain

$$R_C = \frac{n_{BC}kT}{qI_C} \ln \left[\frac{\Delta I_B}{I_{B,BC}^{sat}} \right] \quad (4.24)$$

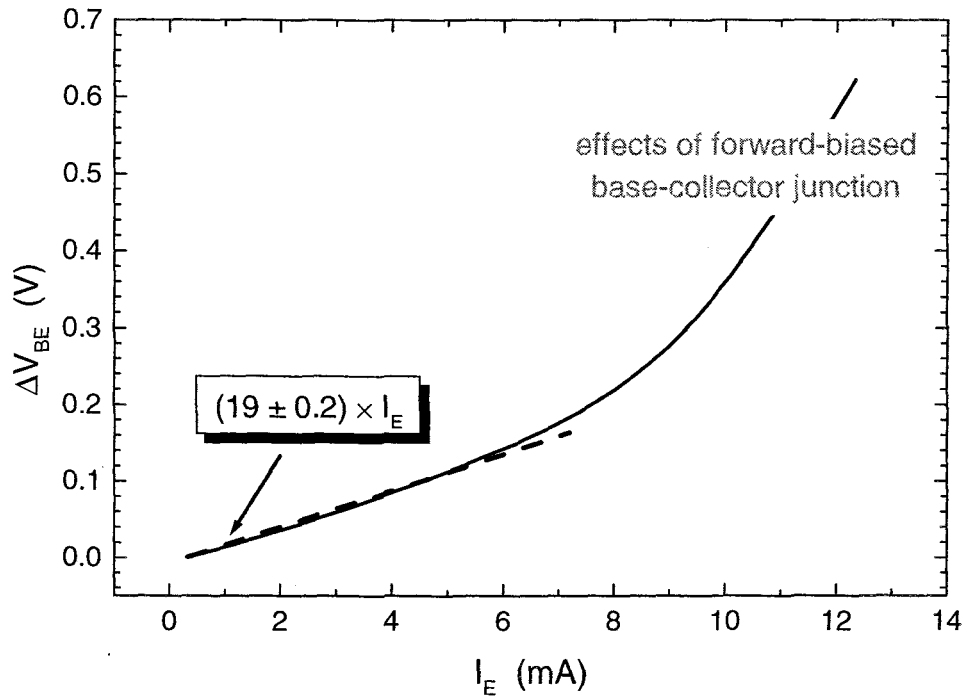


FIGURE 4.13. Estimation of the emitter parasitic resistance from the slope of ΔV_{BE} vs I_E .

where $V_{BC} = 0$ (base and collector are shorted in the experiment) and the base current term ($I_B R_B$) has been neglected.

At higher I_B , region IV, a procedure analogous to R_E estimation can be exploited. Deviation of $\ln \Delta I_B$ vs I_C from its linear fit allows us to evaluate R_B . Namely,

$$R_B = \frac{1}{I_B} \left[I_C R_C - \frac{n_{BC} k T}{q} \ln \left[\frac{\Delta I_B}{I_{B,BC}^{sat}} \right] \right] \quad (4.25)$$

Writing this equation we have neglected the contribution of the BE junction to $I_B R_B$ term due to the fact that most of the base current is supplied by the forward-biased BC junction.

4.3.3. Calculation of $I_C - V_{CE}$ Characteristics

In the model presented in Section 4.3.1 all the terminal currents of an HBT are expressed in terms of the BE and BC applied voltages (Eq. 4.15). As discussed already the collector-emitter voltage is divided between the two junctions of the transistor in order to achieve biasing conditions to match the injected base current. In this situation, it is impossible to obtain a closed form analytical expression for the most important output characteristics – the collector current-voltage dependence in the common-emitter configuration. On the other hand, a simple numerical solution is easily obtained that can provide accurate results. Recall from Eq. 4.16 that the total collector current can be written as a sum of the current injected from the emitter and the total current of the BC junction. Substituting Eqs. 4.13 and 4.14 into Eq. 4.16 we obtain

$$I_C(V_{BE}, V_{BC}) = I_{CL} + I_{C,BE}^{sat} e^{qV_{BE}'/m_{BE}kT} - I_{B,BC}^{sat} e^{(qV_{BC}')/n_{BC}kT} \quad (4.26)$$

The terminal voltages are related through Kirchhoff's voltage law

$$V_{CE} = V_{BE} - V_{BC} \quad (4.27)$$

where, according to our notation, positive V_{BE} and V_{BC} values correspond to the forward-biased junctions for an n-p-n transistor. Using Eq. 4.27 the collector current in Eq. 4.26 can be expressed in terms of V_{BE} and V_{CE} voltages. Analogously to the total collector current, the total base current can be written as

$$I_B(V_{BE}, V_{BC}) = I_{B,BE}^{sat} e^{qV_{BE}'/n_{BE}kT} + I_{B,BC}^{sat} e^{qV_{BC}'/n_{BC}kT} \quad (4.28)$$

On the next step this equation is solved numerically for the BE junction bias at fixed I_B and V_{CE} values. Then calculated V_{BE} 's are substituted back in Eq. 4.26 together with the corresponding values of V_{CE} and the total collector current is

calculated. Following this procedure the whole set of $I_C - V_{CE}$ curves for different given base currents is calculated by sweeping V_{CE} . To obtain the numerical solutions a program employing Newton-Raphson method was written. Alternatively, standard SPICE simulators, which have all the necessary equations programmed into their BJT models, can be employed to find $I_C - V_{CE}$. The calculated set of $I_C - V_{CE}$ characteristics is shown in Fig. 4.8 in dashed lines.

Despite its obvious simplicity and success in relatively accurate modeling of the device, this approach does not give much physical insight into the operation of HBT and can hardly be exploited for attempts of thorough examination and physical understanding of the radiation effects in HBTs. Most of the empirical parameters used in the model do not represent parameters of the actual device structure and its operation and therefore are often not very useful for any further device analysis.

4.4. Analytical Model

In this section a detailed analysis of the minority carrier transport in an abrupt HBT is performed and the steady state output characteristics of the device are calculated. First, the theoretical basis for calculations of the current transport through the emitter-base heterojunction is introduced. Then, the methods for calculating the collector current and the base recombination currents are formulated. And finally, the influence of the high level injection effects on the device performance is evaluated.

4.4.1. Emitter-Base Heterojunction Modeling

We start with a detailed analysis of the energy band structure and transport properties of the base-emitter heterojunction, assuming a wide bandgap *InP* emitter layer ($E_g = 1.35 \text{ eV}$) and a smaller bandgap $\text{In}_{0.53}\text{Ga}_{0.47}\text{As}$ base layer ($E_g = 0.75 \text{ eV}$). The emitter layer is doped with *Si* making it an n-type semiconductor, and the base is heavily doped with p-type dopant - *Zn*. Energy band diagrams of the two materials when they are isolated and when they are in contact with each other are shown in Figs. 4.14a and 4.14b, respectively. When the heterojunction is formed, the edge of the conduction band, E_c , remains parallel to the local vacuum level, which is continuous across the interface. According to Anderson's model, the difference in the electron affinities of the two materials (*InP* and *InGaAs*) determines the discontinuity of the conduction band, i.e. $\Delta E_C = \chi_{\text{InP}} - \chi_{\text{InGaAs}} \approx 0.25 \text{ eV}$ and hence $\Delta E_V = \Delta E_g - \Delta E_C \approx 0.38 \text{ eV}$. Finally, as in a homojunction, the Fermi levels ϕ_n (E_{Fn}) and ϕ_p (E_{Fp}) are aligned.

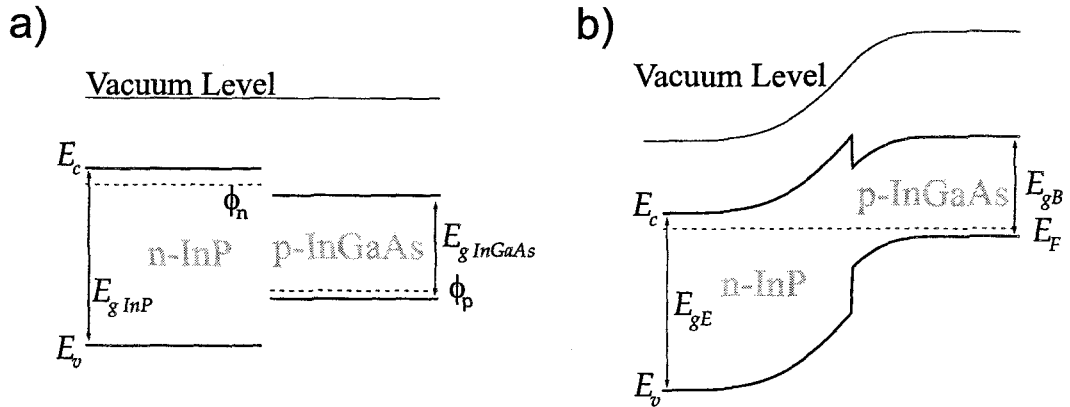


FIGURE 4.14. Energy band diagrams of n-type *InP* emitter and p-type *InGaAs* base layers (a) before and (b) after heterojunction formation.

To improve the emitter injection efficiency and to prevent the base dopant outdiffusion, a thin ($50 - 100 \text{ \AA}$) undoped *InGaAs* setback layer is often deposited between the base and emitter layers. In the further analysis, the BE heterojunction is assumed to have a very thin base setback layer deposited at the interface. A detailed energy band diagram of such a structure under a forward bias V_{BE} is shown in Fig 4.15. Assuming depletion approximation and solving Poisson's equation on both sides of the junction we obtain the depletion region widths in the emitter and base layers, w_E and w_B , respectively [76]:

$$w_E(V_{BE}) = -\frac{w_{sb}\epsilon_E N_{AB}}{\epsilon_B N_{DE} + \epsilon_E N_{AB}} \quad (4.29)$$

$$+ \sqrt{\left(\frac{w_{sb}\epsilon_E N_{AB}}{\epsilon_B N_{DE} + \epsilon_E N_{AB}}\right)^2 + \frac{2\epsilon_B\epsilon_E(V_{bi} - V_{BE})N_{AB}}{qN_{DE}(\epsilon_B N_{DE} + \epsilon_E N_{AB})}}$$

$$w_B(V_{BE}) = -\frac{w_E N_{DE}}{N_{AB}} + w_{sb} \quad (4.30)$$

where V_{bi} is the total junction built-in voltage and can be approximated by [76]

$$V_{bi} = \Delta E_C - \frac{\Delta E_g}{2q} + k_B T \ln \frac{N_{DE} N_{AB}}{n_{iE} n_{iB}} + \frac{k_B T}{2} \ln \frac{N_{CB} N_{VE}}{N_{CE} N_{VB}} \quad (4.31)$$

In the equations above N_{AB} and N_{DE} , and ϵ_B and ϵ_E are the doping concentrations and dielectric constants of the base and emitter layers, respectively; N_{CB} and N_{CE} , and N_{VB} and N_{VE} are the effective densities of states in the conduction and valence bands of the base and emitter, respectively; n_{iE} and n_{iB} are the intrinsic carrier concentrations in the emitter and base, and finally, w_{sb} is the thickness of the base setback layer.

The total potential drop of the junction is divided into partial drops across the depletion regions in the emitter and base, V_{bE} and V_{bB} , respectively:

$$V_{bE} + V_{bB} = V_{bi} - V_{BE} \quad (4.32)$$

$$V_{bE} = qN_{DE}w_E^2/2\epsilon_E \quad (4.33)$$

$$V_{bB} = qN_{AB}(w_B - w_{sb})w_{sb}/\epsilon_B + qN_{AB}(w_B - w_{sb})^2/2\epsilon_B \quad (4.34)$$

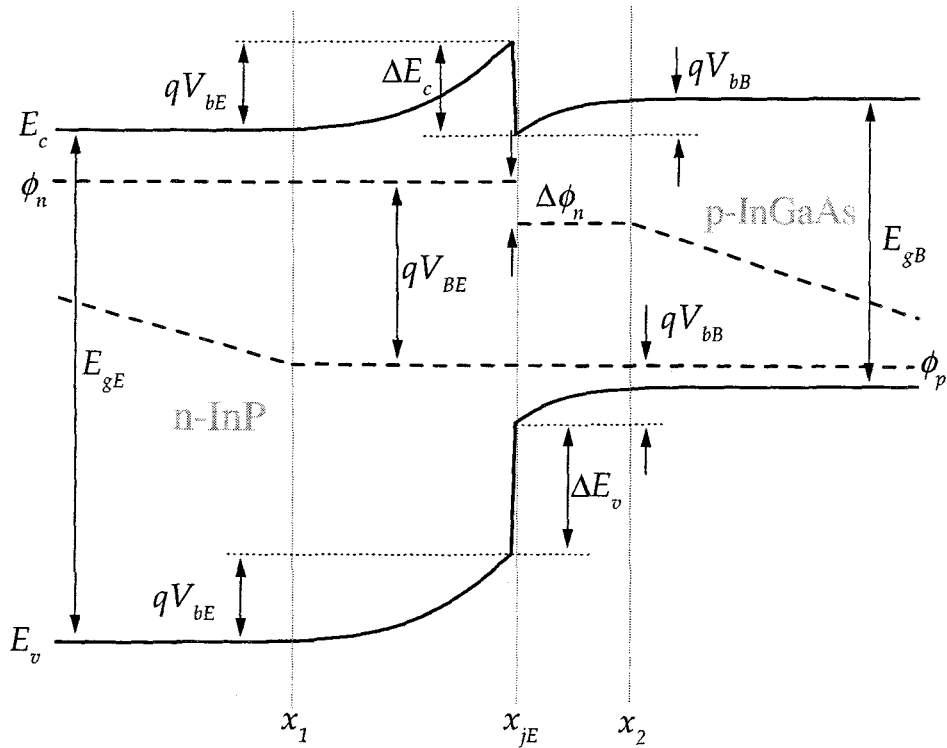


FIGURE 4.15. Energy band diagram of forward-biased *InP/InGaAs* emitter-base heterojunction.

First, let us consider the process of electron injection from the emitter into the base. There are several physical mechanisms responsible for the flow of current across the BE heterojunction. Similarly to the transport in homojunctions there are (1) drift of carriers in the electric field of the BE SCR and (2) diffusion due to the significant carrier gradient between the p and n regions. Furthermore, carriers having sufficient thermal energy can be thermionically emitted over the junction barrier. In the presence of the notch in the conduction band at the BE heterointerface the conventional drift-diffusion theory is inappropriate as the electron quasi-Fermi level may become discontinuous across the interface (see, e.g. Refs. [76–78]). Then the thermionic emission concept is used to model the current

across the conduction band spike, while the diffusion concept is still employed to calculate the transport across the quasi-neutral base. It should be noted that since the potential barrier (notch in the conduction band) is relatively thin, electrons can tunnel through the spike, thereby enhancing the current transport. Hence, the total current through the BE heterointerface is described as a net effect of thermionic and field emission. In the case of continuous slowly varying potential, the quantum mechanical tunneling can be described by employing the WKB approximation [79]. The current tunneling coefficient γ_n can be calculated from

$$\gamma_n = \exp \left[-2 \int_{x_1}^{x_2} k dx \right] \quad (4.35)$$

where k is the wavevector of a tunneling electron and can be written as $k = \sqrt{2m^*(qV(x) - E)}/\hbar$ in the effective mass approximation. This yields

$$\gamma_n = \exp \left[-\frac{2}{\hbar} \int_{x_1}^{x_2} \sqrt{2m^*(qV(x) - E)} dx \right] \quad (4.36)$$

where E is the energy of an electron, m^* - conduction band effective mass and $V(x)$ is the potential barrier, i.e. the potential spike in the conduction band. Assuming triangular or parabolic-shaped $V(x)$ an analytical solution for γ_n can be obtained (see for example [11, 76]). For the triangular barrier the tunneling coefficient is given by

$$\gamma_n = 1 + \frac{e^{qV_{bE}/kT}}{kT} \int_{V^*}^{V_{bE}} D(\xi) e^{-\beta V} dV \quad (4.37)$$

where $\xi = V/V_{bE}$, $V^* = [V_{bE} - \Delta E_C]\Theta(V_{bE} - \Delta E_C)$, Θ is the standard unit step function, and $D(\xi)$ is the barrier transparency given by

$$D(\xi) = \exp \left[-\eta \sqrt{1 - \xi} - \frac{\eta \xi}{2} \ln \xi + \eta \xi \ln (1 + \sqrt{1 - \xi}) \right] \quad (4.38)$$

with

$$\eta = \frac{4\pi V_{bE} \sqrt{\epsilon_E m_e^*}}{100h\sqrt{N_E}}$$

Voltage dependence of the tunneling coefficient shown in Fig. 4.16 demonstrates that the field emission mechanism not only enhances the current across the junction but can also introduce some dependence of the current ideality factor on the applied voltage.

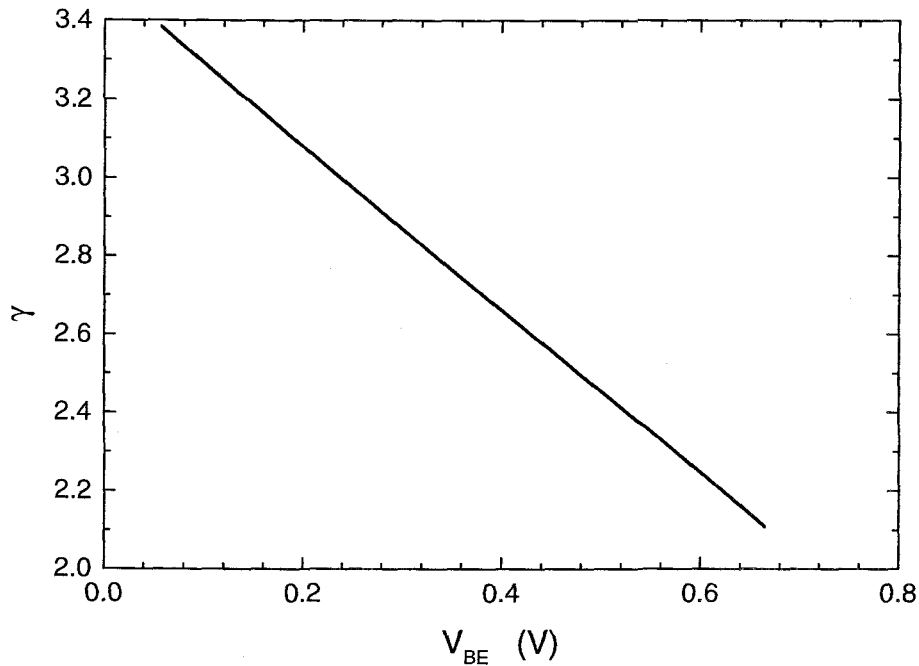


FIGURE 4.16. Field emission tunneling coefficient as a function of applied base-emitter voltage.

It should also be noted that since the current transport is typically limited by the thermionic emission over the barrier and field emission through the conduction band spike, the electron quasi-Fermi level becomes discontinuous at the heterointerface [80]. The discontinuity, denoted by $\Delta\phi_n$, develops only when there is a flow of electrons through the junction, and remains practically constant for any “non-negligible” current/bias (see further in the text). As a very unfortunate con-

sequence, the Shockley's boundary conditions can not be used for the calculations of the electron concentration in a biased heterojunction.

4.4.2. Carrier Transport in HBT

We now proceed with the derivation of the steady state current-voltage characteristics of an HBT. The electron concentration on the base side of the junction can be calculated by setting the electron current across the BE heterointerface to be equal to the diffusion current in the base region of the device. For the sake of simplicity all the recombination currents of the BE space charge region are ignored at this point.

Once again, we use the energy band diagram of an abrupt SHBT biased in the active mode, shown in Fig. 4.17, in which x_1 , x_2 , x_3 and x_4 denote the edges of the base-emitter and base-collector junctions, x_j is the position of the BE heterointerface and $W_B = x_3 - x_2$ is the neutral base width. Clearly, $x_2 - x_j$ is simply w_B and $x_j - x_1$ equals w_E .

Neglecting the recombination current in the $x_j < x < x_2$ region, the diffusion current can be set equal to the electron current density at the base-emitter heterointerface, $J_n(x_j)$ (see Fig. 4.15). As already discussed $J_n(x_j)$ is due to the thermionic and field emission and consists of the two opposing electron fluxes:

$$J_n(x_j) = -\frac{qv_n\gamma_n}{4} \left[n(x_j^-) \frac{N_C^B}{N_C^E} - n(x_j^+) e^{-\Delta E_C/kT} \right] \quad (4.39)$$

where $v_n = \sqrt{8kT/\pi m_n^*}$ is the mean electron thermal velocity in the emitter region, $n(x_j^-)$ and $n(x_j^+)$ are electron concentrations at the emitter and base side of the heterojunction, respectively. These concentrations can be expressed in terms of electron concentrations at the boundaries of the depletion region, x_1 and x_2 :

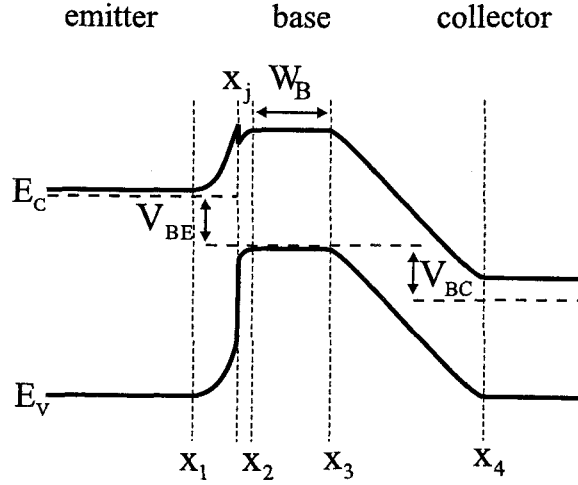


FIGURE 4.17. Energy band diagram of an SHBT biased in the active mode.

$$n(x_j^-) = n(x_1)e^{-qV_{BE}/kT} \quad (4.40)$$

$$n(x_j^+) = n(x_2)e^{qV_{BC}/kT} \quad (4.41)$$

Substituting these into the expression for the electron current through the junction gives

$$J_n(x_j) = -\frac{qv_n\gamma_n}{4} \left[n(x_1) \frac{N_C^B}{N_C^E} e^{-qV_{BE}/kT} - n(x_2) e^{(qV_{BC} - \Delta E_C)/kT} \right] \quad (4.42)$$

After more algebraic manipulations we obtain the following

$$\begin{aligned} J_n(x_j) &= -\frac{qv_n\gamma_n}{4} \left[n(x_1) \frac{N_C^B}{N_C^E} e^{-qV_{BE}/kT} - [n(x_2) - n_0(x_2) + n_0(x_2)] e^{(qV_{BC} - \Delta E_C)/kT} \right] \\ &= -\frac{qv_n\gamma_n}{4} \left[n(x_1) \frac{N_C^B}{N_C^E} e^{-qV_{BE}/kT} - [\Delta n(x_2) + n_0(x_2)] e^{(qV_{BC} - \Delta E_C)/kT} \right] \end{aligned} \quad (4.43)$$

where electron concentration at x_1 and base equilibrium electron concentration at x_2 are expressed in terms of the equilibrium concentration in the emitter $n_0(x_1)$

$$n(x_1) = n_0(x_1) \quad (4.44)$$

$$n_0(x_2) = n_0(x_1) e^{(\Delta E_C - qV_{bi})/kT} \quad (4.45)$$

We now set up and solve the minority carrier diffusion equation in the base of the transistor:

$$D_n \frac{d^2 \Delta n}{dx^2} = \frac{\Delta n}{\tau_n} \quad (4.46)$$

The general solution for this differential equation is

$$n = C_1 e^{x/L_n} + C_2 e^{-x/L_n}$$

where $L_n = \sqrt{D_n \tau_n}$ is the electron diffusion length in the base layer, and then applying boundary conditions we obtain an expression for the excess electron concentration in the base

$$\Delta n(x) = \Delta n(x_2) \frac{\sinh((x_3 - x)/L_n)}{\sinh(W_B/L_n)} \quad (4.47)$$

Then at $x = x_2$ the electron current density due to diffusion can be written as

$$J_n(x_2) = -q D_n \frac{d\Delta n}{dx} = -\frac{q D_n}{L_n \sinh(W_B/L_n)} [\Delta n(x_2) \cosh(W_B/L_n) - \Delta n(x_3)] \quad (4.48)$$

Our next step is to set Eqs. 4.43 and 4.48 equal and solve for $\Delta n(x_2)$ - concentration of electrons injected into the base. Introducing

$$A_n = \frac{4D_n}{v_n L_n \gamma_n \sinh(W_B/L_n)} \quad (4.49)$$

we obtain

$$\Delta n(x_2) = \frac{A_n \Delta n(x_3) + n(x_1) e^{-qV_{bE}/kT} N_C^B/N_C^E - n_0(x_2) e^{(qV_{bB} - \Delta E_C)/kT}}{e^{(qV_{bB} - \Delta E_C)/kT} + A_n \cosh(W_B/L_n)} \quad (4.50)$$

Denote

$$\Delta E_{nB} = -\Delta E_C - qV_{bB} \quad (4.51)$$

$$B_n = 1 + A_n \cosh(W_B/L_n) e^{-\Delta E_{nB}/kT} \quad (4.52)$$

Then $\Delta n(x_2)$ can be rewritten as

$$\begin{aligned}\Delta n(x_2) &= \frac{1}{B_n} \left[A_n \Delta n(x_3) e^{-\Delta E_{nB}/kT} + n(x_1) \frac{N_C^B}{N_C^E} e^{(-qV_{bE} - \Delta E_{nB})/kT} - n_0(x_2) \right] \\ &= \frac{1}{B_n} \left[A_n \Delta n(x_3) e^{-\Delta E_{nB}/kT} + n(x_1) \frac{N_C^B}{N_C^E} e^{(qV_{BE} - qV_{bi} + \Delta E_c)/kT} - n_0(x_2) \right] \quad (4.53)\end{aligned}$$

Assuming generation current of the base-collector junction is negligible the electron component of collector current density must be equal to the electron current density at the edge of base-collector depletion region. $J_n(x_3)$ is readily evaluated from the solution of Eq. 4.46:

$$J_n(x_3) = -\frac{qD_n}{L_n \sinh(W_B/L_n)} [\Delta n(x_2) - \Delta n(x_3) \cosh(W_B/L_n)] \quad (4.54)$$

Using identity $\cosh^2 x + \sinh^2 x = 1$ we arrive at

$$J_{Cn} = -\frac{qD_n}{L_n B_n \sinh(W_B/L_n)} \left[A_n \Delta n(x_3) \sinh^2(W_B/L_n) e^{-\Delta E_{nB}/kT} + \quad (4.55)$$

$$n(x_1) \frac{N_C^B}{N_C^E} e^{(qV_{BE} - qV_{bi} + \Delta E_c)/kT} - n_0(x_2) - B_n \Delta n(x_3) \cosh(W_B/L_n) \right] \quad (4.56)$$

Electron concentration at the boundary x_3 between the quasi-neutral base and the base-collector depletion region can be expressed as

$$n(x_3) = n_0(x_3) e^{-qV_{BC}/kT} \quad (4.57)$$

However, this commonly used relation can be inaccurate for the case of short base devices, i.e. when $W_B \sim D_n/v_s$ where v_s is electron saturation velocity. In this case $n(x_3)$ has to be evaluated by setting the diffusion electron current traversing the base region equal to the drift current through the base-collector junction [76]. This approach will be discussed later in the text. Using $n_0(x_2) = n_0(x_3)$

$$\Delta n(x_3) = n_0(x_2) [e^{-qV_{BC}/kT} - 1] \quad (4.58)$$

Substituting all this into Eq. 4.56 we obtain

$$J_{Cn} = \frac{qD_n n_0(x_1) e^{(\Delta E_c - qV_{bi})/kT}}{L_n B_n \sinh(W_B/L_n)} \left[(e^{qV_{BE}/kT} - 1) - \zeta (e^{qV_{BC}/kT} - 1) \right] \quad (4.59)$$

where

$$\zeta = A_n \sinh^2 (W_B/L_n) e^{-\Delta E_{nB}/kT} + \cosh (W_B/L_n) \quad (4.60)$$

The calculated electron component of the collector current is shown in Fig. 4.18 for several different combinations of the emitter and base doping. Table 4.2 lists parameters of the HBT heterostructure and properties of the bulk *InP* and *InGaAs* [81, 82] used in the calculations. As we can see from the figure, both, the magnitude and local slope of the calculated I_{Cn} 's depend on the carrier concentrations in the base and emitter. For heterostructures used in these experimental studies the ideality factor of the current (black line) changes from 1.0 at low biases to 2.0 at higher biases.

Self-consistent calculation of J_{Cn} and $n(x_2)$ allows us to evaluate the discontinuity of the electron quasi-Fermi level at the base-emitter heterointerface. It can be readily shown that $\Delta\phi_n$ can be found from (see, e.g. Refs. [78, 83])

$$\Delta\phi_n = kT \ln \left[1 - \frac{J_{Cn} e^{\Delta E_c/kT}}{qn(x_2)v_R} \right] \quad (4.61)$$

where $v_R = \sqrt{kT/2\pi m^*}$ is the Richardson velocity. Calculations show that for all non-negligible collector currents $\Delta\phi_n \approx 0.23 \text{ eV} \approx \Delta E_C$.

The hole component of the collector current arising from the BC junction can be calculated from the conventional drift-diffusion theory (see, for example, Ref. [84]) as

$$J_{Cp} = \frac{qD_{pC}p_0(x_4)}{L_{pC}} \coth (W_C/L_{pC}) [e^{qV_{BC}/kT} - 1] \quad (4.62)$$

Finally, the total collector current can be found as a sum of the electron and hole components given by Eqs. 4.59 and 4.62, respectively

$$J_C = J_{Cn} + J_{Cp} \quad (4.63)$$

Parameter	<i>InP</i> Emitter	<i>In</i> _{0.53} <i>Ga</i> _{0.47} <i>As</i> Base	<i>In</i> _{0.53} <i>Ga</i> _{0.47} <i>As</i> Collector
N_C (cm^{-3})	5.72×10^{15}	2.084×10^{17}	2.084×10^{17}
N_V (cm^{-3})	3.459×10^{18}	7.831×10^{18}	7.831×10^{18}
n_i (cm^{-3})	1.2×10^8	7.983×10^{11}	7.983×10^{11}
E_g (eV)	1.344	0.750	0.750
ϵ_s (ϵ_0)	12.61	13.88	13.88
Dopant	<i>Si</i>	<i>Zn</i>	<i>Si</i>
E_d or E_a (meV)	7.3	22	7.3
N_D or N_A (cm^{-3})	5×10^{17}	2×10^{19}	1×10^{15}
n_{n0} (cm^{-3})	5×10^{17}	–	1×10^{15}
p_{p0} (cm^{-3})	–	2×10^{19}	–
Width (Å)	5000	500	5000

TABLE 4.2. Heterostructure and bulk *InP* and *InGaAs* parameters used in calculations (at 300 K, low frequency).

In this derivation an ideal structure and no recombination currents were assumed. For relatively high gain devices, when $I_C \gg I_{rec,tot}$, the latter assumption does not alter the results significantly.

4.4.3. Base Recombination Currents

The total base current of an HBT can be presented in the following form

$$J_B = J_{Bp} + J_{sr} + J_{br} + J_{scr} - J_g \quad (4.64)$$

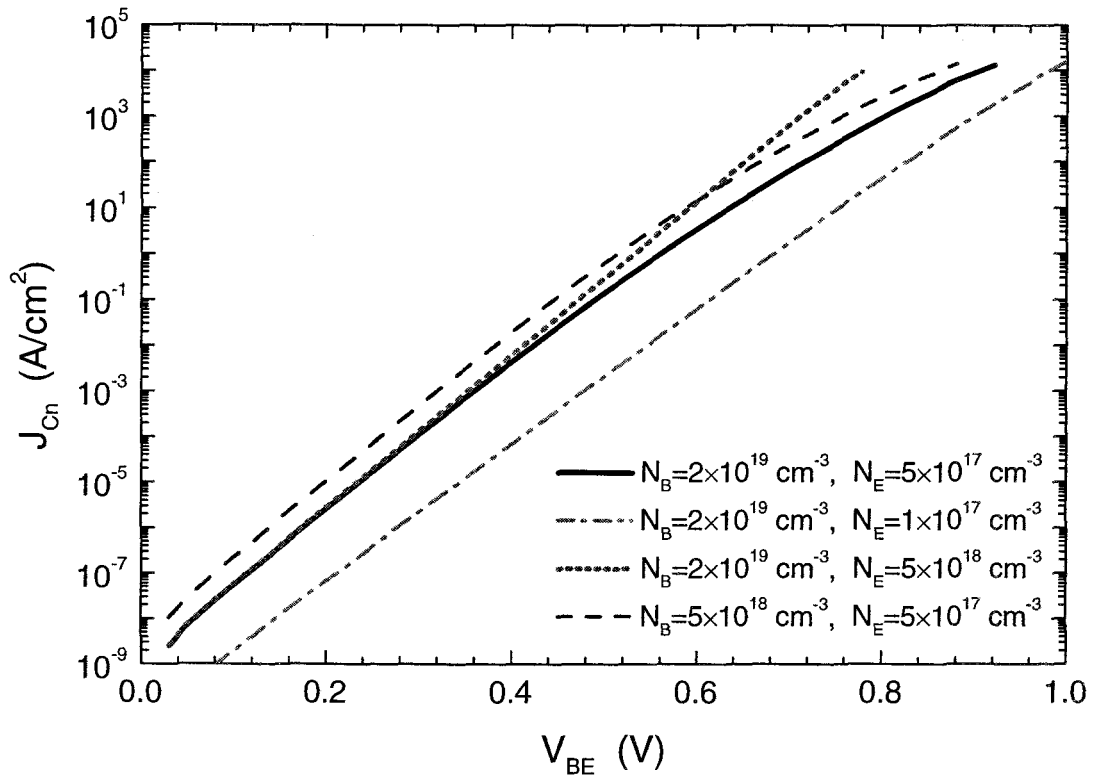


FIGURE 4.18. Calculated collector current density as a function of base emitter voltage.

where J_{Bp} is the hole current corresponding to injection of holes from the base into the emitter, J_{br} is the quasi neutral base recombination current, J_{scr} is recombination current in the BE space charge region, J_{sr} is the surface recombination current, and, finally, J_g is the generation current of the base-collector depletion region. In this section all the individual components of the base current are analyzed and calculated.

In most practical HBT designs, J_{Bp} is negligible because of the large potential step in the valence band at the BE interface. The magnitude of the surface recombination current varies drastically from one material to another and

also shows a very strong dependence on the fabrication procedure and passivation schemes employed. In addition, for smaller geometry devices the surface component of the base current becomes more dominant and is typically one of the major concerns during the fabrication. The magnitude of J_{sr} is usually expressed in terms of the so-called surface recombination velocity, s_0 , and the surface diffusion length, L_s , (see, e.g., Refs. [80, 85–87])

$$J_{sr} = \frac{qs_0L_sP_E}{A_E} \sqrt{n(x_2)p(x_2)} \quad (4.65)$$

where P_E is the emitter perimeter. Experimentally, J_{sr} can be separated from the rest of the base current by studying a number of devices with different perimeter-to-area ratios, P/A . Ignoring J_g for the moment, the total base current can be written as a sum of bulk ($J_{B,bulk} = J_{br} + J_{scr}$) and surface recombination components

$$J_B = J_{B,bulk} + i_{sr} \times \frac{P_E}{A_E} \quad (4.66)$$

where i_{sr} is the surface recombination current per unit length. Substituting this expression into the equation for the dc gain yields

$$1/\beta = 1/\beta_{bulk} + \frac{i_{sr}}{J_C} \times \frac{P_E}{A_E} \quad (4.67)$$

Fig. 4.19 shows a typical $\beta^{-1}(P/A)$ plot which can be used to extract the magnitude of the surface recombination current. In all the devices in the current studies J_{sr} shows some detectable contribution. However, as will be shown in the later chapters, the irradiation seems to have no noticeable effect on the surface recombination current.

Bulk recombination current consists of three components corresponding to Auger, radiative (or band-to-band) and Shockley-Read-Hall (SRH) recombination. The total carrier lifetime is determined by a combination of the lifetimes for the

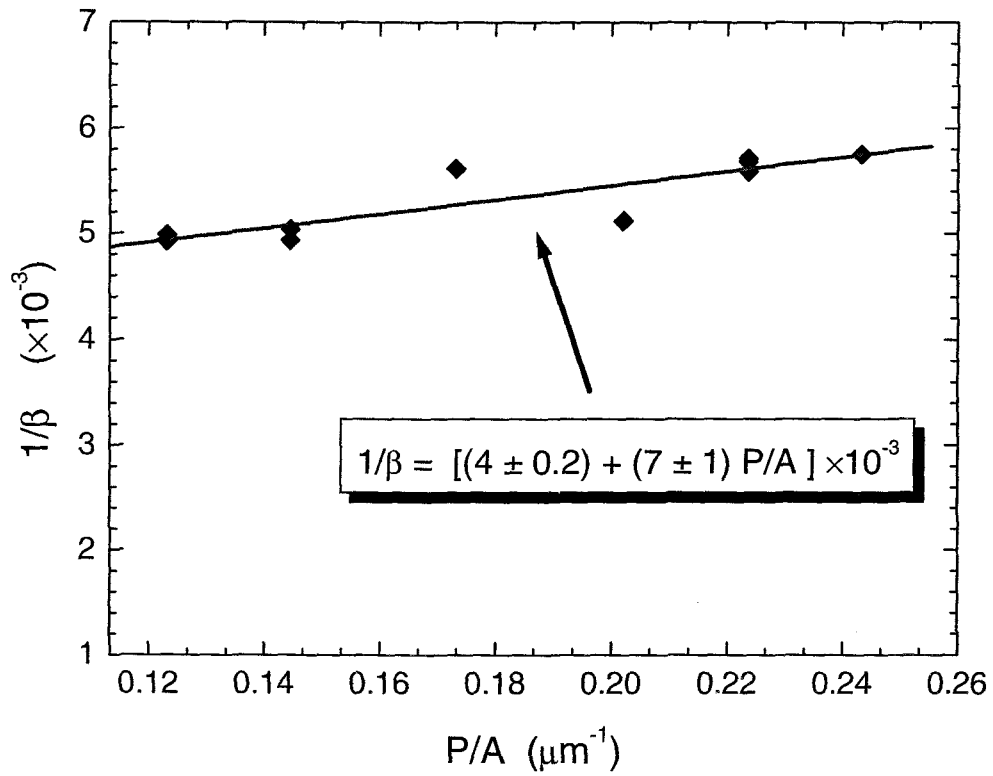


FIGURE 4.19. Inverse current gain as a function of perimeter-to-area ratio for devices with different geometry.

individual processes

$$\frac{1}{\tau} = \frac{1}{\tau_{rad}} + \frac{1}{\tau_{Aug}} + \frac{1}{\tau_{SRH}} \quad (4.68)$$

And the total current is given by

$$J = q \int U dx = q \int \frac{-\Delta p}{\tau_p} dx \quad (4.69)$$

for an n-type material and

$$J = q \int U dx = q \int \frac{-\Delta n}{\tau_n} dx \quad (4.70)$$

for a p-type material. From the form of these expressions it is very important to note that the recombination mechanism with the shortest lifetime determines the overall carrier lifetime and therefore the recombination current. Next we briefly cover each of the recombination mechanisms.

Auger recombination process involves two electrons and a hole or two holes and an electron with the recombination rate proportional to pn^2 in the first case and np^2 in the second. As a result Auger recombination becomes important in heavily doped semiconductors only. The total Auger recombination current is given by [78]

$$J_{Aug} = q \int U_{Aug} dx = q \int (A_n n + A_p p)(pn - n_i^2) dx \quad (4.71)$$

where U_{Aug} is the total Auger recombination rate, A_n and A_p are the electron and hole Auger coefficients. The Auger carrier lifetime is given by $\tau_n^{Aug} \approx 1/A_n n^2$ and $\tau_p^{Aug} \approx 1/A_p p^2$ for n- and p-type materials, respectively.

Band-to-band recombination is important in direct bandgap materials and is determined by the recombination rate of the following form [76, 78]

$$J_{rad} = q \int U_{rad} dx = q \int B(pn - n_i^2) dx \quad (4.72)$$

where U_{rad} is the radiative recombination rate and B is the radiative recombination coefficient. The minority carrier lifetimes are given by $\tau_n^{rad} \approx 1/Bp$ and $\tau_p^{rad} \approx 1/Bn$ for p- and n-type materials, respectively.

Finally, SRH recombination rate under non-equilibrium steady-state conditions for a continuous energy distribution of traps in the bandgap is given by [88]

$$U = \int_{E_v}^{E_c} \frac{(pn - n_i^2) D_t(E) dE}{[n + n_1(E)]/c_p(E) + [p + p_1(E)]/c_n(E)} \quad (4.73)$$

where D_t is the density of the trap states, p_1 and n_1 are the concentrations of holes and electrons if the Fermi level were at the trap level, and c_p and c_n are the capture rate coefficients for the carriers

$$c_n = \sigma_n < v_{th,n} > \quad (4.74)$$

$$c_p = \sigma_p < v_{th,p} > \quad (4.75)$$

with σ_n and σ_p , and $< v_{th,n} >$ and $< v_{th,p} >$ denoting the capture cross sections and mean thermal velocities for electrons and holes, respectively. For a single trap level the expression for the recombination rate can be simplified to

$$U = \frac{pn - n_i^2}{(n + n_1)\tau_{p0} + [p + p_1(E)]\tau_{n0}} \quad (4.76)$$

where the SRH carrier lifetimes for electrons and holes are defined as

$$\tau_{n0}^{SRH} = \frac{1}{c_n N_t} \quad (4.77)$$

$$\tau_{p0}^{SRH} = \frac{1}{c_p N_t} \quad (4.78)$$

The SRH current is given by

$$J_{SRH} = q \int U_{SRH} dx \quad (4.79)$$

Neutral bulk recombination occurring in the p-type base region is determined by the overall minority carrier lifetime τ_n calculated from Eq. 4.68

$$I_{br} = qA_E \int_{x_2}^{x_3} \frac{\Delta n(x)}{\tau_n} dx$$

Substituting Eq. 4.47 into the integral for I_{br} yields

$$I_{br} = \frac{qA_E L_n \Delta n(x_2) [\cosh(W_B/L_n) - 1]}{\tau_n \sinh(W_B/L_n)} \quad (4.80)$$

It should be noted from Eq. 4.80 that the neutral base recombination current is directly proportional to the number of electrons injected into the base ($\Delta n(x_2)$).

Therefore I_{br} should have the same functional dependence on the applied bias as the collector current. This indeed can be seen from Fig. 4.20, where the calculated collector current (black line) and neutral base recombination (blue line) current are plotted. As a very important result, the gain of an HBT, in which I_{br} is the dominating component of the base current, is practically constant for all biases.

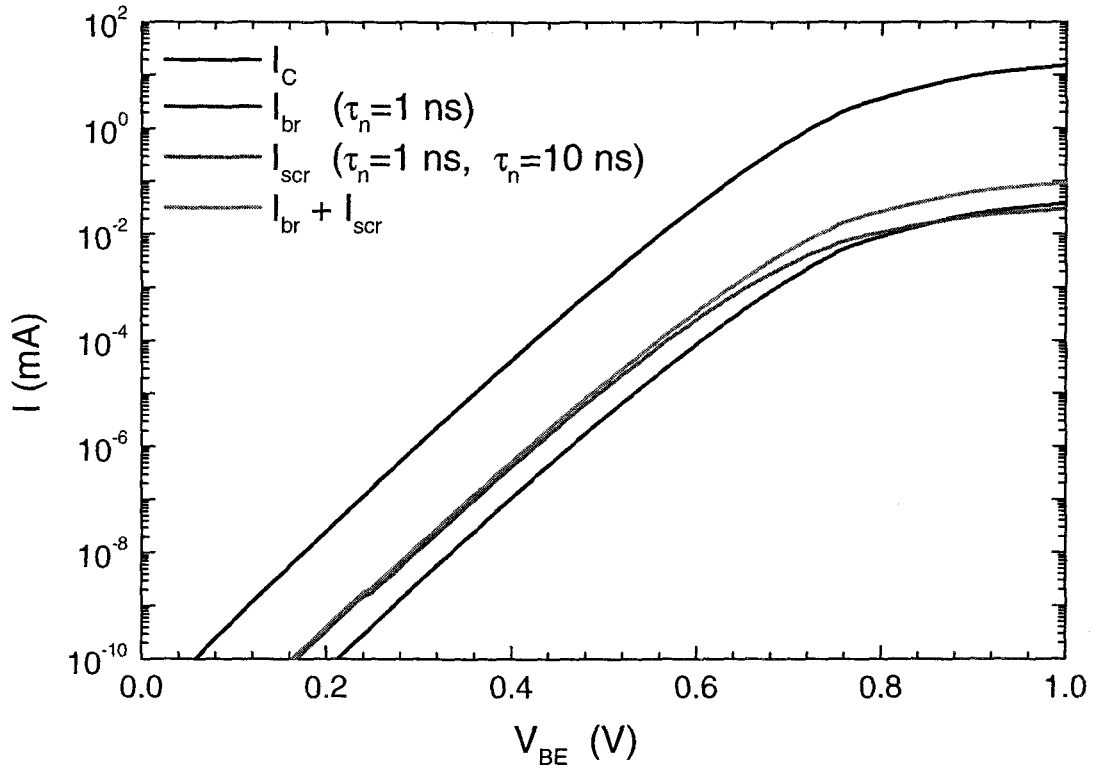


FIGURE 4.20. Calculated collector current and neutral bulk and space charge base recombination currents.

Space charge recombination component of the base current should also include the SRH mechanism. Most of the approximations found in the literature suggest $I_{scr} \propto e^{qV/2kT}$ form and not only give inaccurate bias dependence but of-

ten considerably overestimate the recombination in the depletion region (see, e.g., [89]). As will be shown in later chapters the radiation degradation of HBTs is partially due to the SCR recombination-generation currents; therefore a more precise model needs to be developed to facilitate the analysis of the radiation effects. Consider the recombination on the emitter and base side separately. For the emitter side, the non-equilibrium carrier concentrations are expressed in terms of equilibrium hole and electron concentrations on the base and emitter side, respectively:

$$p(V_{BE}, x) = p_{p0}^B e^{-q(V_{bi} + \Delta E_v)/kT} e^{qV_{bE}(V_{BE}, x)/kT} \quad (4.81)$$

$$n(V_{BE}, x) = n_{n0}^E e^{-qV_{bE}(V_{BE}, x)/kT} \quad (4.82)$$

where $V_{bE}(V_{BE}, x)$ describes the energy band bending as a function of applied bias and position

$$V_{bE}(V_{BE}, x) = \frac{V_{bE}(V_{BE})}{w_E^2(V_{BE})} x^2 \quad (4.83)$$

where $V_{bE}(V_{BE})$ is given by Eq. 4.33. Consequently $n(V_{BE}, x)$ and $p(V_{BE}, x)$ are functions of position x in the depletion region and the bias applied to the junction. Finally, from the definitions of n_1 and p_1

$$p_1 = n_i^E e^{(E_i - E_t)/kT} \quad (4.84)$$

$$n_1 = n_i^E e^{(E_t - E_i)/kT} \quad (4.85)$$

Analogously, for the depletion region on the base side we can write

$$p(V_{BE}, x) = p_{p0}^B e^{-qV_{bB}(V_{BE}, x)/kT} \quad (4.86)$$

$$n(V_{BE}, x) = n(x_2) e^{qV_{bB}(V_{BE}, x)/kT} \quad (4.87)$$

$$p_1 = n_i^B e^{(E_i - E_t)/kT} \quad (4.88)$$

$$n_1 = n_i^B e^{(E_t - E_i)/kT} \quad (4.89)$$

$$V_{bB}(V_{BE}, x) = \frac{V_{bB}(V_{BE})}{w_B^2(V_{BE})} x^2 \quad (4.90)$$

where $V_{bB}(V_{BE})$ is given by Eq. 4.34. Assuming a midgap trap level ($E_t = E_i$), for BE bias of 0.8 V calculated SRH recombination rate (using Eq. 4.76), and electron and hole concentrations as functions of position in the base depletion region (using Eqs. 4.87 and 4.86) are shown in Fig.4.21. As expected the recombination rate has a maximum at the plane where n equals p . Calculated neutral base SRH recombination rate matches the SCR rate at x_2 – the interface between the depletion region and neutral bulk.

Recombination rate (for a midgap trap) calculated as a function of the position in the BE heterojunction and the applied BE bias is shown in Fig. 4.22. Due to the very low concentration of holes in the emitter the recombination rate on the emitter side is less than that on the base side by almost six orders of magnitude. Thus for all the further analysis only the recombination in the base SCR needs to be considered.

The SRH recombination current is calculated by integrating $U(x)$ over the entire depletion region

$$I_{scr}(V_{BE}) = qA_E \int_{x_j}^{x_2} U(V_{BE}, x) dx \quad (4.91)$$

In the base SCR, where $p \gg n$, the recombination process is limited by the electron lifetime. Fig. 4.23 shows the calculated I_{scr} as a function of BE voltage for different τ_n at a fixed hole lifetime of $\tau_p = 10$ ns for a single midgap trap. Decreasing the electron lifetime leads to a practically parallel shift of $I_{scr} - V_{BE}$ curve towards the higher values. The base current ideality factor starts at about 1.1 at low biases and increases significantly for the higher biases.

A set of $I_{scr} - V_{BE}$ curves for different values of τ_p 's at fixed $\tau_n = 10$ ns is shown in Fig. 4.24. This plot once again demonstrates that the trapping of electrons is the mechanism limiting the recombination. For $\tau_p < \tau_n$ the magnitude

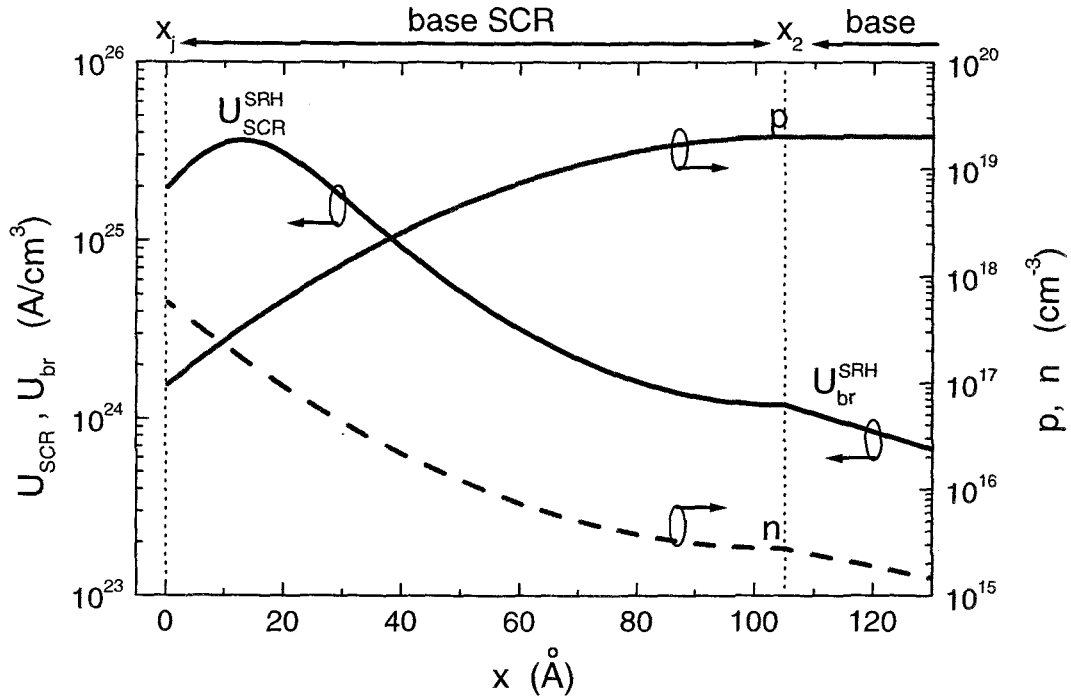


FIGURE 4.21. Calculated SRH recombination rate, electron and hole concentrations as function of position in the base layer (midgap traps; BE bias is 0.8 V).

of the current does not change at all, and only for the range of $\tau_p \gg \tau_n$ the hole trapping becomes slow enough to reduce the current. Also note that for the very large τ_p 's the ideality factor of $I_{scr} - V_{BE}$ increases to 2.0 at the low biases.

Finally, the $I_{scr} - V_{BE}$ curves calculated for single traps with different depth are shown in Fig. 4.25. As expected deep traps with energy levels close to the intrinsic Fermi level ($E_t - E_i$ is small), appear to be the most effective recombination centers. As $E_t - E_i$ increases the magnitude and the ideality factor of the recombination current decrease. It should also be noted that only the absolute value

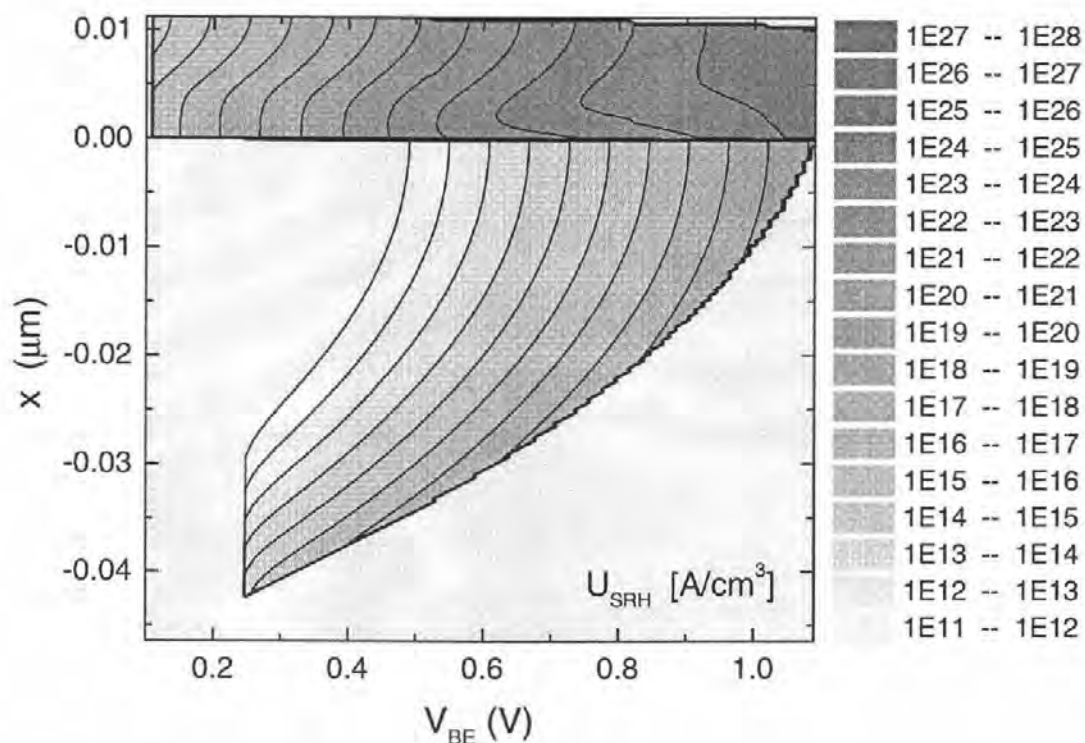


FIGURE 4.22. Recombination rate as a function of position and applied BE bias.

of $E_t - E_i$ is important. The recombination current is the same irrespective of whether the trap levels are in upper or lower halves of the bandgap.

In summary, variations of the three main variables, τ_n , τ_p and $|E_t - E_i|$, may produce recombination currents with significantly different ideality factors and magnitudes. Moreover, the results may show a very strong dependence on bias conditions. Finally, it should be noted that carrier lifetimes, strictly speaking, are functions of the trap density, electric field and the carrier concentration (see, e.g., [90, 91]). As a result the lifetimes in the bulk and space charge regions can be different. Furthermore, after irradiation, when a very large number of traps

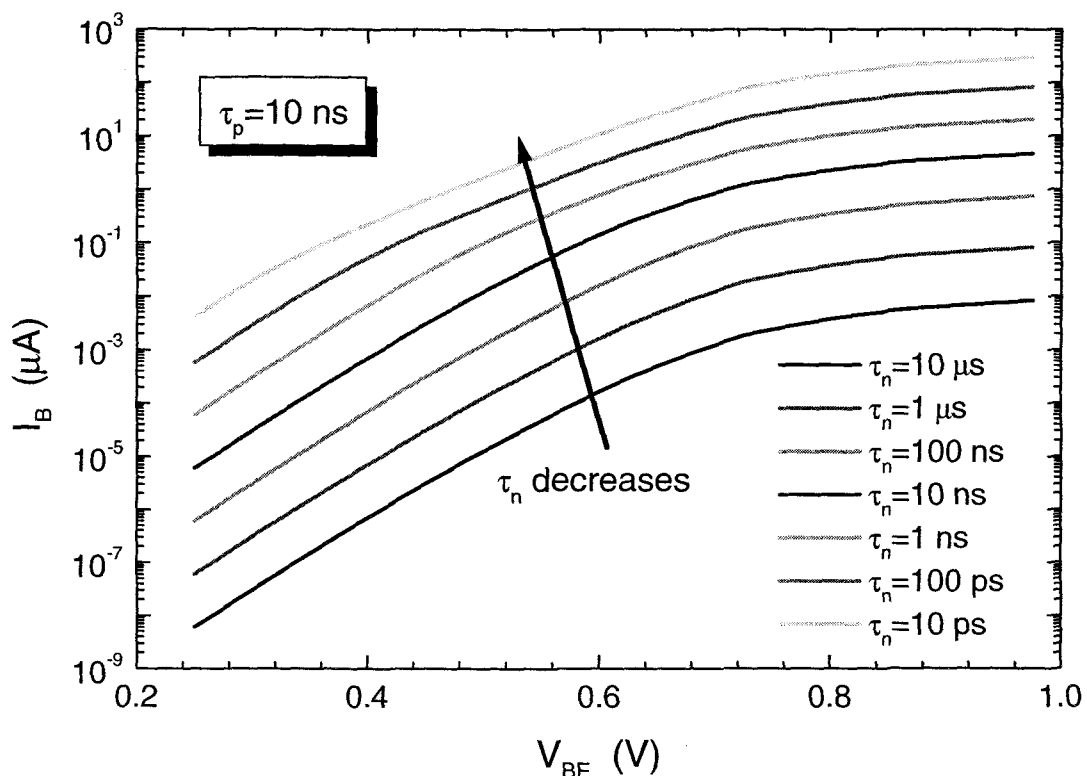


FIGURE 4.23. Base SCR recombination current as a function of BE applied voltage for different electron lifetimes at fixed hole lifetime.

is introduced, the carrier trapping mechanism can change and the conventional expressions used in our analysis may become somewhat inaccurate.

At last we note that the numerical integration of Eq. 4.73 for a number of discrete trap levels for calculation of I_{scr} gives results very similar to the results obtained by using Eq. 4.76. Therefore, in all the calculations the recombination rate is assumed in the form of Eq. 4.76.

The last component of the base current is the generation current of the base-collector space charge region. Under a moderate reverse bias (in the active mode of operation) this current is simply a sum of the saturation currents of the

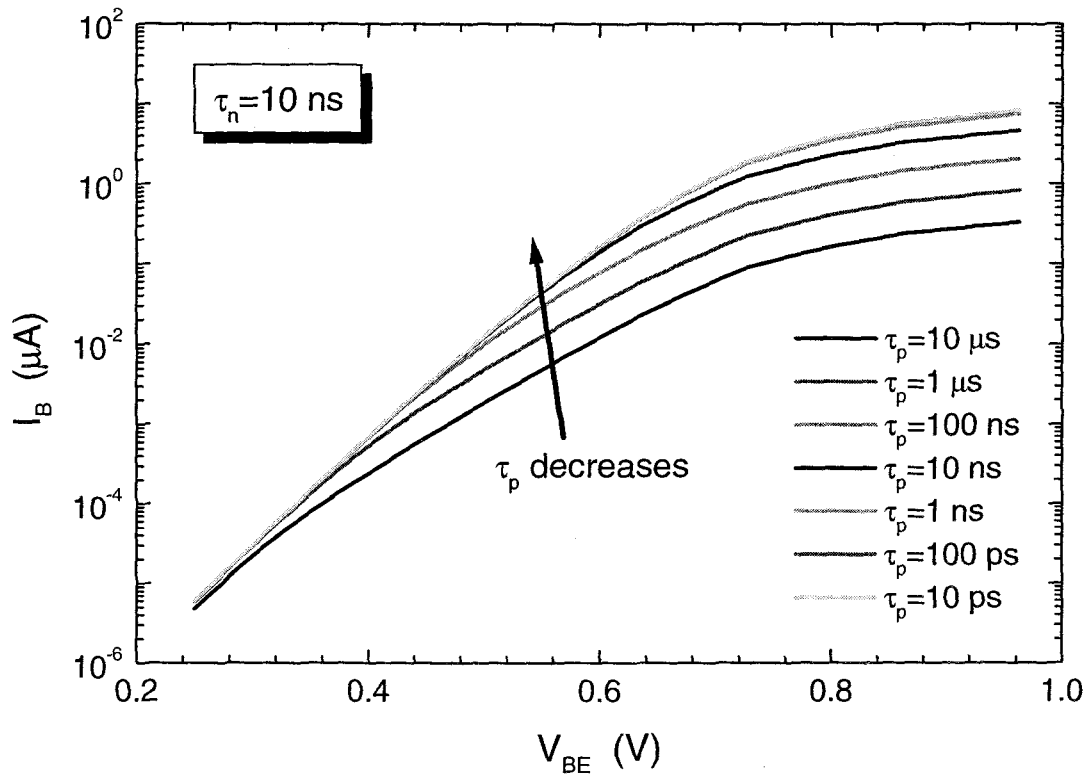


FIGURE 4.24. Base SCR recombination current as a function of BE applied voltage for different hole lifetimes at fixed electron lifetime.

diffusion and generation-recombination components

$$I_g = I_{S,diff} + I_{S,gr} = \frac{qA_C n_i^2 D_p}{L_p N_D} + \frac{1}{2} q A_C W_{BC} \frac{n_i}{\tau_n} \quad (4.92)$$

4.4.4. Tunnel-Assisted Trapping

Before leaving the topic of the base current we briefly consider the so-called tunnel-assisted trapping mechanism. First discovered in the narrow *Ge* Esaki junctions this effect has received a lot of attention (see, e.g., Refs. [92, 93]). Sah *et. al.* [92] have shown that large excess currents observed at low biases in gold-

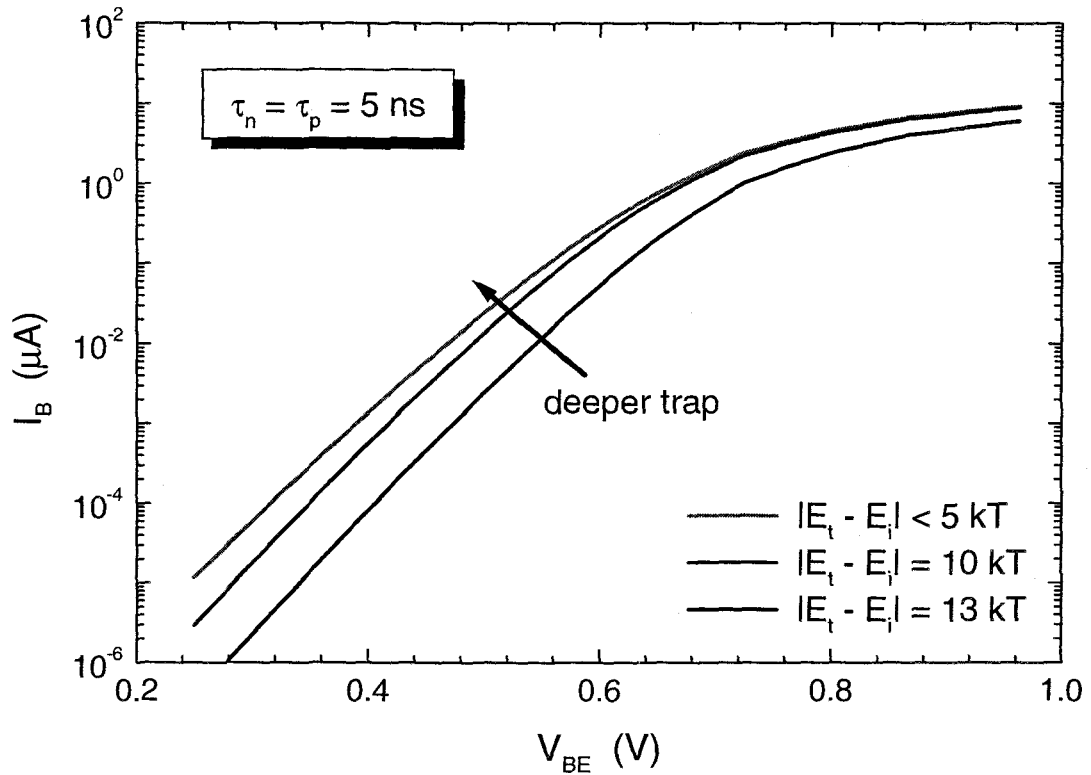


FIGURE 4.25. Base SCR recombination current as a function of BE applied voltage for different single level traps.

doped silicon tunnel junctions can be explained by means of multistep transition processes involving tunneling of electrons from the conduction band horizontally into the valence band through the *Au* trap levels as intermediate states. Chynoweth *et.al.* [93], who also studied narrow *Si* junctions, have introduced a model according to which electrons can drop down to the valence band through a series of tunneling transitions between trap levels, as shown in Fig. 4.26a. Based on the Chynoweth model Riben *et.al.* [94] have developed a model describing recombination-tunneling currents in *n Ge* – *p GaAs* heterojunctions. Their approach was further improved by Donnelly *et.al.* [95], who incorporated processes of thermionic emission and

recombination into the model. We now consider three major carrier transport mechanisms that involve tunneling of the carriers. Figs. 4.26b, c, and d show the diagrams illustrating the current transport. For the sake of clarity, the “staircase” carrier transitions are shown by only one step, and trap states are not shown at all. In Fig. 4.26b the current on both sides of the junction is determined by tunneling of the carriers into the trap states in the forbidden gap. For narrow (heavily-doped) *InP/InGaAs* BE junction with large potential barriers in the both conduction and valence band this mechanism may become very important if sufficient number of bandgap levels is available. In this case for the multistep tunneling process the forward current density J_t is given by [95]

$$J_t = BN_{t0}e^{-\beta_i K_1 V_{BE}} e^{-\alpha \sqrt{s}(V_{bi} - K_1 V_{BE})} \quad (4.93)$$

where B is a constant, N_{t0} is the density of the defect states at an energy level positioned $\phi_p - \phi_n$ above the valence band of the *InGaAs* layer, $\exp[-\beta_i K_1 V_{BE}]$ represents variations in N_t with energy within the bandgap, K_1 is the fraction of the applied voltage dropped across the emitter SCR, $s = E_s/(V_{bi} - K_1 V_{BE})$ relates the height of each potential step in the “staircase” transition, E_s , (see Fig. 4.26a) to the potential drop across the junction, and, finally, constant α is given by

$$\alpha = \frac{4}{3\hbar} \sqrt{\frac{m^* \epsilon_E}{N_{DE} K_1}} \quad (4.94)$$

If uniform distribution of energy levels is assumed then the tunneling current can be rewritten as

$$J_t = B' N_t e^{-\alpha \sqrt{s}(V_{bi} - K_1 V_{BE})} \quad (4.95)$$

where B' is a constant. We postpone the further discussion of this expression and its implications till Chapter 6.

Diagram (c) suggests a situation where diffusion/emission current flows in the wide bandgap emitter and then recombines with the carriers tunneling from the

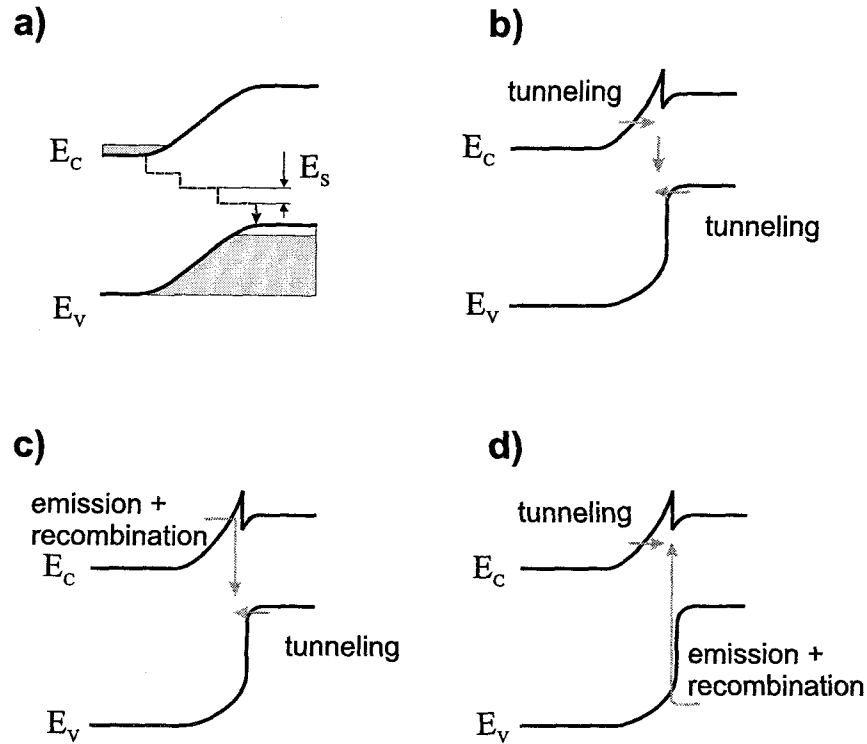


FIGURE 4.26. (a) Diagram illustrating multistep electron tunneling process in Si junction; (b), (c) and (d) three major current transport mechanisms involving tunneling of electron into trap states in *InP/InGaAs* heterojunctions.

base side. At low biases this transport is limited by the emission current provided by the emitter. Hence the voltage dependence should be similar to that of the standard thermionic emission theory. At higher biases however tunneling becomes the limiting mechanism and the current-voltage dependence functionally resembles Eq. 4.95 [95].

Finally, diagram (d) depicts situation opposite to (c), i.e. the current injected from the base side recombines with the carriers tunneling from the emitter side. Due to a large discontinuity present in the valence band (ΔE_v) this

mechanism is incapable of generating any significant current, and can therefore be ignored.

4.4.5. High Level Injection Effects

The model for the collector and base currents was formulated for low and moderate biases. Since in most practical applications HBTs are operated at as high power levels as possible, it is now our task to investigate the so-called high level injection effects that may significantly affect the performance of the device.

First, we review the effects of high level injection at the base-emitter junction in homojunction bipolar transistors. At sufficiently high biases number of electrons injected into the base region may become comparable with the concentration of the majority carriers – holes. The hole concentration then increases to maintain the charge neutrality

$$p(x) = p_0(x) - n_0(x) + n(x) \quad (4.96)$$

The valence (and conduction) band moves up with respect to the Fermi level and as a consequence the barrier for electron injection increases. Furthermore, the quasi-Fermi levels can not be assumed constant in the base SCR and the depletion approximation becomes inappropriate since the carriers traversing the space charge region can not be neglected any more. In a BJT after the onset of the high level injection the collector current ideality factor increases to 2.0, as opposed to 1.0 in the normal mode of operation. The base current, however, keeps increasing at practically the same rate as at moderate biases. As a result the current gain of a homojunction transistor decreases rapidly at high collector currents. In an abrupt HBT, where the base current is limited by the injection of electrons from the emitter, the base current should follow the saturating collector current,

and therefore the device gain will not decrease in the high level injection regime. Additionally, for most applications to improve high-frequency performance of the device the base is very heavily doped ($N_A > 10^{18} \text{ cm}^{-3}$). Thus the concentration of the injected electrons is smaller as compared to the hole concentration in the base ($n(x_2) \leq 10^{16} \text{ cm}^{-3} \ll N_{AB}$). Current levels at which $n(x_2)$ would become comparable to N_A can not be reached in practice because of the series resistance limiting the current.

Finally we discuss the so-called collector current saturation effect also known as the base pushout or Kirk effect. The high field present at the BC junction starts shifting into the collector region as the current flowing from the base into the collector increases. Additionally, voltage drop in the collector region $V = I_C R_C$ may lead to forward-biasing of the otherwise unbiased or reverse-biased base-collector junction and a significant current of holes may be injected into the collector. Consequently, the energy bands in the collector SCR next to the base region move up, as shown in Fig. 4.27 (gray lines). The net effect can simply be viewed as an increase of the base width by W_{cib} (and the corresponding reduction of the collector thickness) and extension of the collector SCR. For even higher currents the entire collector region can become depleted. Mathematically, the base pushout can be estimated from [84]

$$W_{cib} = W_C \left[1 - \sqrt{\frac{J_1 - J_2}{J_C - J_2}} \right] \quad (4.97)$$

where the variables J_1 and J_2 are expressed in terms of the electron saturation velocity v_s as

$$J_1 = qv_s \left[N_C + \frac{2\epsilon_C V_{BC}}{qW_C^2} \right] \quad (4.98)$$

$$J_2 = qv_s N_C \quad (4.99)$$

Having calculated the base pushout, the base and collector thickness can be corrected and then used in the device model derived in the previous sections

$$W'_B = W_B + W_{cib} \quad (4.100)$$

$$W'_C = W_C - W_{cib} \quad (4.101)$$

Calculations show that the collector region gets completely depleted at moderate biases. It is also observed that the base region extends very deep into the collector even before reaching the highest current levels. Despite the very strong base push out virtually no change is observed in the calculated collector current. Experimentally measured device characteristics also do not show any “signatures” specific to the saturation effect. To explain this inconsistency we need to return to the nature of the carrier transport through the structure. The thermionic emission (enhanced by field emission) current across the heterointerface is matched with the drift-diffusion current flowing from the base into collector. For BJTs the current transport is diffusion limited and therefore any, even insignificant, change in the base thickness would affect the current considerably. In the case of an abrupt HBT the current is limited by the injection of carriers into the base region; the subsequent drift-diffusion transport across the base and then collector is capable of removing the carriers at much faster rate even when $W_B + W_{cib} \gg W_B$. As a result, the collector current depends only on the carrier injection at the base-emitter heterojunction and is not affected by the diffusion through the base and drift through the collector.

4.5. Ebers-Moll and Gummel-Poon Models

To complete the discussion on HBT modeling we turn our attention to well-recognized Ebers-Moll and Gummel-Poon BJT models implemented in com-

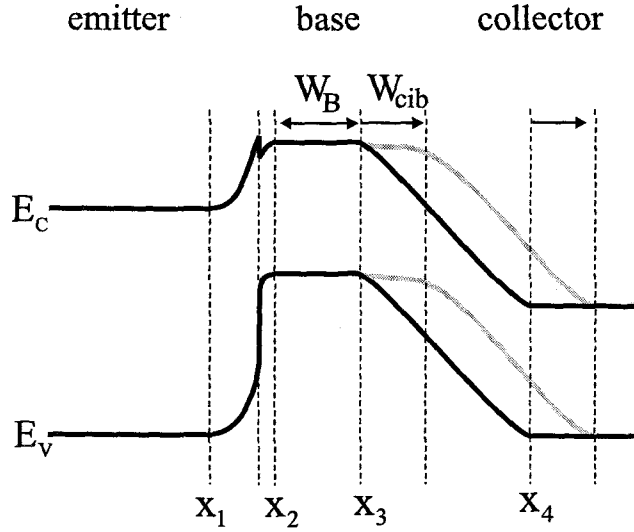


FIGURE 4.27. Energy band diagram of an SHBT biased in the active mode operated in the quasi-saturation regime.

mercially available device/circuit simulation packages such as SPICE. This section is an attempt to analyze the applicability of these models for description of HBT operation and radiation-induced degradation.

Transport version of BJT Ebers-Moll static model implemented in SPICE is shown in Fig. 4.28. In this configuration the transistor is thought to behave as a pair of interacting p-n diodes. The emitter, base and collector currents of the device are given by

$$I_E = -\frac{I_{CC}}{\beta_F} - I_{CT} \quad (4.102)$$

$$I_B = \frac{I_{CC}}{\beta_F} + \frac{I_{EC}}{\beta_R} \quad (4.103)$$

$$I_C = I_{CT} - \frac{I_{EC}}{\beta_R} \quad (4.104)$$

where

$$I_{CC} = I_S (e^{qV_{BE}/n_F kT} - 1) \quad (4.105)$$

$$I_{EC} = I_S (e^{qV_{BC}/n_R kT} - 1) \quad (4.106)$$

$$I_{CT} = I_{CC} - I_{EC} \quad (4.107)$$

and I_S is the collector saturation current, β_F and β_R are the forward and reverse gains, respectively. The base width modulation effects are incorporated into the model through only one extra parameter – the Early voltage, $V_A(V_{BC})$ (see Ref. [73] for details). The saturation current is then adjusted according to

$$I_S(V_{BC}) = I_S(0) \left[1 - \frac{V_{BC}}{V_A} \right] \quad (4.108)$$

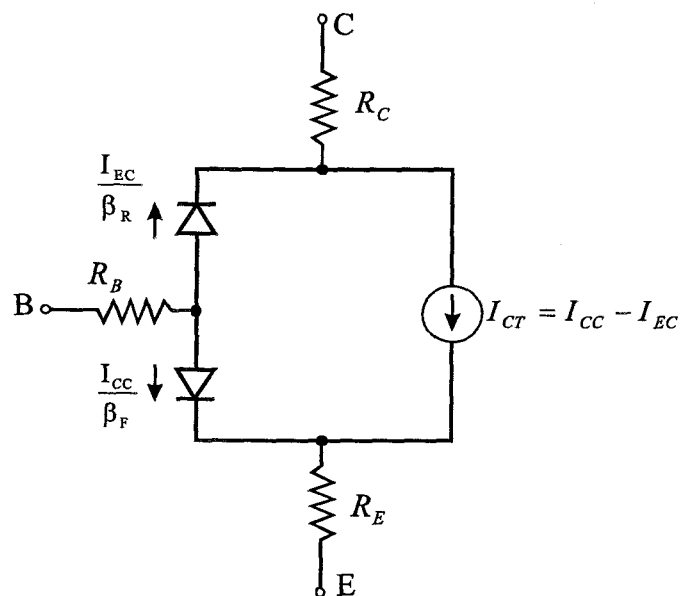


FIGURE 4.28. BJT Ebers-Moll static model implemented in SPICE.

To account for second order effects, e.g. low current and high level injection effects, the charge control model has been developed by Gummel and Poon. BJT

Gummel-Poon static model² implemented in SPICE is shown in Fig. 4.29. In addition to the two main BE and BC diodes present in the Ebers-Moll model, two more nonideal diodes are introduced to simulate possible leakage and recombination currents which may be dominant at the low voltages. The leakage/recombination diode equations are written as

$$I_{BC,leak} = C_4 I_S [e^{qV_{BC}/n_{CL}kT} - 1] \quad (4.109)$$

$$I_{BE,leak} = C_2 I_S [e^{qV_{BE}/n_{EL}kT} - 1] \quad (4.110)$$

The saturation current, I_S , is calculated as a function of the amount of charge stored in the device

$$I_S = \frac{I_{SS}}{q_B} \quad (4.111)$$

where the fundamental constant I_{SS} and normalized base charge q_B are given by

$$I_{SS} = \frac{qD_n n_i^2 A_E}{\int N_A(x) dx} \quad (4.112)$$

$$q_B = \frac{\int_{x_E}^{x_C} q A_E p(x) dx}{\int_{x_E}^{x_C} q A_E p_0(x) dx} \quad (4.113)$$

This representation includes the base width modulation and other high level injection effects. Putting the pieces together the collector and base current in the forward active mode are defined by the following equations

$$I_C = \frac{I_S}{q_B} e^{qV_{BE}/n_F kT} + \frac{I_S}{\beta_R} + C_4 I_S \quad (4.114)$$

$$I_B = \frac{I_S}{\beta_F} e^{qV_{BE}/n_F kT} - \frac{I_S}{\beta_R} + C_2 I_S [e^{qV_{BE}/n_{EL}kT} - 1] - C_4 I_S \quad (4.115)$$

²Due to its length and complexity the model is not described here in detail. Only some of the relevant equations are presented.

For $V_{BE} \gg kT/q$ the expressions can be simplified to

$$I_C = \frac{I_S}{q_B} e^{qV_{BE}/n_F kT} \quad (4.116)$$

$$I_B = \frac{I_S}{\beta_F} e^{qV_{BE}/n_F kT} + C_2 I_S e^{qV_{BE}/n_{EL} kT} \quad (4.117)$$

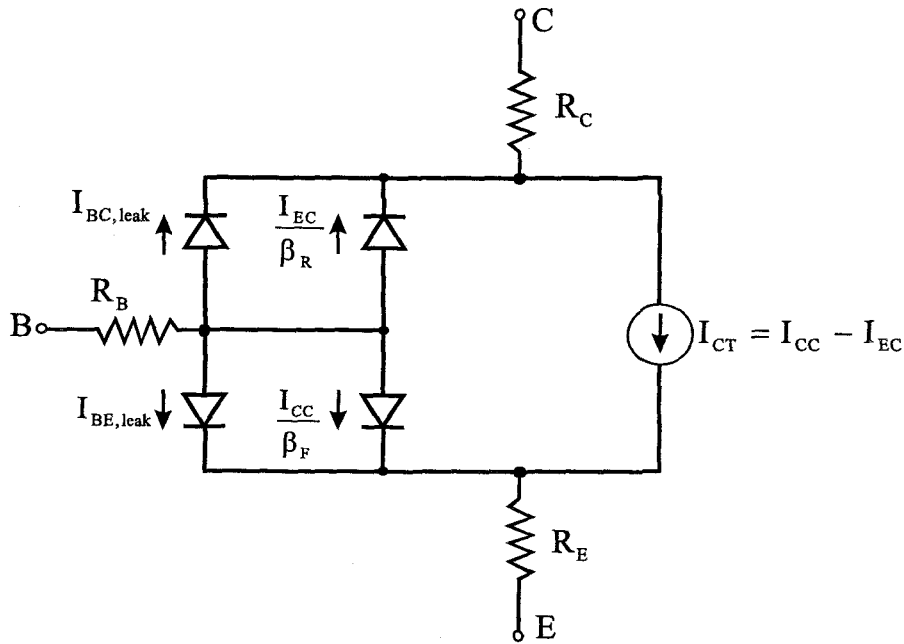


FIGURE 4.29. BJT Gummel-Poon static model implemented in SPICE.

We will now try to demonstrate that this BJT model can be successfully applied to simulate the forward Gummel plots for an SHBT, if its base recombination current has an ideality factor closer to 2 or if the device is operated below its “saturation point” (see later in the text). In the model, the collector current has a constant ideality factor of n_F and the saturation current I_S . The high level injection and series resistance effects are included through q_B and V_{BE} , respectively. The base current is represented by two components with different ideality

factors of n_F and n_{EL} and saturation currents $-I_S/\beta_F$ and $C_2 I_S$. Experimentally measured and calculated Gummel plots (device BAxM) are shown in Fig. 4.30.

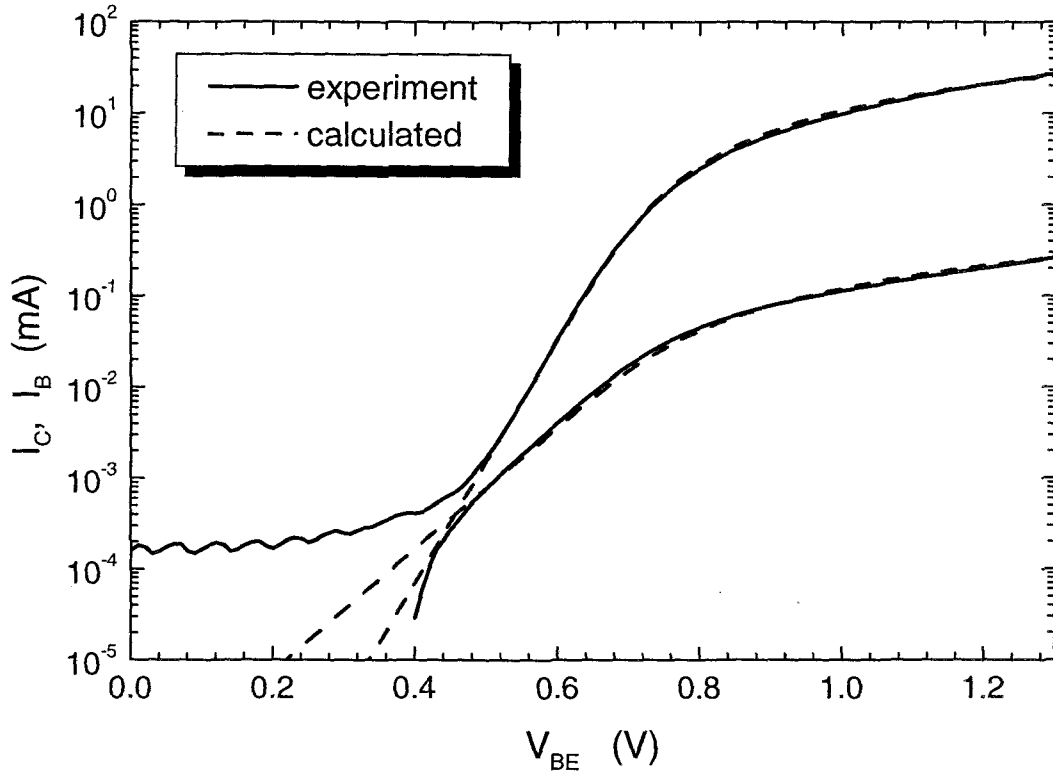


FIGURE 4.30. Experimental and calculated forward Gummel plots for device BAxM3.

4.5.1. Collector Current in Active Mode

As shown in Section 4.4.2 the collector current of an abrupt SHBT has voltage dependent ideality factor (see Fig. 4.18), which as a rule increases to 2 at high biases. This behavior is due to the physical nature of the electron transport

across the emitter-base heterojunction. In the Gummel-Poon BJT model similar results can be obtained by “inducing” high level injection effects. In other words, by setting the knee current I_{KL} (current at which high level injection becomes important) to some experimentally determined value, the Gummel-Poon calculations may be forced to give results similar to those of the HBT model. Additionally incorporating series resistance effects into the SPICE model allows to obtain very accurate fit of the experimentally measured collector currents (see Fig. 4.30).

4.5.2. Base Currents in Active Mode

In a BJT, the main component of the base current has the same ideality factor as the collector current. In an HBT this is not necessarily the same. Ideality factor of the base current (n_B) may depend on the layer doping, and configuration and distribution of traps. We consider three possible situations, when (1) $n_B > n_F$ for all biases, (2) the intermediate case, $n_B > n_F$ for low biases and $n_B \approx n_F$ for high biases, and, finally, (3) $n_B \approx n_F$ for all biases.

In the first case, the HBT base current can be modeled by the Gummel-Poon model, however some of the parameters have to be redefined. Using values of I_S and n_F corresponding to the given I_C we fit the base current with Eq. 4.117. The parameters in the fitting process are β_F , C_2 and n_{EL} . In this procedure β_F loses its meaning of forward gain – in order to reduce the contribution of the first term in Eq. 4.117 β_F becomes much higher than the actual current gain. For high n_B 's the second term in the expression for the base current dominates and n_{EL} approaches n_B . As shown in Fig. 4.30 by dashed line calculated I_B matches the experimental data very well for all biases.

As pointed out already, the contributions of the first and second term in Eq. 4.117 depend on the relative difference between n_F and n_B . At n_B 's slightly above n_F the current will be dominated by the second term at low biases and by the first term at the higher biases. For $n_B \approx n_F$, C_2 becomes very small and the base current reduces to only one term – the first term. Under these conditions β_F restores its original meaning of the forward current gain. Relatively good match with the experimental data can be achieved for low and moderate biases (see Fig. 4.31). Considerable discrepancy between the measured and calculated curves observed at high biases can be explained when the physical origin of the base current in HBTs is analyzed. In an HBT the base current is determined by recombination in the BE SCR and the base region, thus I_B is a function of a number of carriers injected into the base region. Therefore, when the injection efficiency saturates at high biases the base current should exhibit exactly the same behavior. In the Gummel-Poon model, Eq. 4.117 does not include any high level injection or other saturation effects. As a result calculated base current is significantly higher than that observed experimentally.

To summarize, the standard BJT Gummel-Poon SPICE model can be applied for the analysis/simulation of HBT operation in the forward active mode. Devices with the base current with ideality factor close to 2 can be simulated very accurately in the whole bias range, while for devices with $n_B \approx n_F$ the model provides adequate results only at low and moderate biases.

4.5.3. Saturation Mode Analysis

As a final point in our discussion of Gummel-Poon SPICE analysis of HBTs we show that the BJT model can also be used for simulation of HBTs in the

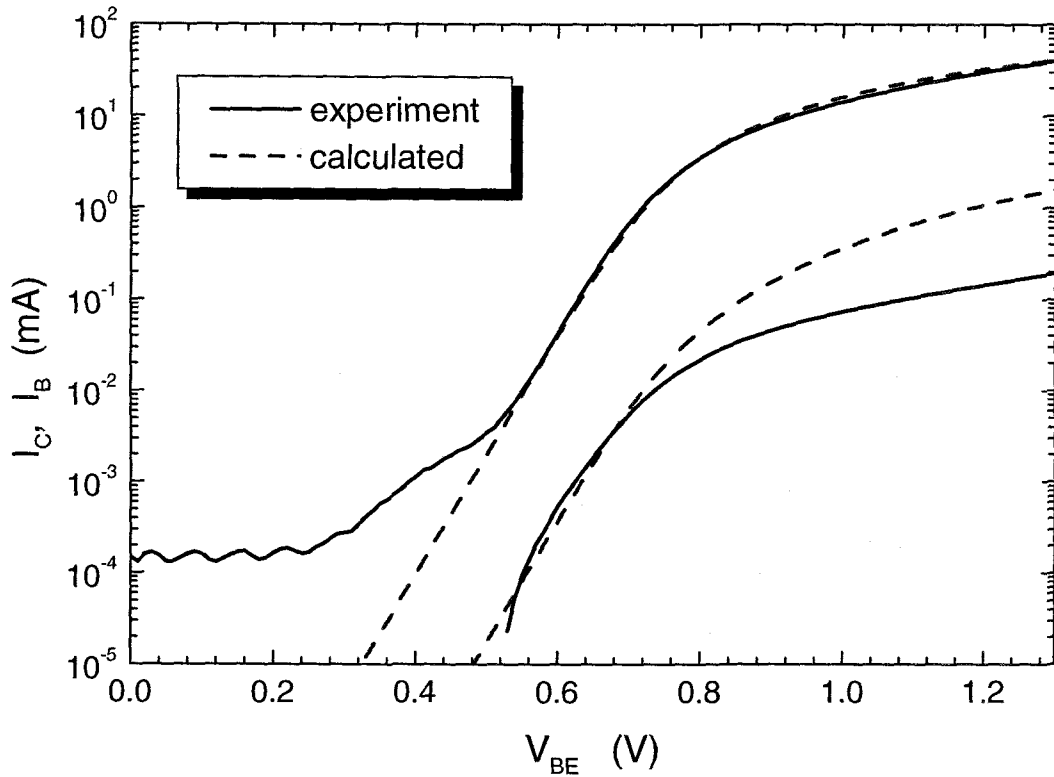


FIGURE 4.31. Experimental and calculated forward Gummel plots for device BAxM1.

saturation mode, in particular for modeling of the offset voltage, $V_{CE,off}$. First, the rest of the model parameters (β_R, n_R, C_4 , and n_{CL}) should be extracted by fitting the inverse Gummel plots of I_B with

$$I_C = I_B \approx \frac{I_S}{\beta_R} [e^{qV_{BC}/n_R kT} - 1] - C_4 I_S [e^{qV_{BC}/n_{CL} kT} - 1] \quad (4.118)$$

For the base collector homojunction (in case of an SHBT), the base current ideality factor is usually constant and no leakage currents are observed. Then relatively accurate analysis can be performed with one term only. Thus, we set C_4 equal to zero. Reverse current gain, β_R , is typically very small due to the spike in the

conduction band at the BE heterointerface. Also, the hole injection from the base into the collector dominates the base-collector current.

Having extracted all the parameters of the model we can calculate the collector and base current in the saturation mode

$$I_C = \frac{I_S}{q_B} [e^{qV_{BE}/n_F kT} - e^{qV_{BC}/n_R kT}] - \frac{I_S}{\beta_R} [e^{qV_{BC}/n_R kT} - 1] \quad (4.119)$$

$$-C_4 I_S [e^{qV_{BC}/n_{CL} kT} - 1]$$

$$I_B = \frac{I_S}{\beta_F} [e^{qV_{BE}/n_F kT} - 1] + \frac{I_S}{\beta_R} [e^{qV_{BC}/n_R kT} - 1] \quad (4.120)$$

$$+C_2 I_S [e^{qV_{BE}/n_{EL} kT} - 1] + C_4 I_S [e^{qV_{BC}/n_{CL} kT} - 1]$$

Since the accuracy of the parameters extracted from the forward Gummel plots may depend on the operating biases one has to exercise special care when using these equations. However, as long as the expressions are used at low current levels, they should always give reliable results. Fig. 4.32 demonstrates excellent match between the experimental and calculated $I_C - V_{CE}$ characteristics for five different devices (BAxM0, BAxM1, BAxM2, BAxM3 and BAxM4). The values of n_F , n_R , I_S , and $I_{SR} = I_S/\beta_R$ used in the calculations are listed in Table 4.3.

To conclude, we once again state that the Gummel-Poon BJT model can be employed for simulation of HBTs in different modes. It should be noted that some precautions should be taken to determine whether or not the model can provide adequate accuracy. As will be shown later some of the effects caused by irradiation can be quantified in terms of the standard model parameters, therefore providing first foundation for incorporating the effects of the radiation-induced degradation into device/circuit simulators.

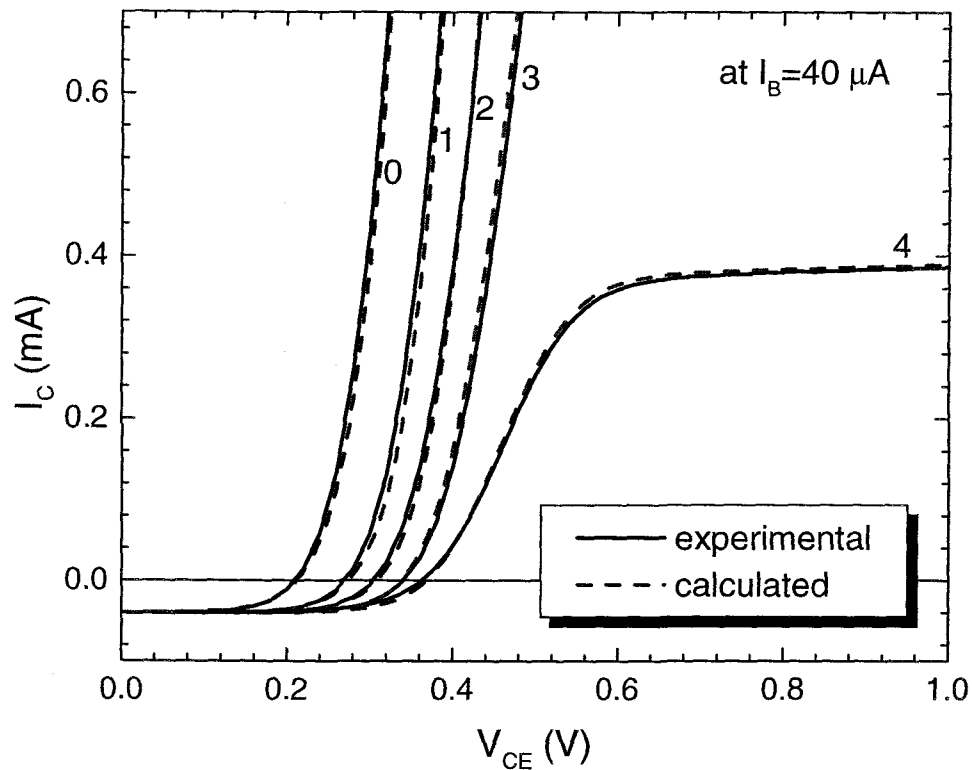


FIGURE 4.32. Experimental and calculated $I_C - V_{CE}$ characteristics for five different devices at $I_B = 40 \mu A$.

4.6. HBT High Frequency Performance

To complete this chapter we introduce several parameters and techniques used for the characterization of HBT performance in high frequency domain, which is very important for practical applications of HBTs.

Any transistor can be viewed as a two-port linear network schematically shown in Fig. 4.33a. A set of the so-called admittance (y), impedance (z), hybrid (h) or scattering (S) parameters can be used to describe such a network completely. Depending on particular applications different parameter sets are used. For exam-

Device	n_F	n_R	I_S (A)	I_{SR} (A)
BAxM0	1.3	1.3	5×10^{-13}	4×10^{-9}
BAxM1	1.3	1.4	5×10^{-13}	4×10^{-9}
BAxM2	1.3	1.4	5×10^{-13}	9×10^{-9}
BAxM3	1.3	1.4	2×10^{-13}	2×10^{-8}
BAxM4	1.3	1.4	1×10^{-13}	8×10^{-8}

TABLE 4.3. Gummel-Poon model parameters used to simulate $V_{CE,off}$ shift observed in different devices.

ple, for DC and low frequency (LF) analysis of BJTs and HBTs the admittance parameter set has proven to be particularly convenient and useful. The transistor terminal currents can be expressed in terms of terminal voltages in the following manner

$$I_1 = y_{11}V_1 + y_{12}V_2 \quad (4.121)$$

$$I_2 = y_{21}V_1 + y_{22}V_2 \quad (4.122)$$

Under DC conditions and in LF region all y parameters can be readily determined through simple measurements realizing open and short circuits at the ports, i.e.

$$y_{11} = \left. \frac{I_1}{V_1} \right|_{V_2=0}, \quad y_{12} = \left. \frac{I_1}{V_2} \right|_{V_1=0} \quad (4.123)$$

$$y_{21} = \left. \frac{I_2}{V_1} \right|_{V_2=0}, \quad y_{22} = \left. \frac{I_2}{V_2} \right|_{V_1=0} \quad (4.124)$$

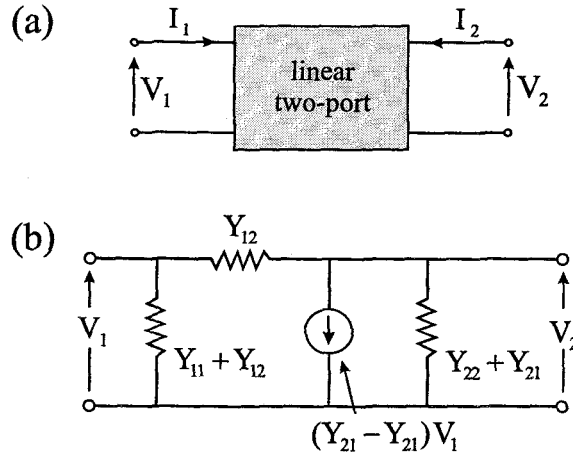


FIGURE 4.33. Two-port linear network representation of a transistor: (a) general case, (b) y -parameter model.

The y -parameter 2-port equivalent circuit for a bipolar transistor shown in Fig. 4.33b serves as a basis for the very popular hybrid- π small signal equivalent circuit. In hybrid- π schematic shown in Fig. 4.34 g_m , g_π and g_μ represent transconductance, input conductance and reverse feedback conductance, respectively, C_π and C_μ are capacitances of the BE and BC junctions respectively, and, finally, r_e , r_b and r_c are the parasitic emitter, base and collector resistances, respectively.

It should be noted that any of the parameter sets can be calculated from other parameter sets. For example, y and h parameters can be expressed in terms of the scattering coefficients using the following relations [96]

$$y_{11} = \frac{1}{Z_0} \frac{s_{12}s_{21} + (1 - s_{11})(1 + s_{22})}{(1 + s_{11})(1 + s_{22}) - s_{21}s_{12}} \quad (4.125)$$

$$y_{21} = \frac{1}{Z_0} \frac{-2s_{21}}{(1 + s_{11})(1 + s_{22}) - s_{21}s_{12}} \quad (4.126)$$

$$y_{12} = \frac{1}{Z_0} \frac{-2s_{12}}{(1 + s_{11})(1 + s_{22}) - s_{21}s_{12}} \quad (4.127)$$

$$y_{22} = \frac{1}{Z_0} \frac{s_{12}s_{21} + (1 + s_{11})(1 - s_{22})}{(1 + s_{11})(1 + s_{22}) - s_{21}s_{12}} \quad (4.128)$$

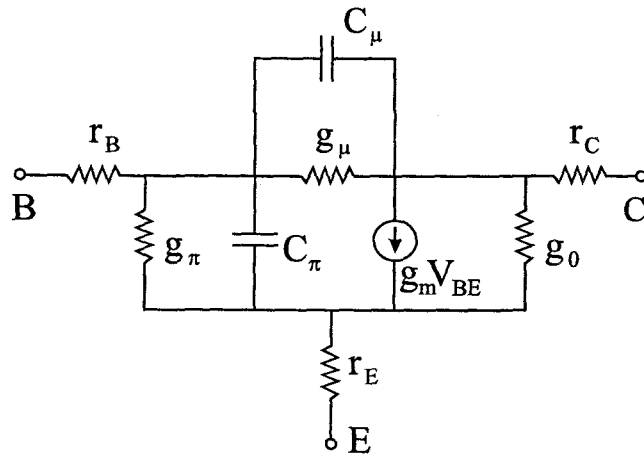


FIGURE 4.34. Hybrid-pi representation of a transistor.

and

$$h_{11} = Z_0 \frac{(1 + s_{11})(1 + s_{22}) - s_{21}s_{12}}{(1 - s_{11})(1 + s_{22}) + s_{21}s_{12}} \quad (4.129)$$

$$h_{21} = \frac{-2s_{21}}{(1 - s_{11})(1 + s_{22}) - s_{21}s_{12}} \quad (4.130)$$

$$h_{12} = \frac{2s_{12}}{(1 - s_{11})(1 + s_{22}) - s_{21}s_{12}} \quad (4.131)$$

$$h_{22} = \frac{1}{Z_0} \frac{(1 - s_{11})(1 - s_{22}) - s_{21}s_{12}}{(1 - s_{11})(1 + s_{22}) + s_{21}s_{12}} \quad (4.132)$$

y parameters are commonly used to calculate rf transistor characteristics, e.g. stability factor, maximum available power gain, noise figure, etc. From h parameters h_{21} is by far the most “famous” one as it refers to common-emitter short-circuit current gain $h_{FE} = I_C/I_B$.

In high frequency domain it is very difficult, if at all possible, to realize short and open circuits at the ports of the transistor network needed to determine the transconductance or impedance parameters. Besides, for RF analysis it is more convenient and meaningful to use wave formulation. In the two-port network shown in Fig. 4.35 incident and reflected voltage wave signals are represented by

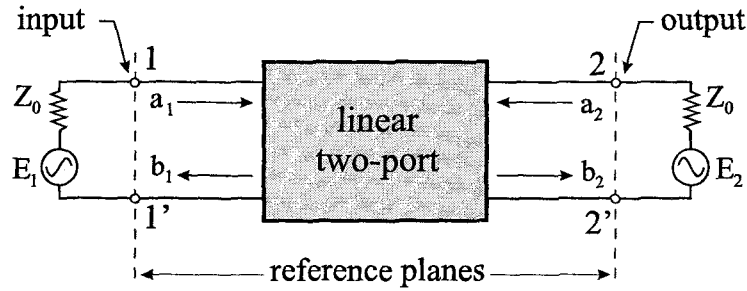


FIGURE 4.35. Two-port S-parameter definition schematic.

a_1 and b_1 , and a_2 and b_2 at the port 1 and 2, respectively. Mathematically,

$$a_i = \frac{V_i^{inc}}{\sqrt{Z_0}}, \quad b_i = \frac{V_i^{refl}}{\sqrt{Z_0}} \quad (4.133)$$

where Z_0 is the input and output network impedance, commonly made equal to $50\Omega + j \times 0$. Clearly, $|a_i|^2$ and $|b_i|^2$ are simply incoming and outgoing power at Port i . The scattering S-matrix is defined in the following manner:

$$\begin{bmatrix} b_1 \\ b_2 \end{bmatrix} = \begin{bmatrix} S_{11} & S_{12} \\ S_{21} & S_{22} \end{bmatrix} \begin{bmatrix} a_1 \\ a_2 \end{bmatrix} \quad (4.134)$$

For zero incident power at port 2 ($E_2 = 0$), $a_2 = 0$, and

$$S_{11} = \frac{b_1}{a_1} = \frac{\text{Reflected Voltage}}{\text{Incident Voltage}} = \text{Input Reflection Coefficient} \quad (4.135)$$

$$\begin{aligned} S_{21} &= \frac{b_2}{a_1} = \left[\frac{\text{Outgoing Output Power}}{\text{Incoming Input Power}} \right]^{1/2} \\ &= [\text{Forward Transducer Gain}]^{1/2} \end{aligned} \quad (4.136)$$

$$|S_{21}|^2 = G_{TF} \quad (4.137)$$

Similarly, at Port 2 for $E_1 = 0$ ($a_1 = 0$) S_{22} is found to be the output reflection coefficient and $|S_{12}|^2$ is the reverse transducer gain, G_{TR} . It should be noted that in most cases measurement systems read out the S-parameters in decibels. Then the following relation can be used to convert these results to the conventional form

$$|S_{ij}|_{db} = 10 \log |S_{ij}|^2 = 20 \log |S_{ij}| \quad (4.138)$$

Once a complete set of S-parameters is obtained, it can be used to calculate any other parameter set and to extract rf figures of the transistor.

An important figure of merit for a microwave transistor is the so-called cutoff frequency f_T . Usually defined as a frequency at which the common-emitter short-circuit current gain h_{FE} becomes unity, f_T can be estimated from the emitter-collector transit time τ_{EC}

$$f_T = \frac{1}{2\pi\tau_{EC}} \quad (4.139)$$

τ_{EC} can be divided into separate components associated with charging/transit delays of emitter SCR, base, SCR and bulk of collector. Therefore, for a good device, it is critical to minimize the capacitances of the BE and BC junctions, and reduce the base and collector layer thickness. Also, to reduce the charging times, the transistor should be operated at higher current levels. As a consequence, transistors with higher current gains (h_{fe}) would have higher cutoff frequencies. It should be noted that adjusting the structure parameters (layer doping, thickness, etc.) to improve, for example, gain of the device may increase the capacitances or cause reliability problems. Therefore, when optimizing a transistor, some tradeoffs are typically made to achieve optimum performance required for a specific application.

Another figure of merit for a bipolar transistor is the so-called maximum available power gain G_{MA} obtained by matching both the input and output port networks

$$G_{MA} = \frac{|y_{21}/y_{12}|}{K + \sqrt{K^2 - 1}} \quad (4.140)$$

with the stability factor K

$$K = \frac{2\text{Re}(y_{11})\text{Re}(y_{22}) - \text{Re}(y_{12}y_{21})}{|y_{12}y_{21}|} \quad (4.141)$$

The maximum frequency of oscillation f_{max} is the frequency at which the maximum available power gain reaches unity. f_{max} can be calculated from the transition

frequency using the following relation [66]

$$f_{max} = \sqrt{\frac{f_t}{8\pi r_b C_\mu}} \quad (4.142)$$

Hence minimized base resistance and base-collector capacitance result in better performance devices in terms of f_{max} .

Minimum noise figure NF_{min} of a transistor can be estimated through a noise SPICE model from measured y -parameters. In the model derived by Voinigescu *et al.* [97] the emitter and base thermal noise, and base and collector shot noises generate

$$NF_{min} = 10 \log \left[1 + \frac{qI_C}{kT|y_{21}|^2} [\text{Re}(y_{11}) + A] \right] \quad (4.143)$$

$$A = \sqrt{\left[1 + \frac{2kT|y_{21}|^2 r_{BE}}{qI_C} \right] \left[|y_{11}|^2 + \frac{I_B|y_{21}|^2}{I_C} \right] - \text{Im}^2(y_{11})} \quad (4.144)$$

4.7. Summary

An empirical approach to HBT modeling has proven to be very useful and relatively accurate in some cases. Very easy to use it is often employed when estimating the values of series resistances, saturation currents and ideality factors of a transistor for the subsequent SPICE modeling. The empirical model can not, however, be correlated with the structure of an HBT and does not provide adequate physical representation of the device operation. More complex physical model developed for an abrupt SHBT is used to gain better understanding of the carrier transport in the transistor. Furthermore, irradiation effects can be superimposed onto the model to simulate the radiation-induced device degradation/failures and vice versa. Finally, commercially available BJT SPICE models can provide satisfactory accuracy when applied to HBTs. Special care, however, should be exercised

as some of the SPICE model parameters have to be redefined and lose their original meaning in such an analysis.

5. HBT FABRICATION

In course of this work the radiation-induced degradation of III-V materials and devices was studied on the devices developed and fabricated in the clean room facility of Department of Electrical and Computer Engineering at OSU. For the in-house manufacturing the complete mask set containing different geometry HBTs, test and calibration structures was designed and fabricated. MOCVD-grown heterostructures were used as a starting material in the fabrication. Several complete process sequences were developed and all individual process steps standardized. This chapter is to briefly present all the phases of the development and fabrication.

5.1. SHBT Heterostructure Growth

InP/InGaAs HBT heterostructures were grown by metal-organic chemical vapor deposition (MOCVD) at the Lucent Technologies Crawford Hill Laboratory. The schematic diagram of a typical SHBT structure is shown in Fig. 5.1 with the layer parameters listed in Table 5.1 [98]. Starting from the bottom of the structure, the first layer deposited on the semi insulating *InP : Fe* substrate is the n-type heavily doped *InP* subcollector. This choice of the material allows one to utilize the convenience of selective wet etching when exposing subcollector contact layer during HBT fabrication. Heavy doping is necessary for formation of low resistance ohmic contacts. On top of the subcollector thick *InGaAs* collector layer is deposited. In SHBT structures, collector material is the same as that of the base region to avoid a notch in the conduction band at the collector-base interface. This notch occurring at the *InP/InGaAs* heterointerfaces may lead to reflection of the emitter-injected electron current back into the base. To further improve

the device performance the collector layer is usually grown either undoped or with very low doping (10^{16} cm^{-3}).

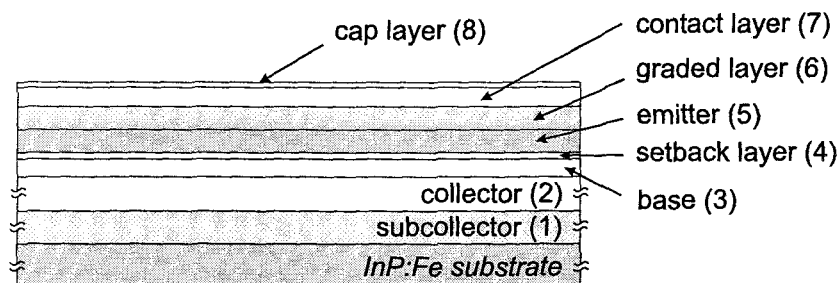


FIGURE 5.1. Qualitative cross-section of *InP/InGaAs* polyimide-passivated SHBT.

Following the collector a thin base layer is formed. The overall quality of the base region is crucial to the device performance as it determines minority carrier lifetime and therefore the gain of the device. Also, extremely high doping, required for good RF performance, leads to a problem of dopant outdiffusion into the emitter region, which may result in shifting of p-n junction away from the heterointerface into the emitter layer. Very thin (100 \AA) lightly doped *InGaAs* spacer at the base-emitter interface can act as an effective shield preventing further redistribution of the base dopants. Furthermore, this so-called base setback layer is also found to significantly reduce the spike in the conduction band at the heterointerface, therefore greatly increasing emitter injection efficiency. Quality of the *InP* wide band gap emitter is also vitally important as the recombination current of the heterointerface and the space charge region are one of the major HBT parasitic currents. Most of the depletion region will be on the emitter side since the emitter doping is much lighter than that of the base. The transition to the very heavily

doped *InGaAs* emitter contact layer is smoothed out by means of the *InGaAs* – *InP* graded layer. Finally, the structure is protected with a thin *InP* emitter cap layer.

Layer	Material	Dopant	N_A/N_D (cm^{-3})	Thickness(\AA)
Emitter Cap	<i>InP</i>	–		100
Emitter Contact	<i>InGaAs</i>	n^+ <i>Si</i>	2×10^{19}	500
Emitter Grading	<i>InGaAs</i> \rightarrow <i>InP</i>	n^+ <i>Si</i>	5×10^{18}	750
Emitter	<i>InP</i>	n <i>Si</i>	5×10^{17}	750
Base Setback	<i>InGaAs</i>	n^-	–	50
Base	<i>InGaAs</i>	p^+ <i>Zn</i>	2×10^{19}	500
Collector	<i>InGaAs</i>	n^-	–	5000
Subcollector	<i>InP</i>	n^+ <i>Si</i>	8×10^{18}	5000
SI Substrate	<i>InP</i>	SI <i>Fe</i>	–	–

TABLE 5.1. MOCVD grown HBT heterostructure parameters (wafer I3420).

Structures I3257 and I3377, also used for HBT fabrication, differ from I3240 by collector thickness only. The collector thickness is 1 μm and 0.7 μm for I3257 and I3377, respectively.

5.2. Mask Set Design

As technology continuously advances critical device dimensions shrink and new effects emerge. One of the recently appeared important issues is the surface

recombination currents in bipolar transistors. In the large devices the bulk components of the recombination current were dominant leaving the surface effects unnoticeable. However, considerable reduction of emitter size and base thickness resulted in the situation when the bulk recombination currents can be pretty much neglected when compared to the magnitudes of the surface components. Furthermore, in HBTs, where III-V compound materials with the very high surface recombination velocities are normally used, one can claim that the magnitude of this particular effect in a large extent determines the performance of the device.

In III-V systems, it still remains a not well studied question how the surface and heterojunction components of the recombination current degrade when the device is irradiated with different types of radiation. The mask set used in this work was designed with the intent of studying these problems as well as operation and radiation degradation of high frequency HBTs. Some additional features were incorporated in the design to allow fabrication of the structures necessary for testing at the intermediate steps in the fabrication, structures for calibration of the high frequency equipment, and, finally, the structures which can be used for the sample characterization. The details of the mask design are covered in the following subsections.

There are seven masking steps in the HBT fabrication sequence. The order in which they are used varies slightly for the different material systems. The following description corresponds to the *AlGaAs/GaAs* HBT fabrication procedure (for *InP/InGaAs* see Section 5.4) using the lift-off technique for patterning of metallization layers:

1. **Isolation mesa** bright field mask is used to protect the device regions while the rest of the sample surface is etched down to the semi-insulating substrate.

2. **Collector mesa** bright field mask is to protect the emitter and base regions of the devices when wet etch is used to reach the subcollector layer.
3. **Emitter and collector contact** dark field mask is designed to pattern the sample to form emitter and collector contacts.
4. **Base mesa** bright field mask is used to protect the emitter layer when wet etch is performed to expose the base mesa.
5. **Base contact** dark field mask is used to pattern the sample to form the base metal contacts.
6. **Contact window** dark field mask is to define vias in the passivation layer. Through these vias the final metallization layer should connect to the emitter, base and collector contacts.
7. **Contact pad** dark field mask is used to form large contact pads connected to the device terminals.

5.2.1. DC HBT Unit Cells

There are two DC HBT unit cells on the mask, each containing 8 devices. For identification purposes the devices are marked with symbols – letters *J* through *Y*. An example of the layout for the single DC HBT (ID *W*) with all masking layers shown is depicted in Fig. 5.2. The dimensions of base ($85 \times 70 \mu m^2$) and collector ($125 \times 90 \mu m^2$) mesas are the same for all the devices. The probing contact pads are also of the standard size of $100 \times 100 \mu m^2$ and are equally spaced with the gaps of $100 \mu m$. Base and collector metal contacts and corresponding to them windows in the passivation layer are of the same geometry for all the devices.

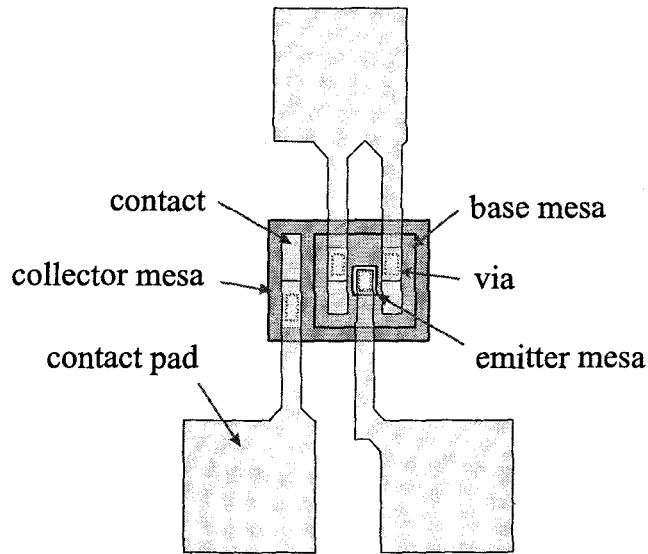


FIGURE 5.2. Layout of DC HBT showing different layers of the mask.

In the first unit cell (devices $J - Q$) all HBTs have emitters of the same perimeter of $130 \mu m$ and the area varying from 510 to $1056 \mu m^2$. The second unit cell (devices $R - Y$) consists of devices with the emitter area of $395 \mu m^2$ and perimeter ranging from 80 to $120 \mu m$. The complete list of the devices showing their IDs, perimeter, area and perimeter-to-area ratios is provided in Table 5.2. Studying operation and radiation degradation of these devices one can separate the surface and bulk effects and gain some understanding of the recombination and degradation mechanisms involved.

Fig. 5.3 shows the layout of the 16 HBT in the unit cells and the unit cell dimensions. The alignment marks shown in the diagram will be discussed in Section 5.2.4.

Device Name	Device ID	Area ($A, \mu m^2$)	Perimeter ($P, \mu m$)	P/A Ratio (μm^{-1})
HBT#1	J	510	124	0.255
HBT#2	K	750	130	0.173
HBT#3	L	900	130	0.144
HBT#4	M	1056	130	0.123
HBT#5	N	900	130	0.144
HBT#6	O	1056	130	0.123
HBT#7	P	900	130	0.144
HBT#8	Q	1056	130	0.123
HBT#9	R	395	120	0.304
HBT#10	S	396	102	0.256
HBT#11	T	393	88	0.223
HBT#12	V	396	80	0.202
HBT#13	U	393	88	0.223
HBT#14	W	396	80	0.202
HBT#15	X	393	88	0.223
HBT#16	Y	396	80	0.202

TABLE 5.2. Emitter perimeters, areas and perimeter-to-area ratios for the devices in DC HBT unit cells.

5.2.2. RF HBT and RF Calibration Structures Unit Cells

High frequency HBT unit cell contains three devices, whose layout is similar to the DC HBTs except that there are two contact pads associated with the emitter contact. This configuration, shown in Fig. 5.4 on the example of RF HBT #1, is necessary for the high frequency measurements. Table 5.3 lists RF and large

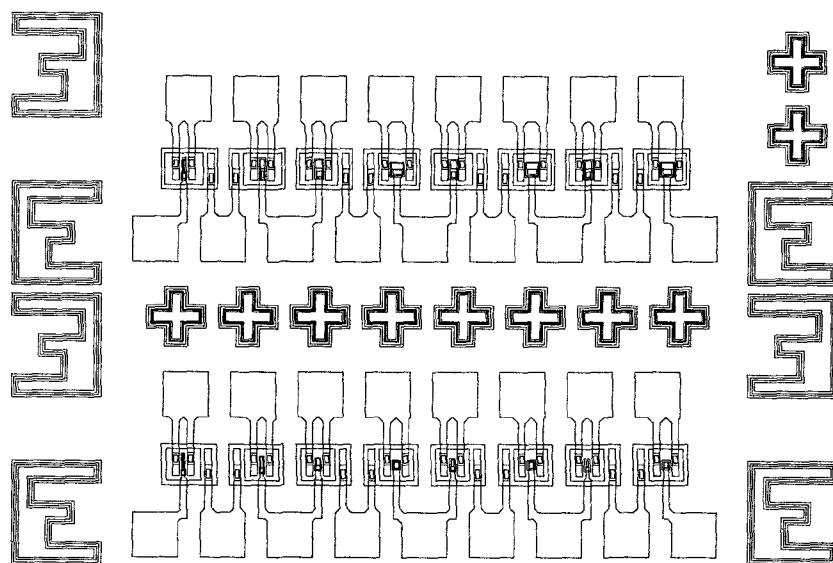


FIGURE 5.3. Mask layout of DC HBT unit cells.

area test (see the next section) device dimensions. For the equipment calibration purpose the RF calibration structures are also included in the design (see Fig 5.5).

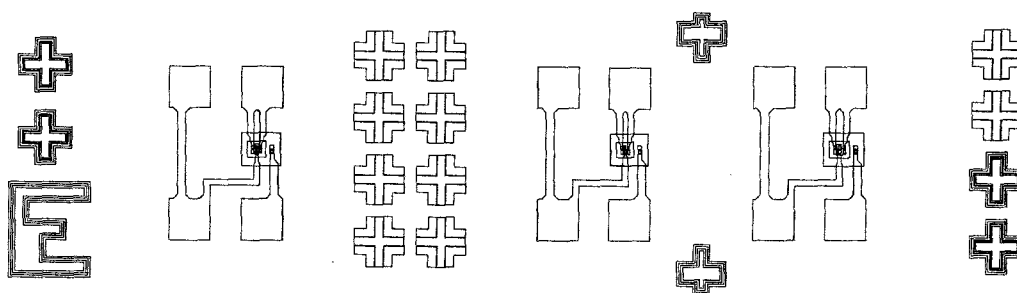


FIGURE 5.4. Mask layout of RF HBT unit cell.

Device Name	Device ID	Area ($A, \mu m^2$)	Perimeter ($P, \mu m$)	P/A Ratio (μm^{-1})
HFHBT#1	1	253	73	3.46
HFHBT#2	2	152.5	61	2.5
HFHBT#3	3	350	82	4.27
THBT#1	I	2604	208	12.52
THBT#2	H	1358.5	167.5	8.11
THBT#3	G	2604	208	12.52
THBT#4	F	1358.5	167.5	8.11

TABLE 5.3. Emitter perimeters, areas and perimeter-to-area ratios for the RF and test HBTs.

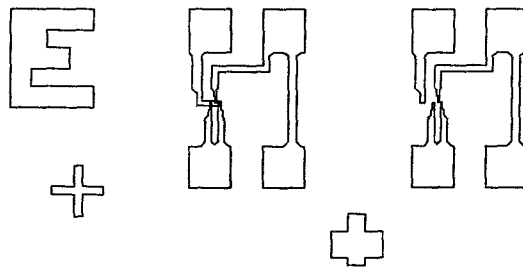


FIGURE 5.5. RF structures for calibration of RF vector network analyzer.

5.2.3. Test Structures

Due to complexity of the fabrication procedure it is often convenient or even necessary to test the wafer status at the intermediate processing steps. In the stage of the process development and standardization it is also sometimes necessary to

be able to fabricate the devices relatively quickly. Furthermore, one may want to study the individual layers of the transistor structure. Keeping this in mind the several test structures were added to the mask design.

Emitter, base and collector transmission line models (TLMs) were incorporated for testing the corresponding layer sheet resistance and for calibration of the different etch processes. Included large area base-emitter (BE) and base-collector (BC) diodes can be used for etch process calibration and for determining the doping depth profiles in all three active layers of the transistor. And, finally, large area HBTs can be used for the tests prior to the device passivation sequence. It should also be noted here that all these devices are relatively insensitive to the alignment errors as they are considerably larger than the other HBTs. Fig. 5.6 shows the arrangement of the test devices in the unit cell. Test HBT emitter dimensions are listed in the Table 5.3.

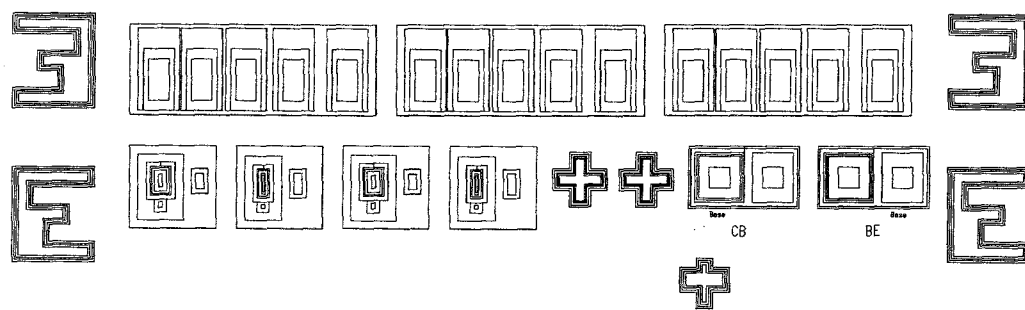


FIGURE 5.6. Mask layout of the unit cell with the test structures.

5.2.4. Alignment Marks

Starting from the second mask level, it is vitally important to precisely align all the subsequent mask patterns with respect to the preceding layers. For this purpose the number of specially designed alignment marks is included in all mask levels. Four types of the alignment marks used are shown in Fig. 5.7. Very large writing – the mask level name and number (a) – is located on top of the layout and is used for the rough initial alignment. Cross (b) and E-shaped (c) marks present on all seven levels are distributed over the entire mask and serve as a main tool in the alignment routine. The marks' size being a very important parameter is determined from the polarity of the level (bright or dark field) and the precision needed. In bright (dark) field masks the marks are made smaller (bigger) than the corresponding marks on the preceding level. The fourth type of marks (d) are put only on the pairs of adjacent levels (2 and 3, 3 and 4, etc.). As a result they are not distorted by the landscape created by all the earlier patterning and allow one to perform alignment more precisely.

5.2.5. DIE Layout. Mask Plates

Test device, RF HBT, DC HBT and calibration structure cells put together form a unit cell shown in Fig. 5.8. Then nine unit cells are combined to form a complete 18×18 mm level shown in Fig. 5.9 (the first level shown in this example). In addition to the HBT mask, a mask for fabrication of large area

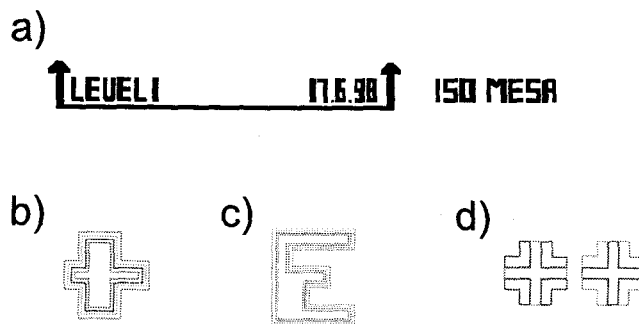


FIGURE 5.7. Alignment marks used in the mask layout.

diodes was designed. Two levels of the mask were laid next to each other, as shown in Fig. 5.10, to form a cell of the size of the HBT DIE.

Finally, eight mask levels (seven HBT levels and one large area diode level) were placed on two 2.5×2.5 inch plates leaving a 0.5 inch wide border all along the edges (see Fig. 5.11). The sets of both polarities were chrome-printed on the glass plates at HTA Photomask Inc.

5.3. Processing Steps

In this section individual processes used in the HBT fabrication sequence are discussed. The detailed recipes, recommendations for use and possible limitations are presented.

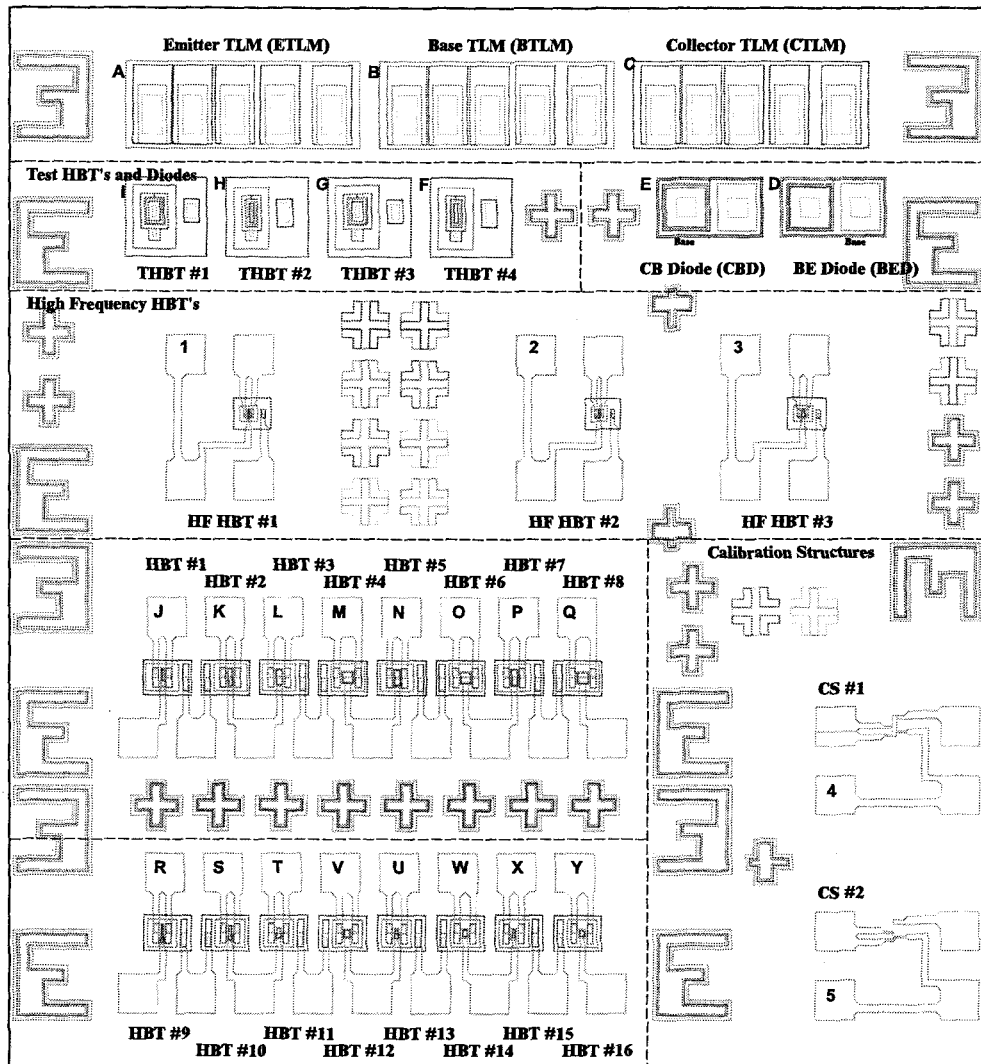


FIGURE 5.8. Mask layout of the entire unit cell for HBT fabrication.

5.3.1. Cleaning

One of the most commonly used cleaning procedures involves cleaning of the sample by Acetone, followed by a Methanol bath and Deionized water rinse. This sequence is usually called AMD clean and is used at all intermediate processing

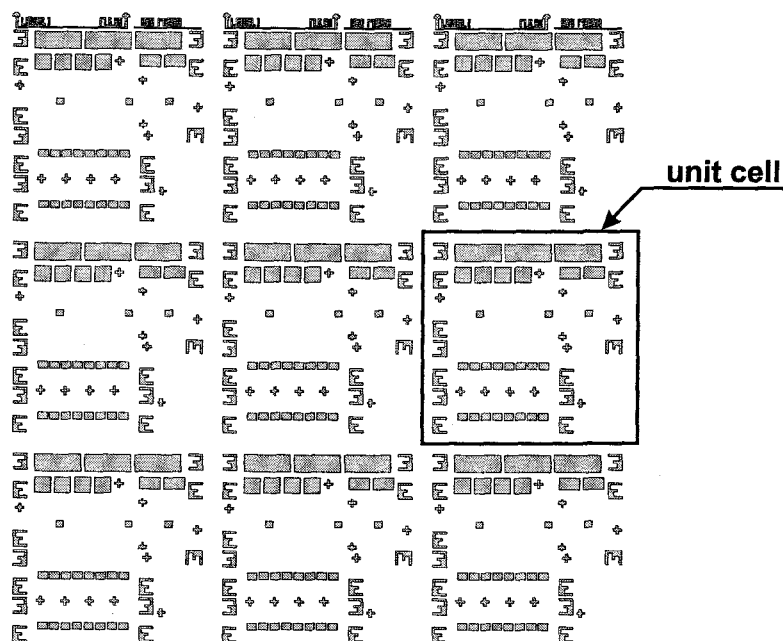


FIGURE 5.9. Level #1 of the mask (includes nine unit cells).

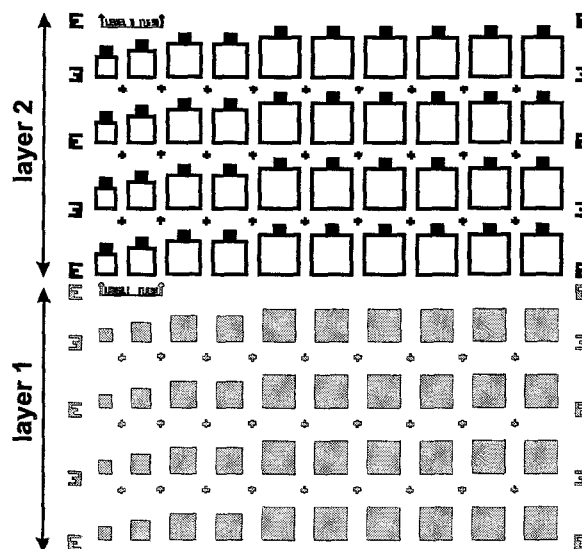


FIGURE 5.10. Two layers of mask layout for diode fabrication.

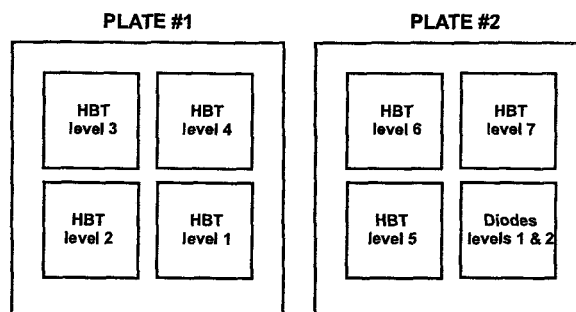


FIGURE 5.11. Plates 1 and 2 with the eight levels of mask layout.

steps in attempt to remove organic and inorganic contaminants. AMD is also employed to remove photoresist layers left after patterning steps. After the AMD clean samples are thoroughly blown-dry with a nitrogen gun.

5.3.2. Photolithography

Positive photoresist¹ is spin-coated onto AMD cleaned sample typically at 4000 *rpm* for 40 seconds. The sample is then soft-baked for at least 10 minutes at about 85°C. This is followed by the pattern printing for which Canon FPA-120 mask aligner is used. The exposed photoresist is then developed by soaking the sample in a developer solution² for about 45 seconds. Finally, if the next processing

¹Shipley Microposit 1818

²Shipley Microposit MF-321

step is wet or RIE etch the sample is hard-baked for at least 10 minutes at about 110°C . Long or “aggressive” etches may require prolonged hard-baking.

5.3.3. Wet Etches

There are several materials that may have to be etched in the fabrication sequence, these include *InP*, *InP : InGaAs*, *InGaAs*, *SiO₂*, *Au* and *Ti*. Wet etching of *InP* is usually accomplished with hydrochloric acid solutions, e.g. *HCl* + *H₂O*, that do not attack *InGaAs*. The etch rates, of course, depend on the *HCl* concentration, but are, in general, very high, e.g., around few thousand angstroms per minute for 5% solution. This however does not present a problem, since the etching is highly selective.

A freshly prepared mixture of a citric acid solution and fresh hydrogen peroxide (*Citric Acid* : *H₂O₂* = 1 : 1) (*CAHO*) is used to selectively etch *InGaAs* at the rates of about 1000 Å/min [99]. The citric acid solution is prepared by mixing 30 g of anhydrous citric acid with 100 ml of *H₂O*.

The graded emitter layer – *InP : InGaAs* – can be readily removed by freshly mixed hydrochloric and phosphoric acids, *HCl* : *H₃PO₄* = 1 : 1. As *H₃PO₄* attacks (although very slowly) the underlying thin base setback and base layers, one has to be very careful in order to not to etch them away. Estimated etch rate for the *InP : InGaAs* graded layer is about 200 Å/sec.

As one may note *InP* and *InGaAs* are of noticeably different colors. While *InGaAs* is a light grey-yellow material, *InP* has a much darker appearance with a hint of violet color. Because of this color difference one can readily see what layer is reached, when performing mesa etches. Table 5.4 gives a summary of wet etching chemicals and etch times used to define the device mesas.

Layer	Material	Etchant	Duration (sec)
Emitter Cap	<i>InP</i>	diluted <i>HCl</i>	7
Emitter <i>InGaAs</i>	<i>InGaAs</i>	"CAHO"	35-40
Emitter <i>InP</i>	<i>InP</i>	<i>HCl</i> : <i>H₃PO₄</i>	9
Collector	<i>InGaAs</i>	"CAHO"	300
Subcollector	<i>InP</i>	<i>HCl</i> : <i>H₃PO₄</i>	10

TABLE 5.4. Typical wet etch mixtures and etch times used to remove layers of HBT heterostructure (wafer I3420).

Silicon dioxide used as a passivation layer can be removed by a soak in a buffered *HF* solution. The solution is prepared by dissolving 40 g of ammonium fluoride in a mixture of 100 cc of *H₂O* and 10 cc of *HF*. The etch rates, in general, depend strongly on the oxide quality. For the high quality thermally-grown oxides the solution is expected to etch at about 1000 Å/min. The lower quality PECVD oxides are typically etched two times faster.

Metallization layers can be patterned by either lift-off or wet etch techniques. Gold is removed by a solution prepared by dissolving 10 g of iodine and 20 g of potassium iodide in 100 ml of deionized water. Titanium layer is etched by a mixture of $H_2O : H_2O_2 : HF = 20 : 1 : 1$ at a rate of about 8800 Å/min. The end point for the etches can be determined from the visual appearance of the samples – the colors change as the layers get etched away.

In most cases wet etching seems to be a convenient, easy-to-use, and relatively reliable and reproducible method. However due to its isotropic nature it always produces significant mask undercutting and therefore can not be used for etching of the patterns with a small feature size (less than a few microns). Instead anisotropic dry etch techniques have to be employed. Reactive Ion Etch (RIE) – one of the most popular methods used in the research applications and industry – is very effective and can be used for selective etches of III-V compounds, metals, and all of the dielectrics used for the device passivation. In course of this work RIE was used for the etching of the contact windows in the passivation layers.

5.3.4. Passivation Techniques

It is very critical to minimize the sample exposure to the atmosphere. Small amounts of water vapor and other contaminants may result in large recombination currents at the emitter-base periphery dramatically affecting the device performance. Therefore it is vitally important to complete all the steps as soon as

possible and then immediately passivate the surface with a film of dielectric. Apart from providing physical and chemical protection of the surface, this layer also isolates the device structure from the final metallization lines running from the device contacts to large probing/bonding pads.

A number of passivation schemes was explored in the course of this work. Most of the devices were fabricated using polyimide passivation developed by Sarkar [100]. Also, cyclotene, silicon nitride, oxide, and oxynitride schemes were investigated as potential passivation materials to be used in the fabrication.

It should be noted that the polyimide passivation procedure used in this work and briefly described herein differs slightly from the original one [100]. A sample after AMD cleaning is baked for 10 minutes and then spin-coated with polyimide at 7000 *rpm* for 40 *sec*. The sample is then baked in the several steps: at 75°C for 10 minutes, at 90°C for 10 minutes, at 120°C for 10 minutes, at 150°C for 20 minutes, and, finally, at 220°C for 30 minutes. Then photolithography routine is carried out in a standard manner, except that after the pattern developing the photoresist is hard baked at 110°C for 25-30 minutes. Contact windows are etched by means of RIE, followed by AMD cleaning of the sample.

Cyclotene passivation is analogous to the polyimide passivation sequence. The sample is cleaned, soft-baked and spin-coated with bcb at 6000 *rpm* for 40 *sec*. One step baking is performed in an *oxygen free* atmosphere at 300°C for 3 minutes.

Then photolithography, RIE and AMD clean are used to complete this processing phase.

Plasma Enhanced Chemical Vapor Deposition (PECVD) process recipes were developed to deposit silicon nitride, oxide and oxynitride used as the passivation layer in the HBT fabrication. Typical process parameters and deposited film characteristics (thickness, refraction index, maximum thickness variation across the sample) are shown in Table 5.5. The rest of the passivation process is similar to the polyimide passivation sequence.

5.3.5. Reactive Ion Etching

Reactive Ion Etching (RIE) is commonly used for etching of the small vias in the passivation films. The operating pressure, power density, duration, gas composition and flow rates are the main variables in this process. The chamber pressure and power density are generally kept low to make the etch more anisotropic, decreasing undercutting. Specific choice of values for the rest of the parameters is dictated by the chemistry of material being etched and etch rates desired. The detailed recipes for RIE etching of polyimide, cyclotene, silicon nitride and silicon dioxide are provided in Table 5.6. In each case, however, the etch time had to be adjusted as the passivation layer thickness and quality tend to vary slightly from one sample to another. It should also be noted that the protective photoresist

Process Parameter	Si_3N_4	SiO_2	Si Oxynitride
Power (%)	14	14	14
Pressure (<i>mTorr</i>)	700	700	700
Temperature ($^{\circ}C$)	350	300	350
SiH_4 flow (%)	15	17	22
SiH_4 flow (sccm)	75	85	110
N_2O flow (%)	–	10	3.7
N_2O flow (sccm)	–	10	3.7
N_2 flow (%)	50	–	5.3
N_2 flow (sccm)	250	–	26.5
Time (<i>min</i>)	30	30	30
Thickness (\AA)	2450	2200	2950
Variation (\AA)	50	140	70
Refraction index	2.0	1.5	1.65

TABLE 5.5. Typical PECVD process parameters used for deposition of silicon nitride, dioxide and oxynitride.

layer may get damaged at the powers above 170 *W*; as a result the subsequent acetone soak fails to dissolve the photoresist.

5.3.6. Metallization

In the vast majority of depositions the lift-off technique was used to pattern the metal layer. First, the photolithography step is performed to expose the desired regions of the sample surface. The overhanging profile of the photoresist

Process Parameter	Polyimide	Cyclotene	Si_3N_4	SiO_2
RF Power (W)	75	75	100	125
Pressure($mTorr$)	200	200	30	50
O_2 flow ($sccm$)	5	5	—	—
CHF_3 flow ($sccm$)	—	1.3	4.0	—
CF_4/O_2 flow ($sccm$)	—	—	—	5.0
Rate ($\text{\AA}/min$)	560	1400	330	420

TABLE 5.6. RIE process parameters used for etching of polyimide, cyclotene, silicon nitride and silicon dioxide.

is achieved by soaking the exposed sample in a chlorobenzene for 5 minutes. The sample is then *scrupulously* blow-dried with nitrogen and developed for 3 minutes. The chlorobenzene soak hardens the top layer of the photoresist reducing its development rate. This, in turn, causes the developer to undercut the photoresist structure leaving overhanging edge profiles shown in Fig. 5.12a. Developed sample is thoroughly rinsed in DI water and subjected to a 5 second clean-etch in the $InGaAs$ etching solution. It is then rinsed again, blow-dried with a nitrogen gun and mounted on a glass slide. After the thermal deposition (Fig. 5.12b) the sample is soaked in acetone, which dissolves the photoresist, thus lifting off the overlying metal layer. Regions, where metal was in contact with the sample's surface, remain unaffected by the acetone soak as shown in Fig. 5.12c.

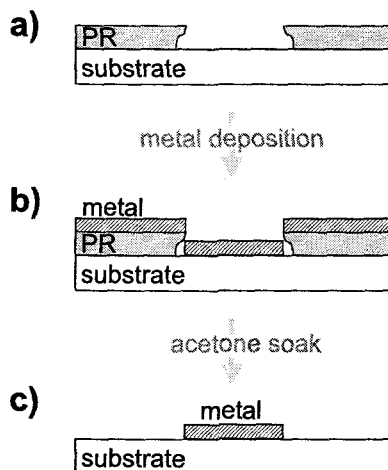


FIGURE 5.12. Metal patterning by lift-off with chlorobenzene soak.

Alternative to the lift-off process there is a more industry-standard metalization sequence. To begin, the sample is cleaned and the blanket metallization is carried out. On the next step the photolithography is used to pattern the sample (note that, in contrast to the lift-off technique, the bright field mask has to be used here) and then wet etch is performed to remove the metal film from the unprotected regions of the surface.

VEECO thermal evaporation system typically operated in 10^{-6} Torr pressure range was used for all the depositions. Titanium, nickel, aluminum and palladium were evaporated from tungsten wire baskets, while molybdenum boats were used for gold. The deposition rate and film thickness was monitored via quartz crystal monitor through a Maxtek TM-100 thickness meter. A number of metalization schemes was tested (see Section 6.3.3), however, only $Ti - Au$, $Pd - Au$ and $AuGe - Au$ films were used for the HBT fabrication. In the first system, which

initially was the only one used, thin (about $100 - 150 \text{ \AA}$) layer of titanium is used as an adhesion promoter for the subsequently deposited thick (typically 1200 \AA) film of gold. Somewhat difficult to control thermal evaporation of titanium leading to poor repeatability, its relatively high resistivity and radiation reliability problems do not speak in favor of this scheme. The $Pd - Au$ films consist of 700 \AA thick layer of palladium topped with 700 \AA of gold. Although these films exhibit mediocre adhesion, they have considerably lower resistivity and do not show any signs of radiation degradation. Due to their poor adhesion $Pd - Au$ layers often can not withstand thermal and mechanical stress introduced by CVD deposition of oxide or nitride passivation layers. Finally, $AuGe - Au$ annealed system can be used to form low resistance, good adhesion, stable films on n-type semiconductor. This combination, however, can not be used when depositing emitter, base and collector contacts simultaneously, and therefore requires several additional steps in the fabrication sequence. Analogously to $AuGe - Au$, $AuZn - Au$ can be used to form low resistivity annealed contacts on the p-type base. Unfortunately, alloying of the ohmic contact often results in a punch-through of the very thin base layer, hence it is highly desirable to employ non-alloyed metallization schemes for the base contacts.

5.4. Process Flow

MOCVD-grown *InP/InGaAs* heterostructure wafer is cut into small $1 \times 1 \text{ cm}^2$ samples. After thorough cleaning of tweezers, sample holder, glassware and processing area, the sample is subjected to a short ultrasonic bath in acetone followed by a standard AMD clean. Then the *InP* emitter cap layer is removed by a 7 second etch³ in diluted hydrochloric acid ($\text{HCl} : \text{H}_2\text{O} = 1 : 1$), the sample is thoroughly rinsed in DI water and blown-dry with a nitrogen gun. The standard photolithography procedure, using bright field mask #4, is carried out to pattern the sample for the base mesa etch. Layer of the photoresist covers the HBT emitter regions leaving the rest of the surface unprotected. The sample is wet etched by the *InGaAs* etchant solution for 35 seconds to remove *InGaAs* emitter cap layer. The *InP* graded layer and the *InP* emitter are removed by the $\text{HCl} : \text{H}_3\text{PO}_4$ solution in about 7 seconds. The photoresist is then stripped by an AMD clean. Corresponding HBT cross section is shown in Fig. 5.13.

In the next step the collector mesa regions are defined by means of photolithography (bright field mask #2) and wet etch of the *InGaAs* base setback, base and collector layers in the *InGaAs* etchant for about 5 minutes. The visual

³All etch times given in this section are those for SHBT I3420. For other heterostructures the etch times have to be adjusted

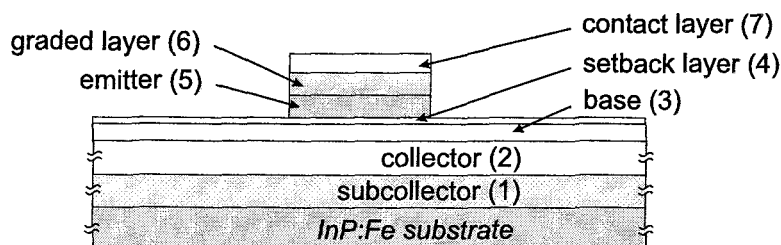


FIGURE 5.13. Schematic of HBT cross section after the base mesa etch.

appearance of the sample can easily be used for determining the end point for the etch.

To complete the device profile the bright field mask #1 is used in the photolithography routine to protect the device mesa regions. Then, a short 10 seconds etch in the *InP* etchant solution is performed to remove the subcollector layer and reach the semi insulating substrate, thus isolating the HBT devices from each other. Fig. 5.14 shows the schematic cross section of the HBT structure after this step.

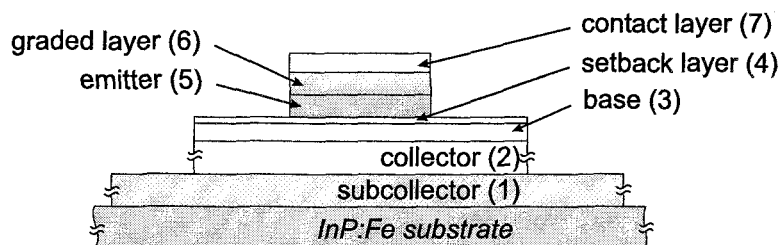


FIGURE 5.14. Schematic of HBT cross section after the isolation mesa etch.

6. IRRADIATION EFFECTS

Having introduced the radiation effects in semiconductor materials and developed comprehensive HBT model we are now ready to proceed with the analysis of the HBT irradiation experimental results. This chapter offers sections dedicated to results, analysis and discussion of electron, neutron and gamma irradiation effects. To understand and model behavior of an HBT as a whole, in each section the device damage is examined at different levels. First, the most basic compact model (see Section 4.3) is used to identify different terminal currents responsible for the detected changes in device output characteristics. Second, the compact model and/or analytical model are employed to further separate out the current components causing the changes in the terminal currents. Finally, the analytical model is used to link the degradation of the individual current components with the radiation effects observed in different layers of a device. The neutron irradiation results are used to perform the most detailed analysis of the radiation effects. All levels of the HBT device models in conjunction with the damage production calculations are employed to develop a complete picture of the device degradation. At the same time the main purpose of the results of electron and gamma irradiation experiments is to demonstrate that the devices follow the same degradation

pattern¹ for all three types of radiation. The displacement damage introduced in beta and gamma irradiation experiments is too low to attempt quantitative analysis of the degradation effects, but still sufficiently high to qualitatively identify the general deterioration trends.

The chapter is organized in four sections – first three covering the electron, neutron and gamma irradiation experiments, and their analysis and discussion. The fourth section provides a brief summary of the results.

6.1. Beta Irradiation

In this section the results on electron irradiation effects in *InP/InGaAs* SHBTs are presented. Analysis of the material degradation is based on the radiation damage calculations discussed earlier in Chapter 3, while the device effects are analyzed using the different level transistor models introduced in Chapter 4. The section starts with presentation of the experimental results. Then the BC junction degradation is briefly discussed and the gain degradation mechanisms are analyzed. The current results are also compared to the studies on unpassivated devices. Finally, analysis of devices with different P/A ratios is performed to isolate

¹ignoring second order effects

surface effects from the bulk degradation. The section is concluded with a short summary of the results and conclusions.

6.1.1. Experimental Details

Using a non-self-aligned process sequence with selective wet chemical etching techniques (see Chapter 5) a large number of devices (about 40) was fabricated on the *I*3420 transistor structure. After the device mesas were defined, the structure was passivated with polyimide followed by opening of contact windows, and deposition of Ti/Au (120/2000) metal contacts and probing pads.

Electron irradiation of the devices was performed at the OSU Radiation Center using already described $^{90}\text{Sr}/^{90}\text{Y}$ 100 *mCi* beta-radiation source. The wafer was placed directly under the source in close proximity of about 2 mm (see Fig. 3.7). The device terminals were left in a floating condition at ambient temperature during irradiation. We believe that the biasing condition during irradiation is not a serious issue in the present experiments since the ionizing damage does not play a significant role in the performance degradation of these devices (HBTs). The electrical characterization of the devices (see Section 4.2) was performed using an HP 4145B parameter analyzer before irradiation and after various intermediate doses. Typically, the devices were characterized within a few hours after the irradiation. Some annealing of the defects during this time interval can not be ruled out. However, it is believed that the devices have reached a stable condition before

the characterization started since the measurement results were reproducible even after a day.

Exposure durations used in the study and the corresponding calculated cumulative electron fluences, ionizing doses, displacement doses, and number of radiation-induced displacements are listed in Table 3.4.

6.1.2. Experimental Results and Discussion

The common emitter $I - V$ ($I_C - V_{CE}$) characteristics of a typical device of emitter area $750 \mu m^2$ ($P/A = 0.173 \mu m^{-1}$) at different base currents (I_B) prior to irradiation are shown in Fig. 6.1. The $I_C - V_{CE}$ characteristics of the same device after electron irradiation to a cumulative fluence of $2.7 \times 10^{16} e/cm^2$ are shown in Fig. 6.2. The $I_C - V_{CE}$ characteristics of the same device at a base current of 50 mA after various intermediate electron fluences are shown in Fig. 6.3. The most significant effect of electron irradiation observed in Figs. 6.1 and 6.3 is a change in the slope of the $I_C - V_{CE}$ characteristics of the device in the saturation regime after electron irradiation. The maximum collector current for a given I_B is found to be unaffected for electron fluences less than $2.4 \times 10^{15} e/cm^2$. For higher electron fluences, the collector current begins to decrease. However, the maximum decrease of the collector current in the active regime after the highest cumulative fluence of $2.7 \times 10^{16} e/cm^2$ was found to be only 9 percent. The output conductance of the passivated devices is seen to be completely unaffected even after the highest

electron dose. Finally, a slight increase of $V_{CE,off}$ is observed; its discussion will however be postponed till Section 6.2.

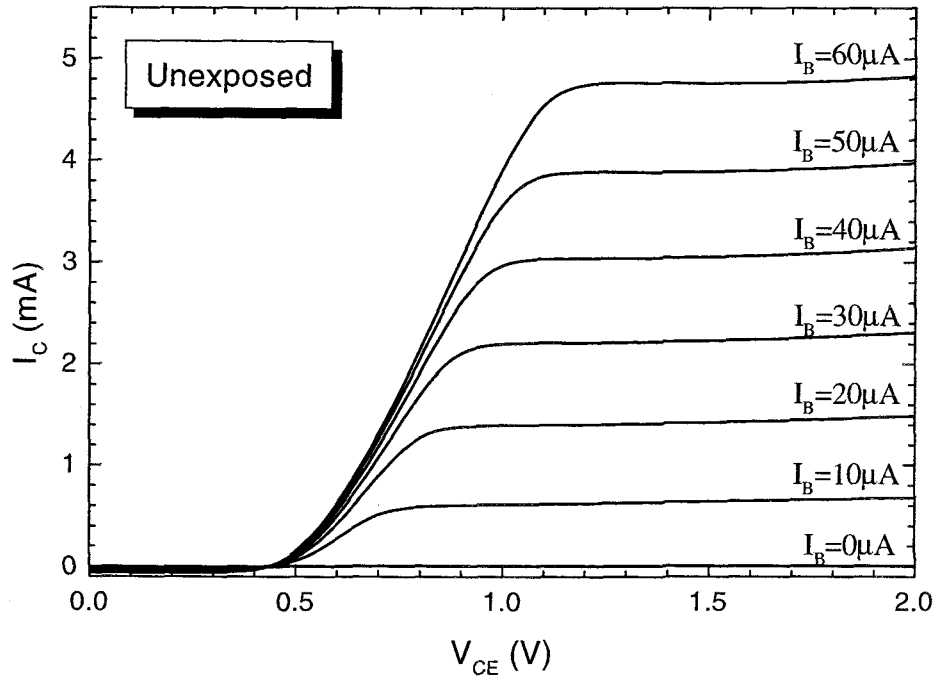


FIGURE 6.1. The common emitter $I - V$ ($I_C - V_{CE}$) characteristics of an *InP/InGaAs* SHBT at different base currents (I_B) prior to irradiation. Emitter area of $750 \mu m^2$.

The degradation of the transistor's DC current gain ($\beta = I_C/I_B$) with electron dose is found to obey the Messenger-Spratt relationship of the form [45]

$$\frac{1}{\beta} = \frac{1}{\beta_0} + K_\beta \phi_e$$

as shown in Fig. 6.4. From the slope of the best fit line the gain degradation coefficient K_β is found to be about $3.7 \times 10^{-20} \text{ cm}^2/e$.

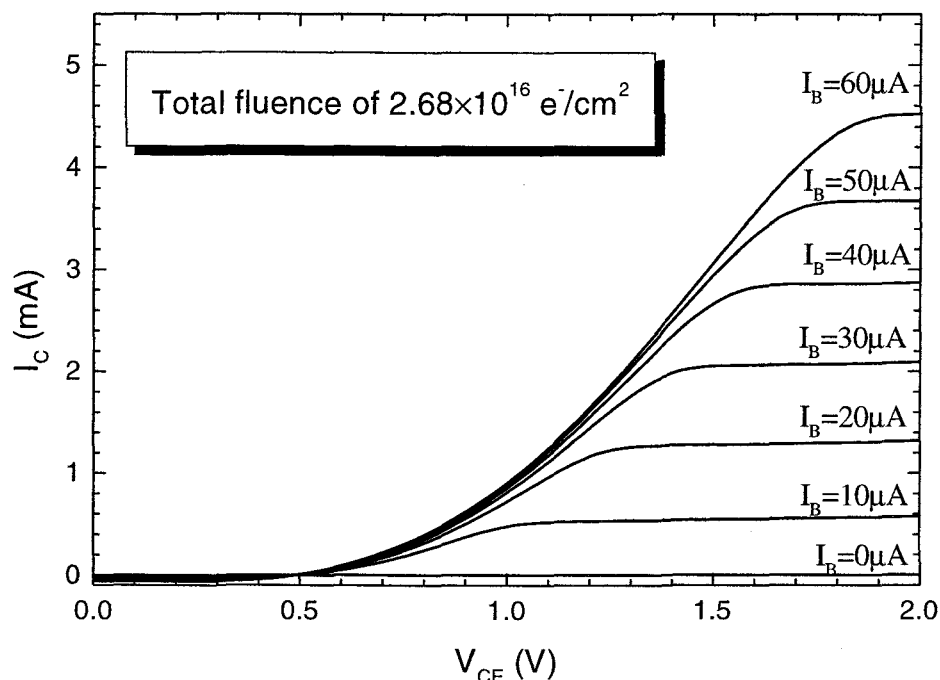


FIGURE 6.2. The common emitter $I - V$ ($I_C - V_{CE}$) characteristics of the same device (as in Fig. 6.1) at different base currents (I_B) after electron irradiation.

The Gummel plots of I_C and I_B as functions of V_{BE} for different electron fluences are shown in Fig. 6.5. The collector current shows a constant leakage current ($I_{CL} \sim 10^{-7} A$) for $V_{BE} < 0.6 V$. At intermediate values of V_{BE} ($0.6 < V_{BE} < 0.9$) the collector current is unaffected for all the electron doses. The collector current saturates at high values of V_{BE} . We believe that this saturation is caused by the collector series resistance. The maximum collector current, as well as the value of V_{BE} at which the collector current reaches a maximum, decreases with electron fluence implying an increase in the collector series resistance with the dose.

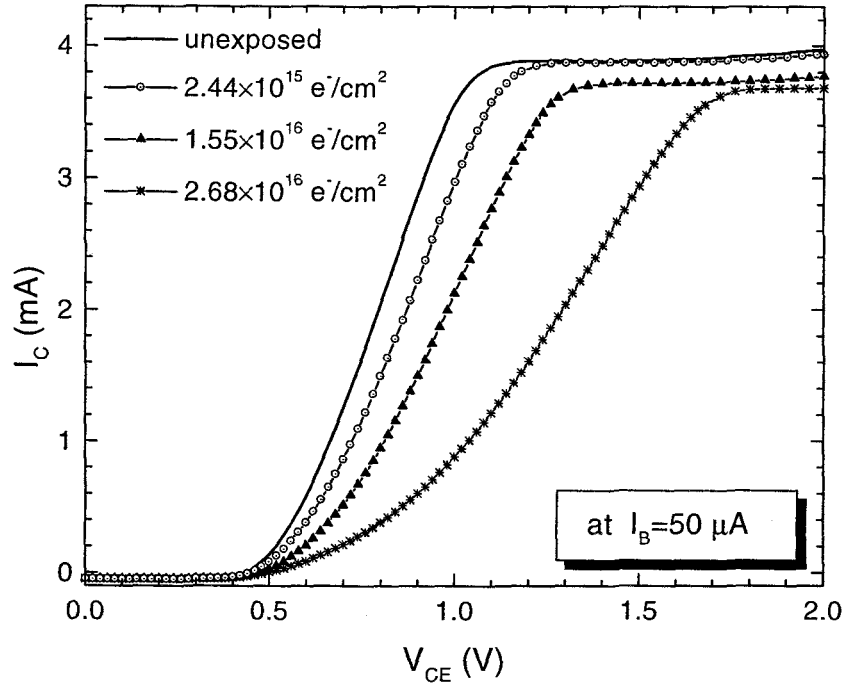


FIGURE 6.3. The common emitter $I - V$ ($I_C - V_{CE}$) characteristics of the same device (as in Fig. 6.1) at base current of $50 \mu\text{A}$ for various intermediate doses.

The base current, on the other hand, shows a sharp increase in the high V_{BE} regime. We believe that this behavior is caused by the collector series resistance as shown by Liou *et al.* [101] and Sotoodeh *et al.* [102]. The Gummel measurements are normally done with a zero voltage applied across the base and collector probes (i.e. $V_{CB} = 0$). The collector current causes a voltage drop across the collector series resistance, which in turn forward biases the internal base-collector junction and gives rise to additional base current. The voltage drop across the series resistor becomes significant as I_C increases giving rise to a sharp increase in I_B in the high V_{BE} regime. This model is also independently verified by Gummel measurements

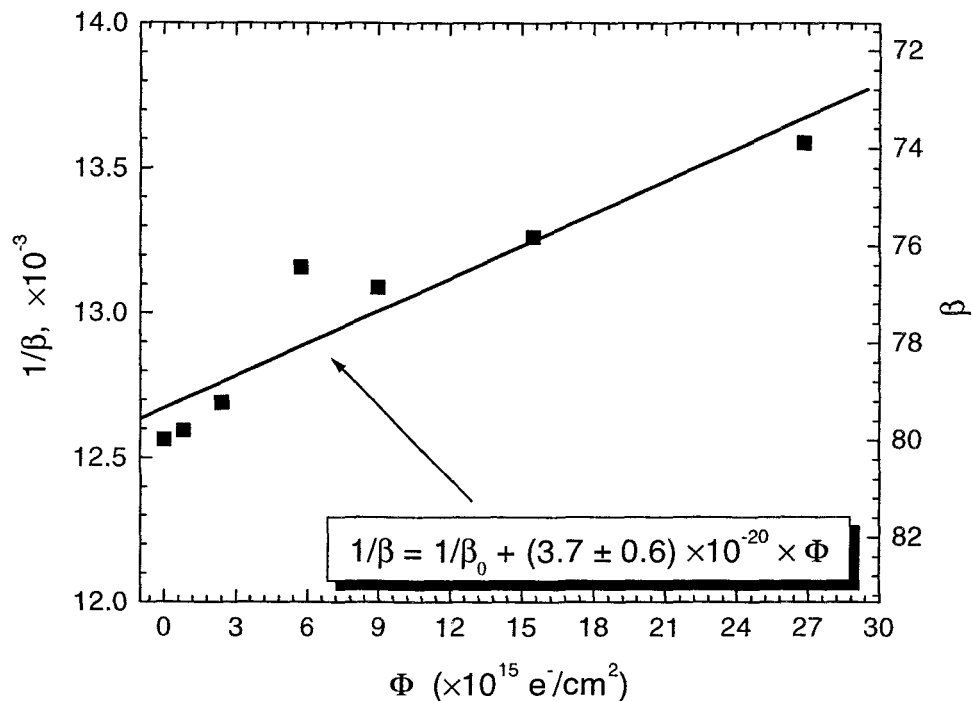


FIGURE 6.4. DC current gain as a function of electron fluence.

at $V_{CB} = 2.5\text{V}$. At this value of V_{CB} the base-collector junction remains reverse biased even at the highest value of V_{BE} eliminating the sharp increase in I_B as shown in Fig. 6.5 for the highest dose. It is also significant to note that the sharp increase in I_B (with $V_{CB} = 0$) occurs at progressively lower values of V_{BE} with increasing electron dose. Once again this behavior is consistent with a gradual increase in the collector series resistance with increasing electron irradiation dose.

In the low V_{BE} regime ($V_{BE} < 1.0\text{ V}$), the base current decreases slightly for small doses (up to $2.44 \times 10^{15} \text{ e}/\text{cm}^2$) and then begins to increase for larger doses. The DC common emitter current gain β as a function of the collector current is shown in Fig. 6.6 for various electron doses. At low collector currents ($I_C < 1\text{ mA}$),

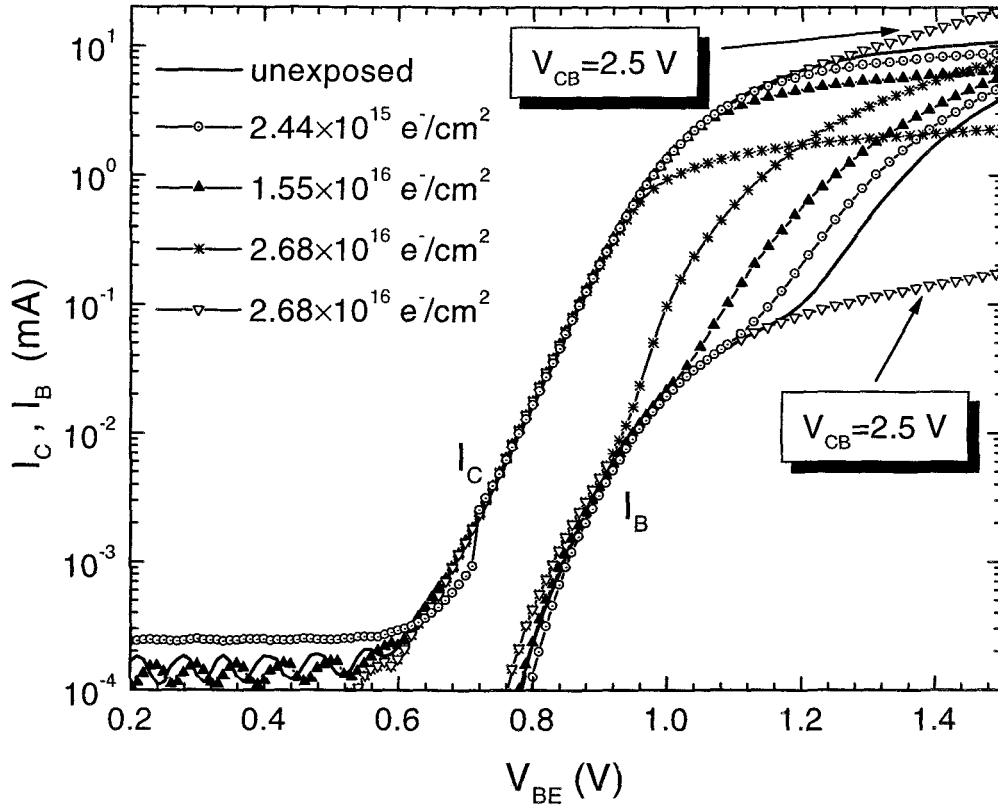


FIGURE 6.5. Gummel plots of I_C and I_B for various intermediate doses.

the current gain increases slightly for low doses ($\phi_e < 2.44 \times 10^{15} \text{ e/cm}^2$) and then begins to decrease for the higher doses. This behavior correlates with the decrease of I_B for low doses followed by an increase at higher doses shown in Fig. 6.5. A similar decrease in I_B for small doses of gamma irradiation of *InAlAs/InGaAs* HBTs has been reported [4].

It is also seen from Fig. 6.6 that the gain increases with collector current, reaches a maximum at some value of I_C and then begins to decrease for higher I_C .

The decrease in gain at higher I_C is also due to the collector series resistance. The value of I_C at which the gain reaches a maximum decreases with the increase in electron dose confirming an increase in the collector series resistance with electron irradiation.

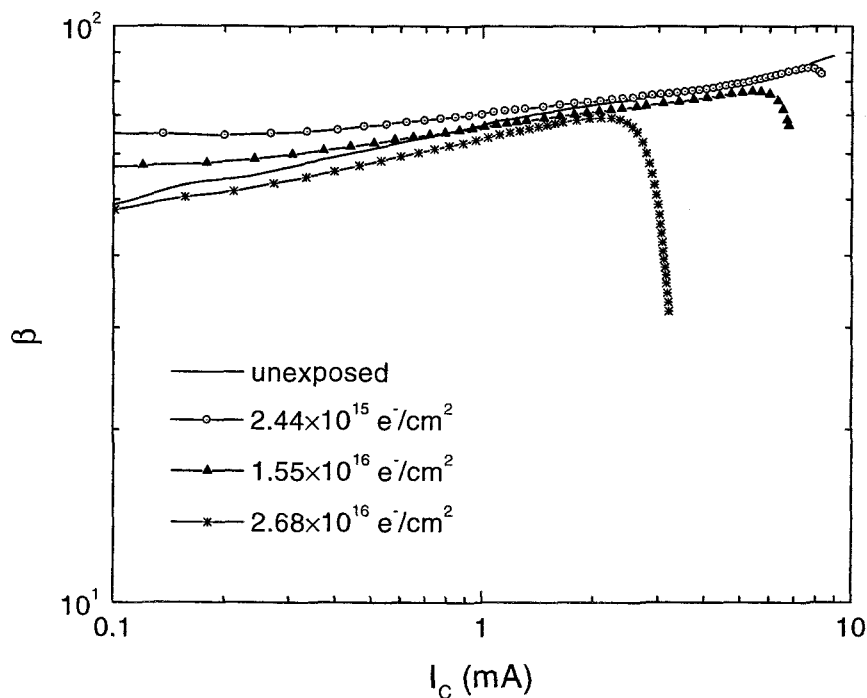


FIGURE 6.6. Collector current gain of DC current gain for different intermediate doses. The measurements are performed at $V_{CE} = 1.5$.

In order to check independently the hypothesis of the increase in the collector series resistance with increasing electron dose, we also performed $I - V$ measurements of base-emitter and base-collector junctions of the HBTs. While the BE diodes showed no evidence of increase in series resistance, the BC diodes

showed a gradually increasing series resistance with increasing electron fluence as shown in Fig. 6.7. The ideality factor for the BC diode (n_{BC}) showed an increase from 1.27 prior to irradiation to 1.82 after the highest dose. This increase in the ideality factor is easily explained by the increase in the generation-recombination current (which has an ideality factor of 2.0) caused by the radiation induced defects in the collector depletion region.

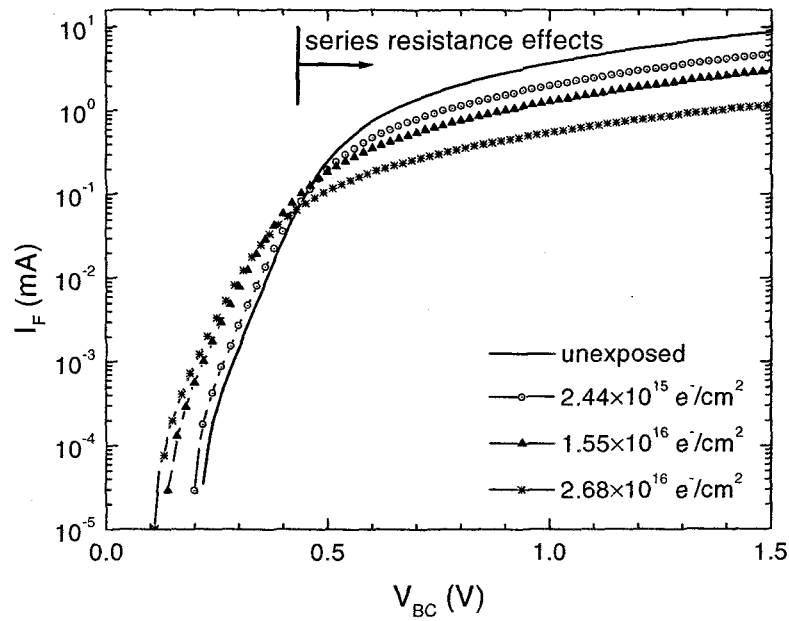


FIGURE 6.7. Semilog plot of BC diode current-voltage characteristics for different intermediate doses.

6.1.2.1. Analysis of BC Diode Saturation Current

In the first approximation the current through the BC homojunction diode may be written as a sum of diffusion, $I_{BC,diff}$, and generation-recombination, $I_{BC,G-R}$, currents

$$I_{BC} = I_{BC,diff}^{sat} e^{\frac{qV_{BC}}{kT}} + I_{BC,G-R}^{sat} e^{\frac{qV_{BC}}{2kT}} \quad (6.1)$$

where $I_{BC,diff}^{sat}$ and $I_{BC,G-R}^{sat}$ are the saturation currents. The ideality factors (n_{BC}) already discussed in this section were simply determined from the average slope of the experimental data of $\ln(I_{BC})$ vs. V_{BC} . A more careful analysis by fitting these data to Eq. 6.1 yields the values of $I_{BC,diff}^{sat}$ and $I_{BC,G-R}^{sat}$ and these results are summarized in Table 6.1. As noted earlier, $I_{BC,G-R}$ arises from the radiation induced defects in the BC junction depletion region. $I_{BC,G-R}^{sat}$ may be written as

$$I_{BC,G-R}^{sat} = \frac{1}{2} q A_J W_{BC} \sigma v_{th} N_d n_i \quad (6.2)$$

where A_J is the junction area, W_{BC} is the width of the BC junction depletion region, σ is the capture cross-section of the traps, N_d is the trap concentration, v_{th} is thermal velocity of the carriers and n_i is intrinsic carrier concentration in *InGaAs*. Since the doping concentration in the base ($\sim 10^{19} \text{ cm}^{-3}$) is much larger than that of the collector ($\sim 10^{15} \text{ cm}^{-3}$), the BC junction depletion region is predominantly in the collector. Using Eq. 3.27 to relate N_d to the electron fluence Φ_e , Eq. 6.2 gives a linear relation between $I_{BC,G-R}^{sat}$ and ϕ_e . This is indeed found to be the case as shown in Fig. 6.8. From the previously determined value of the

damage production rate a_T , the slope of the best fit line in Fig. 6.8 gives the value of the cross-section of the trap to be $0.4 \times 10^{-15} \text{ cm}^2$, which is indeed in the right range of capture cross-sections reported for defects in many semiconductors.

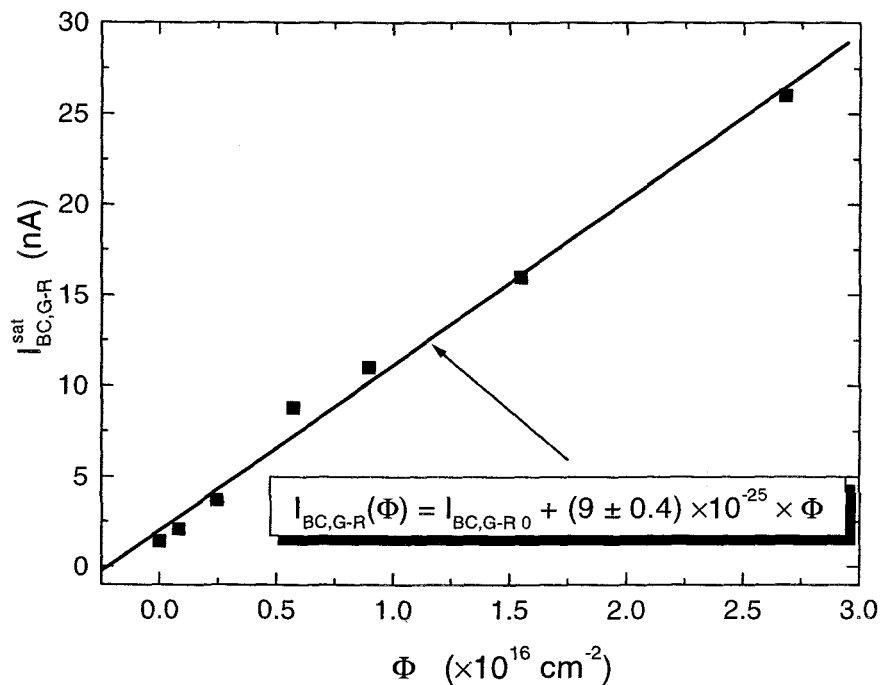


FIGURE 6.8. BC diode generation-recombination saturation current as a function of electron fluence.

6.1.2.2. Gummel Plots and Gain Degradation Mechanisms

The collector current ideality factor determined from the Gummel plot in Fig. 6.5 is found to be 1.2. A collector current ideality factor greater than 1.0 is not uncommon for abrupt heterojunctions. It arises from the conduction band

Dose	$\Phi_{tot} (e^-/cm^2)$	n_{BC}	$I_{BC}^{sat} (A)$	$I_{BC,diff}^{sat} (A)$	$I_{BC,G-R}^{sat} (A)$
0	–	1.27	1.6×10^{-10}	8.3×10^{-12}	1.7×10^{-9}
1	8.14×10^{14}	1.30	2.4×10^{-10}	1.0×10^{-11}	2.3×10^{-9}
2	2.44×10^{15}	1.35	4.7×10^{-10}	1.3×10^{-11}	3.9×10^{-9}
3	5.70×10^{15}	1.50	2.1×10^{-10}	1.7×10^{-11}	9.1×10^{-9}
4	8.96×10^{15}	1.52	2.8×10^{-9}	1.9×10^{-11}	1.1×10^{-8}
5	1.55×10^{16}	1.58	5.0×10^{-9}	2.1×10^{-11}	1.6×10^{-8}
6	2.68×10^{16}	1.82	1.7×10^{-8}	1.1×10^{-11}	2.7×10^{-8}

TABLE 6.1. Base-collector ideality factor, n_{BC} , base-collector diode saturation current, I_{BC}^{sat} at $V_{BC} = 0.29 V$ (determined by fitting the inverse Gummel plots).

notch and the division of applied voltage between the emitter and the base regions [15]. The base current ideality factor is found to be 1.8 and is nearly the same for all the electron doses. Recall that the base recombination current in an HBT consists of three components.

1. The recombination current in the bulk and the surface (perimeter) of the emitter base junction space charge region (SCR) with an ideality factor ~ 2.0 .
2. The recombination current in the bulk quasi-neutral base region with an ideality factor ~ 1.0 .

3. The surface recombination current at the extrinsic base region with an ideality factor ~ 1.0 .

Depending upon the relative contribution from these three components of the base current, the net ideality factor for the base current may be anywhere between 1.0 and 2.0.

The slight increase of gain observed at low base currents for small electron doses followed by a decrease of gain at the higher doses (see Fig. 6.6) may be explained by the following argument. Generally, the emitter-base junction region recombination (bulk + surface) component tends to be dominant at low base currents. It is well known that the surface recombination at the heterojunction region is strongly influenced by the surface Fermi level [103]. The results of two-dimensional simulation by Tiwari *et al.* [103] show that the ability of electrons from the emitter to enter a surface channel created by Fermi level pinning at the surface governs the magnitude of surface recombination. We believe that the decrease of base current (and the associated increase in current gain) at smaller doses is related to the charge build up in the polyimide layer due to the ionization damage. Even though a part of this charge may be discharged during the handling of the device after irradiation, a part of the charge may be trapped near the polyimide-semiconductor interface. This in turn increases the barrier for the bulk electrons to enter the surface channel and decreases the base current. This hypothesis is supported by the results of our test experiments on *Si* MIS capacitors using the

polyimide as the insulating layer that shows a shift of the $C - V$ curves after electron irradiation suggesting the trapping of negative charges in the polyimide layer. For higher electron doses, this effect saturates and the increased recombination due to the radiation-induced defects in the bulk and the periphery of the depletion region causes the base current to increase again.

As the collector current is increased, it is seen from Fig. 6.6 that the gain curves for the different electron doses tend to merge together indicating that the gain degradation is small at higher base currents. It is well known that the quasi-neutral base region recombination begins to dominate at the higher base currents. The smaller gain reduction at higher base currents indicates that the quasi-neutral region recombination is not significantly affected by electron irradiation. The quasi-neutral bulk recombination predominantly takes place via radiative recombination and Auger recombination [78]. The radiative recombination rate is proportional to the product (pn) of the hole and electron concentration in the base. The Auger recombination rate goes as pn^2 or np^2 . Since the base region of an HBT is typically very heavily doped ($\sim 10^{19} \text{ cm}^{-3}$) the radiation induced defects do not significantly affect the carrier concentrations in the base. Hence the base current arising from these mechanisms is also not affected by electron irradiation.

As the collector current is further increased, the gain begins to decrease due to the collector series resistance. Using an Ebers-Moll model described in Section 4.3, we fitted the Gummel plots in Fig. 6.5 to extract the values of the

series resistances associated with the emitter (R_E), the base (R_B) and the collector (R_C). The extracted values of R_E , R_B , and R_C were found to be 21, 50 and 52 ohms, respectively, before irradiation, and 31, 81, and 380 after the highest dose of electron irradiation.

6.1.2.3. Comparison with Unpassivated Devices

In contrast with the studies on unpassivated *InP/InGaAs* SHBTs and DHBTs [6, 7], our study shows much less degradation of the polyimide-passivated devices. The degradation effects in the unpassivated devices include a larger gain reduction, increase in the output conductance and an increase in $V_{CE,sat}$ due to an increase in series resistance. As is evident from the Gummel measurements, the decrease of current gain is caused by an increase in the base current. The difference in the base currents between the passivated and unpassivated devices can only arise from the BE junction surface (perimeter) recombination and the extrinsic-base surface recombination. The recombination in the bulk depletion region (under the emitter contact) and in the intrinsic quasi-neutral base region are expected to be identical in both the cases. The increased radiation hardness of the passivated devices is not due to the 'radiation shield' provided by the polyimide layer since the energy loss of electrons in the polyimide layer is very small (less than 0.02 MeV) and hence the total ionizing dose rate (dD/dt) in the active volume of the device is nearly the same for both the passivated and the unpassivated samples.

We attribute the larger degradation of the unpassivated devices to the presence of the free surface. We believe that the free surface of a semiconductor is more susceptible to radiation damage than a passivated surface is due to the presence of a large number of dangling bonds at the free surface. The earlier studies by Subramanian *et al.* [104] on the mobility degradation of unpassivated modulation-doped heterostructures also show evidence of the susceptibility of a free surface to more radiation damage.

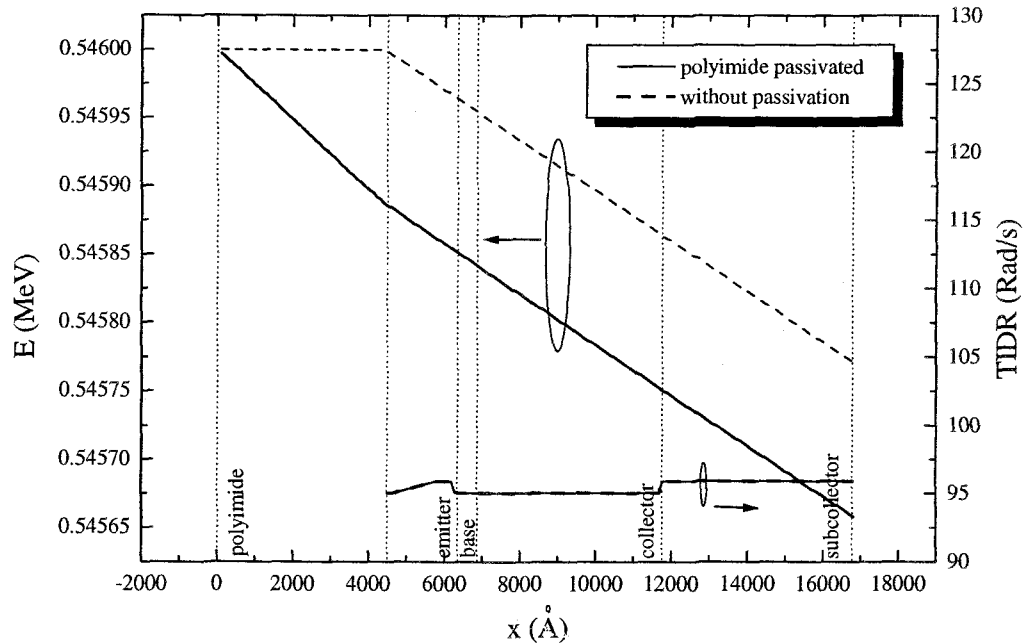


FIGURE 6.9. Energy of incident electrons, E , and TIDR for electrons as they pass through layers of SHBT.

The increase in the output conductance of the unpassivated devices after irradiation was argued to be caused by the avalanche multiplication in the collector

depletion region due to a reduction of BC junction breakdown voltage [6, 7]. On the other hand, the passivated devices studied in this work did not show any increase in the output conductance even after the highest electron dose. This difference in behavior between the passivated and the unpassivated devices is again believed to be due to the breakdown of the BC junction of the unpassivated devices at the edges rather than in the bulk since the bulk damage in both types of devices is expected to be same.

The increase in $V_{CE,sat}$ has been observed in both the unpassivated and the passivated devices. However, this increase in the unpassivated devices in our earlier work [6, 7] was found to be related to an increase in the emitter series resistance whereas it is found to be related to an increase in the collector series resistance in this work. It should be also pointed out that the magnitude of the increase in $V_{CE,sat}$ is not uniform for all the devices studied. While some devices show a larger increase other devices show a much smaller increase. The results shown in Figs. 6.2 and 6.3 are typical. This non-uniform degradation of $V_{CE,sat}$ suggests that the increase in series resistance might be related to the degradation of the contact resistance rather than the bulk resistance. The variability of the surface conditions on the wafer just before the metal deposition may be responsible for the non-uniform degradation of contacts on different devices. Further work is necessary to understand and eliminate this degradation behavior.

6.1.2.4. *P/A Ratio Dependence of Gain Degradation*

The gain degradation in the active region of the $I_C - V_{CE}$ characteristics (similar to those shown in Fig. 6.1) of devices with different size emitters were found to be nearly the same and did not show any correlation with the P/A ratio of the devices. However, this comparison is not quite meaningful since the current densities of the different emitter size devices in the active region are different for the same value of I_B . The gain degradation at a given collector current density for a wide range of P/A ratio devices could not be compared due to the parasitic series resistance effects on the gain at high collector currents. The P/A ratio dependence of the gain degradation for devices within a limited range of P/A shows that the normalized gain degradation is smaller for the larger P/A devices. This result is explained as follows. As argued earlier in this Section, the radiation-induced damage at the emitter periphery is small for the passivated devices. Thus one may assume that the base current arising from the surface recombination at the BE junction periphery is not affected by irradiation. Since this component of the current is more dominant in the larger P/A devices, the overall gain degradation is smaller. A similar behavior has been observed for the neutron irradiation effects in AlGaAs/GaAs HBTs [3] and for the electron irradiation effects in AlGaAs/GaAs HBTs [100].

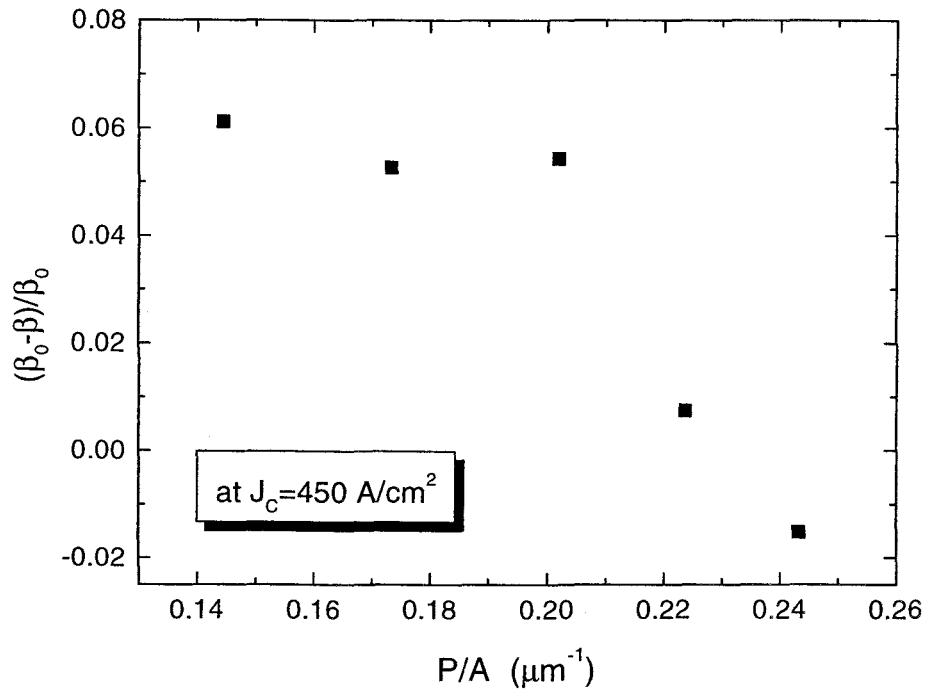


FIGURE 6.10. BC diode generation-recombination saturation current as a function of electron fluence.

6.1.2.5. Degradation Variation

To conclude the analysis of the beta-induced degradation of *InP/InGaAs* HBTs we briefly present some information on the variation of the parameters between different devices. Unirradiated transistors exhibited gain in the range from 51 to 70 (see Fig. 6.11) with the mean of 60 and standard deviation of 6. After irradiation some of the devices showed lower gains in the range of 80% - 100% of β_0 . The distribution of the gain for different devices is shown in Fig. 6.12 for the highest dose used. A few devices showed either little improvement or no

degradation at all, while majority of the devices have gains of 80-90% of their initial values.

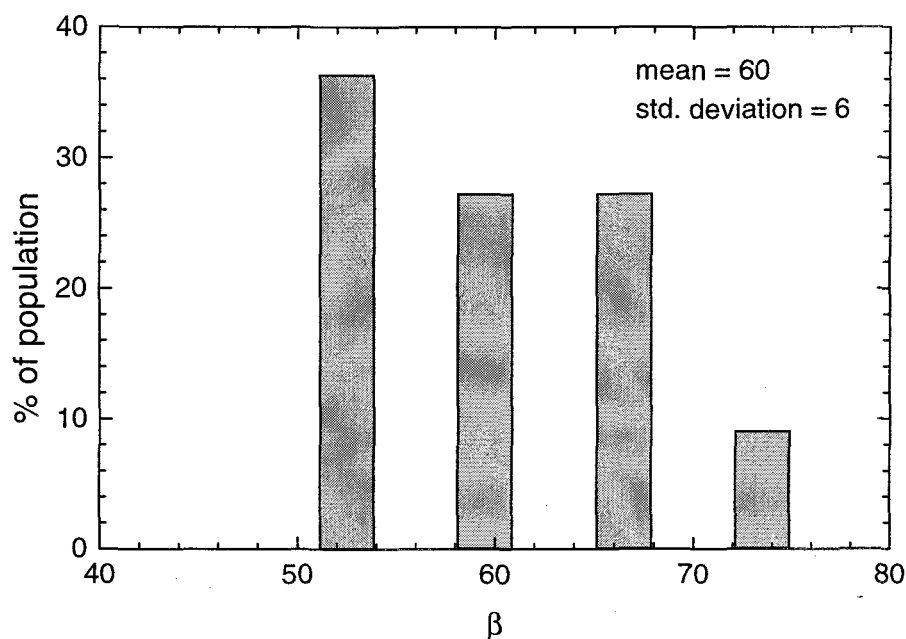


FIGURE 6.11. Initial DC gain distribution for entire device “population”.

Initial $V_{CE,sat}$'s, which are determined by the series resistance effects, fall into the range of 0.95 – 1.05 V. For most of the devices $V_{CE,sat}$ degrades very quickly. Some devices, however, show relatively little change of this parameter. No correlation is observed between the initial and final values of the saturation voltage. Final distribution of $V_{CE,sat}$ is shown in Fig. 6.13 for the devices after the highest dose. The voltages vary in the range of 1 – 3 V. The exact cause of such

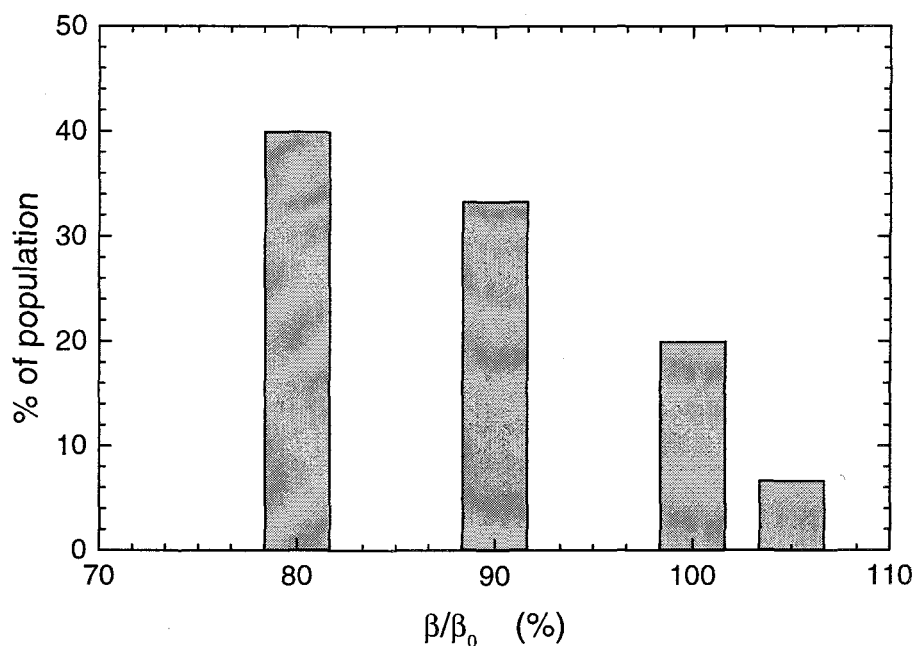


FIGURE 6.12. Distribution of radiation-induced changes in DC gain parameter for entire device “population” after the highest dose.

a wide $V_{CE,sat}$ distribution is not currently understood, but is most likely related to the sample surface conditions immediately before the contact deposition.

6.1.3. Conclusions

Total dose electron irradiation effects on polyimide passivated *InP/InGaAs* single heterojunction bipolar transistors were investigated. The devices show excellent radiation performance. After a cumulative dose of $2.7 \times 10^{16} e/cm^2$ ($\sim 620 \text{ Mrad}^{InGaAs}$), the devices showed a typical decrease of only 9 percent in the collector current in the active regime and no change in the output conductance.

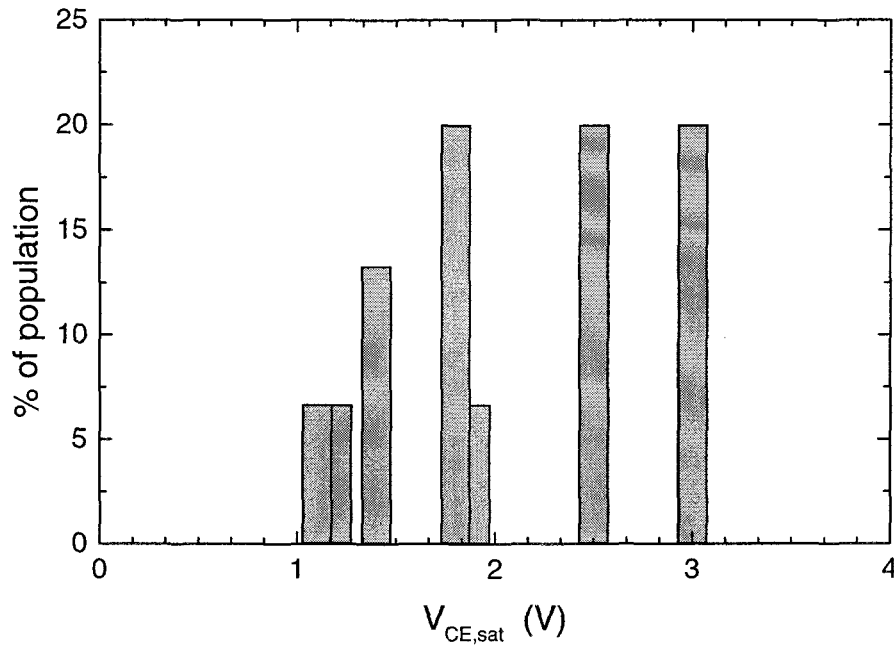


FIGURE 6.13. Distribution of radiation-induced changes in $V_{CE,sat}$ for entire device “population” after the highest dose.

For low base currents, the devices show an increase in the current gain for smaller doses ($2.5 \times 10^{15} e/cm^2$) followed by a decrease at the higher doses. A plausible explanation of this behavior based on the effect of the ionization damage in the polyimide layer at the periphery of the BE junction is discussed. The slope of the common emitter $I - V$ characteristics in the saturation regime decreases after electron irradiation causing an increase in the $V_{CE,sat}$. We believe this increase is caused by an increase in the collector series resistance. The increase in the collector series resistance is also shown to be responsible for a decrease of the current gain at high base currents. Finally, smaller emitter size (larger perimeter/area) devices

show less degradation than the larger emitter devices. This is explained by the smaller radiation damage at the junction periphery of the passivated devices.

6.2. Neutron Irradiation

This section presents the results and analysis of the neutron irradiation of *InP/InGaAs* SGBTs. The discussion is organized similarly to the previous section, however much more attention is paid to description of the radiation effects by means of the analytical model. The main purpose of this section is to show, on the example of neutron irradiation, how the radiation effects can be modeled and therefore device response to any given radiation environment can be theoretically estimated.

First, the section presents the experimental results of the irradiation experiments. Then the attention is turned to analysis of the gain degradation mechanisms. Functional dependence of the gain degradation coefficient on the collector current density is carefully analyzed and theoretical expression is developed. Then degradation of the base-collector junction is considered to explain the observed increase in the collector-emitter turn-on voltage. Moreover, theoretical expression is derived to link the $V_{CE,off}$ shift to the changes in the individual current components. The section is concluded with a short summary of the results.

6.2.1. Experimental Details

In contrast to electron and gamma irradiation studies all the neutron irradiation experiments followed slightly different scheme, i.e.:

1. A large wafer (large enough to fit at least four unit cells of the mask) was used to fabricate devices.
2. Upon the completion of the fabrication sequence the wafer was cut into four pieces containing identical devices.
3. The devices on each wafer fragment were characterized.
4. Each wafer fragment was encapsulated into a cadmium box and the boxes were positioned into the RSR of the OSU TRIGA "Marc II" 1 *MW* reactor operated at 100 *kW* and irradiated separately for individual doses of 7, 20, 60 and 180 minutes.
5. After irradiation all samples were left to "cool down" (typically one or two weeks), until their radioactivity had reached the acceptable safety limits.
6. All the devices on each wafer fragment were characterized again.
7. Similar devices from the different wafer fragments were compared to study the device degradation as a function of neutron fluence.

The calculated total neutron fluence (excluding thermal neutrons) and corresponding 1 *MeV* equivalent fluence for all individual irradiation times are listed in Table 3.8.

All SHBT devices used in the neutron irradiation experiments were fabricated from the wafer I3257 following the procedures described in Chapter 5.

6.2.2. Radiation-Induced Device Degradation

Fig. 6.14² shows the common emitter $I_C - V_{CE}$ characteristics of device ID:BAxM measured at base currents of 0, 10, 20, 30, 40, 50 and 60 μA before irradiation and after exposure to $2.0 \times 10^{14} \text{ n/cm}^2(1 \text{ MeV}(\text{InGaAs}))$. $I_C - V_{CE}$ characteristics of the same device at a base current of 40 μA for different intermediate neutron fluences are shown in Fig. 6.15. There are two pronounced degradation effects: (1) reduction of the collector current levels, implying significant degradation of the common-emitter current gain, and (2) shift of the device turn-on voltage ($V_{CE,off}$) towards higher values. The subsequent sections are to identify and analyze possible physical mechanisms responsible for the observed degradation effects.

²in this and the subsequent figures in this section the units for the neutron fluences are omitted in the plot legends to avoid crowding. Unless otherwise specified, the reader should assume units of $\text{n/cm}^2(1 \text{ MeV}(\text{InGaAs}))$ for the neutron fluence.

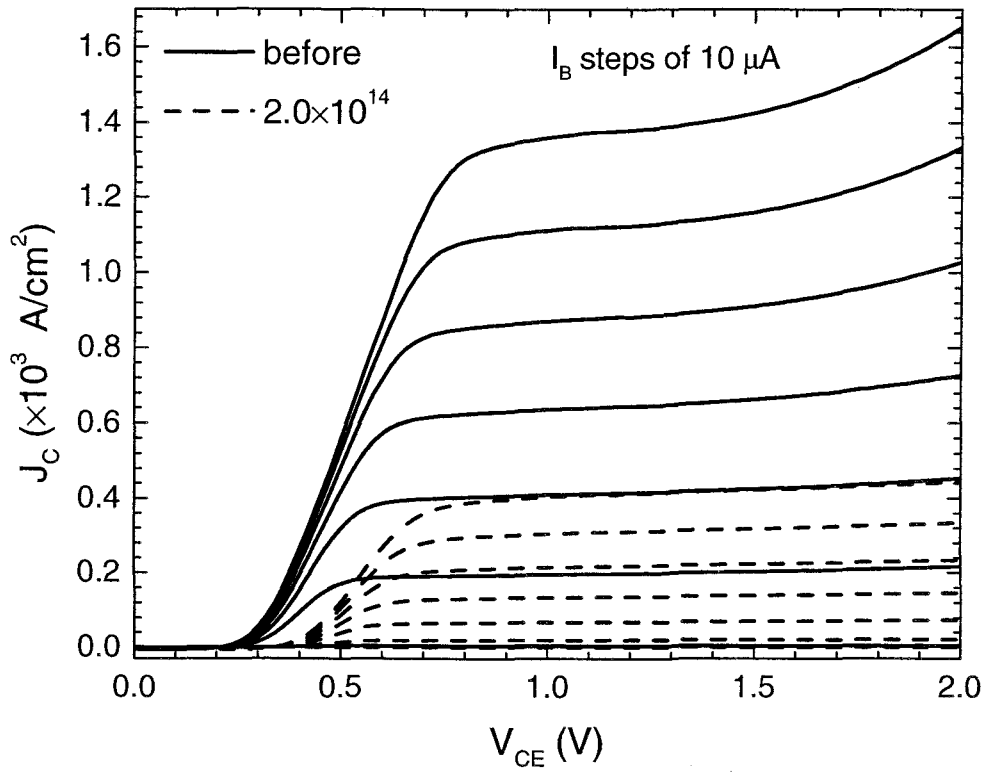


FIGURE 6.14. The common emitter $J_C - V_{CE}$ characteristics measured at base currents of 0, 10, 20, 30, 40, 50 and 60 μA before and after $2.0 \times 10^{14} \text{ n/cm}^2 (1 \text{ MeV } InGaAs)$ irradiation for device ID:BAxM.

6.2.2.1. Gain Degradation Mechanisms

Degradation of the DC current gain is demonstrated in Fig. 6.16, where β is shown as a function of the collector current density for different intermediate doses. Before irradiation the gain is practically constant throughout the whole range of collector current. At very high collector currents the gain drops down quickly due to the series resistance effects (see Section 4.3.2). After irradiation the gain decreases dramatically showing collector current dependent degradation

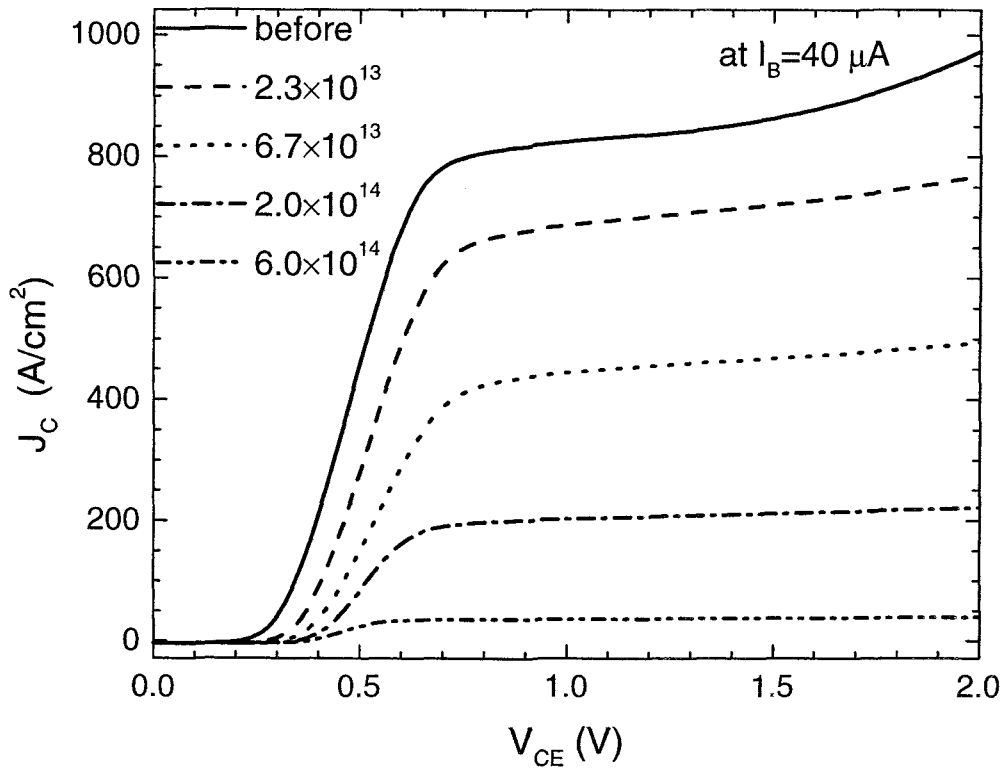


FIGURE 6.15. The common emitter $J_C - V_{CE}$ characteristics of the same device (as in Fig. 6.14) at base current of $40 \mu A$ for different intermediate doses.

– the reduction in gain is noticeably higher at low collector currents. In general, the gain degradation should obey the Messenger-Spratt relation

$$1/\beta = 1/\beta_0 + K_\beta \Phi_n \quad (6.3)$$

Since the gain degrades differently depending on the value of the collector current, or biasing conditions, the K_β should also be a function of J_C or V_{BE} . Fig. 6.17 shows inverse current gain plotted as a function of the neutron fluence measured at BE biases of 0.65 and 0.95 V. As expected, under both biasing conditions $1/\beta$

shows linear dependence on the fluence. K_β is extracted from the slope of the lines. As expected, the gain degradation coefficient K_β is significantly higher at the lower bias. The gain degradation coefficient extracted for different values of the collector current is shown in Fig. 6.18. Starting at very high values K_β decreases very quickly as J_C is increased to few hundred A/cm^2 . At higher collector currents K_β softly saturates at about $2 \times 10^{-17} \text{ cm}^2/n$. An important conclusion can be made here – to reduce radiation tolerance of HBT device/circuit HBTs should be operated at high current levels, where (1) the gain degradation is minimized and (2) the degradation is practically uniform and relatively independent of the biasing conditions.

Before analyzing the $K_\beta - J_C$ dependence we first turn our attention to the forward Gummel plots of the base and collector currents shown in Fig. 6.19 in order to understand the physical origin of the observed gain degradation better. The collector current has a significant leakage component in the low V_{BE} range in the unirradiated device. The origin of this leakage current is not presently understood. However this leakage current decreases significantly after neutron irradiation. In the intermediate V_{BE} range, the collector current is found to be practically unaffected by neutron irradiation. The saturation of the collector current in the high V_{BE} range is caused by the emitter series resistance and a slight saturation of electron injection (see Fig. 4.18) from the emitter. The collector saturation current J_S , ideality factor n_F and emitter series resistance R_E were extracted from the

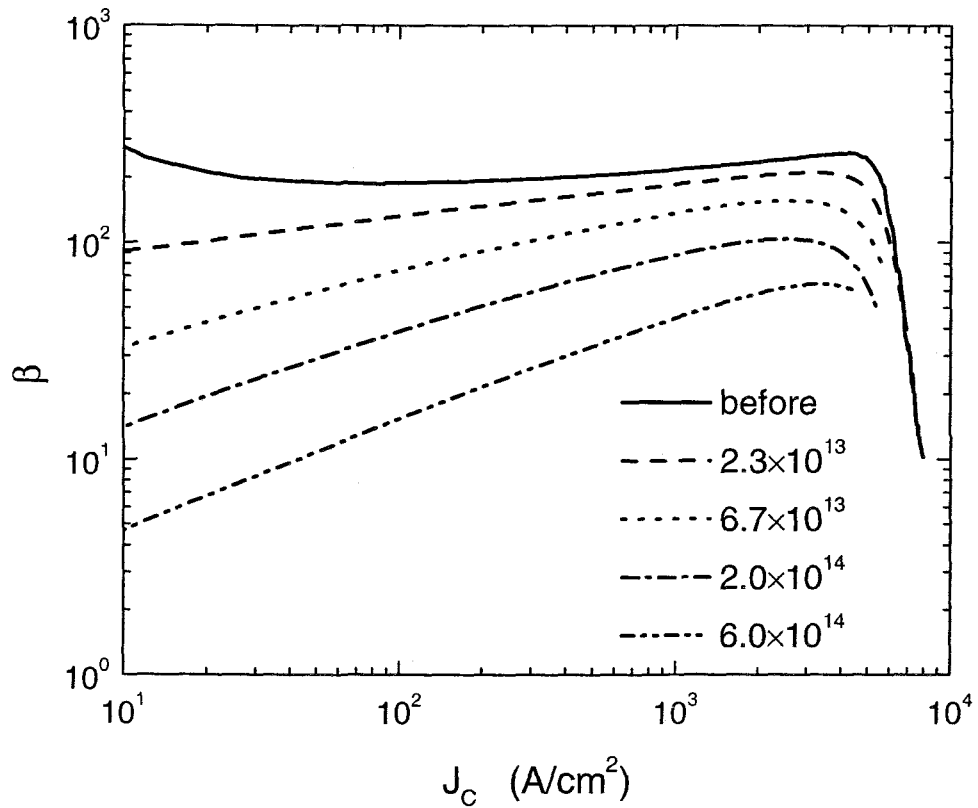


FIGURE 6.16. DC current gain as a function of the collector current density for different intermediate doses.

$J_C - V_{BE}$ characteristics for different doses by using simple SPICE equation

$$J_C(V_{BE}) = J_S e^{V'_{BE}/n_F kT} \quad (6.4)$$

with $V'_{BE} = V_{BE} - I_C R_E$. The results are shown in Table 6.2. It is observed that the saturation current ($\approx 2 \times 10^{-7} \text{ A/cm}^2$) and the ideality factor (≈ 1.3) for the collector current are relatively unaffected by neutron irradiation. The insensitivity of the values of n_F and J_S to neutron irradiation shows that the current injection mechanism (thermionic emission) at the BE heterojunction is

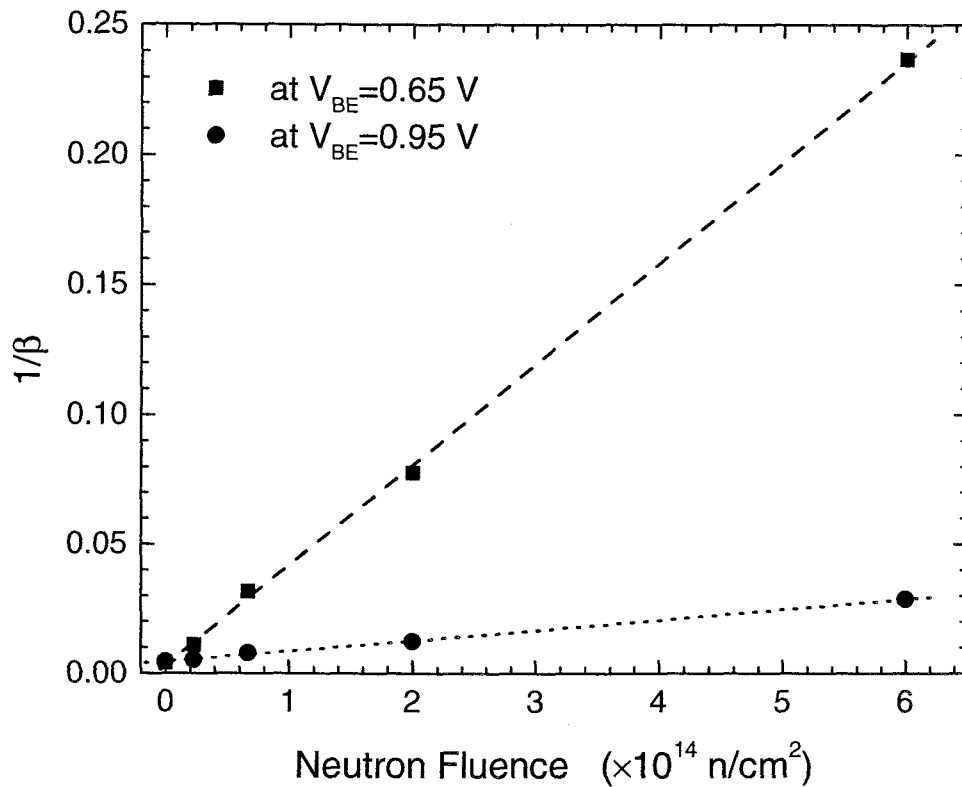


FIGURE 6.17. Inverse DC current gain as a function of neutron fluence for $V_{BE} = 0.65 \text{ V}$ and $V_{BE} = 0.95 \text{ V}$.

not affected by radiation. The normalized emitter series resistance is found to increase from 1.0 to 1.8 after the highest dose used.

The base current, on the other hand, increases steadily with the neutron fluence (see Fig. 6.19). Since the collector current remains constant after radiation, it is the increase in the base current that leads to the degradation of the current gain with the increasing neutron dose. To gain further understanding of the gain degradation mechanisms we analyze the different components of the base current

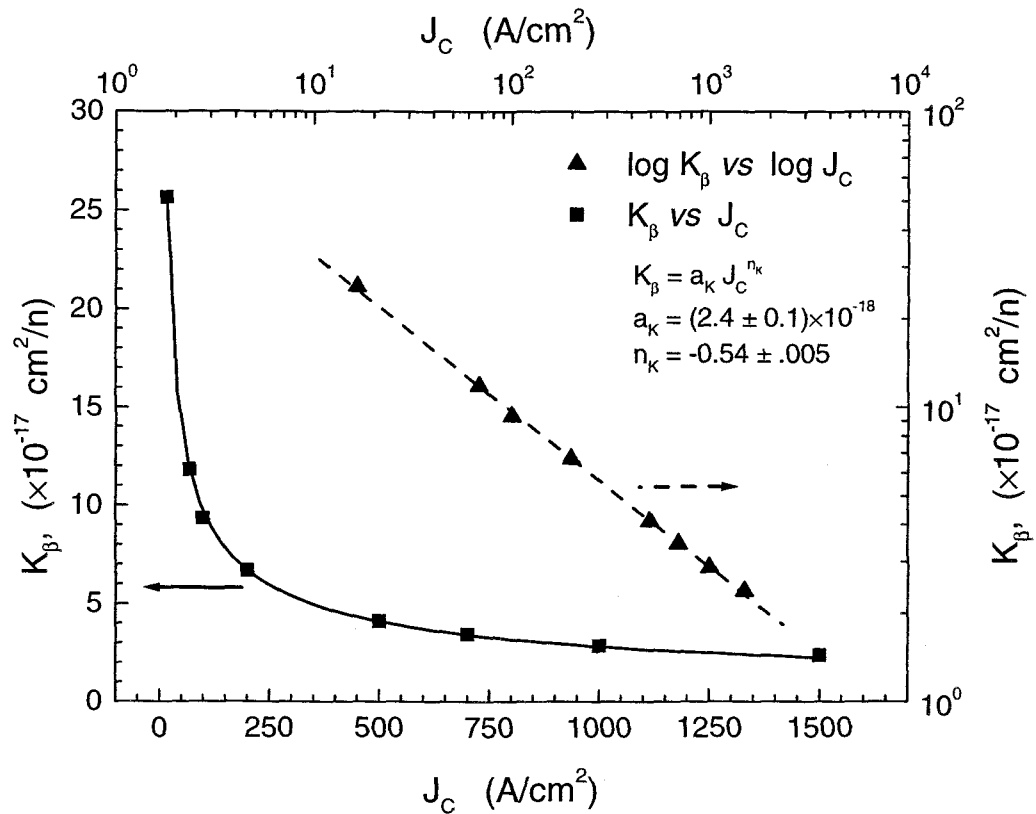


FIGURE 6.18. DC current gain degradation coefficient as a function of collector current.

separately. Recall that J_B for an HBT in the active mode can be written as

$$J_B = J_{sr} + J_{br} + J_{scr} \quad (6.5)$$

First consider the surface recombination base current J_{sr} . As shown in Fig. 6.20 the surface recombination component of J_B has some noticeable contribution in devices before irradiation. Fig. 6.21 shows the normalized gain reduction for devices of different sizes (different P/A ratio). It is observed that the gain degradation depends on the size of devices and is somewhat lower for the smaller devices. As

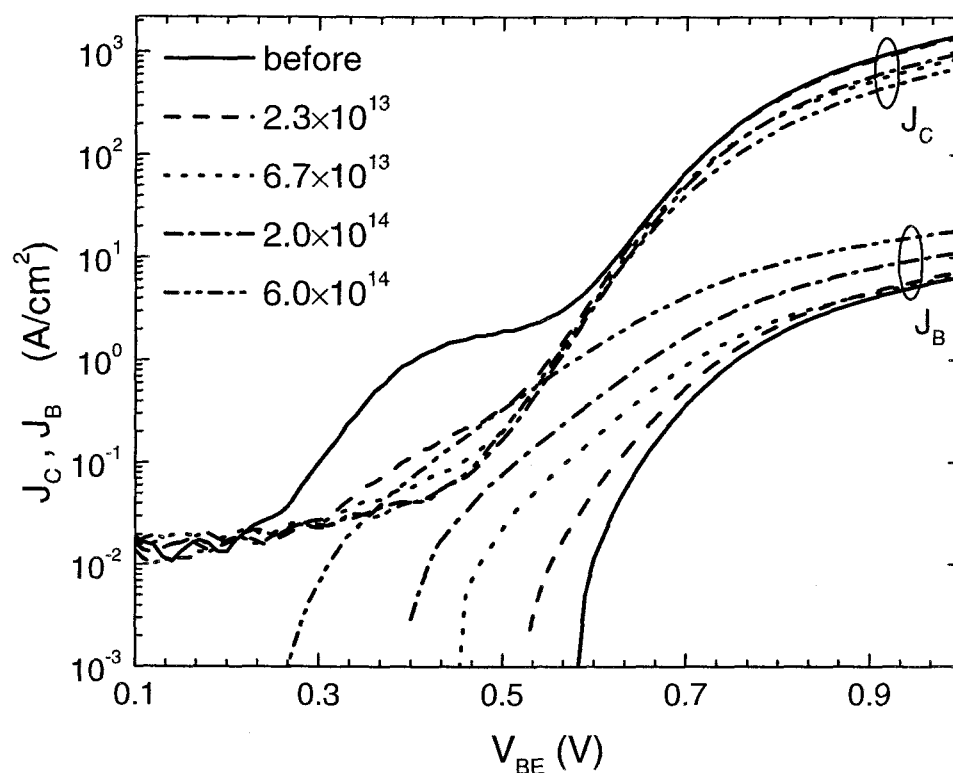


FIGURE 6.19. Gummel plots of J_C and J_B for various intermediate doses.

demonstrated in Fig. 6.20 after irradiation the gain of different size devices becomes independent of P/A . This suggests that the gain reduction or, in other words, the increase in the base current is dominated by the degradation of the bulk properties of devices. Therefore, the surface component of the base current can be ignored in further analysis of radiation-induced effects.

To analyze behavior of the two remaining components of the base current we now invoke Gummel-Poon model (see Section 4.5). Strictly speaking this approach may not necessarily yield physically reliable representation of the observed

$\Psi_{eq, InGaAs}$	J_{S0}	J_S	n_{F0}	n_F	R_{E0}	R_E
(n/cm^{-2})	$(\times 10^{-7} A/cm^2)$	$(\times 10^{-7} A/cm^2)$			(Ω)	(Ω)
2.3×10^{13}	1.8	0.6	1.3	1.3	14	16
6.7×10^{13}	1.2	0.4	1.3	1.4	24	28
2.0×10^{14}	1.6	0.7	1.4	1.3	18	24
6.0×10^{14}	3.4	3.5	1.4	1.4	18	33

TABLE 6.2. Saturation current and ideality factor for the collector current, and emitter series resistance extracted from forward Gummel plots of the collector current for different neutron fluences.

degradation. However, it can be very useful as a first step in an attempt to understand the radiation effects. Additionally, an investigation of applicability of a commercially available model for describing the radiation-induced degradation is always a very important step.

According to the Gummel-Poon model at low and moderate biases the base current can be fitted with

$$J_{br} = \frac{J_S}{\beta} e^{qV'_{BE}/n_F kT} \quad (6.6)$$

$$J_{scr} = C_2 J_S e^{qV'_{BE}/n_{EL} kT} \quad (6.7)$$

The extracted results are listed in Table 6.3. For the unirradiated device the base current is contributed by J_{br} entirely. After the lowest dose the recombination in

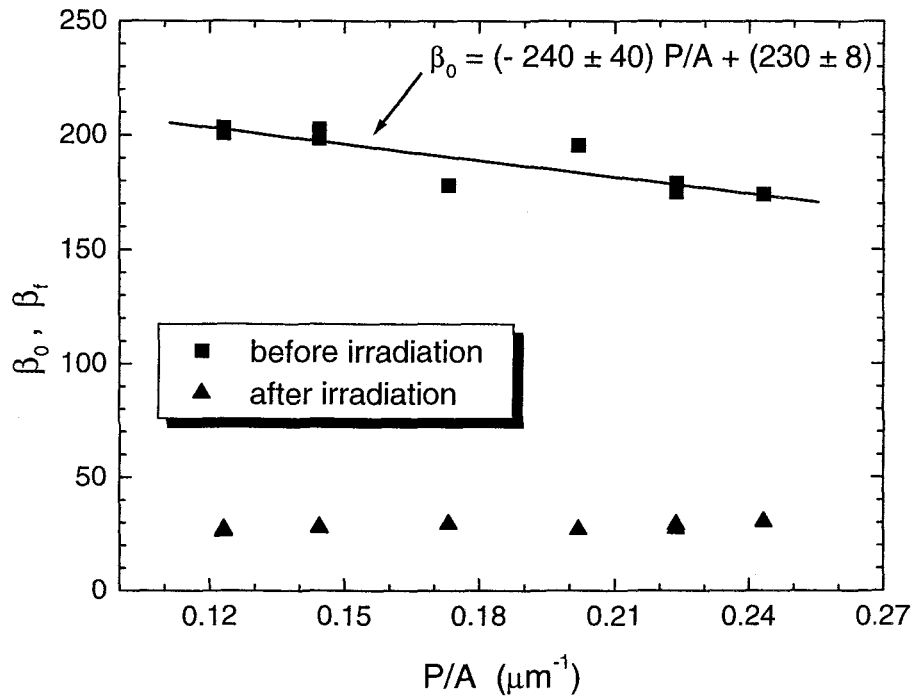


FIGURE 6.20. Initial, β_0 , and final, β_f , DC current gains measured at constant $J_C = 250 \text{ A/cm}^2$ as a function of perimeter-to-area ratio for different devices.

BE SCR comes into play and J_{scr} starts to contribute. As explained in Section 4.5 β used to fit J_{br} does not represent the actual current gain of the device anymore. For the second and higher doses the base current is dominated by J_{scr} while J_{br} is neglected. C_2 , which essentially represents changes in the SCR saturation current, increases steadily with the neutron fluence. n_{EL} also shows the same tendency rising from initial values of about 2 to a final value of 2.6 after the highest dose. If C_2 and n_{EL} are plotted as a function of the neutron fluence nonlinear correlation with Φ_n is observed. The SCR current calculated at a fixed V_{BE} (J_{scr} listed in

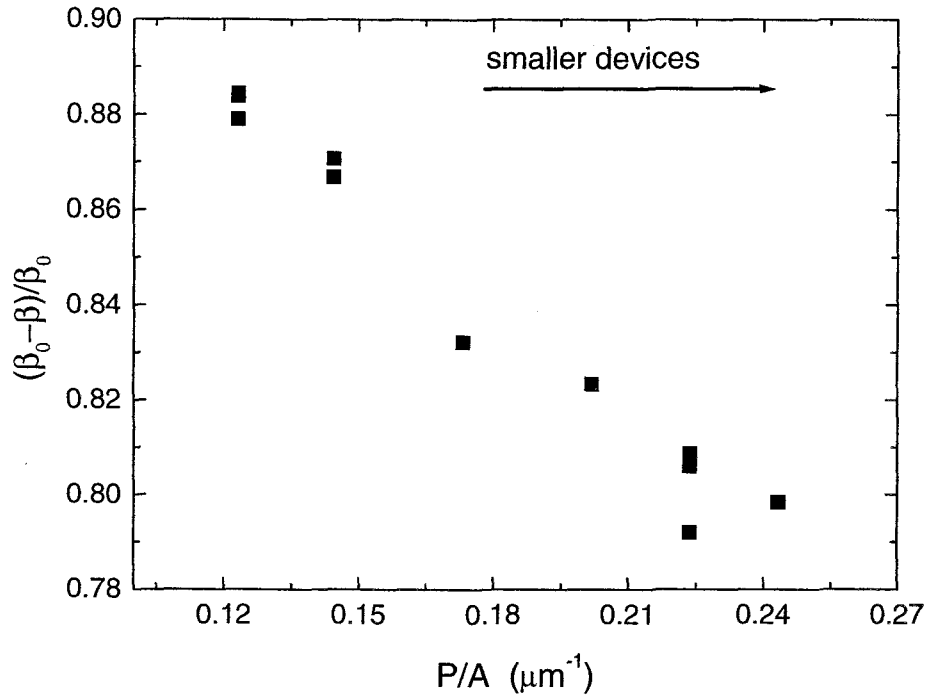


FIGURE 6.21. Normalized DC current gain degradation as a function of perimeter-to-area ratio for different devices.

Table 6.3) by using the extracted values of C_2 and n_{EL} , however, increases linearly with the neutron doses.

In conclusion, the base current at low doses can be described as a sum of neutral bulk and SCR recombination components. The GP model can be used to fit the data at low and moderate biases only. At higher doses J_{scr} becomes dominant as its saturation current and ideality factor rise. The model accurately describes the experimental data over the whole bias range. Values of n_{EL} in excess of 2.0 suggest that J_{scr} may be induced by effects other than SRH recombination.

Although, in general, the ideality factor n_{EL} for SCR recombination is close to 2 for recombination involving a single mid-gap level defect, strictly speaking it is theoretically possible to obtain ideality factors greater than 2 for recombination involving defects with a distribution of energy levels in the band gap. In order to arrive at more conclusive results regarding the origin of J_{scr} with high ideality factors we first investigate the behavior of the SRH current (J_{scr}^{SRH}) using the analytical model developed in Section 4.4.3. In this model the electron and hole lifetimes can be estimated by fitting the model's J_{scr}^{SRH} to experimentally determined J_{scr} . From the value of J_B at $V_{BE} = 0.6$ V, for a single midgap trap level the lifetimes, τ_n and τ_p , after the first dose are found to be 2.3 and 4.5 ns. Since carrier lifetime is directly proportional to the neutron fluence (see Eq. 2.14) τ_n and τ_p for the second, third and fourth dose should simply scale with neutron fluence. Calculated electron and hole lifetimes and corresponding J_{scr}^{SRH} are shown in Table 6.3. Using the calculated defect introduction rate $a_T^{InGaAs} \approx 127$ cm⁻¹ the capture cross section for the generation-recombination levels is found to be $\sigma_{BE} \approx 1.1 \times 10^{-14}$ cm². Although at $V_{BE} = 0.6$ V there is a good agreement between the model and experimentally observed J_{scr} the accuracy of this approach varies drastically as a function of the BE bias. In general the lifetimes needed to fit the experimental data with the SCR SRH model vary depending on the BE bias and the neutron dose. We must conclude that the SCR SRH with a single trap level recombination model is incapable of reproducing the experimentally mea-

sured base currents. SCR SRH mechanism also can not explain excess currents with ideality factors greater than 2.0 observed at the low biases.

Before continuing with the further discussion we should note that in a general case, when a large number of different traps is present, the recombination current should be calculated through Eq. 4.73. Instead of τ 's it is more meaningful then to use $(\sigma v_{th} N_t)^{-1}$ for each defect level. Still, the so-called "equivalent" carrier lifetime can often be used in calculations to represent all different recombination centers by a single energy level producing the same recombination current.

Φ_n (cm^{-2})	β	C_2	n_{EL}	$J_{scr,exp}(0.6 V)$ ($\times 10^{-2} A/cm^2$)	τ_n (ns)	τ_p (ns)	$J_{scr,calc}^{SRH}(0.6 V)$ ($\times 10^{-2} A/cm^2$)
–	210	t/n	t/n	0	t/n	t/n	t/n
2.3×10^{13}	227	7	2.0	4.4	2.3	4.5	5.4
6.7×10^{13}	t/n	76	2.2	17	0.8	1.5	17
2.0×10^{14}	t/n	473	2.4	44	0.27	0.5	41
6.0×10^{14}	t/n	3331	2.6	148	0.08	0.17	134

TABLE 6.3. GP and analytical model parameters used to fit base current at different intermediate doses. ("t/n" – term neglected)

To model the excess base currents observed at the low BE biases we invoke tunnel-assisted trapping mechanism presented earlier (Section 4.4.4). First consider current-voltage curves of the large-area BE diodes (see Fig. 6.22), where the measured characteristics are not affected by the adjacent BC junction unlike in the forward Gummel plots. At low biases ($V_{BE} < 0.4 \text{ V}$) the current quickly increases with the dose. Fitting the currents with $J_S \exp qV_{BE}/nkT$ (results are shown in Table 6.4) we observe that only the magnitude of the saturation current increases, while the slope remains constant. With each dose, except the first one, the saturation current increases varies linearly with neutron fluence. The discrepancy observed for the first dose $J - V$ curve can be attributed to the difference in the preirradiated values of J_B between the different samples used for different doses as shown by solid black lines in Fig. 6.22. This behavior of the $J - V$ characteristics suggests the following functional dependence of the current

$$J \propto B_0 N_t e^{B_1 V_{BE}} \quad (6.8)$$

where B_0 and B_1 are constants, and N_t is number of defects introduced by neutron irradiation $N_t = a_T \Phi_n$.

In the presence of a large number of defect levels in the forbidden gap of the junction the tunneling and emission-tunneling currents can flow in the diode (see Section 4.4.4). Relatively high current levels even at very low BE biases suggest that it is pure tunneling-recombination transport that is responsible for the observed $J - V$ characteristics [95, 93]. From Eq. 4.95 the tunneling current

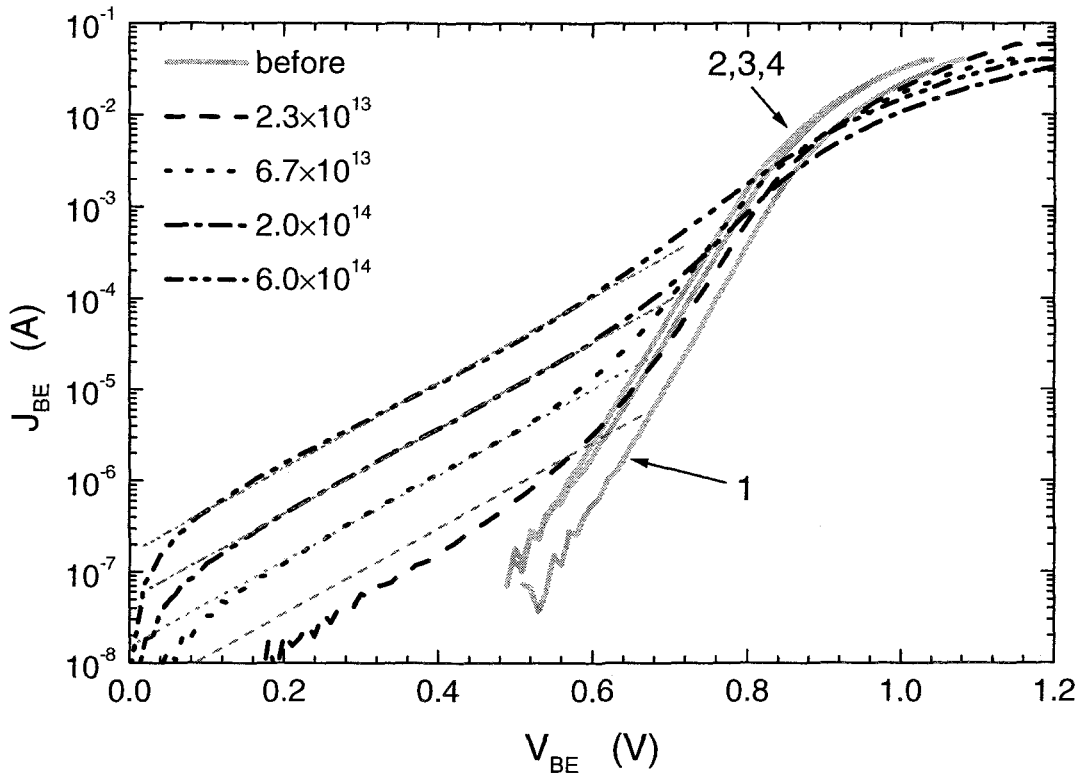


FIGURE 6.22. Measured (thick lines) and calculated (thin grey lines) current-voltage characteristics of large-area BE diodes for different intermediate doses.

density is given by

$$J_t = B' a_T \Phi_n e^{-\alpha \sqrt{s}(V_{bi} - K_1 V_{BE})} \quad (6.9)$$

Assuming calculated $\alpha \approx 58.68 \text{ eV}^{-1}$, $a_T \approx 141 \text{ cm}^{-1}$, $\Phi_n \approx 2.9 \times 10^{14} \text{ cm}^{-2}$ and $K_1 \approx 0.7$ we obtain $B' \approx 1.5 \times 10^{-9} \text{ A} \cdot \text{cm}$ and $s \approx 0.075$. As shown in Fig. 6.22 there is a good agreement between the tunneling currents calculated from these values and the experimental BE $I - V$ curves in the low bias regime.

Having introduced the tunneling recombination current we are now ready to proceed with the final complete analysis of the base current degradation. First

Φ_n	J_S	n	τ_n^{SRH}	τ_p^{SRH}
(cm^{-2})	(A/cm^2)		(ns)	(ns)
2.3×10^{13}	2×10^{-4}	3.5	10	20
6.7×10^{13}	1.5×10^{-3}	3.5	3	6
2.0×10^{14}	4.6×10^{-3}	3.5	1	2
6.0×10^{14}	1.4×10^{-2}	3.5	0.3	0.6

TABLE 6.4. Saturation current and ideality factor parameters used to fit current of large-area BE diodes in low bias regime at different intermediate doses.

consider the base current from the forward Gummel measurements for an unexposed device shown in Fig. 6.23. In this case the electron lifetime in the base layer is determined by the Auger and radiative recombination. Fitting our analytical model to the experimental curve we obtain

$$\tau_n^{Aug+rad} = 0.3 \text{ ns} \quad (6.10)$$

Measured and calculated base currents agree very well for all biases except the region where the the currents are very low ($V_{BE} < 0.5 \text{ V}$). Anomalous behavior of the measured current in that area is not currently understood. Since in real applications the devices are always operated at much higher current levels this discrepancy between measured and calculated is not a serious concern.

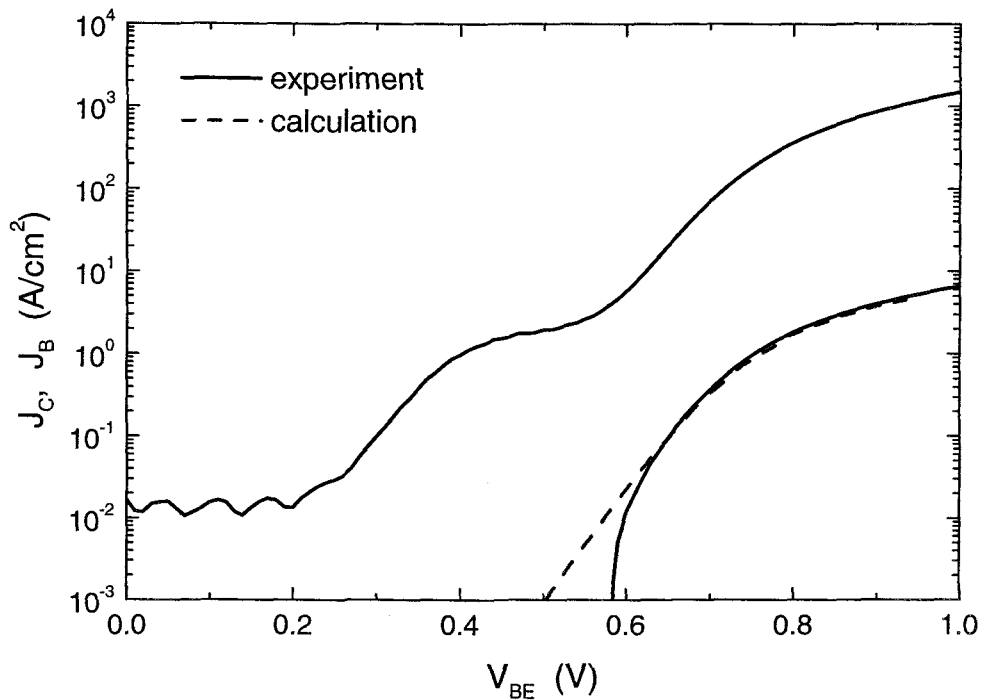


FIGURE 6.23. Measured and calculated forward Gummel plots for unirradiated device BA1M0.

During irradiation a significant number of defects is introduced in the semiconductor. Because of the very high doping of the base region the carrier concentration does not change noticeably. This was confirmed independently by Hall measurements performed on the base layer, and by $C-V$ measurements performed on the large area BE diodes. As a result, $\tau_n^{Aug+rad}$ is not affected by irradiation, and is assumed to be constant in all further calculations.

As the number of defects is increased due to irradiation, the SRH lifetime decreases and SCR and bulk SRH recombination currents start to contribute to the total base current. Additionally the tunneling-recombination current starts to

flow across the BE junction. Measured and calculated base currents of the forward Gummel plots are shown in Fig. 6.24a for a dose of $2.3 \times 10^{13} \text{ n/cm}^2$. At the high BE biases the current is still dominated by the Auger and radiative recombination. The two calculated curves are shown at the low biases. The first includes contribution of SRH current in the SCR only and is somewhat lower than the measured current. The second calculation takes into account both the SRH and tunneling components and provides very good fit down to the very low current range. Table 6.4 lists SRH electron and hole lifetimes used in these calculations. In the evaluation of the tunneling component $B' \approx 1.5 \times 10^{-9} \text{ A} \cdot \text{cm}$ and $s \approx 0.13$ were assumed. Number of defects in the *InP* emitter was estimated from $N_t^{InP} = a_T^{InP} \Psi_{eq, InP}$.

After a dose of $6.7 \times 10^{13} \text{ n/cm}^2$ contribution of the SRH and tunneling-recombination currents increases further. According to Eq. 2.14 the SRH lifetime should decrease by a factor of 3 (because the neutron fluence was increased by a factor of 3). The saturation current of the tunneling component should also increase by the same factor as it is simply proportional to the neutron fluence. The rest of the parameters in the model should stay unaffected, except maybe slight changes in parasitic resistances. Measured and calculated base currents of the forward Gummel plots are shown in Fig. 6.24b. The experiment and model show good agreement.

Further introduction of defects takes place as the device is irradiated to the higher $2 \times 10^{14} \text{ n/cm}^2$ dose. Once again the SRH lifetime is decreased and

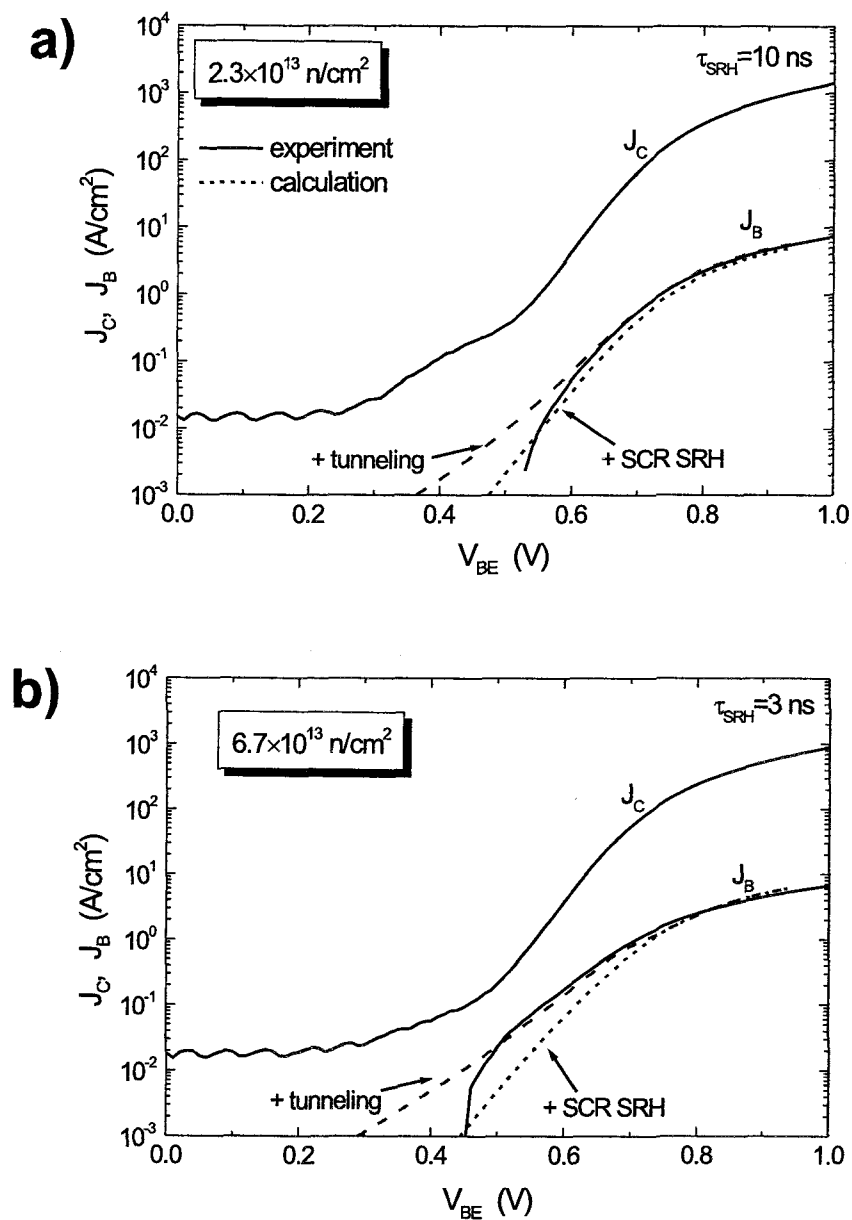


FIGURE 6.24. Measured (solid lines) and calculated (dashed lines) forward Gummel plots for devices irradiated to (a) 2.3×10^{13} and (b) $6.7 \times 10^{13} \text{ n/cm}^2$ (1 MeV (InGaAs)).

tunneling current is increased by a factor of 3. The SRH lifetime, $\tau_n = 1 \text{ ns}$, becomes comparable to the overall Auger and radiative recombination lifetime. For this reason an increase of the base current in the high bias range is observed. This is shown in Fig. 6.25a, where measured and calculated base currents of the forward Gummel plots are plotted. At low biases the current continues to rise as a net effect of increasing SCR SRH and tunneling components. The model fits the experimental data very well.

Modeled and measured data for the highest dose of $6 \times 10^{14} \text{ n/cm}^2$ are shown in Fig. 6.25b. In the calculations the SRH lifetime is decreased by a factor of 3 and number of defects is increased by the same factor. The model shows relatively good agreement with the experimental data. The slight discrepancy observed between the datasets can be attributed to possible change in the energy distribution of traps. This would affect s parameter of the tunneling model, which was assumed to be constant in all the calculations. Further investigation of this issue is needed.

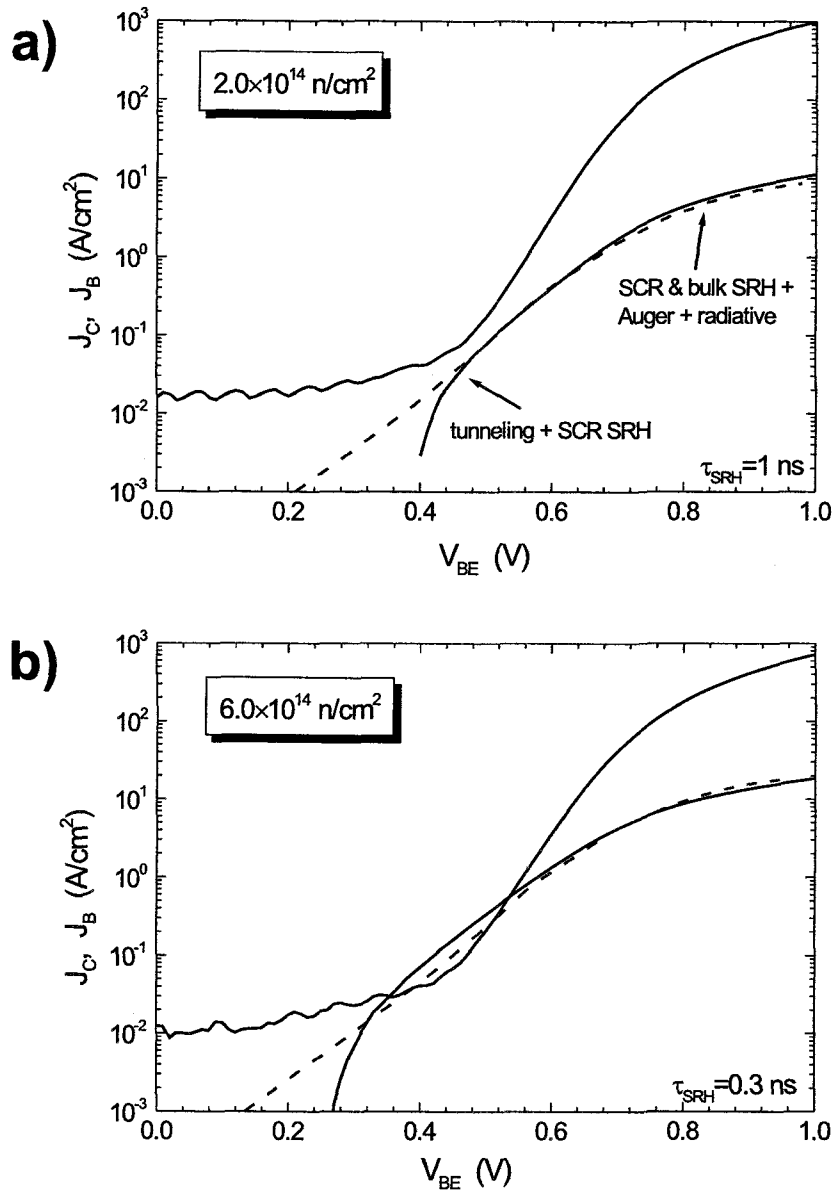


FIGURE 6.25. Measured (solid lines) and calculated (dashed lines) forward Gummel plots for devices irradiated to (a) 2×10^{14} and (b) $6 \times 10^{14} \text{ n/cm}^2$ (1 MeV *InGaAs*).

6.2.2.2. Gain Degradation Coefficient

To analyze the dependence of the gain degradation coefficient on the collector current we express K_β in the following form

$$K_\beta = \frac{\partial}{\partial \Phi} \left(\frac{1}{\beta} - \frac{1}{\beta_0} \right) = \frac{\partial}{\partial \Phi} \left(\frac{1}{\beta} \right) = \frac{\partial}{\partial \Phi} \left(\frac{J_B}{J_C} \right) \quad (6.11)$$

As was demonstrated for moderate and high doses the base current density can be written as

$$J_B = C_2 J_S e^{qV_{BE}/n_{EL}kT} \quad (6.12)$$

Calculating difference between logarithms of J_C and J_B we arrive at

$$\ln J_B - \ln J_C = \ln C_2 J_S + \frac{1}{n_{EL}} \frac{qV_{BE}}{kT} - \ln J_S - \frac{1}{n_F} \frac{qV_{BE}}{kT} \quad (6.13)$$

$$\ln \frac{J_B}{J_C} = \ln C_2 + \left[\frac{1}{n_{EL}} - \frac{1}{n_F} \right] \frac{qV_{BE}}{kT} \quad (6.14)$$

Expressing V_{BE} in terms of the collector current we can rewrite this equation as

$$\ln \frac{J_B}{J_C} = \ln C_2 + \left[\frac{n_F}{n_{EL}} - 1 \right] \ln \frac{J_C}{J_S} \quad (6.15)$$

which reduces to

$$1/\beta = \frac{J_B}{J_C} = C_2 \left[\frac{J_C}{J_S} \right]^{\frac{n_F}{n_{EL}} - 1} \quad (6.16)$$

In this equation only C_2 and n_{EL} are functions of the neutron fluence. The gain degradation coefficient is then found as

$$K_\beta = \frac{\partial C_2}{\partial \Phi} \left[\frac{J_C}{J_S} \right]^{\frac{n_F}{n_{EL}} - 1} - \frac{\partial n_{EL}}{\partial \Phi} \frac{n_F C_2}{n_{EL}^2} \left[\frac{J_C}{J_S} \right]^{\frac{n_F}{n_{EL}} - 1} \ln \left[\frac{J_C}{J_S} \right] \quad (6.17)$$

From analysis of the experimental results the second term can be neglected leaving

$$K_\beta = \frac{\partial C_2}{\partial \Phi} \left[\frac{J_C}{J_S} \right]^{\frac{n_F}{n_{EL}} - 1} \quad (6.18)$$

For high neutron fluences n_F/n_{EL} becomes close to 1/2 producing $K_\beta \propto J_C^{-1/2}$, which is confirmed by the experimental data shown in Fig. 6.18.

6.2.2.3. Base Collector Diode Degradation

Fig. 6.26 shows inverse Gummel plots of the base and emitter currents measured at different intermediate doses. At low biases the base current increases steadily with increase in the neutron fluence. The slope of I_B , however, remains practically constant for all neutron doses. In the bias range of 0.3 – 0.5 V the base current starts to saturate softly – typical signature of high-level injection effects induced by the low collector doping. At higher biases the current is series-resistance limited and all curves are bunched together suggesting a small degradation of the base and collector resistances. Initially low emitter current (inverse gain of 10^{-3}), on the other hand, decreases by more than two orders of magnitude as the neutron dose is increased.

For the further analysis we fit the base current with the following simple expression (see Section 4.3.1)

$$J_{B,BC} = J_{C,BC} = J_{B,BC}^{sat} e^{V_{BC}/n_R kT} \quad (6.19)$$

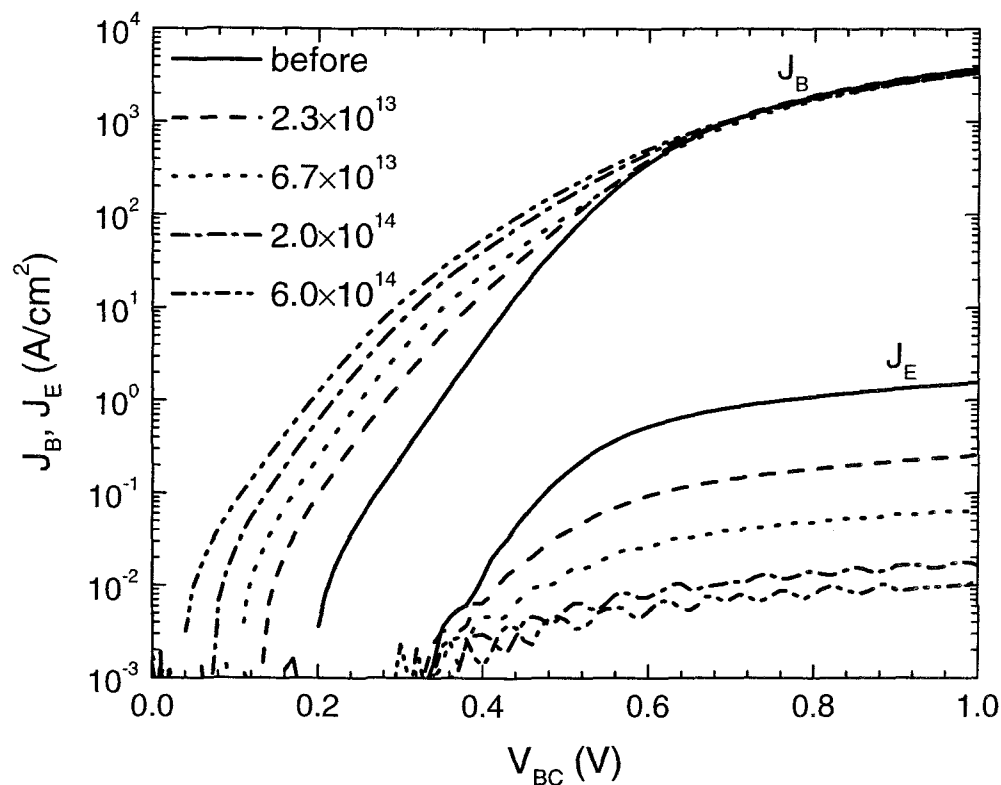


FIGURE 6.26. Inverse Gummel plots of J_B and J_E for various intermediate doses.

The extracted values of $J_{B,BC}^{sat}$ and n_R before irradiation (with an additional subscript 0) and after irradiation are listed in Table 6.5. As expected the saturation current increases significantly (from 4 to $550 \times 10^{-5} \text{ A/cm}^2$), while the ideality factor stays virtually unaffected at about 1.3-1.4. Recall that the base current can also be written as a sum of two components - diffusion and recombination - with ideality factors of about 1 and 2, respectively. Since n_R does not change significantly after irradiation, it suggests that both diffusion and recombination components are increased due to the displacement damage caused by neutrons.

We now extract $I_{BC,diff}^{sat}$ and $I_{BC,G-R}^{sat}$ by using the following expression

$$J_{BC} = J_{BC,diff}^{sat} e^{\frac{qV_{BC}}{kT}} + J_{BC,G-R}^{sat} e^{\frac{qV_{BC}}{2kT}} \quad (6.20)$$

The results are summarized in Table 6.6. Both $J_{BC,diff}^{sat}$ and $J_{BC,G-R}^{sat}$ increase steadily with the neutron dose. If plotted against the fluence $J_{BC,diff}^{sat}$ produces linear plot, while $J_{BC,G-R}^{sat}$ shows some deviations from the expected linear behavior. This can be explained by the fact that the diffusion component of the current is very much dominant in this regime making an accurate extraction of $J_{BC,G-R}^{sat}$ values very difficult. Approximating the recombination current with the following expression we can extract equivalent lifetimes and therefore trap capture cross sections for an assumed midgap defect level

$$J_{BC,G-R}^{sat} = \frac{1}{2} q W_{BC} \sigma v_{th} N_d n_i \quad (6.21)$$

At the first dose, for example, the carrier lifetime and the capture cross sections are found to be 3.9 ns and $7 \times 10^{-15} \text{ cm}^2$, respectively. Recall that from the BE junction analysis we obtained $\tau_n \approx 2.3 \text{ ns}$, $\tau_p \approx 4.5 \text{ ns}$ and $\sigma \approx 1.1 \times 10^{-14} \text{ cm}^2$, which lie in the same range as the BC results.

6.2.2.4. $V_{CE,off}$ shift

As already pointed out the collector-emitter offset voltage increases with the neutron dose. This is demonstrated in Fig. 6.27 showing magnified part of the $J_C - V_{CE}$ plot (Fig. 6.15). We start with a review of the device operation in the inverse active to saturation mode.

Sample #	J_{sat0}^{BC} ($\times 10^{-5} A/cm^2$)	n_{R0}	J_{sat}^{BC} ($\times 10^{-5} A/cm^2$)	n_R
1	3.3	1.3	39	1.4
2	5.0	1.4	84	1.4
3	3.5	1.3	221	1.4
4	4.3	1.4	550	1.4

TABLE 6.5. Saturation currents and ideality factors determined from inverse Gummel plots of base current before and after neutron irradiation.

Total collector current can be written as a sum of the components provided by the BE and BC junctions

$$J_C = J_{C,BE} - J_{C,BC} \quad (6.22)$$

where $J_{C,BE}$ and $J_{C,BC}$ are the collector currents from the forward and inverse Gummel plots, respectively. $J_{C,BC}$ is simply a sum of the base $J_{B,BC}$ and emitter $J_{E,BC}$ currents obtained in the inverse Gummel measurements. From Fig. 6.26 $J_{E,BC} \ll J_{B,BC}$, hence the total collector current can be written as

$$J_C = J_S [e^{V_{BE}/n_F kT} - 1] - J_{B,BC} \quad (6.23)$$

By definition $V_{CE,off}$ is given by the condition $J_C = 0$ yielding

$$J_S [e^{V_{BE}/n_F kT} - 1] = J_{B,BC} \quad (6.24)$$

Sample #	$J_{BC,diff}^{sat}$	$J_{BC,G-R}^{sat}$
	$(\times 10^{-5} \text{ A/cm}^2)$	$(\times 10^{-3} \text{ A/cm}^2)$
1	0.8	2.2
2	2.6	4.2
3	9.1	8.2
4	21	15

TABLE 6.6. Saturation currents of the diffusion and recombination J_{BC} components determined from inverse Gummel plots of base current after neutron irradiation.

In other words the offset point is determined from the balance between the collector current supplied by the BE and BC junctions. Hence, the observed $V_{CE,off}$ shift is produced by the radiation-induced degradation of $J_{C,BE}$ and $J_{C,BC}$. From our analysis (see Fig. 6.19 and Table 6.2) $J_{C,BE}$ remains practically unaffected by irradiation while magnitude of $J_{C,BC}$ increases over two orders of magnitude. Thus, it is the base-collector junction degradation that is responsible for the $V_{CE,off}$ shift. To confirm this hypothesis, a set of $J_C - V_{CE}$ curves for different doses was calculated using the Gummel-Poon model. In the simulation the saturation current and ideality factor of $J_{C,BE}$ and ideality factor of $J_{C,BC}$ were kept constant while the saturation current of $J_{C,BC}$ was changed as a function of dose (see Table 6.5).

The calculated $J_C - V_{CE}$ characteristics at base current of $40 \mu A$ are shown in Fig. 6.27 in dashed lines. The agreement between the simulated and experimental results is excellent.

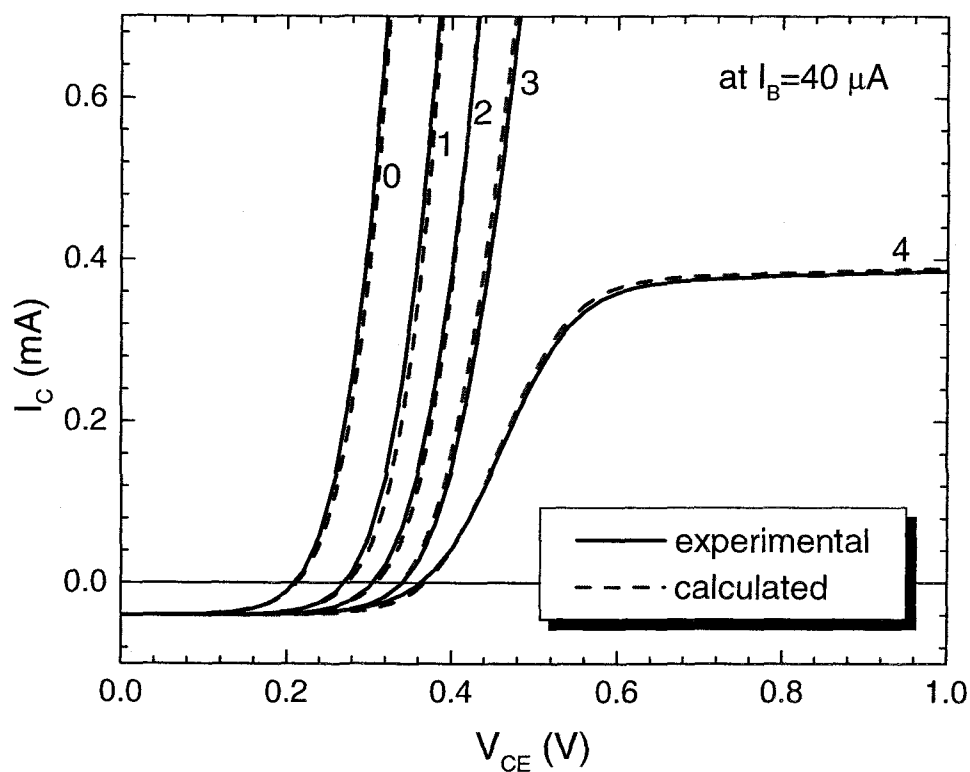


FIGURE 6.27. Experimental and calculated $I_C - V_{CE}$ characteristics for five different devices at $I_B = 40 \mu A$.

We now proceed to derive an analytical expression for the $V_{CE,off}$ shift. Analogously to the collector current the total base current can be presented as a sum of the base recombination current due to the BE junction $J_{B,BE}$ and the base

current due to the BC junction $J_{B,BC}$

$$J_B = J_{B,BE} + J_{B,BC} \quad (6.25)$$

$J_{B,BE}$ and $J_{B,BC}$ can be measured independently by the forward and inverse Gummel measurements, respectively. In the inverse active mode, also called offset mode, ($0 < V_{CE} < V_{CE,off}$) the base recombination current due to the BE junction is negligible. Hence,

$$J_B = J_{B,BC} = J_{B,BC}^{sat} e^{V_{BC}/n_R kT} \quad (6.26)$$

From Kirchhoff's voltage law $V_{CE,off}$ can be written as

$$V_{CE,off} = V_{BE,off} - V_{BC,off} \quad (6.27)$$

where $V_{BE,off}$ and $V_{BC,off}$ are the BE and BC junction voltages at the offset point, calculated from Eqs. 6.26 and 6.24 yielding

$$V_{CE,off} \approx \frac{n_F kT}{q} \ln \left[\frac{J_B}{J_S} \right] - \frac{n_R kT}{q} \ln \left[\frac{J_B}{J_{B,BC}^{sat}} \right] \quad (6.28)$$

This can also be presented graphically. Fig. 6.28 shows the collector current from the forward and inverse Gummel plots. At any given base current (horizontal line) $V_{CE,off}$ is simply a “voltage”-separation between the $J_{C,BE}$ and $J_{C,BC}$ curves. To confirm that representation $V_{CE,off}$ extracted from Fig. 6.28 and from $J_C - V_{CE}$ characteristics (Fig. 6.27) are shown in Fig. 6.29. The agreement is excellent.

We now discuss why neutron irradiation increases only the BC junction saturation current and not that of the BE junction. Neutron irradiation no doubt

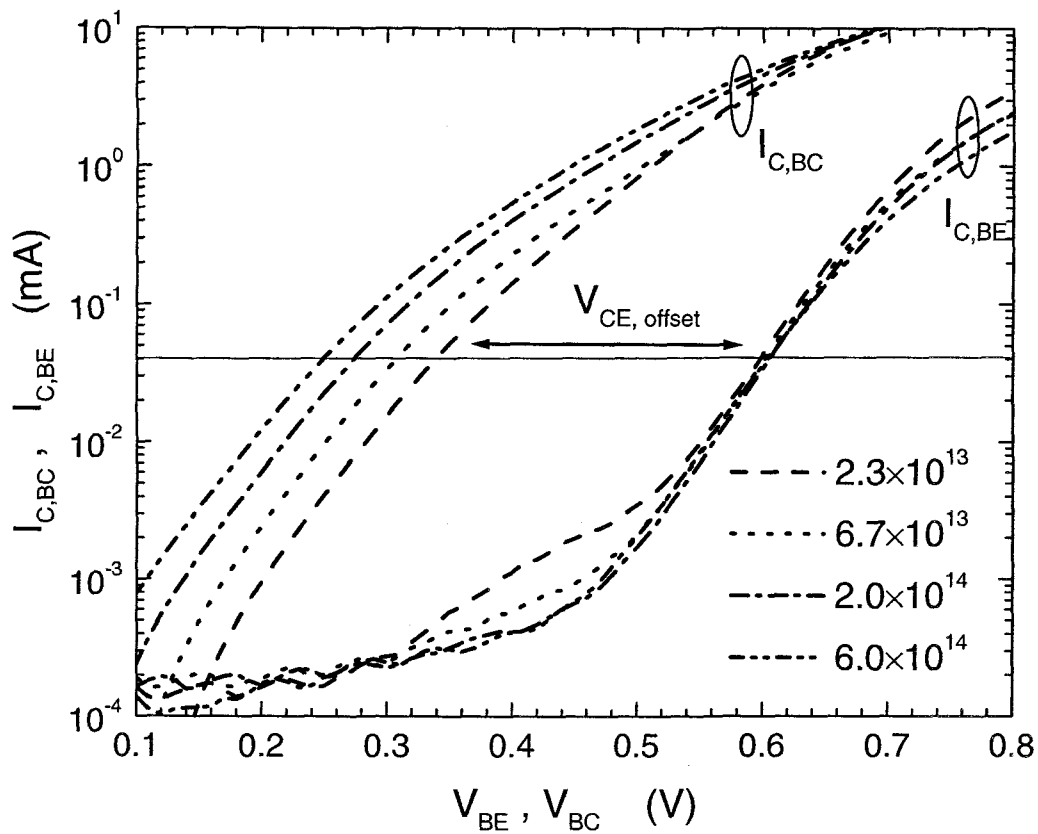


FIGURE 6.28. I_C ($I_{C,BE}$) from forward Gummel plots and I_B ($I_{C,BC}$) from inverse Gummel plots for various intermediate doses.

produces defects uniformly in all the regions of the device. The defects introduced in the BE junction region give rise to additional recombination and increase the base current. However, the saturation current of the BE junction is determined by the thermionic emission at the BE heterojunction and the diffusion across the base region. For a narrow base transistor such as the one used in this work, the diffusion across the base is mainly determined by the base thickness. Hence the collector current due to the BE junction is not significantly affected by the defects introduced

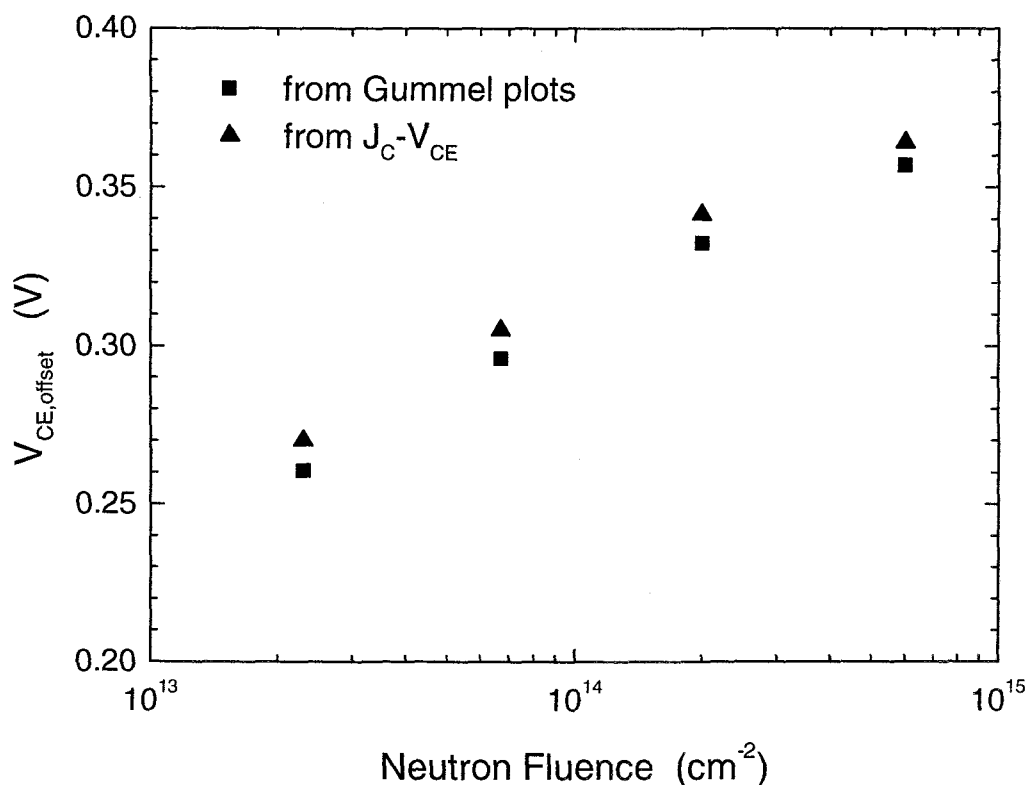


FIGURE 6.29. $V_{CE,off}$ extracted from $J_C - V_{CE}$ and Gummel plots as a function of neutron fluence.

in the base region. On the other hand, the current due to the BC junction of an SHBT is mainly due to the holes injected by the p^{++} base into the undoped collector whose thickness is usually larger than the hole-diffusion length. Hence the defects incorporated in the collector region increase the saturation current of the BC junction through additional recombination in the collector space charge region and/or decrease of hole-diffusion length in the neutral collector region.

6.2.3. Conclusions

In conclusion, experimental studies of *InP/InGaAs* SHBT neutron-induced degradation were carried out and results presented, analyzed and discussed. Two most pronounced radiation effects are (1) the decrease of collector current or equivalently the common-emitter DC current gain reduction and (2) the collector-emitter offset voltage shift. Current gain degradation is thought to be caused by increasing base current, mainly due to growing neutral bulk, BE SCR recombination and recombination-tunneling components. Rise of J_{br} and J_{scr} is caused by displacement damage produced by neutron irradiation. The $V_{CE,off}$ shift is produced by the increase of the BC junction current due to growing diffusion and SCR recombination components. Rise of $J_{BC,diff}^{sat}$ and $J_{BC,G-R}^{sat}$ is again caused by the defects introduced in the bulk of the semiconductor, in this case collector region.

The comprehensive analytical model developed in Chapter 4 has been successfully applied to simulate the current gain degradation. Hence, by combining the results of the damage production calculations with the model, device response to any given epi and fast neutron radiation environment can be estimated.

6.3. Gamma Irradiation

To conclude this chapter we briefly present the outcome of our preliminary *InP/InGaAs* SHBT gamma-irradiation experiments. This section starts with a brief discussion of the experimental results. In contrast to beta and neutron

irradiation sections much less attention is paid to modeling of the observed damage, though a detailed qualitative discussion is offered. The studied devices are divided into several groups basing on the dominating physical degradation mechanisms. Reliability of different metallization schemes in gamma irradiation environment is also investigated and results are briefly summarized.

6.3.1. Experimental Details

Standard processing procedure described in Chapter 5 was used to fabricate a large number of polyimide-passivated devices (47) with different emitter sizes with area ranging from $150 \mu m^2$ to $2600 \mu m^2$ and perimeter/area (P/A) ratio ranging from 0.08 to $0.4 \mu m^{-1}$. Heterostructure I3240 (see Table 5.1) was used for the fabrication. Gamma irradiation of the devices was performed using a ^{60}Co gamma cell with the typical dose rate of $250 \text{ krad}(Si)/\text{hour}$. The device terminals were left in a floating condition at ambient temperature during irradiation. The maximum cumulative dose used in the present experiments was $44.3 \text{ Mrad}(Si)$. The electrical characterization of the devices was done using an HP 4145B semiconductor parameter analyzer before irradiation and after intermediate doses of 0.3, 1.3, 4.3, 14.3 and 44.3 Mrad . The measurements were typically performed within a few hours after the irradiation.

6.3.2. Results and Discussion

The devices investigated in this study may be classified into three groups depending on the extent and nature of degradation after gamma irradiation. The first group, which comprises of about forty percent of the total number of devices studied, suffered least degradation. Typical common-emitter $I_C - V_{CE}$ characteristics measured at base current of $40 \mu A$ at different intermediate doses are shown in Fig. 6.30. Only very slight decrease in the collector current and increase in $V_{CE,off}$ is observed. To understand the current gain mechanism we turn to the Gummel plots of the base (I_B) and collector (I_C) current shown in Fig. 6.31. Except for the small increase in I_B in the low V_{BE} regime, there was very little change either in I_B or in I_C up to a cumulative dose of $14.3 Mrad$. After the highest dose ($44.3 Mrad$) there was a slight increase in both I_B and in I_C in the high V_{BE} regime. This slight increase in the current is believed to be due to a decrease in the emitter series resistance. The BE diode $I - V$ measurements indeed confirmed a decrease of series resistance from 17 to 16 ohms. The local heating of the device after the highest dose may have caused the metal contacts to sink into the emitter layer resulting in the decrease of series resistance. The collector current dependence of DC current gain of these devices for various doses is shown in Fig. 6.33. There is very little change in gain at the high collector currents. The small decrease of gain in the low V_{BE} regime is associated with the base current increase in the same V_{BE} regime observed in Fig. 6.31. This increase in the base current is believed to be

caused by the displacement damage in the BE depletion region associated with the gamma radiation and the additional recombination at these defect sites. Finally, inverse Gummel plots of the base and emitter currents (see Fig. 6.32) do not show significant degradation. In the low V_{BC} range at very low doses ($\leq 1.3 \text{ Mrad}$) the base current decreases slightly, perhaps, due to burn in effects. At higher doses the displacement damage introduced by gamma irradiation results in slightly higher current levels. As discussed in Section 6.2.2.4 it is these changes in the base current that are responsible for the $V_{CE,off}$ shift observed in Fig. 6.30.

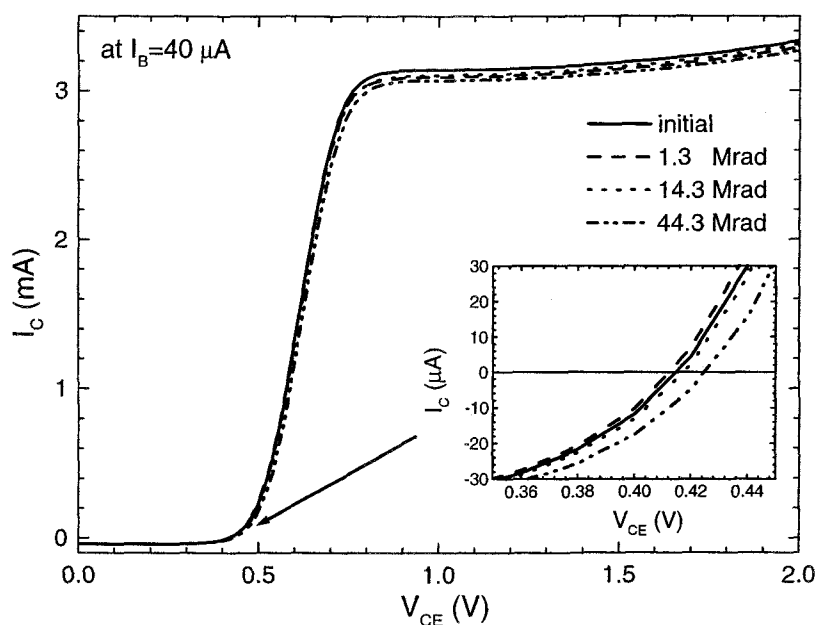


FIGURE 6.30. The common emitter $I_C - V_{CE}$ characteristics at base current of $40 \mu A$ for different intermediate doses (device ID:AN1Q).

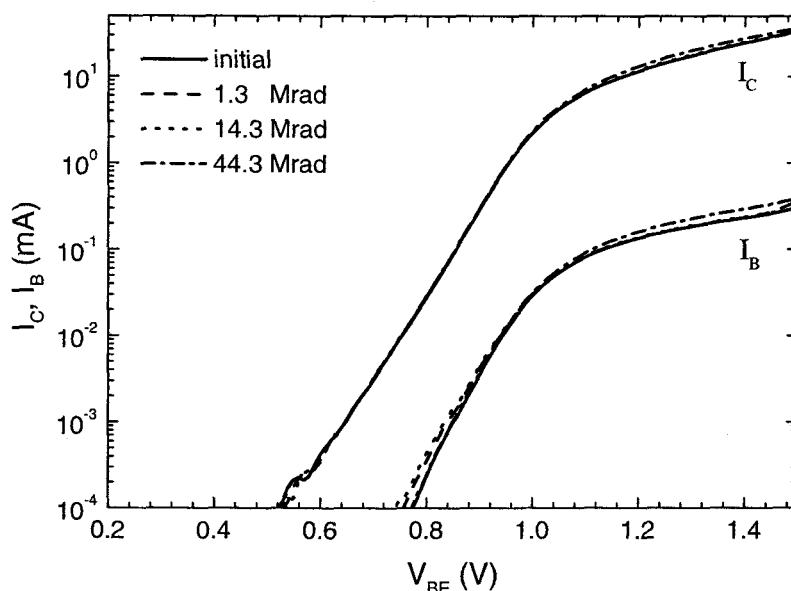


FIGURE 6.31. Gummel plots of I_C and I_B for various intermediate doses (device ID:AN1Q).

The second group of devices showed no degradation up to a certain dose and then a sudden jump in the collector, base and emitter leakage currents in the low bias range as shown in Figs. 6.36 and 6.37. In the high bias regime, the degradation is small, but is larger than that of the first group of devices. The common-emitter I_C-V_{CE} characteristics measured at base current of $40\ \mu A$ at different intermediate doses are shown in Fig. 6.34. The collector current dependence of the gain of this group of devices is shown in Fig. 6.35. It may also be mentioned that the dose at which the devices showed the sudden degradation was not the same for all the devices in this group. About forty percent of the devices studied belong to this group. We believe that the large increase in the leakage currents in the low bias

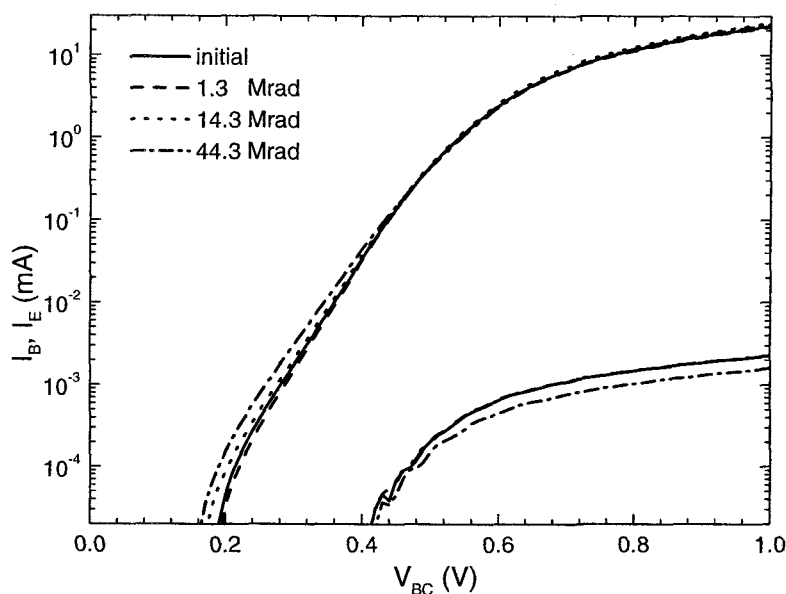


FIGURE 6.32. Inverse Gummel plots of I_B and I_E for various intermediate doses (device ID:AN1Q).

regime is caused by the degradation of the polyimide-semiconductor interface. The physical mechanism of the degradation is not exactly understood at this time. It is most likely related to the ionization damage in the polyimide and the subsequent trapping of the charges at the defects near the polyimide-semiconductor interface. This in turn causes a surface channel to be formed at the mesa edges of the device through which the leakage current can flow. Confirming this, Figs. 6.38 and 6.39 show dramatic increase of the BE and BC diode leakage currents at the dose when the device fails.

The remaining-twenty percent of the devices that belong to the third group behaved somewhat similarly to the second group in that the degradation occurred

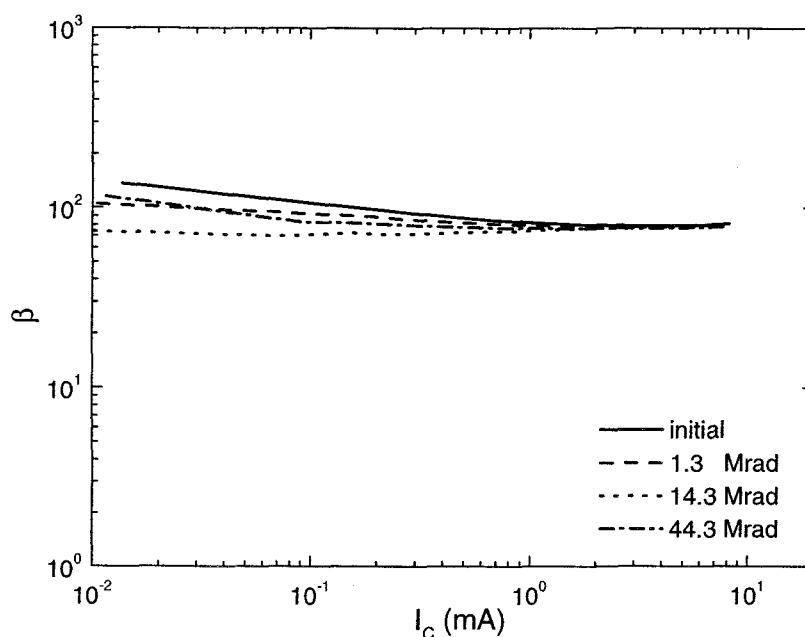


FIGURE 6.33. DC current gain as a function of collector current for different intermediate doses (device ID:AN1Q).

suddenly after a certain dose. However, the degradation was not as severe, so that the devices did not fail catastrophically with loss of transistor action. Subsequent to the sudden degradation, these devices did not show much further deterioration for higher doses. The Gummel plots of I_B and I_C for this group of devices are shown in Fig. 6.41. And the common-emitter $I_C - V_{CE}$ characteristics measured at base current of $40 \mu A$ are shown in Fig. 6.40. The physical mechanism of degradation is believed to be the same as that of the second group. Only the extent of degradation is less severe leading to only a partial “failure” of the device. The evolution of the cumulative percentage of the devices in the groups II and III with gamma radiation dose is shown by the histograms in Fig. 6.42.

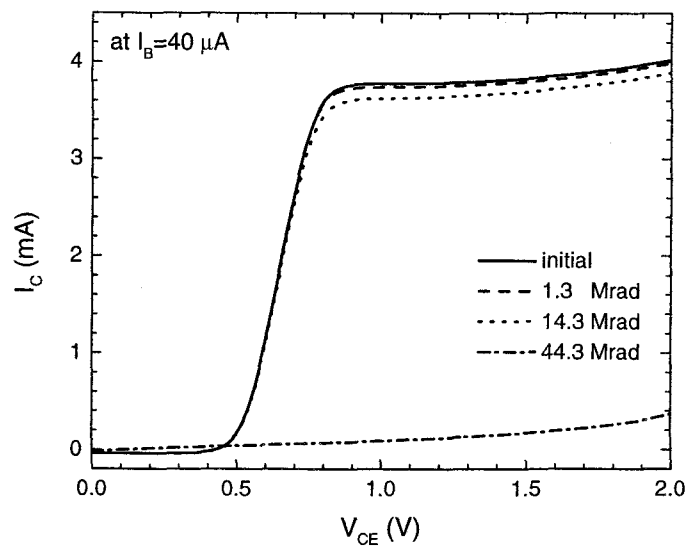


FIGURE 6.34. The common emitter $I_C - V_{CE}$ characteristics at base current of $40 \mu A$ for different intermediate doses (device ID:AN2Y).

6.3.3. Radiation-hard Metallization Schemes

Gamma irradiation studies on *InAlAs/InGaAs* SHBTs reported by Witmer *et. al.* [4] also showed a catastrophic failure of a certain fraction of the devices. The nature of failure in this case was reported to be an open-device between the emitter and the collector terminals after the gamma irradiation. This failure was attributed to the deterioration of contacts resulting from the lift-off of the contact metals as evidenced by the debris around the contact metals after irradiation. The failure mechanism in our devices was always related to the excess leakage currents causing loss of transistor action. The contact metallization consisting of 500 \AA of *Ti* followed by 1200 \AA of *Au* showed only very little signs of deterioration even

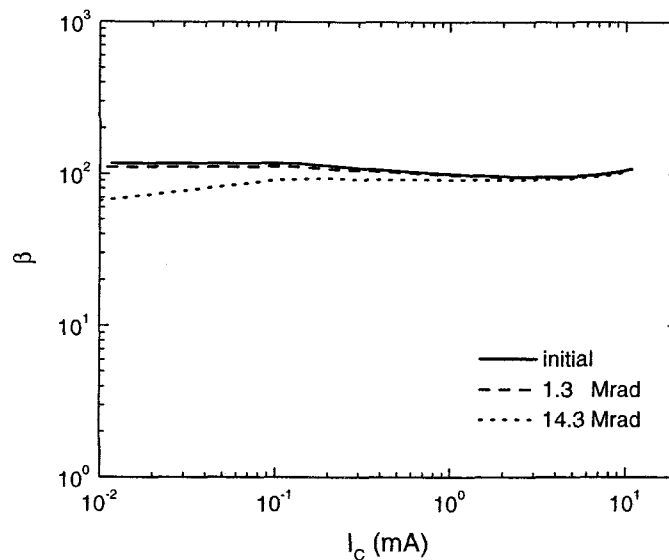


FIGURE 6.35. DC current gain as a function of collector current for different intermediate doses (device ID:AN2Y).

after the highest dose. However, we have observed contact metal deterioration and the debris around the metals after gamma irradiation similar to the observation of Witmer *et. al.* when we used a thin layer of *Ti* (100 Å) followed by 1200 Å of *Au*. In a search for a reliable radiation-hard metallization scheme a number of different metal systems was tested. Table 6.7 lists investigated metal/substrate combinations and shows whether or not the contact metal degraded (✓ means no degradation observed, × – visible deterioration). Since sometimes contact metal needs to be deposited on a passivation dielectric polyimide, *SiO₂* and cyclotene were included in this study.

- *Au* contacts offer very low resistivity and good stability, but adhere to the substrates very poorly.

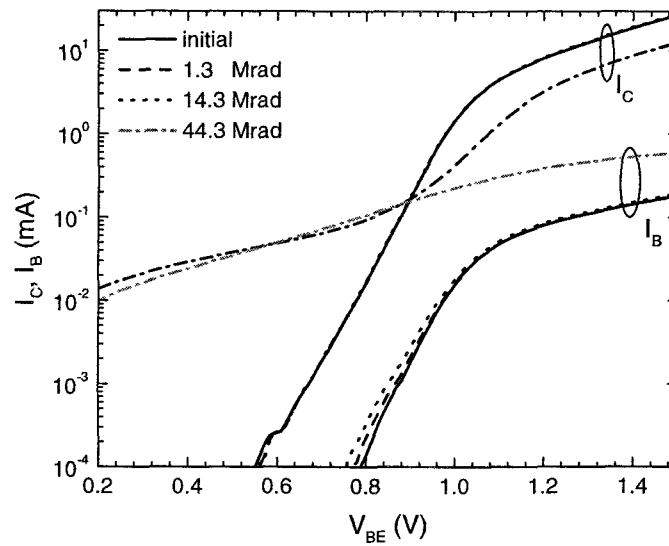


FIGURE 6.36. Gummel plots of I_C and I_B for various intermediate doses (device ID:AN2Y).

- $Ti/Au(150/1000\text{\AA})$ metallization employs thin layer of Ti as an adhesion promoter. This, however, increases resistivity and makes the contact unstable if exposed to gamma radiation or elevated temperatures.
- In $Ti/Au(1000/1000\text{\AA})$ films thick Ti layer is used to eliminate the stability problems by further sacrificing conductivity of the contact.
- Alternatively thin layer of Ti can be separated from Au contact layer by a film of low resistive Pd or Pt as done in $Ti/Pd/Au(150/500/1000\text{\AA})$ and $Ti/Pt/Au(150/500/1000\text{\AA})$ schemes, respectively. These films exhibit very good adhesion, relatively low resistivity and are very stable under irradiation. Both schemes offer the comparable characteristics. How-

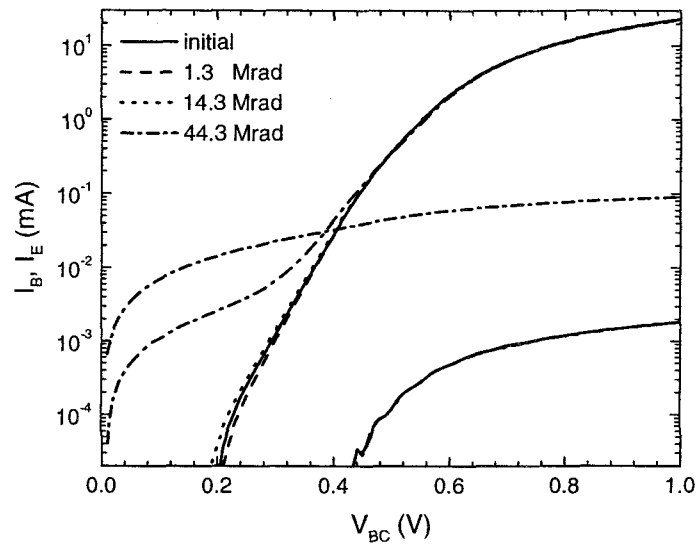


FIGURE 6.37. Inverse Gummel plots of I_B and I_E for various intermediate doses (device ID:AN2Y).

ever, very high temperatures needed for evaporation of Pt make PVD of $Ti/Pt/Au(150/500/1000\text{\AA})$ contacts very difficult.

- In $Pd/Au(1000/1000\text{\AA})$ films to further reduce resistivity adhesion-promoting Ti layer is removed entirely. The films still offer acceptable adhesion, are much easier to deposit and are very stable under irradiation.
- $Ni/AuGe(100/1000\text{\AA})$ annealed scheme can be used to produce low resistivity, stable contacts on n-type $GaAs$ and $InGaAs$. It was also shown to form a good ohmic contact on n-type InP layers. $Ni/AuGe$ can not however be used to contact p-type layers ($Ni/AuZn$ must be used instead) sometimes making the fabrication sequence more complex.

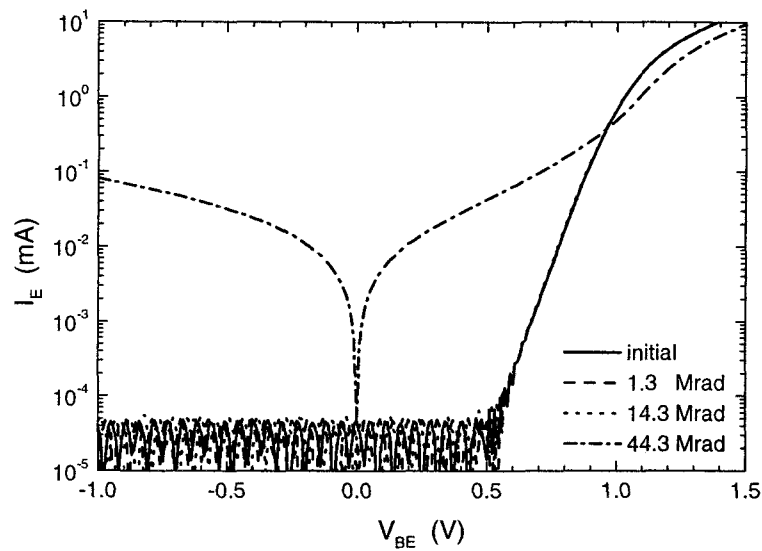


FIGURE 6.38. Semilogarithmic plot of $I-V$ characteristics of BE diode for various intermediate doses (device ID:AN2Y).

- Finally, in $Ni/Au(150/1000\text{\AA})$ contacts a thin layer of Ni is used as a wetting agent instead of Ti . The films, however, degrade rapidly under irradiation stress and therefore can not be used for device fabrication in our studies.

The optimum contact metal schemes for smaller contact resistance and no degradation after gamma irradiation are found to be annealed $Ni/AuGe$ for emitter/collector contacts, Pd/Au for the base layer and $Ti/Pd/Au$ for the final metallization performed on top of a passivation layer.

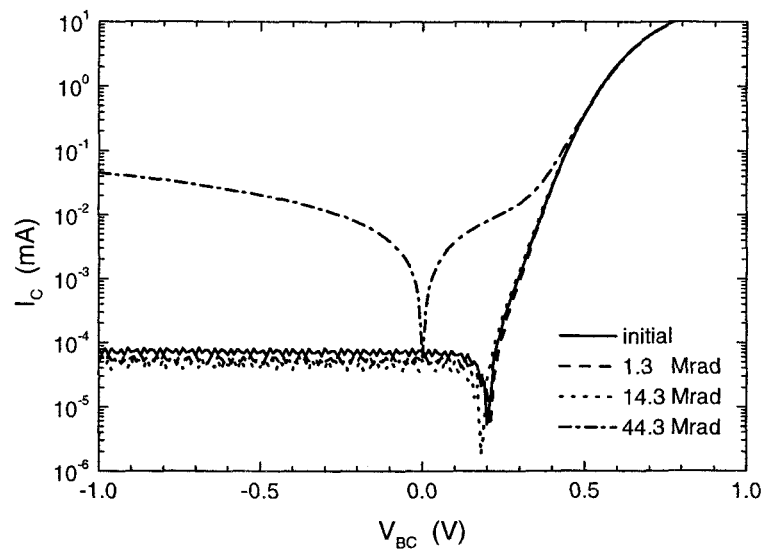


FIGURE 6.39. Semilogarithmic plot of $I-V$ characteristics of BC diode for various intermediate doses (device ID:AN2Y).

6.3.4. Summary

Preliminary studies of *InP/InGaAs* SHBT gamma-induced degradation were carried out and results briefly presented and discussed. Two typical device responses are observed. First, as expected for the low doses used in this experiment, displacement-related degradation is little and fits the degradation pattern observed in our electron and neutron-irradiation studies. That is, defects introduced in the BE and BC junctions are responsible for most of the observed damage – current gain reduction and $V_{CE,off}$ shift, respectively. The other type of device response is HBT catastrophic failures of very erratic behavior. The failures can be attributed to formation of leakage channels along the passivation/semiconductor interface due

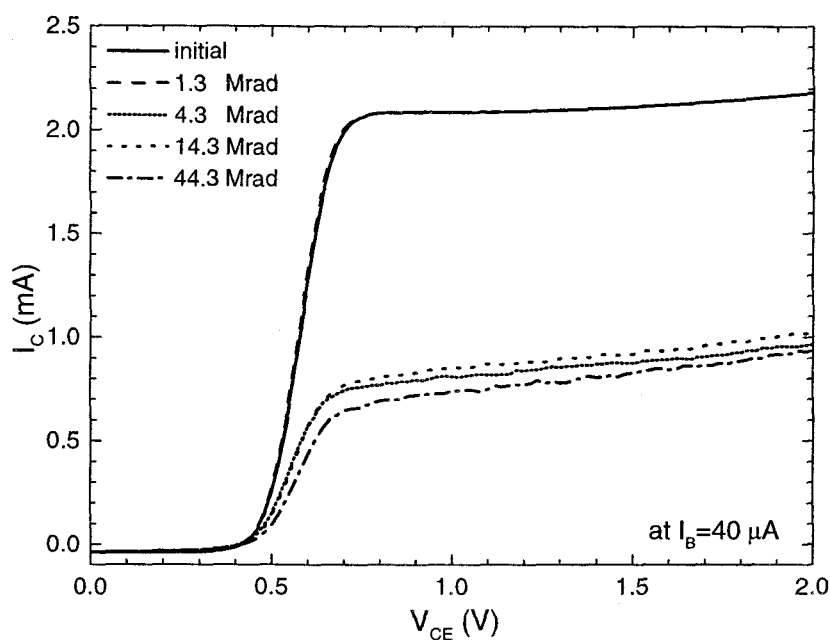


FIGURE 6.40. The common emitter $I_C - V_{CE}$ characteristics at base current of $40 \mu A$ for different intermediate doses (device ID:AN40).

to charge build-up in the passivating dielectric. Further experiments are needed to investigate this problem.

6.4. Conclusions

In conclusion, several different degradation patterns were observed in our SHBT irradiation experiments. With the exception of the catastrophic failures induced by gamma-irradiation the rest of the deterioration effects are common to beta, neutron and gamma environments. Careful analysis of the changes in the device characteristics suggests that it is the displacement effects that are responsible

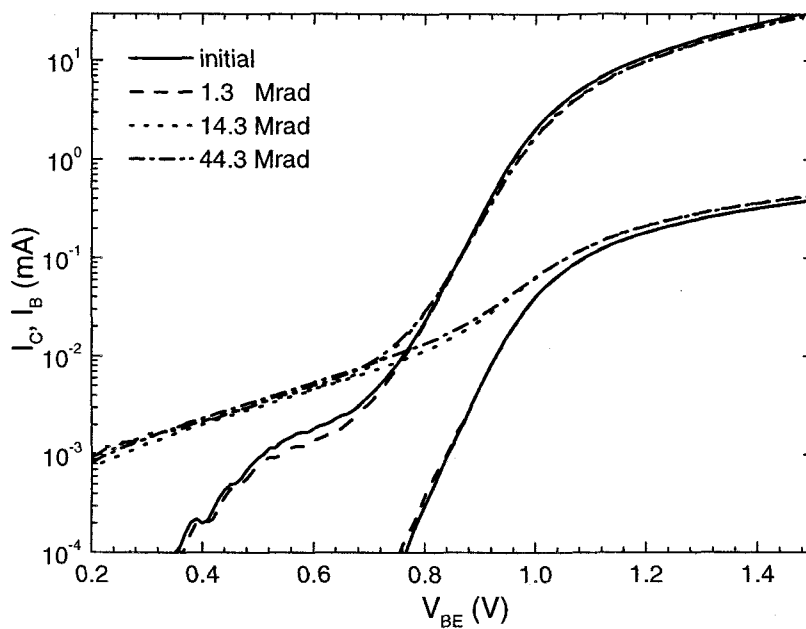


FIGURE 6.41. Gummel plots of I_C and I_B for various intermediate doses (device ID:AN4O).

for the permanent damage of the devices. Calculations of the displacement damage production combined with the comprehensive analytical HBT model can therefore be employed to evaluate device response to a given radiation environment.

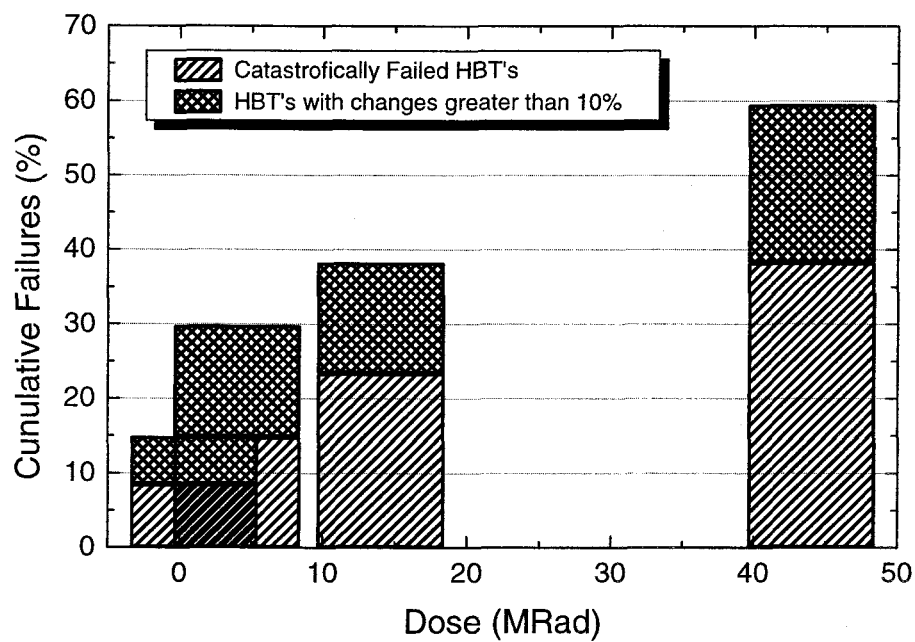


FIGURE 6.42. Cumulative number of degraded HBT's as a function of total gamma dose.

	<i>SiO₂</i>	<i>InGaAs</i>	<i>InP</i>	<i>GaAs</i>	<i>polyimide</i>	<i>bc</i>
<i>Au</i> (1000Å)	✓	✓	✓	✓		
<i>Ti/Au</i> (150/1000Å)	×	×	×	×	×	×
<i>Ti/Au</i> (1000/1000Å)	✓	✓	✓	✓	✓	✓
<i>Ti/Pd/Au</i> (150/500/1000Å)	✓	✓	✓	✓	✓	✓
<i>Ti/Pt/Au</i> (150/500/1000Å)	✓	✓	✓	✓	✓	✓
<i>Pd/Au</i> (1000/1000Å)	✓	✓	✓	✓	✓	✓
<i>Ni/AuGe</i> (100/1000Å)		✓	✓	✓		
<i>Ni/Au</i> (150/1000Å)	×	×	×	×	×	×

TABLE 6.7. Stability of gamma-irradiated various metal films deposited on different substrates.

7. CONCLUSIONS AND RECOMMENDATIONS FOR FUTURE WORK

The purpose of this research was to investigate radiation-induced degradation of III-V materials and heterojunction bipolar transistors, with an emphasis on *InP/InGaAs* systems. Furthermore particular attention has been given to development of an accurate physical HBT device model and calculations of radiation damage production. In the course of this work the *InP/InGaAs* SHBTs were fabricated, characterized and modeled. Subsequently, the devices were subjected to beta (or gamma, or neutron) irradiation and the degradation effects were studied and modeled. Fig. 7.1 summarizes the radiation-induced effects observed in the devices and also shows the general approach taken to model the HBT degradation. Two major effects are (1) the decrease of collector current or equivalently the common-emitter DC current gain reduction and (2) the collector-emitter offset voltage shift. Current gain degradation is thought to be caused by increasing base current, mainly due to growing neutral bulk and BE SCR recombination and recombination-tunneling components induced by displacement damage produced by neutron irradiation. In the other branch of the diagram, $V_{CE,off}$ shift is caused by increase of BC junction current due to growing diffusion and SCR recombination components. Rise of the currents is again caused by the defects introduced in the bulk of the semiconductor, in this case collector region. As shown on the chart connections between different levels in the tree can be made only through

an HBT device model which relates material and device properties to the device output characteristics.

Once all the degradation mechanisms are identified, understood and described through the HBT model the problem can be attacked from the other end. Damage production theory can be used to calculate the displacement damage introduced by irradiation in layers of a device. Then the separate current components and total terminal currents can be estimated. Finally, device output characteristics are calculated representing device response to a given radiation environment.

The major achievements and conclusions of this work are:

1. Individual processes and several complete fabrication sequences for fabrication of *InP/InGaAs* SHBTs have been developed and standardized. All of the procedures employ wet etch techniques to define mesas of the devices. Different metallization schemes (*Ni/AuGe* for emitter and collector contacts, *Pd/Au* for base layer and *Ti/Pd/Au* for contact pads) can be used to achieve better performance. And, finally, dielectric passivation is used to protect the devices physically and chemically.
2. A simple Ebers-Moll-like compact model has been adopted to extract device parameters and simulate device output characteristics and some of the radiation induced effects: gain degradation and $V_{CE,off}$ increase.
3. An analytical SHBT device model has been developed. The model is based on matching of thermionic-field-emission current of the BE heterojunction

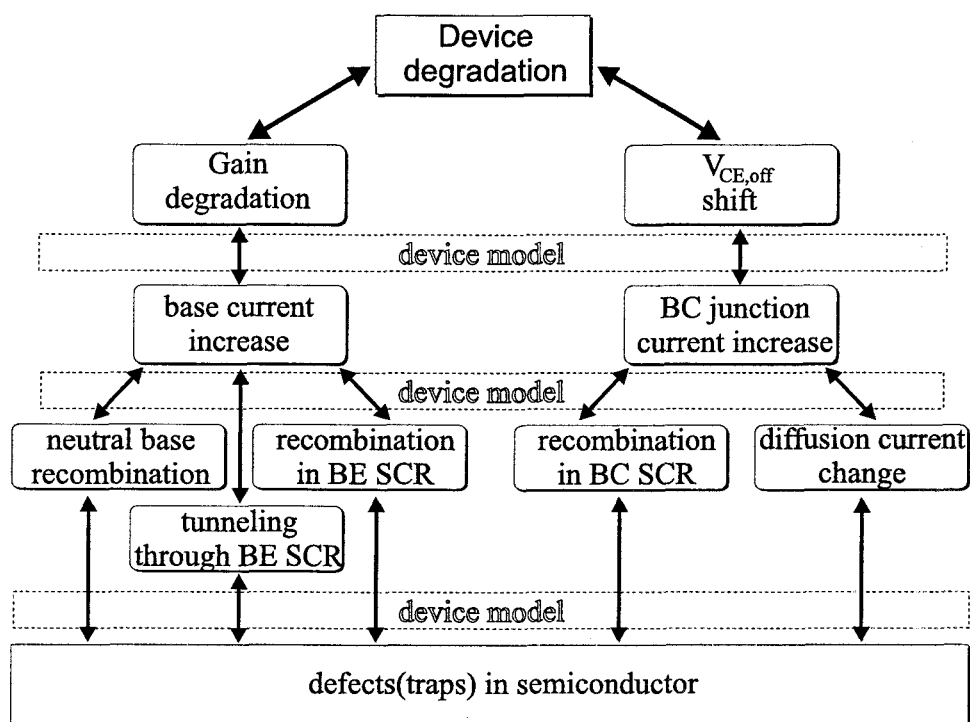


FIGURE 7.1. Modeling tree used to explain/simulate HBT degradation effects induced by irradiation.

with diffusion-drift current in the base layer of an SHBT. The model also incorporates splitting of the electron quasi-Fermi level at the BE heterointerface and provides adequate representation of the BE SCR recombination current through the SRH mechanism.

It has been shown that the diffusion and drift of carriers across the base and collector SCR is much faster than the carrier injection at the BE het-

erointerface; therefore the current transport in an SHBT is limited by carrier injection at the BE junction.

The only high level injection effect observed is the “soft” saturation of electron flux provided by the emitter. In the base layer the high level injection is not observed due to extremely high doping concentration. The base push-out, or Kirk effect, although does take place does not affect output characteristics of the device since the current transport is limited by injection of carriers at the BE junction.

4. It has been shown that standard BJT Gummel-Poon SPICE model can be used for simulation of SHBTs. In the forward active mode, devices with the base current with ideality factor close to 2 can be simulated very accurately in the whole bias range, while for devices with $n_B \approx n_F$ the model provides adequate results only at low and moderate biases.

In the saturation mode, simulations performed at low current levels should always give reliable results. At the higher currents, however, special care must be exercised since accuracy of parameters extracted from experimental data may depend on the operating biases.

5. Methods for calculating doses and displacement damage produced by electron, neutron and gamma irradiation have been presented. Non ionizing energy loss and number of defects introduced by the different types of radia-

tion have been evaluated. 1 MeV electron and neutron equivalent fluxes for all types of radiation have also been calculated.

6. Preliminary beta-irradiation experiments on *InP/InGaAs* SGBTs have been performed. The devices show excellent radiation performance. After a cumulative dose of $2.7 \times 10^{16} \text{ e/cm}^2$ (620 Mrad(*InGaAs*)), the devices showed a typical decrease of only 9 percent in the collector current in the active regime and no change in the output conductance.

For low base currents, the devices show an increase in the current gain for smaller doses ($< 2.5 \times 10^{15} \text{ e/cm}^2$) followed by a decrease at the higher doses. A plausible explanation of this behavior based on the effect of the ionization damage in the polyimide layer at the periphery of the BE junction is discussed.

The slope of the common emitter I-V characteristics in the saturation regime decreases after electron irradiation causing an increase in the $V_{CE,sat}$. We believe this increase is caused by an increase in the collector series resistance.

The increase in the collector series resistance is also shown to be responsible for a decrease of the current gain at high base currents. At lower currents BE SCR SRH recombination is thought to be responsible for the observed gain degradation.

Slight increase in $V_{CE,off}$ observed in common-emitter $J_C - V_{CE}$ characteristics is attributed to the displacement damage in the BC depletion region.

Finally, smaller emitter size (larger perimeter/area) devices show less degradation than the larger emitter devices. This is explained by the smaller radiation damage at the junction peripheries of the passivated devices.

7. Neutron-irradiation experiments on *InP/InGaAs* SHTs have been performed. Devices irradiated up to $6.0 \times 10^{14} \text{ n/cm}^2$ (1 MeV *InGaAs* equivalent) showed significant current gain degradation and noticeable increase in $V_{CE,off}$.

Gradual current gain reduction is attributed to increasing base current, mainly due to growing neutral bulk and BE SCR recombination and recombination-tunneling components. For high doses at low biases increasing base current exhibits ideality factor greater than 2 and is believed to be caused by tunnel-assisted trapping transport.

Current gain degradation has been observed to depend strongly on the current (bias) magnitude – at lower biases gain reduction is much more than that at high biases. Gain degradation coefficient has been shown to have $J_C^{-1/2}$ functional dependence. General models supporting this observation have been developed.

Measured $V_{CE,off}$ shift is believed to be caused by an increase of BC junction current due to growing diffusion and SCR recombination components. Displacement damage introduced in BC SCR and bulk collector is responsible for this effect.

8. Preliminary gamma-irradiation experiments on *InP/InGaAs* SHBTs have been performed. Devices irradiated up to 44.3 *Mrad* can be divided into two groups according to their response to the radiation.

First, as expected for the low doses used in this experiment, displacement-related degradation is little and perfectly fits the degradation pattern observed in our electron and neutron-irradiation studies. That is, defects introduced in the BE and BC junctions are responsible for the observed damage – current gain reduction and $V_{CE,off}$ shift, respectively.

Second type of device response is HBT catastrophic failures of very erratic behavior. The failures can be attributed to formation of leakage channels along the passivation/semiconductor interface due to charge build-up in the passivating dielectric.

9. Finally, a general approach to study/model the radiation-induced device degradation has been presented. According to this gameplan, first the experimentally observed device deterioration and analytical device model are used to identify the physical mechanisms responsible for the degradation. Then, the problem is attacked from the other end – the damage production theory is used to calculate the displacement damage introduced by irradiation in layers of a device. Then using the device model equations the separate current components and total terminal currents are estimated. Finally, device

output characteristics are calculated representing device response to a given radiation environment.

In the progress of this work a number of new questions was raised and a set of further experiments was identified:

1. Gamma irradiation experiments on devices with cyclotene, Si_3N_4 and SiO_2 passivation may be performed to gain better understanding of the device failure mechanism.
2. Further electron, neutron and gamma irradiation experiments are required to identify a metallization scheme minimizing contact resistance degradation.
3. Having investigated degradation effects on the devices operated under DC conditions, one should proceed with a full set of experiments to characterize device high-frequency performance and HF parameter (f_T , f_{max} , NF , etc.) degradation.
4. Further work, in cooperation with the OSU Radiation Center staff, is needed to improve the dosimetry for electron and neutron radiation sources. The Sr/Y beta-source can be calibrated using commercially available RadFETs. The epi-thermal and fast neutron fluxes in the Rotary Specimen Rack of the Mark II Triga reactor can be determined through a set of foil activation experiments as described in Ref. [105].

5. In gamma irradiation experiments samples have to be encapsulated into *Al* plates to achieve the charged-particle-equilibrium necessary if accurate dose calculations are to be performed. The thickness of the *Al* plates can be determined from the procedure described in Ref. [63].
6. Also, gamma irradiation experiments on devices with different metallization schemes (for example, *Al* and *Au*) can be performed to study interface dose enhancement effects.
7. Further work on the HBT analytical model is needed to facilitate more accurate modeling of the high-level injection effects at the BE heterojunction. Also more effort should be put into modeling the post-irradiation base currents observed at low biases in the neutron irradiation experiments.

BIBLIOGRAPHY

- [1] J.F. Ziegler, H.W. Curtis, H.P. Muhlfeld, C.J. Montrose, B. Chin, M. Nicewicz, C.A. Russell, W.Y. Wang, L.B. Freeman, P. Hosier, L.E. LaFave, J.L. Walsh, J.M. Orro, G.J. Unger, J.M. Ross, T.J. O'Gorman, B. Messina, T.D. Sullivan, A.J. Sykes, H. Yourke, T.A. Enger, V. Tolat, T.S. Scott, A.H. Taber, R.J. Sussman, W.A. Klein, and C.W. Wahaus. Comparison of the degradation effects of heavy ion, electron and cobalt-60 irradiation in an advanced bipolar process. *IBM Journal of Research and Development*, 40(1):19, 1996.
- [2] G. A. Schrantz, N. W. van Vonno, W. A. Krull, M. A. Rao, S. I. Long, and H. Kroemer. Neutron irradiation effects in AlGaAs/GaAs heterojunction bipolar transistors. *IEEE Transactions on Nuclear Science*, 35(6):1657–1661, 1988.
- [3] Y. Song, M. E. Kim, A. K. Oki, M. E. Hafizi, W. D. Murlin, J. B. Camou, and K. W. Kobayashi. Effects of neutron irradiation on GaAs/AlGaAs heterojunction bipolar transistors. *IEEE Transactions on Nuclear Science*, 36:2155–2160, 1989.
- [4] S. B. Witmer, S. D. Mittleman, and S. J. Pearton. *Radiation effects on InP-based heterojunction bipolar transistors*, chapter 6, pages 195–228. In *HPBTs: Growth, Processing and Applications*. Artech House, 1995.
- [5] A. Shatalov, S. Subramanian, S. Chnadrasekhar, A. Dentai, and S.M. Goodnick. Electron irradiation effects in polyimide passivated *InP/InGaAs* single heterojunction bipolar transistors. *IEEE Transactions on Nuclear Science*, 46(6):1708–1716, 1999.
- [6] A. Bandyopadhyay, S. Subramanian, S. Chandrasekhar, A. G. Dentai, and S. M. Goodnick. Degradation of DC characteristics of *InGaAs/InP* single heterojunction bipolar transistors under electron irradiation. *IEEE Transaction on Electron Devices*, 46:840–849, 1999.
- [7] A. Bandyopadhyay, S. Subramanian, S. Chandrasekhar, A. G. Dentai, and S. M. Goodnick. Degradation of *InGaAs/InP* double heterojunction bipolar transistors under electron irradiation. *IEEE Transaction on Electron Devices*, 46:850–858, 1999.
- [8] R.N. Nowlin, E.W. Enlow, R.D. Schrimpf, and W.E. Combs. Trends in the total-dose response of modern bipolar transistors. *IEEE Transactions on Nuclear Science*, 39(6):2026–2035, 1992.

- [9] R.D. Schrimpf. Recent advances in understanding total-dose effects in bipolar transistors. *IEEE Transactions on Nuclear Science*, 43:787–796, 1996.
- [10] J.A. Zoytendyk and C.A. Goben. Comparison of the degradation effects of heavy ion, electron and cobalt-60 irradiation in an advanced bipolar process. *IEEE Transactions on Nuclear Science*, 35(6):1428–1431, 1988.
- [11] B. Jalali and S.J. Pearton. *InP HBTs: Growth, Processing, and Applications*. Artech House, 1995.
- [12] C.S. Dyer. Space Radiation Environment Dosimetry, 1998 NSREC Short Course, Section II.
- [13] P. Nieminen, E. Daly and P. Truscott, C. Dyer, H. Evans, F. Lei, R. Gurriaran, and J. Allison. Space radiation and its effects. *GEANT4 Workshop 1998, Niigata - Japan*, 1998.
- [14] G.P. Summers. Displacement Damage: Mechanisms and Measurements, 1992 NSREC Short Course, Section IV.
- [15] H.J. Stein. Electrical properties of neutron-irradiated silicon at 76 k: Hall effect and electrical conductivity. *IEEE Transactions on Nuclear Science*, 15(6):69, 1968.
- [16] G.P. Summers, E.A. Burke, C.J. Dale, E.A. Wolicki, P.W. Marshall, and M.A. Gehlhausen. Correlation of particle-induced damage in silicon. *IEEE Transactions on Nuclear Science*, 34(6):1134–1139, 1987.
- [17] G.P. Summers, E.A. Burke, P. Shapiro, S.R. Messenger, and R.J. Walters. Damage correlations in semiconductors exposed to gamma, electron and proton radiations. *IEEE Transactions on Nuclear Science*, 40(6):1372–1379, 1993.
- [18] G.P. Summers, R.J. Walters, M.A. Xapsos, E.A. Burke, S.R. Messenger, P. Shapiro, and R.L. Statler. A new approach to damage prediction for solar cells exposed to different radiations. *IEEE Transactions on Nuclear Science*, 11:11–11, 1994.
- [19] M.A. Xapsos, G.P. Summers, C.C. Blatchley, C.W. Colerico, E.A. Burke, S.R. Messenger, and P. Shapiro. Co^{60} gamma ray and electron displacement damage studies of semiconductors. *IEEE Transactions on Nuclear Science*, 41(6):1945–1949, 1994.
- [20] G.P. Summers, E.A. Burke, M.A. Xapsos, C.J. Dale, P.W. Marshall, and E.L. Petersen. Displacement damage in GaAs structures. *IEEE Transactions on Nuclear Science*, 35:1221–1226, 1987.

- [21] S.M. Khanna, A. Houdayer, A. Jorio, C. Carlone, M. Parenteau, and J.W. Gerdes Jr. Nuclear radiation displacement damage prediction in gallium arsenide through low temperature photoluminescence measurements. *IEEE Transaction on Nuclear Science*, 43(6):2601–2603, 1996.
- [22] C.W. Colerico, H.B. Serreze, S.R. Messenger, M.A. Xapsos, and E.A. Burke. Alpha particle simulation of space radiation damage effects in semiconductor devices. *IEEE Transactions in Nuclear Science*, 42(6):2089–2094, 1995.
- [23] P.J. Griffin, J.G. Kelly, T.F. Luera, A.L. Bary, and M.S. Lazo. Neutron damage equivalence in GaAs. *IEEE Transactions on Nuclear Science*, 38(6):1216–1222, 1991.
- [24] T.R. Luera, J.G. Kelly, H.J. Stein, M.S. Lazo, C.E. Lee, and L.R. Dawson. Neutron damage equivalence for silicon, silicon dioxide, and gallium arsenide. *IEEE Transactions on Nuclear Science*, 34(6):1557–1563, 1987.
- [25] A.M. Ougouag, J.G. Williams, M.B. Danjaji, S.Y. Yang, and J.L. Meason. Differential displacement kerma cross sections for neutron interactions in Si and GaAs. *IEEE Transactions on Nuclear Science*, 37(6):2219–2228, 1990.
- [26] *Characterizing Neutron Energy Fluence Spectra in Terms of an Equivalent Monoenergetic Neutron Fluence for Radiation-Hardness Testing of Electronics*, volume 12.02, pages 340–355. Annual Book of ASTM Standards. ASTM, 1993.
- [27] P.V. Dressendorfer. Basic Mechanisms for the New Millenium, 1998 NSREC Short Course, Section III.
- [28] J.R. Schwank. Basic Mechanisms of Radiation Effects in the Natural Space Environment, 1994 NSREC Short Course, Section II.
- [29] J.Lindhard, V. Nielsen, M. Scharff, and P.V. Thomsen. Integral equations governing radiation effects. *Matematisk-fysiske Meddelelser*, 33(10):1–42, 1963.
- [30] D.G. Doran. Neutron displacement cross section for stainless steel and tantalum based on a Lindhard model. *Nuclear Science and Engineering*, 49:130–144, 1972.
- [31] B.T. Kelly. *Irradiation Damage in Solids*. Pergamon Press, 1966.
- [32] D.R. Olander. *Fundamental aspects of nuclear reactor fuel elements*. Technical Information Center, Office of Public Affairs, Energy Research and Development Administration, Oak Ridge, 1976.

- [33] M.J. Norgett, M.T. Robinson, and I.M. Torrens. A proposed method of calculating displacement dose rates. *Nuclear Engineering and Design*, 33:50–54, 1975.
- [34] K.A. LaBel. Single Event Effect Criticality Analysis/ Code QW [web page] February 15 1996; <http://flick.gsfc.nasa.gov/radhome/papers/seecai.htm>. [Accessed 02/2000].
- [35] A.L. Barry, R. Maxseiner, R. Wojcik, M.A. Briere, and D.Braunig. An improved displacement damage monitor. *IEEE Transactions in Nuclear Science*, 37(6):1726–1731, 1990.
- [36] G.J. Shaw, S.R. Messenger, R.J. Walters, and G.P. Summers. Radiation-induced reverse dark currents in $In_{0.53}Ga_{0.47}As$ photodiodes. *Journal of Applied Physics*, 73:7244–7249, 1993.
- [37] G.J. Shaw, R.J. Walters, S.R. Messenger, and G.P. Summers. Time dependence of radiation-induced generation currents in irradiated $InGaAs$ photodiodes. *Journal of Applied Physics*, 74:1629–1635, 1993.
- [38] H. Ohyama, J. Vanhellemont, Y. Takami, T. Kudou, and H. Sunaga. Radiation damage in $InGaAs$ photodiodes by 1 MeV fast neutrons. *Radiation Physics and Chemistry*, 53:597–602, 1998.
- [39] C.E. Barnes. Radiation effects in $1.06\text{-}\mu$ $InGaAs$ LED's and Si Photodiodes. *Journal of Applied Physics*, 50(8):5242–5250, 1979.
- [40] M. Levinson, J.L. Benton, H. Temkin, and L.C. Kimerling. Defect states in electron bombarded $n - InP$. *Applied Physics Letters*, 40:990–992, 1982.
- [41] S.W.S. McKeever, R.J. Walters, S.R. Messenger, and G.P. Summers. Deep level transient spectroscopy of irradiated p-type InP grown by metalorganic chemical vapor deposition. *Journal of Applied Physics*, 69:1435–1439, 1991.
- [42] J. Koyama, J. Shirafuji, and Y. Inuishi. Annealing behaviour of gamma-ray-induced electron traps in LEC $n - InP$. *Electronics Letters*, 19:609–610, 1983.
- [43] R.J. Walters and G.P. Summers. Degradation and annealing of electron-irradiated diffused junction InP solar cells. *Journal of Applied Physics*, 78:7368–7375, 1995.
- [44] R.J. Walters, M.J. Romero, D. Araujo, R. Garcia, S.R. Messenger, and G.P. Summers. Detailed defect study in proton irradiated InP/Si solar cells. *Journal of Applied Physics*, 86:3584–3589, 1999.

- [45] G. Messenger and J. Spratt. The effects of irradiation on germanium and silicon. *Proceedings IRE*, 46:1038–1044, 1958.
- [46] *Dosimetry of External Beta Rays for Radiation Protection*. ICRU Report 56, 1997.
- [47] F.H. Attix. *Introduction to Radiological Physics and Radiation Dosimetry*. John Wiley & Sons, 1986.
- [48] D.W. Anderson. *Absorption of Ionizing Radiation*. University Park Press, 1984.
- [49] *Stopping Powers for Electrons and Positrons*. ICRU Report 37, 1984.
- [50] M.J. Berger and S.M. Seltzer. *Stopping Powers and Ranges of Electrons and Positrons*. National Bureau of Standards, 1983.
- [51] M. J. Berger. Stopping-Power and Range Tables for Electrons, Protons, and HeliumIons. [web page] October 1999; <http://physics.nist.gov/PhysRefData/Star/Text/contents.html>. [Accessed 01/1999-02/2000].
- [52] S.M. Seltzer and M.J. Berger. Bremsstrahlung spectra from electron interactions with screened atomic nuclei and orbital electrons. *Nuclear Instrumentation and Methods*, B12:95–, 1985.
- [53] R.M. Curr. The coulomb scattering of high-energy electrons and positrons by nuclei. *Proceedings of Royal Physical Society (London)*, A69:156–164, 1955.
- [54] R.B. Firestone, V.S. Shirley, C.M. Baglin, S.Y.F. Chu, and J. Zipkin, editors. *Table of isotopes*. John Wiley & Sons, 1996.
- [55] Y. Lifshitz, J. Levinson, Y. Noter, Y. Shamaï, A. Akkerman, O. Even, A. Zentner, M. Israeli, A. Gibrekhterman, and L. Singer. A portable planar $Sr - 90$ irradiation setup for total dose testing of electronic devices. *IEEE Transaction on Nuclear Science*, 40:1388–1392, 1993.
- [56] Data Available from the Nuclear Information Center. [web page] 23 Dec 1999; <http://t2.lanl.gov/data/data.html>. [Accessed 01/1999-01/2000].
- [57] W.H. Press, S.A. Teukolsky, W.T. Vetterling, and B.P. Flannery. *Numerical Recipes in C*. Cambridge University Press, 1992.
- [58] S. Reese. Private Communication, September 1999.

- [59] M.J. Berger and J.H. Hubbell. NIST XCOM: Photon Cross Section Database. [web page] August 1999; <http://physics.nist.gov/PhysRefData/Xcom/Text/XCOM.html>. [Accessed 01/1999-02/2000].
- [60] J.H. Hubbell, W.J. Veigele, E.A. Briggs, R.T. Brown, D.T. Cromer, and R.J. Howerton. Atomic form factors, incoherent scattering functions, and photon scattering cross sections. *Journal of Physical and Chemical Reference Data*, 4:471–538, 1975.
- [61] L.V. Spencer and U.Fano. Energy resulting from electron slowing down. *Physical Review*, 93(6):1172–1181, 1954.
- [62] Oregon State University Radiation Center. Facilities and Services, 1991.
- [63] *Calculating Absorbed Dose From Gamma or X Radiation*, volume 12.02, pages 246–251. Annual Book of ASTM Standards. ASTM, 1993.
- [64] *Minimizing Dosimetry Errors in Radiation Hardness testing of Silicon Electronic Devices Using Co-60 Sources*, volume 12.02, pages 772–783. Annual Book of ASTM Standards. ASTM, 1993.
- [65] J.C. Garth, E.A. Burke, and S Woolf. Displacement damage and dose enhancement in gallium arsenide and silicon. *IEEE Transactions on Nuclear Science*, 32(6):4382–4387, 1985.
- [66] F. Ali and A. Gupta, editors. *HEMTs and HBTs: devices, fabrication, and circuits*. Artech House, 1991.
- [67] D. Sawdai, J.O. Plouchart, D. Pavlidis, A. Samelis, and K. Hong. Power performance of *InGaAs/InP* single HBTs. *IPRM Conference*, 1996.
- [68] E. Alekseev and D. Pavlidis. DC and high-frequency of *AlGaIn/GaN* heterojunction bipolar transistors. *Solid State Electronics*, 44:245–252, 2000.
- [69] Silicon Germanium BiCMOS Technology. [web page]; <http://www.chips.ibm.com/sige/technology.html> [Accessed 03/2000].
- [70] IEDM to include the latest results from III-V microelectronics: Record HBT performance. *Compound Semiconductor*, Fall 11:11–12, 1998.
- [71] B. Agarwal, D. Mensa, R. Pullela, Q. Lee, U. Bhattacharya, L. Samoska, J. Guthrie, and M.J.W. Rodwell. A 277-GHz f_{max} transferred-substrate heterojunction bipolar transistor. *IEEE Transaction on Electron Devices*, 18:228–232, 1997.

- [72] N. Matine, N.W. Dvorak, C.R. Bolognesi, X. Xu, and S.P. Watkins. *InP/GaAsSb/InP* DHBTs with near-ideal characteristics. *Electronics Letters*, 34(17):1700–1705, 1998.
- [73] G. Massobrio and P. Antognetti. *Semiconductor Device Modeling With SPICE*. McGraw-Hill, 1993.
- [74] J. J. Liou, C.I. Huang, B. Bayraktaroglu, D.C. Williamson, and K.B. Parab. Base and collector leakage currents of *AlGaAs/GaAs* heterojunction bipolar transistor. *Journal of Applied Physics*, 76(5):3187–3193, 1994.
- [75] D. Caffin, A.M. Duchenois, F. Heliot, C. Besombes, J.L. Benchimol, and P. Launay. Base-collector leakage currents in *InP/InGaAs* double heterojunction bipolar transistors. *IEEE Transactions on Electron Devices*, 44(6):930–936, 1997.
- [76] J.J. Liou. *Advanced Semiconductor Device Physics and Modeling*. Artech House, 1994.
- [77] A.A. Grinberg, M.S. Shur, R.J. Fischer, and H. Morko. An investigation of the effect of graded layers and tunneling on the performance of *AlGaAs/GaAs* heterojunction bipolar transistors. *IEEE Transactions on Electron Devices*, 31(12):1758–1765, 1984.
- [78] S. Searles and D.L. Pulfrey. An analysis of space-charge region recombination in HBT's. *IEEE Transactions on Electron Devices*, 41(4):476–483, 1994.
- [79] R. L. Liboff. *Introductory Quantum Mechanics*. Addison-Wesley, 1993.
- [80] S. Tiwari. *Compound Semiconductor Device Physics*. Academic Press, 1992.
- [81] O. Madelung. *Semiconductors – Basic Data*. Springer, 1996.
- [82] P. Bhattacharya, editor. *Properties of Lattice-Matched and Strained Indium Gallium Arsenide*. INSPEC, IEE, 1996.
- [83] A.A. Grinberg and S. Luryi. on the thermionic-diffusion theory of minority transport in heterostructure bipolar transistors. *IEEE Transactions on Electron Devices*, 40(5):859–866, 1993.
- [84] S.M. Sze. *Physics of Semiconductor Devices*. John Wiley & Sons, 1981.
- [85] C.H. Henry, R.A. Logan, and F.R. Merritt. The effect of surface recombination on current in $Al_xGa_{1-x}As$ heterojunction. *Journal of Applied Physics*, 49:3530–3542, 1978.

- [86] B.R. Ryum and I.M. Abdel-Motaleb. Effect of recombination current on current gain of HBTs. *IEEE Proceedings - G*, 138(1):115–119, 1991.
- [87] A. Shatalov. Private Communication, June 1999.
- [88] S. Subramanian. Private Communication, January 2000.
- [89] C. Sah, R.N. Noyce, and W. Shockley. Carrier generation and recombination in $p - n$ junctions and $p - n$ junction characteristics. *Proceedings of IRE*, 45:1228–1243, 1957.
- [90] A. Schenk. *Advanced Physical Models for Silicon Device Simulation*. Springer - Wien - New York, 1998.
- [91] C.T. Sah. The equivalent circuit model in solid-state electronics - part i: Single energy level defect centers. *Proceedings of the IEEE*, 55(5):654–671, 1967.
- [92] C.T. Sah. Electronic processes and excess currents in gold-doped narrow silicon junctions. *Physical Review*, 123(5):1594–1912, 1961.
- [93] A.G. Chynoweth and W.L. Feldman and R.A. Logan. Excess tunnel current in silicon Esaki junctions. *Physical Review*, 121(3):684–694, 1961.
- [94] A.R. Riben and D.L. Feucht. $n\text{ Ge} - p\text{ GaAs}$ heterojunctions. *Solid State Electronics*, 9:1055–1065, 1966.
- [95] J.P. Donnelly and A.G. Milnes. Current/voltage characteristics of $p - n\text{ Ge} - \text{Si}$ and $\text{Ge} - \text{GaAs}$ heterojunctions. *Proceedings of IEE*, 113(9):1468–1476, 1966.
- [96] High-Frequency Transistor Primer. [Hewlett Packard]; Available at <http://www.hp.com/rf/> [Accessed 12/1999].
- [97] S.P. Voinigescu, M.C. Maliepaard, J.L. Showell, G.E. Babcock, D. Marchesan, M. Schroter, P. Schvan, and D.L. Hareme. A scalable high-frequency noise model for bipolar transistors with application to optimal transistor sizing for low-noise amplifier design. *IEEE Journal of Solid State Circuits*, 32(9):1430–1438, 1997.
- [98] A. Dentai and S. Subramanian. Private Communication, June 1998.
- [99] S. Chandrasekhar and S. Subramanian. Private Communication, July 1998.
- [100] A. Sarkar. Radiation effects in compound semiconductor heterostructure devices. Master of Science Thesis, Oregon State University, 1998.

- [101] J. J. Liou, L. L. Liou, and C. I. Huang. Kink effect on the base current of heterojunction bipolar transistors. *Solid State Electronics*, 36:1222–1224, 1993.
- [102] M. Sotoodeh, A.H. Khalid, and A.A. Rezazadeh. DC characterization of HBTs using the observed kink effect on the base current. *Solid State Electronics*, 42(4):531–539, 1998.
- [103] S. Tiwari, D. J. Frank, and S. L. Wright. Surface recombination in GaAlAs/GaAs heterojunction bipolar transistors. *Journal of Applied Physics*, 64:5009–5012, 1988.
- [104] S. Subramanian, A. Sarkar, L. Ungier, and S.M. Goodnick. Integrity of III-V heterojunction interfaces under gamma irradiation. *IEEE Transactions on Nuclear Science*, 44:1862–1869, 1997.
- [105] *Standard Guide for Selection and Use of Neutron-Activation Foils for Determining Neutron Spectra Employed in Radiation-Hardness Testing of Electronics*, volume 12.02. Annual Book of ASTM Standards. ASTM, 1993.